



---

---

About the cover: **Tailor-made suit which consists of hexagonal ZnS bifrustums.** A Transmission Electron Microscopy image of a self-assembled monolayer of hexagonal ZnS bifrustums (described in Chapter 9 of this thesis) was used to construct the cover.

PhD thesis, Universiteit Utrecht

**Tailoring on the nanoscale**

Control over size, shape, composition and self-assembly of copper chalcogenide nanocrystals  
Ward van der Stam, September 2016

Printed by: Uitgeverij BOXPress || Proefschriftmaken.nl

ISBN: 978-94-6295-475-5

---

---

# Tailoring on the nanoscale

Control over size, shape, composition and self-assembly  
of copper chalcogenide nanocrystals

## **Op maat gemaakt op de nanoschaal**

Controle over de grootte, vorm, compositie en zelf-organisatie  
van koper chalcogenide nanokristallen  
(met een samenvatting in het Nederlands)

## Proefschrift

ter verkrijging van de graad van doctor aan de Universiteit Utrecht op gezag van de  
rector magnificus, prof. dr. G. J. van der Zwaan, ingevolge van het besluit van het  
college voor promoties in het openbaar te verdedigen

op maandag 26 september 2016

des middags te 12.45 uur

door

**Ward van der Stam**

geboren op 14 april 1989 te Nieuwegein

---

---

**Promotor:**

Prof. dr. A. Meijerink

**Co-promotor:**

Dr. C. de Mello Donegá

The research described in this thesis was funded by the division of Chemical Sciences (CW) of the Netherlands Organization for Scientific Research (NWO) under grant number ECHO.712.012.001 (applicant: C. de Mello Donegá)

## Table of contents

<b>List of publications</b>	<b>vi</b>
<b>Chapter 1</b> General Introduction to Semiconductor Nanocrystals	<b>1</b>
<b>Chapter 2</b> Synthesis and Optical Properties of Colloidal (Hetero)Nanocrystals	<b>7</b>
<b>Part A - Shape Tailoring</b>	
<b>Chapter 3</b> Shape Control of Colloidal $\text{Cu}_{2-x}\text{S}$ Polyhedral Nanocrystals by Tuning the Nucleation Rates	<b>49</b>
<b>Chapter 4</b> Solution-Processable Ultrathin Size- and Shape-Controlled Colloidal $\text{Cu}_{2-x}\text{S}$ Nanosheets	<b>71</b>
<b>Chapter 5</b> <i>In-situ</i> Probing of Stack-Templated Growth of Ultrathin $\text{Cu}_{2-x}\text{S}$ Nanosheets	<b>93</b>
<b>Part B - Composition Tailoring</b>	
<b>Chapter 6</b> Luminescent $\text{CuInS}_2$ Quantum Dots by Partial Cation Exchange in $\text{Cu}_{2-x}\text{S}$ Nanocrystals	<b>117</b>
<b>Chapter 7</b> Near-Infrared Emitting $\text{CuInSe}_2/\text{CuInS}_2$ Core/Shell Heteronanorods by Sequential Cation Exchange	<b>135</b>
<b>Part C - Superstructure Tailoring</b>	
<b>Chapter 8</b> Self-Assembly of Hexagonal Bipyramid- and Bifrustum-Shaped $\text{ZnS}$ Nanocrystals into 2D Superlattices	<b>153</b>
<b>Chapter 9</b> Oleic Acid-Induced Atomic Alignment of $\text{ZnS}$ Polyhedral Nanocrystals	<b>167</b>
<b>Chapter 10</b> Summary and Outlook	<b>185</b>
<b>Samenvatting in het Nederlands</b>	<b>191</b>
<b>Acknowledgments</b>	<b>201</b>

## List of publications

This thesis was based on the following publications:

1. W. van der Stam, A. C. Berends and C. de Mello Donega, Prospects of Colloidal Copper Chalcogenide Nanocrystals, *ChemPhysChem*, **2016**, 17, 559–581. (Chapter 2) Invited contribution to the Special Issue ‘Beyond Conventional Quantum Dots’, Front Cover
2. W. van der Stam, S. Gradmann, T. Altantzis, X. Ke, M. Baldus, S. Bals and C. de Mello Donega, Shape Control of Colloidal Cu<sub>2-x</sub>S Polyhedral Nanocrystals by Tuning the Nucleation Rates, **2016**, submitted, (Chapter 3)
3. W. van der Stam, Q. A. Akkerman, X. Ke, M. A. van Huis, S. Bals and C. de Mello Donega, Solution-Processable Ultrathin Size- and Shape-Controlled Colloidal Cu<sub>2-x</sub>S Nanosheets, *Chem. Mater.*, **2015**, 27, 283–291. (Chapter 4)
4. W. van der Stam, F. T. Rabouw, J. J. Geuchies, A. C. Berends, S. O. M. Hinterding, R. G. Geitenbeek, J. van der Lit, S. Prévost, A. V. Petukhov and C. de Mello Donega, *In-Situ* Probing of Stack-Templated Growth of Ultrathin Cu<sub>2-x</sub>S Nanosheets, *Chem. Mater.*, **2016**, doi:10.1021/acs.chemmater.6b02787. (Chapter 5)
5. W. van der Stam, A. C. Berends, F. T. Rabouw, T. Willhammar, X. Ke, J. D. Meeldijk, S. Bals and C. de Mello Donega, Luminescent CuInS<sub>2</sub> Quantum Dots by Partial Cation Exchange in Cu<sub>2-x</sub>S Nanocrystals, *Chem. Mater.*, **2015**, 27, 621–628. (Chapter 6)
6. W. van der Stam, E. Bladt, F. T. Rabouw, S. Bals and C. de Mello Donega, Near-Infrared Emitting CuInSe<sub>2</sub>/CuInS<sub>2</sub> Dot Core/Rod Shell Heteronanorods by Sequential Cation Exchange, *ACS Nano*, **2015**, 9, 11430–11438. (Chapter 7)
7. W. van der Stam, A. P. Gantapara, Q. A. Akkerman, G. Soligno, J. D. Meeldijk, R. van Roij, M. Dijkstra and C. de Mello Donega, Self-Assembly of Hexagonal Bipyramid- and Bifrustum-Shaped ZnS Nanocrystals into 2D Superlattices, *Nano Lett.*, **2014**, 14, 1032–1037. (Chapter 8)
8. W. van der Stam, F. T. Rabouw, S. J. W. Vonk, J. J. Geuchies, H. Ligthart, A. V. Petukhov and C. de Mello Donega, Oleic Acid-Induced Atomic Alignment of ZnS Polyhedral Nanocrystals, *Nano Lett.*, **2016**, 16, 2608–2614. (Chapter 9)

## Other publications:

1. S. O. M. Hinterding, W. van der Stam, M. Kurttepli, J. D. Meeldijk, S. Bals and C. de Mello Donega, Tailoring the Ga-precursor Reactivity to Control the Ga<sup>3+</sup> for Cu<sup>+</sup> Cation Exchange Rates in Cu<sub>2-x</sub>S Nanocrystals, in preparation
2. A. C. Berends, W. van der Stam, E. Bladt, S. Bals and C. de Mello Donega, On the heteroepitaxial growth of ZnS on CuInS<sub>2</sub> nanocrystals, in preparation
3. F. T. Rabouw, N. M. B. Cogan, A. C. Berends, W. van der Stam, D. Vanmaekelbergh, A. F. Koenderink, T. D. Krauss and C. de Mello Donega, Non-blinking Single-Photon Emitters in Silica, *Sci. Rep.*, **2016**, 6, 21187–21193.

## List of presentations

### 2013

#### Synthesis & Shape Control of Cu<sub>2-x</sub>S Nanocrystals: SnX Ligands (poster)

*NWO: Chemistry in relation to Physics and Materials Sciences, Veldhoven, The Netherlands, March 2013*

### 2014

#### Shape Control and Self-Assembly of Polyhedral Colloidal Metal Sulfide Nanocrystals (poster)

*Physics @ FOM, Veldhoven, The Netherlands, January 2014*

#### Shape Control of Colloidal Cu<sub>2-x</sub>S Nanocrystals by Sn(IV)-complexes (poster)

*Materials Research Society Spring Meeting, San Francisco, USA, April 2014*

#### Solution-Processable Ultrathin Size- and Shape-Controlled Colloidal 2D Cu<sub>2-x</sub>S Nanosheets (poster)

*Materials Research Society Spring Meeting, San Francisco, USA, April 2014*

#### Self-Assembly of Colloidal Hexagonal Bipyramid- and Bifrustum-shaped ZnS Nanocrystals into Two-Dimensional Superstructures (oral)

*Nanax6 conference, Bad Hofgastein, Austria, May 2014*

#### Solution-Processable Ultrathin Size- and Shape-Controlled Colloidal 2D Cu<sub>2-x</sub>S Nanosheets (poster)

*Nanax6 conference, Bad Hofgastein, Austria, May 2014, winner second poster prize (€150)*

#### Shape Control of Colloidal Cu<sub>2-x</sub>S Nanocrystals by Sn(IV)-complexes (poster)

*Nanax6 conference, Bad Hofgastein, Austria, May 2014*

#### Solution-Processable Ultrathin Size- and Shape-Controlled Colloidal 2D Cu<sub>2-x</sub>S Nanosheets (oral)

*European Materials Research Society Meeting, Lille, France, May 2014*

**Self-Assembly of Colloidal Hexagonal Bipyramid- and Bifrustum-shaped ZnS Nanocrystals into Two-Dimensional Superstructures (oral)**

*European Materials Research Society Meeting, Lille, France, May 2014*

**Solution-Processable Ultrathin Size- and Shape-Controlled Colloidal 2D Cu<sub>2-x</sub>S Nanosheets (poster)**

*30 years of QDs meeting, Paris, France, May 2014*

## 2015

**Solution-Processable Ultrathin Size- and Shape-Controlled Colloidal 2D Cu<sub>2-x</sub>S Nanosheets (poster)**

*Physics @ FOM, Veldhoven, The Netherlands, January 2015*

**Making @ Condensed Matter and Interfaces: Quantum Dots, Lanthanides, Superstructures and STM (oral)**

*Debye Meeting Days, Debye Institute, Corsendonk de Linde, Belgium, April 2015*

**In-situ Small-Angle X-ray Scattering during the Formation of Colloidal Cu<sub>2-x</sub>S Nanosheets (poster)**

*NWO SYnchrotron and NEutron Workshop (SyNew), Utrecht, The Netherlands, June 2015*

**Self-Assembly of Colloidal Nanocrystals into Two-Dimensional Superstructures (oral)**

*SOMATAI meeting, Institute for Theoretical Physics, Utrecht, The Netherlands, August 2015*

**Tailor-made Binary and Ternary Colloidal Nanocrystals and Nanocrystal Superstructures (oral)**

*Debye Lunch Lecture, Debye Institute, Utrecht, The Netherlands, September 2015*

**Near-infrared Emitting CuInSe<sub>2</sub>/CuInS<sub>2</sub> Dot Core/Rod Shell Heteronanorods by Sequential Cation Exchange (oral)**

*FQDots conference, Santiago de Compostela, Spain, September 2015*

**In-situ Small-Angle X-ray Scattering during the Formation of Colloidal Cu<sub>2-x</sub>S Nanosheets (poster)**

*FQDots conference, Santiago de Compostela, Spain, September 2015*

**Formation of 2D Cu<sub>2-x</sub>S Nanosheets Studied by In-situ Small-Angle X-ray Scattering (oral)**

*Materials Research Society Fall Meeting, Boston, USA, December 2015*

**Near-infrared Emitting CuInSe<sub>2</sub>/CuInS<sub>2</sub> Dot Core/Rod Shell Heteronanorods by Sequential Cation Exchange (poster)**

*Materials Research Society Fall Meeting, Boston, USA, December 2015*

**In-situ X-ray Scattering Studies of Formation and Self-Organization of Colloidal Nanocrystals (oral)**

*Nanoseminar Debye Institute, Utrecht, The Netherlands, December 2015*

**2016**

**Tailor-made Colloidal Nanocrystals and Nanocrystal Superstructures (oral)**

*Max-Planck Institute for Polymerforschung, Mainz, Germany, March 2016*

**Tailor-made Colloidal Nanocrystals and Nanocrystal Superstructures (oral)**

*Technical University of Delft, Delft, The Netherlands, March 2016*

**Partial Cation Exchange Reactions Toward Ternary (Hetero)Nanocrystals with Near-Infrared Luminescence (oral)**

*9<sup>th</sup> International Conference on Quantum Dots, Jeju, South-Korea, May 2016*

**Oleic Acid-Induced Atomic Alignment of ZnS Polyhedral Nanocrystals Studied with *In-situ* GISAXS (poster)**

*9<sup>th</sup> International Conference on Quantum Dots, Jeju, South-Korea, May 2016*

**Tailor-made Colloidal Nanocrystals and Nanocrystal Superstructures (oral)**

*RIKEN Institute, Tokyo, Japan, June 2016*

**Tailoring the Carrier Localization Regime in Colloidal CuInSe<sub>2</sub>/CuInS<sub>2</sub> Core/Shell Nanocrystals (oral)**

*FQDots conference, Berlin, Germany, September 2016*

***In-situ* Probing of Stack-Templated Growth of Ultrathin Cu<sub>2-x</sub>S Nanosheets (poster)**

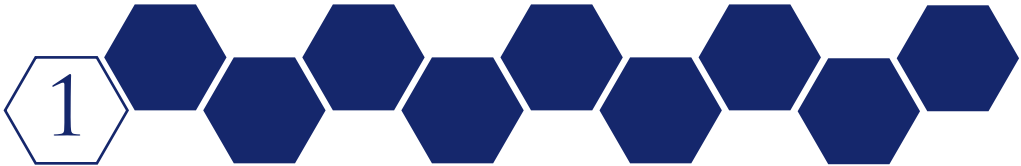
*FQDots conference, Berlin, Germany, September 2016*

**Charge Carrier Dynamics in Colloidal Ultrathin 2D Cu<sub>2-x</sub>S Nanosheets (oral)**

*Sol2D conference, Berlin, Germany, September 2016*



# General Introduction to Semiconductor Nanocrystals



## ABSTRACT

Semiconductors play a pivotal role in our daily lives. Without semiconductors, many technologies that we rely on every day, such as our smartphones, televisions and computers, would not exist. There is a constant search in the scientific community for new materials that can, for example, effectively convert the energy of the sun to electricity (solar cells), or produce light (light-emitting diodes). Colloidal semiconductor nanocrystals are attractive for such applications due to their size and shape tunability. However, their successful implementation into applications is severely hindered by toxicity issues concerning the use of heavy metals such as Cd and Pb. Cu-chalcogenide nanomaterials, however, offer a compelling alternative. This thesis aims to provide a pathway toward tailored Cu-chalcogenide nanomaterials with unprecedented optoelectronic properties.

## 1.1 Semiconductor nanocrystals

Semiconductor materials are commonplace in everyday life and most people could not live without them. For example, silicon chips are used in many technologies, such as smartphones and computers. Recently, colloidal semiconductor nanocrystals have gained a lot of interest, due to the possibility to precisely tune their optoelectronic properties. This tunability is caused by the quantum confinement effect.<sup>1–3</sup> The quantum confinement effect causes that if a semiconductor has dimensions of a few nanometers, the optoelectronic properties change significantly. For example, different photoluminescence energies and colors can be obtained for colloidal CdSe nanocrystals of various sizes (Figure 1.1a).<sup>1</sup> Nowadays, such colloidal semiconductor nanocrystals show potential use in applications such as television screens (Figure 1.1b),<sup>4</sup> solar cells<sup>5</sup> and light-emitting diodes (LEDs).<sup>6</sup> The easy tunability of colloidal semiconductor nanocrystals in terms of size, shape and surface functionalization, makes colloidal nanocrystals extremely interesting for solution processable methods, since layers of different sizes of nanocrystals can be easily printed on any desired substrate. However, the integration of semiconductor nanocrystals into devices is severely hindered by toxicity issues concerning the use of heavy metals such as Cd and Pb.<sup>6,7</sup> Copper chalcogenide nanomaterials offer an interesting alternative, since they have shown to possess similar (*e.g.* photoluminescence), or novel (*e.g.* plasmonics), properties and are comprised of less toxic and more abundant elements such as Cu, Zn and Sn (Figure 1.1c).<sup>7</sup> Although a lot of research has been performed to obtain the same level of mastery

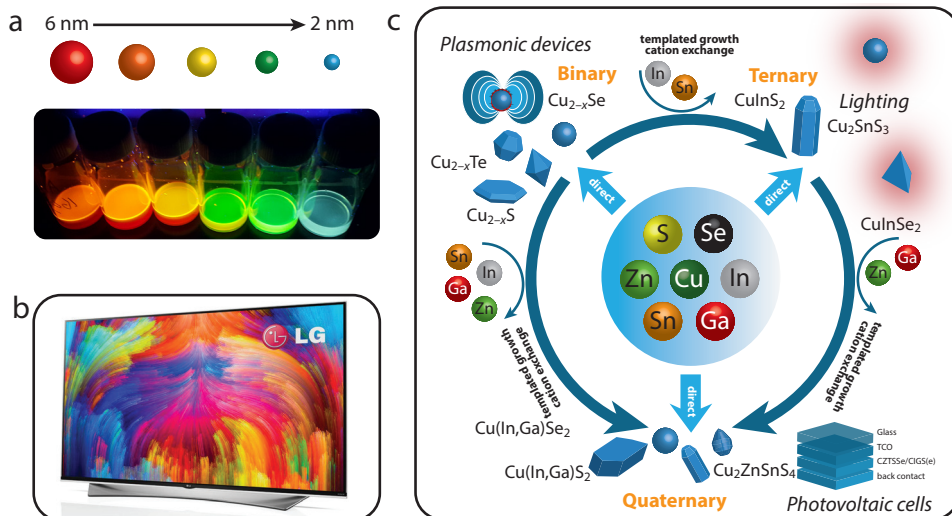


**Figure 1.1. Colloidal semiconductor nanocrystals and their (potential) applications.** (a) When the size of CdSe nanocrystals (NCs) is varied from 6 nm to 2 nm, the photoluminescence can be tuned from red to blue under UV illumination. Sample courtesy of Angela Melcherts. (b) This is particularly relevant for applications such as televisions, due to the bright emission colors.<sup>4</sup> (c) Cu chalcogenides offer an interesting alternative for Cd-containing nanocrystals, due to their less toxic components and size, shape and composition tunability.<sup>7</sup>

over the synthesis of Cu-chalcogenide nanocrystals, as is currently available for Cd- and Pb-chalcogenide nanocrystals, and hence precisely tune the optoelectronic properties of colloidal Cu chalcogenide nanomaterials, there is still room for improvement.

## 1.2 Outline

In this thesis, I will discuss synthetic methodologies that were developed to gain control over the synthesis and the optoelectronic properties of colloidal Cu-chalcogenide nanomaterials, with special emphasis on alternative synthesis approaches (*i.e.* cation exchange). The thesis is divided into three parts (Part A: Shape Tailoring, Part B: Composition Tailoring, Part C: Superstructure Tailoring) and nine chapters.

In **Chapter 2** the theory necessary to understand some key aspects of the thesis will be discussed in more detail. For example, band formation in semiconductors and quantum confinement in semiconductor nanocrystals is touched upon. Furthermore, the developments in the field in terms of synthetic strategies (both for ‘conventional’ colloidal nanomaterials in general, as well as Cu-chalcogenide nanomaterials in particular) will be briefly addressed, together with the optoelectronic properties of Cu-chalcogenide nanocrystals.

**Chapter 3** describes a novel method to control the shape of polyhedral  $\text{Cu}_{2-x}\text{S}$  nanocrystals, in which size and shape are tailored by changing just one single variable: the concentration of an additive ( $\text{SnBr}_4$ ). Our results show that Sn-thiolate complexes formed *in-situ* influence the nucleation and growth rates of  $\text{Cu}_{2-x}\text{S}$  nanocrystals, without incorporation of the  $\text{Sn}^{4+}$  ions in the final product.

In **Chapter 4** the synthesis of ultrathin 2D  $\text{Cu}_{2-x}\text{S}$  nanosheets is discussed. Our data shows that halides promote the formation of 2D nanomaterials with well-defined shapes (chloride: triangular, bromide: hexagonal) and a constant thickness of 2 nm. Furthermore, the lateral dimensions can be tuned from 100 nm to 400 nm by varying the concentration or to several micrometers by removing the coordinating ligand. In this way, well-defined  $\text{Cu}_{2-x}\text{S}$  nanosheets with various shapes and sizes can be synthesized.

**Chapter 5** shows *in-situ* Small-Angle X-ray Scattering (SAXS) data obtained during the synthesis of the ultrathin  $\text{Cu}_{2-x}\text{S}$  nanosheets (NSs) discussed in chapter 4. This *in-situ* study revealed that halides alter the Cu-thiolate precursor, which results in stack-templated nucleation and growth of ultrathin NSs. Since the NSs are directly stacked, the growth in the thickness direction is inhibited and Cu-S monomers are only added in the lateral direction, resulting in anisotropic  $\text{Cu}_{2-x}\text{S}$  NSs.

Chapters 6 and 7 show that the composition of Cu-chalcogenide nanomaterials can be post-synthetically tailored toward ternary compositions. In **Chapter 6** we show that the

exchange of  $\text{In}^{3+}$  for  $\text{Cu}^+$  in  $\text{Cu}_{2-x}\text{S}$  NCs is delicate and needs to be precisely balanced. Furthermore, we found that the exchange is self-limiting, stopping when the ternary  $\text{CuInS}_2$  composition is reached (instead of full conversion to  $\text{In}_2\text{S}_3$ ), since the anionic sublattice has to rearrange from an hcp to an fcc arrangement in order to accommodate all the  $\text{In}^{3+}$  ions and form  $\text{In}_2\text{S}_3$ .

In **Chapter 7** we extended this knowledge to complex dot-in-rod heteroarchitectures. In our novel approach, the in- and outward diffusion rates are coupled due to the use of a stoichiometric  $\text{InCl}_3$ -phosphine complex which simultaneously acts as Cu-extracting and In-delivering agent. In this way,  $\text{CuInSe}_2/\text{CuInS}_2$  dot-in-rod heterostructures were prepared with tunable near-infrared (NIR) photoluminescence, as well as other ternary CuIn-chalcogenide (hetero)architectures.

In **Chapter 8** we discuss the shape-directed self-assembly of polyhedral ZnS nanocrystals, obtained by  $\text{Zn}^{2+}$  for  $\text{Cu}^+$  cation exchange in  $\text{Cu}_{2-x}\text{S}$  nanocrystals. We show that the truncation of the tips of hexagonal bipyramid nanocrystals determines the geometry of the resulting 2D superstructure, changing it from hexagonal (no truncation) to tetragonal (5% truncation) back to hexagonal (20% truncation).

**Chapter 9** describes the effect that oleic acid ligands have on the directionality of the formation of bifrustum-shaped ZnS superstructures. Our *in-situ* Grazing Incidence Small/Wide-Angle X-ray Scattering (GISAXS/GIWAXS) and *ex-situ* Electron Diffraction (ED) study revealed that adding oleic acid ligands to the bifrustum ZnS nanocrystals (NCs) induces atomic alignment of the NC building blocks in the resulting 2D superstructure.

This thesis shows that by controlling the size, shape, composition and interactions of colloidal semiconductor nanocrystals, tailored materials can be prepared with high precision, which should possibly lead to unprecedented properties that will impact on a number of applications. The results discussed in this thesis are summarized in **Chapter 10**.

## References

- (1) Donega, C. d. M. *Chem. Soc. Rev.* **2011**, *40*, 1512–1546.
- (2) Alivisatos, A. P. *J. Phys. Chem.* **1996**, *100*, 13226–13239.
- (3) Murray, C. B.; Norris, D. J.; Bawendi, M. G. *J. Am. Chem. Soc.* **1993**, *115*, 8706–8715
- (4) LG Quantum Dot television: <http://www.cnet.com/news/lg-leaps-quantum-dot-rivals-with-new-tv/>
- (5) Ip, A. H.; Thon, S. M.; Hoogland, S.; Voznyy, O.; Zhitomirsky, D.; Debnath, R.; Levina, L.; Rollny, L. R.; Carey, G. H.; Fischer, A. *et al. Nat. Nanotech.* **2012**, *7*, 577–582.
- (6) Shirasaki, Y.; Supran, G.; Bawendi, M. G.; Bulović, V. *Nat. Photonics* **2012**, *7*, 13–23.
- (7) van der Stam, W.; Berends, A. C.; Donega, C. d. M. *ChemPhysChem* **2016**, *17*, 559–581.





# Synthesis and Optical Properties of Colloidal (Hetero)Nanocrystals



## ABSTRACT

Semiconductor nanocrystals (NCs) possess very interesting optoelectronic properties which render them promising materials for a variety of applications. By precisely tuning the reaction conditions, high-quality nanocrystals can be synthesized with narrow size and shape distributions and exciting optoelectronic properties, such as photoluminescence (PL) and localized surface plasmon resonances (LSPR). Nowadays, a plethora of semiconductor nanocrystals can be successfully prepared. This chapter discusses the nature of these exciting optoelectronic properties and the currently available synthesis protocols that are used to prepare these materials, as well as the underlying chemical and physical principles. This chapter is divided in two parts. First, the fundamentals of colloidal semiconductor nanocrystals are discussed, described in view of the ‘conventional’ heavy metal-based colloidal NCs (CdX and PbX, with X = S, Se and Te). Second, the synthesis and optoelectronic properties of Cu-chalcogenide NCs will be discussed in more detail.

**Partially based on**

**Prospects of Colloidal Copper Chalcogenide Nanocrystals**

W. van der Stam, A. C. Berends, C. de Mello Donega, *ChemPhysChem*, **2016**, 17, 559–581.

Invited contribution to the Special Issue ‘Beyond Conventional Quantum Dots’, Front Cover

## 2.1 Colloidal Semiconductor Nanocrystals: Fundamentals

### 2.1.1 Introduction

Colloidal semiconductor nanocrystals (NCs) have unique size- and shape-dependent properties that emerge when the NC dimensions reach the quantum confinement regime. In order to produce NCs with exciting optoelectronic properties, control over the synthesis process is required. There have been many recent synthetic advances that produce high-quality NCs with novel functionalities. For example, two semiconductor materials can be combined in a single NC or anisotropic NCs can be synthesized with shape-dependent properties. In this chapter, we discuss the nature of the exciting optoelectronic properties of semiconductor NCs, as well as the processes that govern the successful synthesis of NCs with narrow size and shape distributions of a variety of (hetero)architectures.

### 2.1.2 Nanoscale size effects in colloidal semiconductor nanocrystals

When the dimensions of a semiconductor material reach the nanoscale (nano = a billionth of a meter), the properties of the semiconductor material change significantly. Two effects play a crucial role in these different properties: quantum confinement and surface effects. These two effects will be discussed in more detail below.

In a bulk material a lot of atoms (around  $10^{22}/\text{cm}^3$ ) are organized to form a solid. Instead of discrete energy levels like in an atom, a bulk semiconductor has bands of allowed electron states separated by an energy gap (bandgap) of forbidden states.<sup>1</sup> The formation of the energy bands (the conduction and the valence band) can be described by the Linear Combination of Atomic Orbitals (LCAO) theory.<sup>1</sup> The LCAO theory states that bands are formed when a large number of atoms contribute orbitals, which combine and form bonding and antibonding molecular orbitals (MO). Since the Pauli

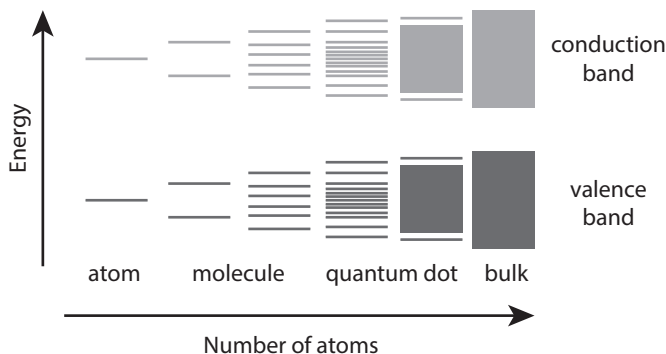


**Figure 2.1. Band formation.** When more atomic orbitals (AO) combine and form bonding and antibonding molecular orbitals (MO), a quasi-continuum of allowed electron states (a band) is obtained (bulk semiconductor). When the number of atoms, and hence the number of AO, is gradually decreased, more discrete energy levels appear near the band edges (quantum dot). On the single atom level, just two atomic orbitals are present. Adapted from ref 1.

exclusion principle states that two electrons cannot occupy the same energy level, there is a build-up of allowed energy states with slightly different energies. Because the energy separation between these states is much smaller than the thermal energy ( $k_B T$ ), the electrons can be thermally excited between the states and therefore the collection of states is better described as a quasi-continuum or a band (Figure 2.1). Between those energy bands are also forbidden states, and this gap is called the bandgap ( $E_g$ ). The energy band that is occupied by electrons is called the valence band (VB) and the unoccupied energy band is the conduction band (CB). The bandgap, *i.e.* the separation between the highest occupied molecular orbital (HOMO) and the lowest unoccupied molecular orbital (LUMO), determines whether a material is a semiconductor or an insulator (if  $E_g < 4$  eV; semiconductor,  $E_g \geq 4$  eV; insulator). When a photon of sufficient energy reaches the semiconductor, an electron can be excited from the VB to the CB. After this excitation, a hole is left in the valence band and an electron is in the conduction band, which form a bound electron-hole pair: the exciton.

A quantum dot (QD) typically has a size between 2 and 20 nm and roughly consists of 100 – 100 000 atoms (compared to  $10^{22}$  atoms/cm<sup>3</sup> in bulk semiconductors). Quantum dots are nanocrystals of semiconductor materials, and therefore an electron can be excited over the bandgap from the valence band to the conduction band (*e.g.* by absorbing a photon of sufficient energy), creating an exciton. As stated above, the properties change when materials reach dimensions on the nanoscale. The quantum confinement effect can be explained according to the LCAO theory presented above, or by the nearly free electron model. From the LCAO theory it follows that when fewer atoms are present, fewer atomic orbitals combine and therefore fewer energy states are present, which leads to discrete energy levels near the band edges and an increase in bandgap (quantum dot regime in Figure 2.1). The increase in bandgap is easily understood from the nearly free electron model. When the dimensions of the QD

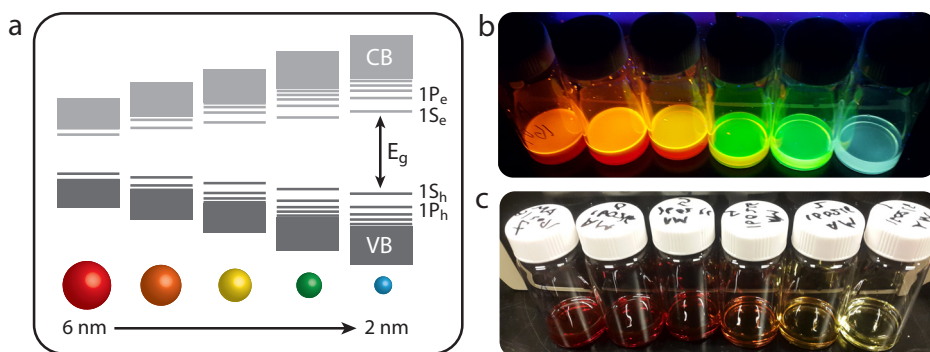


**Figure 2.2. Quantum confinement effect in CdSe nanocrystals.** (a) When the size of CdSe nanocrystals (NCs) is varied from 6 nm to 2 nm, the bandgap increases due to quantum confinement and more discrete energy levels appear near the band edges. (b) This effect is clearly displayed in a photograph of colloidal dispersions of CdSe NCs of various sizes under UV illumination, showing red to blue tunable photoluminescence. (c) The same colloidal dispersions, but under daylight illumination. Sample courtesy of Angela Melcherts.

are smaller than the spatial extension of the exciton wavefunction (called the exciton Bohr radius), the exciton wavefunction is confined. A colloidal QD can be considered as a container with finite walls (a particle in a box in quantum mechanics), which greatly increases the kinetic energy of the exciton and leads to an increase in bandgap (Figure 2.2a).<sup>1,2</sup> The wider the bandgap of the bulk semiconductor, the smaller the exciton Bohr radius, and therefore, smaller particles are needed to observe quantum confinement effects.<sup>1</sup> Besides, the quantum confinement effect displays a strong size dependence, *i.e.* the smaller the box, the stronger the confinement and hence, the larger the bandgap of the quantum dot. Furthermore, the fact that fewer atoms are present in smaller QDs, leads to more discrete energy levels near the band edges. These effects are clearly displayed in Figure 2.2, which shows that the smaller the QD (composition: CdSe), the bigger the bandgap, and more discrete energy states appear near the band edges. In this way, the emission color can be varied from red to blue for CdSe QDs of 6 to 2 nm, respectively (Figure 2.2).<sup>1-3</sup>

As mentioned above, surface effects also play a dominant role in the optoelectronic properties of colloidal semiconductor nanocrystals. Surface effects affect, for example, the photoluminescence of the colloidal NCs. When the size of the NCs is reduced, a larger portion of the atoms is on the surface, and therefore, the surface-to-volume ratio increases. Surface atoms have a higher free energy because they have fewer chemical bonds, which results in so-called dangling orbitals, resulting in localized states in the bandgap. Such localized states in the bandgap can greatly affect the luminescence. Surface defects can also lead to energy levels that lie in the bandgap, which can trap generated charge carriers (electrons or holes) after excitation and hence, decrease the photoluminescence quantum yield (PLQY).<sup>1,2,4</sup> If there is a single (or multiple) of these midgap energy levels, the luminescence of the QDs can be entirely quenched (*i.e.* the recombination of the electron and hole is completely non-radiative). This is highly undesirable for the envisioned applications of colloidal QDs, such as LEDs, where high PLQYs are necessary.<sup>5</sup> However, these surface defects can be passivated by organic ligand molecules, by selectively binding to the dangling orbitals at the NC surface. In this way, the quality of the colloidal NCs can be greatly improved (in terms of PLQY, exciton lifetimes etc.). Therefore, colloidal NCs are often seen as hybrid inorganic-organic nanomaterials (Figure 2.4a). Besides, the layer of organic ligand molecules coating the NC surface is dynamic, which makes colloidal NCs highly amenable to surface manipulation and solution processing.<sup>1</sup> The above mentioned characteristics have turned colloidal NCs into promising materials for a wide variety of applications (optoelectronics, photonics, spintronics, catalysis, solar energy conversion, thermoelectrics, information processing and storage, sensors, and biomedical applications).<sup>1</sup>

### 2.1.3 Nanocrystal dimensionality

If the dimensions and shape of the NCs are such that the exciton is confined in all directions, a colloidal quantum dot (QD) is obtained. Similarly, anisotropic NCs can be synthesized in which the exciton is confined only in the diameter direction (quantum rods), while in a quantum well the exciton is confined in the thickness direction only. Over the last decades, a wide variety of synthesis protocols to produce colloidal QDs and quantum rods have been developed.<sup>1</sup> Recently, synthetic methodologies for producing colloidal quantum wells have emerged, and these quantum well structures have shown to possess remarkable properties.<sup>1,23</sup> The quantum confinement effect, which was discussed in the previous section, depends strongly on the dimensionality of the NCs. The difference between bulk, quantum wells, quantum wires and quantum dots can be further explained by looking at the density of states (DOS, Figure 2.3). With decreasing dimensionality, the carrier energy distribution is narrowed to specific energies, *i.e.* discrete energy levels. For a quantum well, the density of states distribution changes from a square root dependence (bulk) to a step-like dependence, as shown in Figure 2.3. The quantum confinement effects, and thus the properties, differ for quantum dots, rods and wells with the same thickness (or diameter for QDs). This generated an intense research effort into the preparation of low-dimensionality NCs, since they are expected to possess unparalleled optoelectronic properties.<sup>23,24</sup>

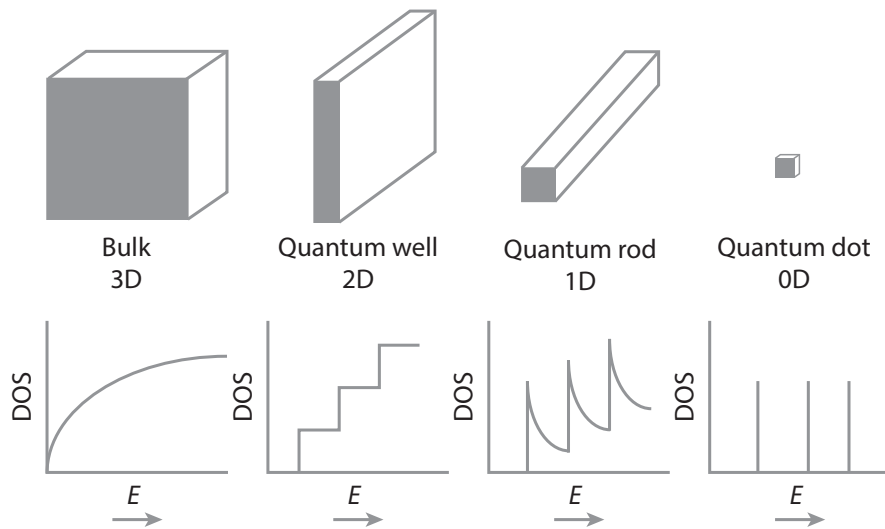


**Figure 2.3. Density of states dependence on nanocrystal dimensionality.** When the dimensionality of colloidal nanocrystals changes from a 0D quantum dot to a 1D quantum rod or a 2D quantum well, the density of states (DOS) changes from discrete energy levels (0D) to a step-like dependence (2D). Bulk semiconductor have a square root dependence of the DOS. Adapted from <http://www-opto.e-technik.uni-ulm.de/lehre/cs/DOS-DIM.jpg>

### 2.1.4 Synthesis of colloidal semiconductor nanocrystals

Over the past few years, several synthetic strategies have been developed to produce high-quality colloidal semiconductor NCs, such as the ‘hot-injection’ method,<sup>1,3,6</sup> the heating-up of all reactants to the desired reaction temperature,<sup>7-9</sup> seeded growth<sup>1,10-12</sup> and post-synthetic modifications *via* cation exchange (CE) reactions.<sup>13-16</sup> Among those synthetic protocols, the hot-injection is the most used and investigated methodology (Figure 2.4). In the hot-injection method, a cold solution containing one of the precursors (typically the cationic precursor) is swiftly injected into a hot coordinating solvent (containing the anionic precursor, Figure 2.4c). However, variations on this procedure are reported as well, in which the cationic and anionic precursors are mixed and injected into a hot coordinating solvent. After the injection, a burst of nucleation occurs due to the sudden availability of monomers at sufficiently high temperatures to allow for the formation of nuclei (Figure 2.4d).<sup>3,17</sup> Since a cold solution was injected, the temperature drops below the nucleation threshold, thereby preventing the formation of new nuclei. In this way, all precursors present, which form monomers due to precursor to monomer conversion, will only contribute to further growth of the already existing nuclei (Figure 2.4e). The effective separation between nucleation and growth allows for the synthesis of colloidal NCs with narrow size and shape distributions (often within 5%). In order to obtain different sizes of the colloidal NCs, samples can be taken at different times, or the reaction can be quenched by cooling, so that growth can no longer occur.

The total free energy change during the formation of a crystal ( $\Delta G_{\text{tot}}$ ) consists of two opposing contributions,  $\Delta G_{\text{s}}$  and  $\Delta G_{\text{v}}$ , which are the surface excess free energy and the volume excess free energy, respectively.<sup>1</sup> As displayed in Figure 2.4b, the formation of surface is energetically unfavorable (*i.e.* costs energy) and the creation of volume is energetically favorable (*i.e.* releases energy). As a result, there is an energy barrier that has to be overcome to form nuclei, as shown in Figure 2.4b, denoted as  $\Delta G_{\text{c}}$ . This is the critical Gibbs free energy that is needed for creating nuclei with the critical radius  $r_{\text{c}}$ . The energy barrier  $\Delta G_{\text{c}}$  is overcome when the nuclei in the solution have the critical radius  $r_{\text{c}}$ , after which the growth rate is positive, allowing the crystal nuclei to grow to larger sizes. When the nuclei are smaller than  $r_{\text{c}}$ , the growth rate is negative so the nuclei are sub-critical and tend to redissolve.

Several synthetic strategies have also been developed to produce anisotropic NCs with narrow size and shape distributions. For the production of Cd-based nanorods, usually phosphonic acids ligands are used, since they promote growth along the {001} wurtzite facets (or in other words: inhibit growth in the other crystallographic directions).<sup>10,19</sup> Ligands often have a preferred crystallographic facet to which they bind and therefore, by choosing the right surfactants/ligands, chemists have been able to produce anisotropically shaped NCs such as 1D nanorods (phosphonic acid as ligands)<sup>10,19</sup> or 2D CdSe nanosheets (oleic acid as ligands).<sup>23</sup> For the synthesis of colloidal nanosheets, mostly soft-templating mechanisms have been proposed, in which Cd- or Pb-precursors

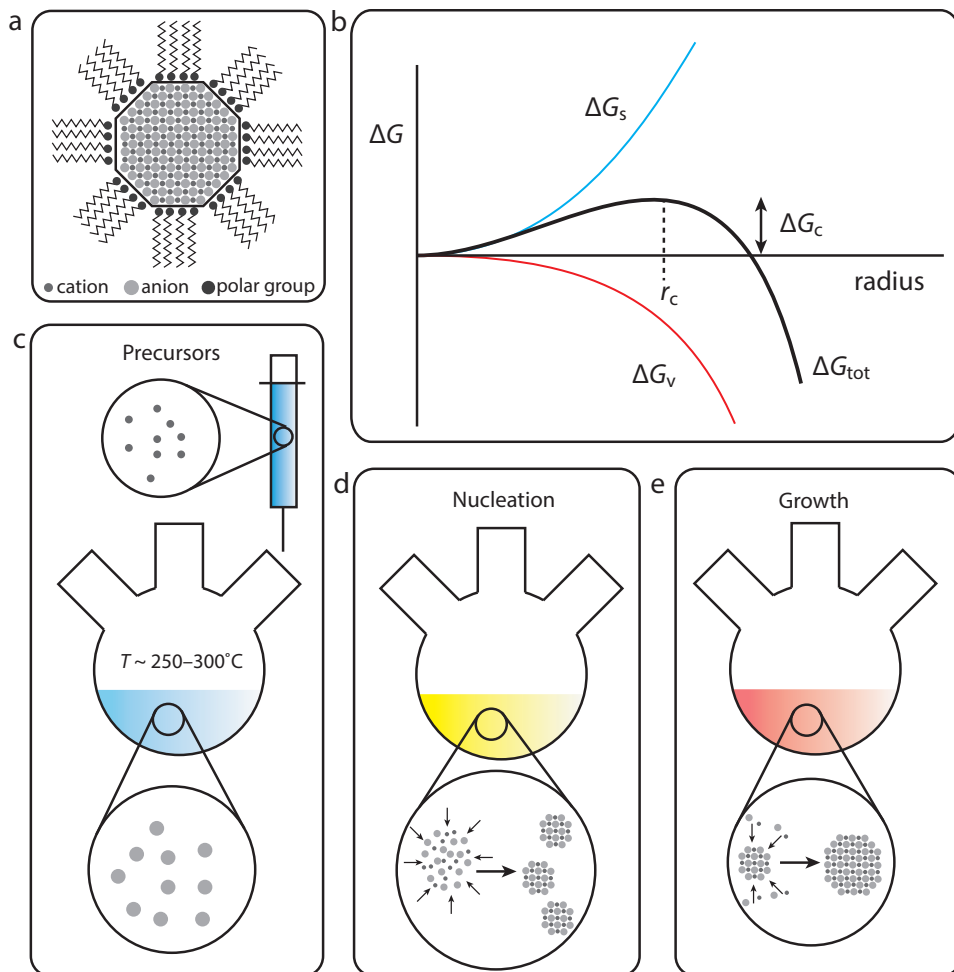


**Figure 2.4. Bottom-up formation of colloidal semiconductor nanocrystals via the hot-injection method.** (a) Schematic representation of a colloidal quantum dot, which can be considered as a hybrid inorganic-organic nanomaterial. (b) Gibbs free energy diagram for the formation of a spherical crystal (also valid for the heating-up method). (c) In the hot-injection method, a cold precursor solution (for example, containing the cations) is injected in a hot coordinating solvent (for example, containing the anions). (d) This creates a burst of nucleation. (e) Since the temperature drops due to the injection of a cold solution, the remaining precursors only contribute to further growth of the nanocrystals.

form a 2D template that assists the lateral growth.<sup>23,25</sup> Other works have proposed oriented attachment mechanisms for the production of 2D PbS nanosheets. However, the exact formation mechanisms that govern the 2D growth of colloidal nanosheets are still under debate and will be further discussed in Chapters 4 and 5 of this thesis.

### 2.1.5 Colloidal semiconductor heteronanocrystals

When two semiconductors are joined in a single NC *via* nanoscale heterojunctions, a colloidal semiconductor heteronanocrystal (HNC) is obtained. In order to prepare colloidal HNCs, two synthetic pathways can be followed. In the first approach, the second semiconductor nucleates on an existing NC seed, forming segmented HNCs. This process is called heterogeneous nucleation, which often occurs at preferential, high energy sites, such as phase boundaries, impurities or more reactive crystallographic facets. The energy for heterogeneous nucleation is equal to the product of the energy barrier for homogeneous nucleation and a function of the wetting angle,  $f(\theta)$ , which is always between 0 and 1. Therefore, the energy required for heterogeneous nucleation is always lower than for homogeneous nucleation. Hence, syntheses that require heterogeneous nucleation can be carried out at lower temperatures. Examples of heterogeneous nucleation protocols, resulting in HNCs, are the formation of PbSe/CdSe/PbSe dumbbells upon addition of Pb- and Se-precursors to CdSe nanorods (NRs),<sup>18</sup> or the formation of Cu<sub>2</sub>S/CuInS<sub>2</sub> heterostructures after nucleation of CuInS<sub>2</sub> on one particular facet of Cu<sub>2</sub>S seeds.<sup>11</sup>

In the second approach, the slow addition of precursors results in heteroepitaxial overgrowth of the second semiconductor on the existing NC seed. In this way, spherical core/shell HNCs of various compositions are successfully prepared, such as CdSe/ZnS, CdSe/CdS and CdTe/CdSe core/shel NCs.<sup>1</sup> A combination of both processes is also possible, in which heterogeneous nucleation on preferred crystallographic facets is followed by heteroepitaxial growth, which can result in highly anisotropic core/shell nanomaterials, such as CdSe/CdS dot-in-rod heterostructures.

Surfactants play an essential role in homogeneous nucleation, but their impact on heterogeneous nucleation is even more dramatic.<sup>1,10,19</sup> This is because they not only regulate the monomer chemical potential in solution, but also the free energy and accessibility of the surfaces. The surfactant molecules modify the free energies of the different facets of the seed nanocrystal, thereby enhancing or suppressing the heterogeneous nucleation rates on specific facets. Moreover, surfactant molecules sterically hinder incoming monomers, limiting or even blocking the access to certain facets or surface sites. This makes it possible to use surfactants to control the accessibility of surfaces, thereby accelerating, slowing down, or preventing heteroepitaxial growth on selected facets of a nanocrystal seed. For instance, anisotropic core/shell CdSe/CdS heteronanorods have been successfully prepared, by taking advantage of the preferred growth of wurtzite CdS on the {001} facets of the wurtzite CdSe seeds, due to the presence of phosphonic acid ligands, which increase the heteroepitaxial growth rate on the {001} facets of the CdSe seeds.<sup>10</sup> A rich library of complex CdSe/CdS HNCs (and other Cd-based compositions) has been prepared (*e.g.* CdSe/CdS dot-in-octapod,<sup>20</sup> CdSe/CdS core/crown nanoplatelets,<sup>21</sup> CdTe/CdSe dot-in-bipods<sup>22</sup>) and researchers still attempt to produce novel colloidal (hetero)nanostructures *via* colloidal pathways

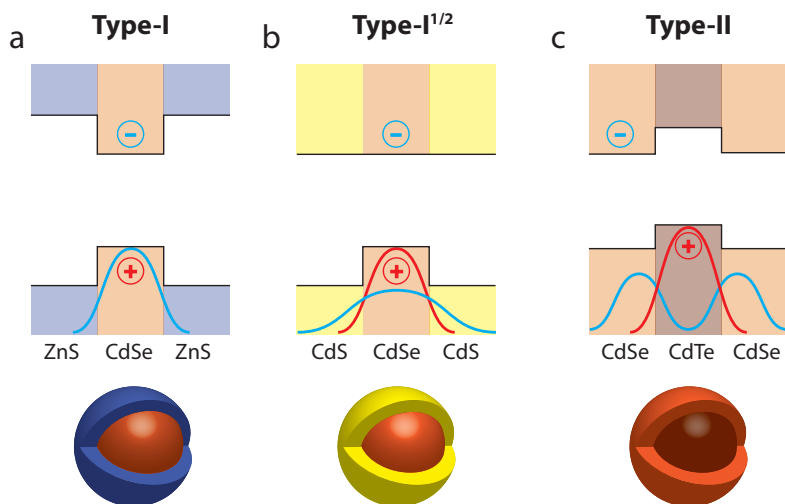


**Figure 2.5. Colloidal semiconductor heteronanocrystals.** By a proper choice of the compositions of two semiconductors, and combining them in a single nanocrystal *via* nanoscale heterojunctions, the overlap between the electron wavefunction (blue line) and the hole wavefunction (red line) can be tailored. Three carrier localization regimes are defined: (a) Type-I (bandgap of one semiconductor lies entirely within the bandgap of the second semiconductor, both carriers in the same material, large electron-hole wavefunction overlap), (c) Type-II (staggered band offset, electron and hole spatially separated, small electron-hole wavefunction overlap) and (b) an intermediate regime, Type-I<sup>1/2</sup> (one carrier localized, the other carrier delocalized, intermediate electron-hole wavefunction overlap). Adapted from ref 1.

with unprecedented and improved optical properties.

The combination of two (or more) different semiconductors in the same NC, joined *via* nanoscale heterojunctions (*i.e.*, a hetero-NC, HNC) extends the possibilities for property engineering of colloidal NCs even further, since the carrier localization regime can be precisely tailored.<sup>1</sup> Three carrier localization regimes are distinguished for semiconductor HNCs: Type-I, Type-II and Type-I<sup>1/2</sup> (Figure 2.5). In the Type-I band alignment, the bandgap of one material lies entirely within the bandgap of the other material and therefore both the electron and hole localize in the same part of the HNC. This localization regime is typically used to obtain core/shell QDs in which the exciton is confined in the core (*e.g.* CdSe/ZnS). Recombination of charge carriers (electrons and holes) on surface defects is thus severely hindered due to the wider bandgap material surrounding the core. This greatly suppresses the non-radiative recombination of the photoexcited exciton and hence increases the photoluminescence quantum yield (PLQY). In the Type-II configuration, the band edges have a staggered offset. This results in spatial separation of the exciton, which reduces the overlap between the electron (blue line in Figure 2.5) and hole wavefunctions (red line in Figure 2.5), increasing the

exciton radiative lifetimes. Moreover, the PL red shifts due to the staggered band offset. Between the Type-I and Type-II configurations, lies an intermediate regime (Type-I<sup>1/2</sup>), where one charge carrier is delocalized over the whole HNC volume and the other is localized in one of the segments. This is caused by the very small offset between the conduction (or valence) band edges, allowing the electron (or hole) wavefunctions to delocalize throughout the whole HNC. By controlling the composition, size and shape of each segment of the HNC (Figure 2.5), different localization regimes can be obtained and hence, the optoelectronic properties of the HNCs can be tailored.<sup>1</sup> This yields a remarkable degree of control over the properties of nanoscale excitons in HNCs, since the different carrier localization regimes are beneficial for several applications in which, for example, effective charge carrier injection/extraction is crucial, such as photovoltaic devices and LEDs.

#### 2.1.6 Cation exchange in colloidal semiconductor nanocrystals

The composition of colloidal (H)NCs can also be post-synthetically tailored, for example by deploying cation exchange (CE) reactions.<sup>13–16</sup> As the name implies, one cation, which is in the parent nanocrystals, is exchanged for another cation, thereby producing NCs that are not attainable in a direct fashion. In this way, also metastable crystal structures can be easily accessed, such as wurtzite ZnS.<sup>26,27</sup> Cation exchange reactions are often topotactic, which means that the size and shape of the parent NCs are preserved in the product NCs. Cation exchange reactions consist of a chain of inherently linked elementary kinetic and thermodynamic steps, which must proceed in a concerted manner.<sup>13–15</sup> The driving force for the reaction is determined by the energy balance of the overall reaction and the relative stabilities of the reactant and product phases, and the relative stabilities of the cations in solution and in the nanocrystal. It should also be noted that the cation exchange would not proceed beyond the surface in the absence of solid state diffusion fluxes in the NC,<sup>13–15</sup> allowing the native cations to diffuse outward and the new cations to diffuse inward. The solid state diffusion of cations is actually the reason why CE reactions are favorable in NCs, but are negligible in bulk materials. The overall energy balance is thus also strongly dependent on the activation energies for diffusion of both the incoming and outgoing cations in the NC. The overall free energy balance of the reaction has to be in favor of CE, otherwise the CE reaction will not proceed. In other words, the sum of the chemical potential of the starting crystal (denoted as  $(AX)_{\text{NC}}$ ) and the reacting cations in solution (denoted as  $(B^{n+})_{\text{sol}}$ ) has to be larger than the sum of the chemical potential of the product crystal (denoted as  $(BX)_{\text{NC}}$ ) and the native cation in solution (denoted as  $(A^{n+})_{\text{sol}}$ ).

The chemical potential of the crystal phases depends on a number of factors, such as crystal structure (*i.e.* ordering and bonds of cations and anions within the lattice), composition, NC morphology and the ligands that cap the NC.<sup>1</sup> This makes it difficult to precisely tailor the chemical potentials of the parent and product crystals. However, a high concentration of incoming cations  $(B^{n+})_{\text{sol}}$  will drive the system into a non-equilibrium

state, which favors the formation of the product NCs  $(BX)_{NC}$ . Therefore, an excess amount of the product cation is often used in CE reactions. Furthermore, it is possible to lower the chemical potential of  $(A^{n+})_{sol}$  by a proper choice of coordinating ligand. Due to the hard and soft nature of Lewis acids and bases, where hard acids preferentially bind to hard bases, the  $(A^{n+})_{sol}$  cations can form stable complexes in solution, which are more favorable than remaining in the parent NC crystal structure. An example is the use of a soft Lewis base to preferentially bind to the soft product cation and not to the harder reactant cation. Tertiary phosphines (soft Lewis bases), such as trioctylphosphine ( $\eta \approx 6$  eV),<sup>28</sup> are therefore often used as ligands to selectively exchange soft Lewis acids,

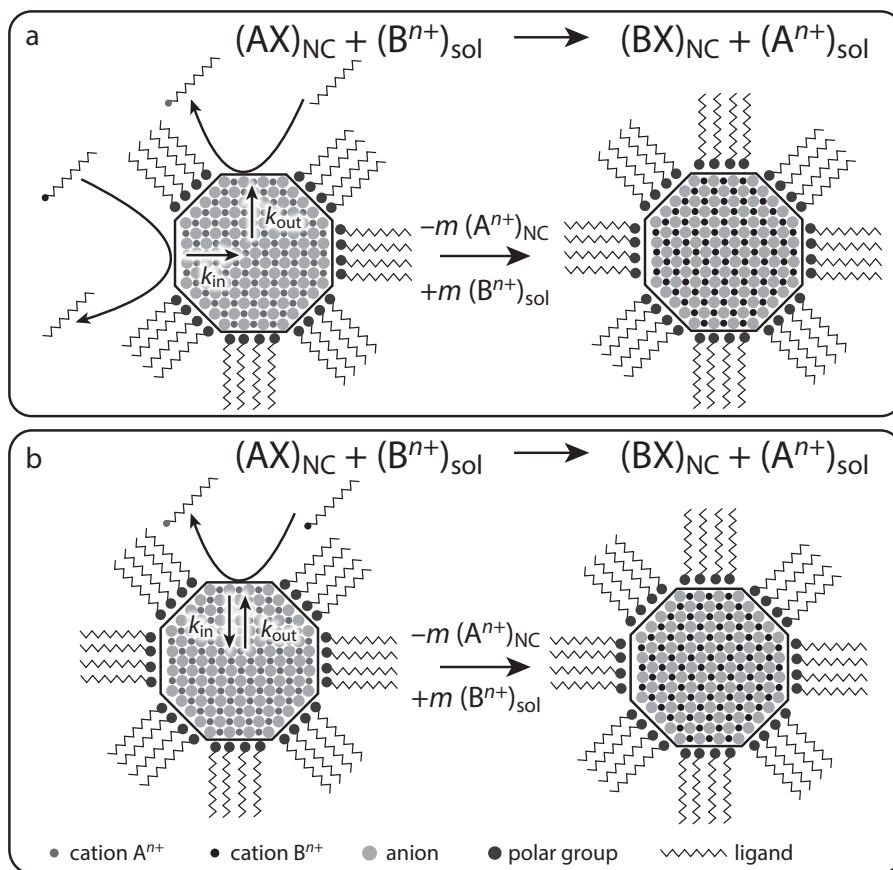


**Figure 2.6. Cation exchange (CE) reactions in colloidal semiconductor nanocrystals.** (a) CE reactions can proceed via two separate chemical pathways, viz. extraction of parent cations  $(A^{n+})_{NC}$  and incorporation of product cation  $(B^{n+})_{sol}$ . Furthermore, cation-ligand bonds have to be formed and cleaved. Another important parameter is the diffusion of parent cations out of the NC ( $k_{out}$ ) and of product cations into the NC ( $k_{in}$ ), which depend non-linearly on the reaction conditions. All these chemical processes have to be balanced for successful cation exchange to occur, which makes it a hard process to control. (b) Another approach involves a single cation-ligand precursor, which acts as cation supplier and extractor. In this way, cation exchange is a direct place exchange reaction and therefore can occur in larger/more anisotropic nanocrystals, since the inward and outward diffusion fluxes ( $k_{in}$  and  $k_{out}$ ) are now inherently linked.

such as  $\text{Cu}^+$  ( $\eta = 6.28$  eV), as will be discussed in more detail in Part B of this thesis.<sup>28</sup> For successful CE reactions, several criteria have to be met. First, the parent cations have to be extracted from the NCs. This step includes the formation of cation-ligand bonds and the cleavage of cation-anion bonds. Second, the product cations have to be incorporated in the NCs. This step includes cleavage of cation-ligand bonds in solution and the formation of cation-anion bonds in the NCs. Third, the product cations ( $\text{B}^{n+}$ )<sub>NC</sub> have to diffuse into the NCs ( $k_{\text{in}}$ ) and simultaneously the parent cations ( $\text{A}^{n+}$ )<sub>NC</sub> have to diffuse out of the NCs to the NCs surface ( $k_{\text{out}}$ ), as displayed in Figure 2.6. If any of these steps does not occur, or is slow compared to the other steps, the CE reaction is quenched and completely stops (*i.e.*  $k_{\text{in}}$  too slow), or the parent NCs might dissolve completely (*i.e.*  $k_{\text{out}}$  too fast). Therefore, it is important to balance the rate of extraction and the rate of incorporation. Otherwise the CE may not occur at all, the NC may dissolve, or voids may form due to the nanoscale Kirkendall effect.<sup>13,15,29,34</sup> Sometimes, two different reactants are necessary for the first two criteria: one to supply the product cation ( $\text{B}^{n+}$ )<sub>sol</sub> and one to extract the parent cation ( $\text{A}^{n+}$ )<sub>NC</sub>, as displayed in Figure 2.6a. This approach requires a precise tuning of the reaction parameters (*e.g.*, temperature, concentrations, etc.), which makes CE reactions difficult to control, since the diffusion of cations depends non-linearly on the reaction parameters (as will be discussed in more detail in Chapter 6).<sup>30</sup> In another approach, the in- and outward diffusion rates are inherently linked by deploying a single-step CE precursor.<sup>31</sup> This precursor acts both as product cation supplier and parent cation extractor, thus coupling the rate of extraction and of incorporation (Figure 2.6b). This makes the CE reaction a direct place exchange reaction, instead of a vacancy driven reaction, where first a

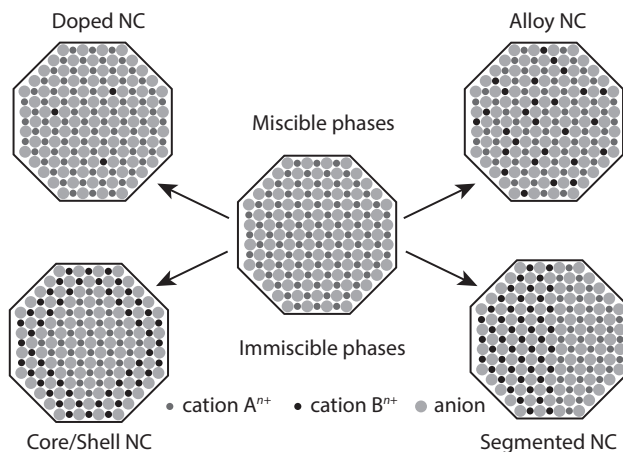


**Figure 2.7. Partial and full cation exchange pathways in colloidal semiconductor nanocrystals.** If the crystal structures of the parent and product nanocrystals (NCs) are miscible, doped or alloyed NCs can be obtained with novel functionalities (top). However, if the crystal structures are immiscible, core/shell NCs or segmented NCs can be formed (bottom) By the proper choice of the reaction temperature, concentrations of seeds and incoming cation, as well as the parent and product crystal structures, novel materials can be designed with CE reactions that are not attainable in a direct fashion. Adapted from ref 13.

vacancy is created which shifts the overall energy balance in favor of CE. An example of such a single-step exchange approach ( $\text{In}^{3+}$  for  $\text{Cu}^+$ ) will be discussed in more detail in Chapter 7, but many more examples have been reported in the literature ( $\text{Cd}^{2+}$  for  $\text{Zn}^{2+}$ , or  $\text{Cd}^{2+}$  for  $\text{Pb}^{2+}$ ).<sup>13–15</sup>

Apart from the exchange at the surface, the formation/cleavage of cation-ligand bonds, and the formation/cleavage of cation-anion bonds within the NCs, diffusion of cations inside the NCs plays an important role. By a proper choice of the reaction parameters, CE reactions might occur partially or fully. In the case of partial exchange, doped NCs, alloyed NCs or complex HNCs may be obtained, depending on the miscibility between the parent and product phases.<sup>13–16</sup> If the lattice mismatch between the parent and product NCs is small, or if the parent and product phases can form solid solutions, the incoming cations can easily diffuse in the new host lattice (miscible phases in Figure 2.7). However, if the parent and product phases are immiscible, heterostructures might form,<sup>13</sup> such as core/shell NCs (*e.g.* PbSe/CdSe core/shell QDs)<sup>16</sup> and segmented NCs (*e.g.* PbSe/CdSe bi-hemispheres).<sup>16</sup> The immiscibility between two phases originates from different coordination numbers (CN) for the cations, as in the case of PbSe (rocksalt crystal structure, CN = 6) and CdSe (zinc blende, CN = 4). Besides, when the NC is large, only a portion of the crystal experiences the CE reaction, resulting in a local distortion due to the lattice mismatch between the parent phase and the product phase. If the lattice mismatch is small enough, the system will be able to accommodate the distortion and the exchange will proceed. However, if the mismatch is too large, the exchange stops, resulting in heterostructures,<sup>32</sup> or segmented NCs.<sup>33</sup> Similar structures (*i.e.* heterostructures and segmented NCs) can also be formed by preferential CE reactions at particular crystallographic facets, which allows the diffusion front (the diffusion of cations from the surface of the NCs inwards) to be monitored over time.<sup>13</sup> In this case, diffusion of the cations in the NCs is the rate-limiting process in the CE reaction, as was the case for the exchange of  $\text{Cd}^{2+}$  for  $\text{Zn}^{2+}$  in ZnSe QDs.<sup>32</sup> This exchange was characterized by an initial fast CE at the NC surface, followed by slow diffusion of  $\text{Zn}^{2+}$  and  $\text{Cd}^{2+}$  within the crystal. Because the rate of diffusion is temperature dependent, the authors were able to prepare HNCs by CE at low temperatures ( $\sim 150$  °C) and homogeneous  $\text{Zn}_x\text{Cd}_{1-x}\text{Se}$  alloyed NCs by reaction at higher temperatures ( $\sim 200$  °C).<sup>32</sup>

The examples discussed above show that there are many compositions, crystal structures and hetero-architectures accessible *via* nanoscale CE reactions, which are not attainable in a direct fashion. Depending on the reaction conditions, the CE can proceed only partially, resulting in alloyed NCs or complex HNCs. This highlights the versatility and promise of nanoscale CE reactions for the preparation of novel nanostructures, with possibly unparalleled properties.

### 2.1.7 Self-assembly

Colloidal nanocrystals (NCs) are able to form three-dimensional (3D) and

two-dimensional (2D) self-assembled superstructures with properties that are dictated not only by the size, shape, and composition of the building blocks but also by the geometry into which they self-assemble.<sup>35</sup> For example, the precise geometry can be important to the electrical transport properties of the superstructure or to the directionality and polarization of emitted light.<sup>35</sup> The geometry of the 2D superstructure can be tailored by a proper choice of size and shape, composition and surface functionalization<sup>36</sup> of the NC building blocks.<sup>35</sup> But how do these NC superstructures form and what are the key driving forces?

The formation of superstructures is, under suitable experimental conditions, a spontaneous process. This means that the change in Gibbs free energy,  $\Delta G$ , is in favor of superlattice formation. The Gibbs free energy ( $\Delta G$ ) for the self-organization of colloidal NCs is given as,

$$\Delta G = \Delta H - T\Delta S \quad (2.1)$$

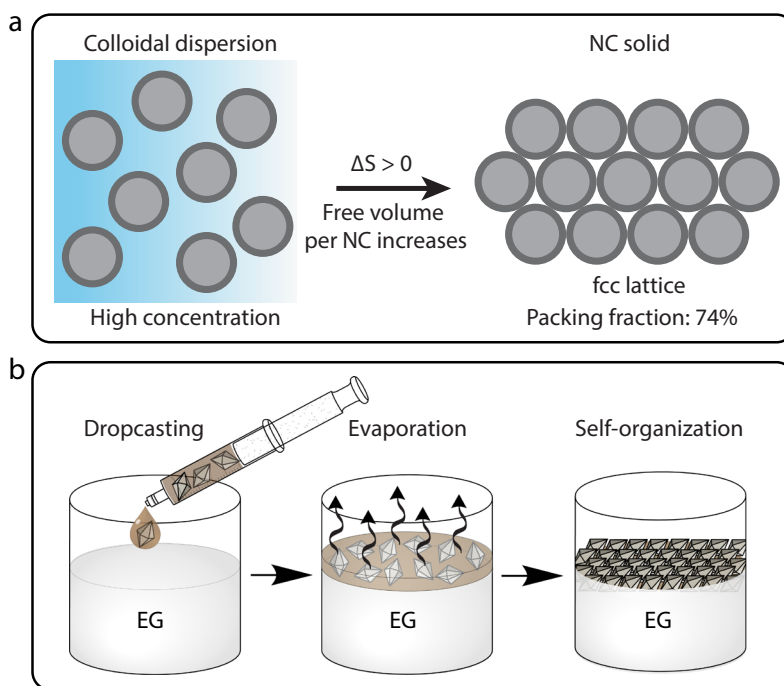


**Figure 2.8. Self-organization of colloidal NCs into 2D superstructures.** (a) In a concentrated colloidal dispersion of semiconductor nanocrystals, the free volume per NC is small. In a NC solid, the free volume per NC increases, which results in an increase in entropy ( $\Delta S > 0$ ). This makes the crystallization of NC into a NC solid spontaneous. (b) A colloidal dispersion of semiconductor nanocrystals (NCs) is placed on top of a dense liquid substrate, usually ethylene glycol (EG), after which the toluene is allowed to evaporate. This creates a driving force for the NCs to close-pack into ordered 2D superstructures, which can be collected on any desired substrate. Image courtesy of Quinten Akkerman.

where  $\Delta H$  is the net formation enthalpy,  $T$  is the temperature and  $\Delta S$  is the net entropy of the entire reaction system. The enthalpy contribution accounts for the attractions between the nanocrystals in the superlattice with respect to those in the suspension.

As shown in Figure 2.4a, colloidal NCs can be capped by organic molecules (as well as by charges), which make them stable in dispersion.<sup>1</sup> During the formation of NC superstructures, these organic molecules also play a substantial role. They can either give directionality to the superstructure formation *via* attractive van der Waals interactions (as will be discussed in Chapter 9 of this thesis), or they can shield the inorganic cores of the NCs from each other, thereby decreasing the inter-NC interactions (*viz.*, the interaction energy is smaller than  $k_B T$ ).<sup>35</sup> Therefore, the NCs can be considered as hard spheres, for which  $\Delta H = 0$ . The equation for  $\Delta G$  for superlattice formation now reads  $\Delta G = -T\Delta S$ . From this equation it follows that  $\Delta S > 0$  for spontaneous crystallization. This counterintuitive idea can be understood by looking at the free volume per NC (Figure 2.8a). In a chaotic dense dispersion, the free volume per NC is small when compared to a NC solid with packing fractions up to 74% (fcc lattice). This increase in free volume per NC upon formation of a NC solid, causes an increase in entropy, which makes the self-organization of NCs spontaneous and energetically favorable. This can also be understood in terms of the chemical potential of a NC freely dispersed in solution or fixed in a NC superstructure. Several synthetic strategies can result in an increase of the chemical potential of the freely dispersed NC (thereby making it favorable to form a superstructure). The most effective strategy is increasing the concentration of NCs, which is achieved for example by evaporating the solvent in which the NCs are dispersed, as will be discussed below.

Several preparation methods have been developed in order to form 2D superstructures of colloidal nanocrystals, of which the liquid substrate procedure is the most studied (Figure 2.8b).<sup>27,36–38</sup> In this method, a concentrated NC solution in toluene is dropcasted on a dense liquid substrate (ethylene glycol, EG) after which the toluene evaporates. This results in pressure on the NCs (and raises the chemical potential of freely dispersed NCs), which creates a driving force for the NCs to close-pack into ordered 2D superstructures. The NCs preferentially adhere to the high energy air-toluene interface, which gives additional directionality to the formation of 2D superstructures. After evaporation of the solvent, the 2D superstructure floats on the liquid substrate, after which they can be easily transferred to any desired substrate (*e.g.* TEM-grid, electrode, Si wafer). Other methods include the tilted evaporation method, in which the NCs assemble on a substrate while the solvent is evaporated under an angle with respect to the solvent-substrate interface. Preparation methods for tailored 3D superstructures have also been developed, which depend on close-packing of NCs after evaporating the solvent as well.<sup>39</sup> In this method, an oil-in-water microemulsion is obtained, with the colloidal NCs in the oil phase, which close-pack into 3D supraballs after evaporating the solvent. 3D supraballs are expected to become a novel class of supercrystals with

exciting functionalities, in which the individual properties of the NC building blocks should be coupled and enhanced due to the close-packing of the NCs.<sup>40</sup> These examples highlight that there is a wide variety of 2D and 3D NC superstructures that can be experimentally obtained, resulting in novel structures with interesting properties.

## 2.2 Colloidal Cu-chalcogenide nanocrystals

### 2.2.1 Introduction

Over the past few years, much research has been done on the colloidal synthesis of Cu chalcogenide nanocrystals (NCs).<sup>41</sup> Due to their size, shape and composition tunability, Cu chalcogenide NCs hold a large promise for implementation into several devices.<sup>9,41,42</sup> Besides, Cu chalcogenides have a low toxicity, since they are comprised of earth-abundant elements, and they can attain a very wide range of compositions and crystal structures.<sup>5</sup> This latter point makes them an extremely versatile class of materials, capable not only of offering similar properties to those already demonstrated by Cd- and Pb-chalcogenide based NCs and HNCs, but also characteristics that are unparalleled by the conventional NCs and HNCs (for example, plasmonic properties).<sup>41</sup> The largest control over the synthesis has been achieved for the binary  $\text{Cu}_{2-x}\text{A}$  NCs, whereas direct synthesis of ternary and quaternary compositions is mainly hindered by the availability and reactivity of the different precursors.

In this section, the colloidal synthesis of Cu chalcogenide NCs with narrow size and shape distributions is discussed, as well as their possible applications. Furthermore, we show that topotactic cation exchange reactions offer solutions to circumvent the direct synthetic limitations of multinary Cu chalcogenides and result in high quality ternary and quaternary NCs. Finally, we discuss the potential applications of these NCs. This section is divided into three subsections: binary copper chalcogenides (section 2.2.2), ternary copper chalcogenides (section 2.2.3) and quaternary copper chalcogenides (section 2.2.4).

### 2.2.2 Binary Copper Chalcogenides

Colloidal binary copper chalcogenide ( $\text{Cu}_{2-x}\text{A}$ , with  $\text{A} = \text{S}, \text{Se}$  and  $\text{Te}$ ) NCs have attracted increasing attention over the last decade, because their properties make them interesting materials for implementation into several applications, such as solution-processable photovoltaic and nanoplasmonic devices, photocatalysis, photothermal therapy, or biomedical sensing.<sup>43-49</sup> To realize these applications, the size, shape and polydispersity of the NC ensemble must be strictly controlled, since these characteristics are crucially important not only for the optoelectronic properties of the NCs themselves, but also for the quality of the NC thin films obtained by solution based deposition techniques.<sup>50</sup> This motivated an extensive worldwide research effort into colloidal synthesis methods for  $\text{Cu}_{2-x}\text{A}$  NCs, which resulted in a remarkable degree of control over the size and

shape of colloidal  $\text{Cu}_{2-x}\text{A}$  NCs.<sup>51–56</sup>

### *Crystal structure of binary Copper Chalcogenides*

The most investigated copper chalcogenide is  $\text{Cu}_{2-x}\text{S}$ , which can easily accommodate Cu vacancies. As a result, the binary Cu-S system has a very rich phase diagram,<sup>57</sup> with a variety of equilibrium crystal structures: monoclinic low-chalcocite  $\alpha\text{-Cu}_2\text{S}$ , hexagonal high-chalcocite  $\beta\text{-Cu}_2\text{S}$ , monoclinic djurleite  $\text{Cu}_{1.96}\text{S}$ , hexagonal digenite  $\text{Cu}_{1.8}\text{S}$ , monoclinic roxbyite  $\text{Cu}_{1.78}\text{S}$ , orthorhombic anilite  $\text{Cu}_{1.75}\text{S}$ , and hexagonal covellite CuS. These crystal structures are characterized by either hexagonal or cubic close-packing of S atoms, with Cu atoms positioned at the interstices. Rearrangement of S atoms from cubic to hexagonal (and *vice versa*) is extremely slow, and therefore a number of metastable phases is also possible.<sup>57</sup> The crystal structure of  $\text{Cu}_{2-x}\text{S}$  is determined by the number of Cu vacancies. The crystal structures range from klockmannite hexagonal CuSe,<sup>58</sup> umangite tetragonal  $\text{Cu}_3\text{Se}_2$ ,<sup>58</sup> berzelianite cubic  $\text{Cu}_{2-x}\text{Se}$ <sup>58</sup> and bellidoite cubic  $\text{Cu}_2\text{Se}$ .<sup>58–61</sup> Copper telluride can exist as orthorhombic CuTe, hexagonal  $\text{Cu}_2\text{Te}$ ,  $\text{Cu}_3\text{Te}_4$ , and  $\text{Cu}_7\text{Te}_5$ , and also as nonstoichiometric  $\text{Cu}_{2-x}\text{Te}$  phases.<sup>62–64</sup>

### *Colloidal synthesis of $\text{Cu}_{2-x}\text{A}$ nanocrystals*

The compositional and structural diversity of binary copper chalcogenides creates a very rich parameter space that can be exploited to tailor the size and shape of colloidal  $\text{Cu}_{2-x}\text{A}$  NCs over a very wide range, opening up routes toward a plethora of morphologies not attainable for other binary semiconductor NCs. For example, nanodisks, nanoplatelets, (ultrathin) nanosheets and other polyhedral shapes have been successfully synthesized with astonishingly narrow size and shape distributions (Figure 2.9).<sup>51–56</sup> As will be discussed below, by strictly controlling the reaction conditions (nature of precursors and ligands, concentrations, reaction temperatures), the desired compositions and crystal structures can be obtained. This determines the chemical and crystallographic nature of the facets of the nascent NC, which in turn dictates the fate of the NC growth, since the growth kinetics of the individual facets are governed both by their intrinsic free energies and by their affinity for the ligands present in the growth solution.<sup>1</sup>

$\text{Cu}_{2-x}\text{A}$  NCs with narrow size and shape distributions have been prepared by both hot-injection and heating-up synthesis protocols.<sup>51–56,65–69</sup> The heating-up process typically results in larger NCs,<sup>52,54,66</sup> suggesting that the heating-up rates are not sufficiently fast to induce a sudden burst of monomer formation from the precursors, thereby resulting in relatively slow nucleation rates. This implies that the precursor to monomer formation is the rate limiting step in the synthesis of colloidal  $\text{Cu}_{2-x}\text{A}$  NCs, in line with the general mechanism proposed for the formation of colloidal NCs of metal chalcogenides.<sup>1</sup> This is also illustrated by the use of Cu(II)-salts for the synthesis of  $\text{Cu}_{2-x}\text{A}$  NCs,<sup>55,65</sup> which introduces one additional kinetic step, since the  $\text{Cu}^{2+}$  ions must

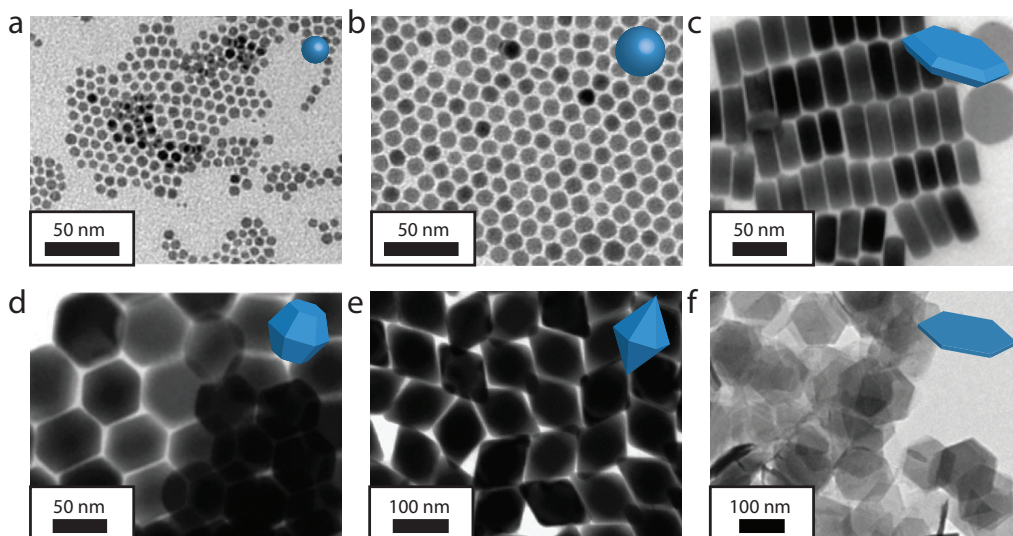


**Figure 2.9. Size and shape control of colloidal  $\text{Cu}_{2-x}\text{S}$  nanocrystals.** By choosing the right synthetic parameters, the size and shape of colloidal  $\text{Cu}_{2-x}\text{S}$  nanocrystals (NCs) is controlled from (a,b) isotropic spherical NCs with different diameters (diameters 3–10 nm), to more anisotropic NCs such as (c) hexagonal nanoplatelets (thickness 20 nm, lateral dimensions 50 nm), (d) bifrustums (50 nm), (e) bipyramids (50 nm width by 100 nm length) and (f) ultrathin nanosheets (thickness 2 nm, lateral dimensions 110 nm). Reproduced with permission from ref 41.

first be reduced to  $\text{Cu}^+$  before CuA monomers can form. This also stalls nucleation, leading to fewer nuclei, and hence larger NCs. It is thus clear that the precursor reactivities are one of the key factors in the synthesis of  $\text{Cu}_{2-x}\text{A}$  NCs with narrow size and shape distribution.

The exact formation mechanism of colloidal  $\text{Cu}_{2-x}\text{A}$  NCs, however, is still under debate. Cabot and co-workers proposed an oriented attachment pathway through which hexagonal nanodisks form hexagonal  $\text{Cu}_{2-x}\text{S}$  bifrustums and eventually hexagonal bipyramids.<sup>55</sup> Other groups presented evidence that Cu-thiolate lamellar complexes act as both Cu-precursors and shape templating agents.<sup>47,56,70,71</sup> Organic surfactant molecules are commonly used as shape templating agents, whereas inorganic surfactant molecules have only recently been used in order to stabilize nanomaterials in polar solvents as water and ethanol.<sup>72–74</sup> The advances for Cd-based nanomaterials (discussed in section 2.1) may lead to synthetic strategies resulting in designed Cu chalcogenide architectures with tailored surface functionalities, which may prove beneficial for the implementation of these NCs into devices and bio-applications.

Nevertheless, the synthesis protocols for colloidal  $\text{Cu}_{2-x}\text{A}$  NCs are also subjected to

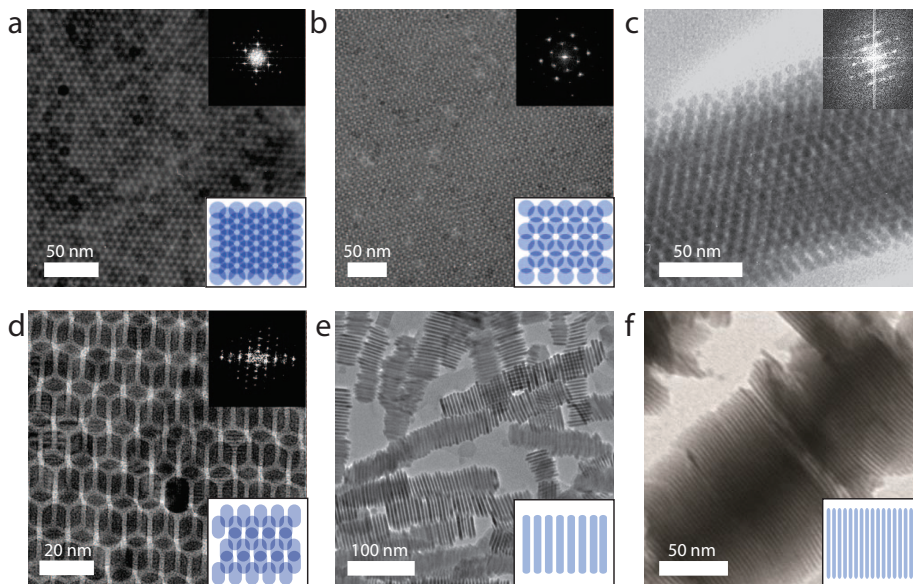


**Figure 2.10. Self-organization of colloidal  $\text{Cu}_{2-x}\text{S}$  nanocrystals.** Spherical  $\text{Cu}_{2-x}\text{S}$  NCs readily self-assemble into a variety of ordered 3D superstructures, such as (a,b) hexagonal close packed (hcp) and (c) corncob structures. (d) Self-assembly of anisotropic NCs results in distortion of the hcp packing to a rhombohedral geometry. (e)  $\text{Cu}_{2-x}\text{S}$  nanoplatelets and (f) ultrathin nanosheets form stacks. Reproduced with permission from ref 41.

limitations, especially in the case of selenides and tellurides, for which very few anion precursors are available. Several chalcogenide precursors have been reported, but the most extensive library is that of the sulfide precursors. The most commonly used sulfide precursors are tri-*n*-octylphosphine sulfide (TOP-S), 1-dodecanethiol (DDT), thiourea, bis(dimethylsilyl)sulfide, and elemental sulfur dissolved in 1-octadecene (S-ODE).<sup>9,42</sup> The use of the selenide and telluride analogues of these precursors is hindered by stability issues. In fact, only TOP-Se and TOP-Te are suitable precursors in terms of stability and reactivity, but the presence of TOP (a soft Lewis base) is undesirable, since it strongly binds to the  $\text{Cu}^+$  ions (a soft Lewis acid),<sup>28</sup> thereby slowing the nucleation rates and enhancing ripening. In some cases, Se-ODE is used as precursor, but the poor solubility of Se in ODE leads to relatively large and polydisperse NCs.<sup>59,60,75,76</sup> Selenourea has emerged as an alternative, but the resulting NCs are limited in terms of size and shape, since only large NCs are obtained.<sup>77</sup> Moreover, Te is almost completely insoluble in ODE. An alternative is to mix all reactants, including the elemental chalcogen as a powder, and heat the mixture up to the reaction temperature.<sup>78</sup> However, this method offers a limited size and shape control, and therefore the search for a suitable Se/Te-precursor that allows for size- and shape-controlled growth of  $\text{Cu}_{2-x}\text{A}$  NCs continues.

The limitations in the synthesis of  $\text{Cu}_{2-x}\text{A}$  NCs can also be circumvented by using cation exchange (CE) reactions (discussed in more detail in section 2.1.6). For example, ultrathin  $\text{Cu}_{2-x}\text{Se}$  NPLs,<sup>79</sup>  $\text{Cu}_{2-x}\text{S}$  nanowires,<sup>80</sup>  $\text{Cu}_{2-x}\text{Te}$  QDs, nanorods and tetrapods,<sup>81</sup> and several  $\text{Cu}_2\text{Se}/\text{Cu}_2\text{S}$  core/shell heteronanocrystal (HNC) architectures,<sup>82–84</sup> which cannot be prepared by a direct synthesis, have been obtained from template Cd-based NCs by topotactic  $\text{Cu}^+$  for  $\text{Cd}^{2+}$  CE. CE reactions involving Cu-chalcogenide NCs will be discussed in more detail below.

The narrow size distribution of the colloidal  $\text{Cu}_{2-x}\text{A}$  NCs produced by the methods discussed above allow them to readily self-assemble into ordered 3-dimensional superstructures (Figure 2.10). This may prove beneficial for the successful implementation of  $\text{Cu}_{2-x}\text{A}$  NCs into PV and other optoelectronic devices. The tunability of the size and shape of  $\text{Cu}_{2-x}\text{A}$  NCs offers another possibility to tune the geometry, and therefore the properties, of the self-assembled superlattices. Since  $\text{Cu}_{2-x}\text{A}$  NCs can grow anisotropically or have polyhedral shapes, the packing geometry can be altered, ranging from face-centered cubic to hexagonal close packing (Figure 2.10a,b), or to corncoblike superstructures (Figure 2.10c), and long range stacking of nanoplatelets (Figure 2.10e) and nanosheets (Figure 2.10f).<sup>41</sup>

### *Optical Properties of $\text{Cu}_{2-x}\text{A}$ Nanocrystals and Plasmonics*

Binary copper chalcogenides are p-type semiconductors, regardless of the chalcogenide.  $\text{Cu}_{2-x}\text{S}$  is a direct semiconductor with a bandgap that depends on its stoichiometry (1.1 – 1.4 eV for djurleite, where  $x = 0 - 0.04$ ; 1.5 eV for digenite, where  $x = 0.2$ ; 2.0 eV for covellite, where  $x = 1$ ).<sup>65,85,86</sup>  $\text{Cu}_{2-x}\text{Te}$  also has a direct bandgap, which can be tuned between 1.1 and 1.5 eV, depending on its stoichiometry.<sup>62–64</sup> In contrast to  $\text{Cu}_{2-x}\text{S}$  and  $\text{Cu}_{2-x}\text{Te}$ ,  $\text{Cu}_{2-x}\text{Se}$  has been reported to have both direct and indirect band gaps (2.1 to 2.3 eV and 1.2 to 1.4 eV, respectively).<sup>48,59,60</sup> This increase of the bandgap with increasing number of copper vacancies, indicated by  $x$ , has been explained by an increase in the concentration of free carriers (holes) in the material.<sup>43</sup> The excess holes will occupy the top of the valence band, thereby increasing the effective band gap.<sup>97</sup> This effect leads to a low energy absorption tail in the spectra of  $\text{Cu}_{2-x}\text{A}$  NCs, which makes the precise determination of the NC band gap difficult. This typically precludes the clear observation of the lowest energy exciton transition in NCs that are sufficiently small to experience quantum confinement effects (the estimated exciton Bohr radius in  $\text{Cu}_2\text{S}$  is  $\sim 5$  nm).<sup>45,86</sup> Interestingly, the hole concentration in  $\text{Cu}_{2-x}\text{A}$  NCs is sufficiently high to give rise to localized surface plasmon resonances (LSPRs).<sup>45</sup> For example, metallic-like covellite  $\text{CuS}$  NCs display a broad absorption band in the NIR, which is associated with an LSPR of the free holes introduced in the material by the copper vacancies ( $x = 1$  in  $\text{CuS}$ , but the Cu atoms are still in the (+1) oxidation state).<sup>65</sup> The LSPR can be tuned by introducing additional  $\text{Cu}^+$  ions (Figure 2.11), which decreases the concentration of free holes, thereby weakening the LSPR and simultaneously shifting it to lower energies.<sup>65</sup> When the fully stoichiometric  $\text{Cu}_2\text{S}$  composition is reached, the LSPR

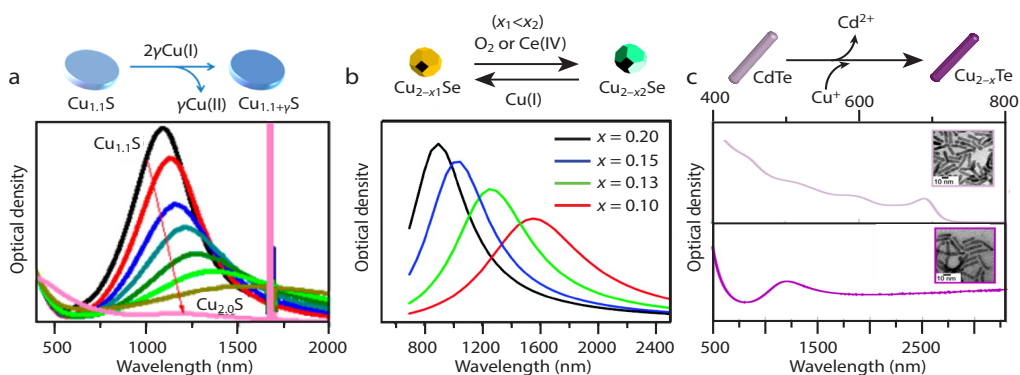


**Figure 2.11. Localized Surface Plasmon Resonance (LSPR) in Cu chalcogenide nanocrystals.** Cu chalcogenide nanocrystals have shown to have tunable LSPR, which can be effectively increased by oxidizing the NCs, or damped by reduction of the NCs. (a) The LSPR in  $\text{Cu}_{2-x}\text{S}$  NCs is tuned between 1000 nm and 1500 nm, whereas (b)  $\text{Cu}_{2-x}\text{Se}$  NCs can hold LSPR between 800 and 1600 nm. (c) Also LSPR around 1000 nm has been observed in  $\text{Cu}_{2-x}\text{Te}$  nanorods, obtained by  $\text{Cu}^+$  for  $\text{Cd}^{2+}$  cation exchange. Reproduced with permission from ref 41.

band is completely damped, and the radiative recombination of the exciton becomes observable.<sup>98</sup> The same holds for  $\text{Cu}_{2-x}\text{Se}$  NCs, in which the LSPR band can be damped by the addition of  $\text{Cu}^+$  ions or enhanced by oxidation of the NCs with  $\text{O}_2$  or  $\text{Ce(IV)}$ .<sup>99</sup> The NIR LSPR of  $\text{Cu}_{2-x}\text{A}$  NCs can also be damped by incorporating other metal ions (such as  $\text{In}^{3+}$ ).<sup>100</sup> This shows that  $\text{Cu}_{2-x}\text{A}$  NCs possess the unique property of holding excitons and highly tunable localized surface plasmon resonances (LSPRs) on demand (Figure 2.11). The LSPR band of  $\text{Cu}_{2-x}\text{A}$  NCs has been shown to depend not only on the composition of the NCs, but also on their size<sup>45</sup> and shape.<sup>101,102</sup> The combination of these characteristics makes  $\text{Cu}_{2-x}\text{A}$  NCs promising materials for photovoltaics,<sup>88</sup> photocatalysis,<sup>103</sup> and nanoplasmonics.<sup>45,81,99</sup>

#### *$\text{Cu}_{2-x}\text{A}$ nanocrystals as templates for topotactic nanoscale cation exchange reactions*

Nanoscale cation exchange (CE) offers a versatile alternative for direct synthesis protocols, since it allows for post-synthetic control over the NC composition, while preserving the size and shape of the parent NCs (section 2.1.6 above).<sup>14,26,27,30,31,104–107</sup> Colloidal  $\text{Cu}_{2-x}\text{A}$  NCs, prepared by direct synthesis protocols, are often used as parent (template) NCs in CE reactions yielding other metal chalcogenide NCs. In this way, the size and shape control already achieved for  $\text{Cu}_{2-x}\text{A}$  NCs can be translated to other metal chalcogenides.

$\text{Cu}^+$  ions in copper chalcogenides have been shown to be easily exchangeable by other cations, mainly because of their small size and charge, which results in fast

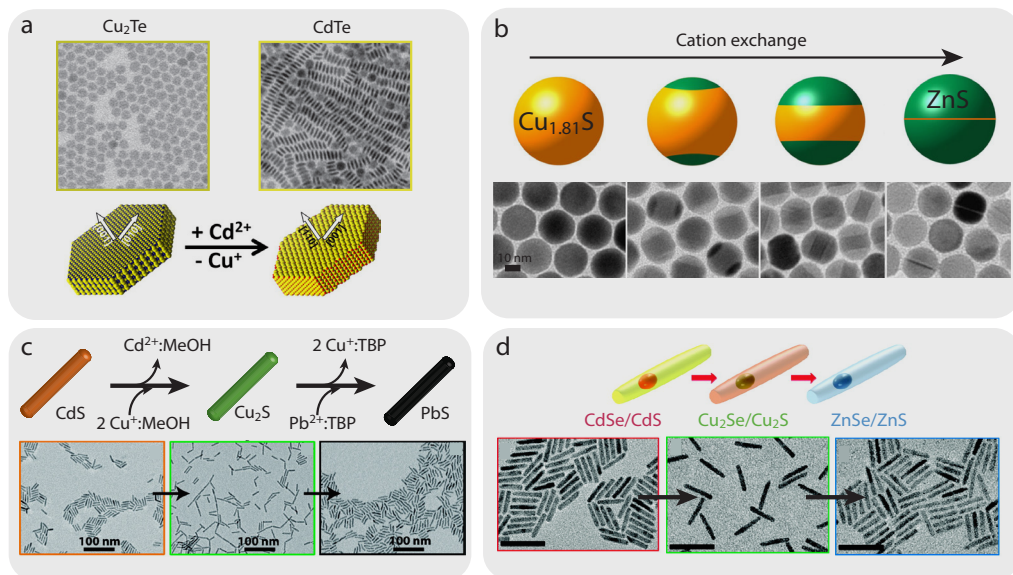


**Figure 2.12. Cation exchange reaction with binary Cu-chalcogenide nanocrystals (NCs) as parent or intermediate NCs.** Cation exchange reactions in Cu-chalcogenide NCs are commonplace, effectively resulting in NCs that are not attainable in a direct synthesis. For example, (a) CdTe nanodisks with visible PL have been obtained using  $\text{Cu}_{2-x}\text{Te}$  nanoplates as starting NCs. (b) Partial  $\text{Zn}^{2+}$  for  $\text{Cu}^+$  cation exchange in roxbyite  $\text{Cu}_{1.81}\text{S}$  NCs resulted in hamburger-like  $\text{Cu}_2\text{S}$ - $\text{ZnS}$  heteronanocrystals with tunable  $\text{Cu}_2\text{S}$  portion depending on reaction time. Sometimes, direct exchange is energetically unfavorable and in those cases, Cu chalcogenide NCs serve as stable intermediate, as in the conversion of (c) CdS nanorods into PbS nanorods via  $\text{Cu}_2\text{S}$  nanorods as well as (d) CdSe/CdS heteronanorods into ZnSe/ZnS heteronanorods via  $\text{Cu}_2\text{Se/Cu}_2\text{S}$  heteronanorods. Reproduced with permission from ref 41.

diffusion through the anionic sublattice. These characteristics, in combination with the availability of Cu-extracting ligands, make it possible to effectively extract  $\text{Cu}^+$  ions from the NCs and replace them with other cations, without disrupting the anionic sublattice. Alkylphosphines, such as tri-*n*-octylphosphine (TOP), are commonly used to extract  $\text{Cu}^+$  from NCs,<sup>14,26,27,30,31,104–107</sup> due to the strong affinity of the soft Lewis acid  $\text{Cu}^+$  (absolute hardness  $\eta = 6.28$  eV)<sup>28</sup> and the soft base TOP ( $\eta = 6$  eV).<sup>28</sup> In this way, NCs can be obtained with unprecedented size, shapes and crystal structures. For example, luminescent CdTe nanodisks (Figure 2.12a)<sup>62</sup> and InP nanoplatelets<sup>106</sup> have been obtained from template  $\text{Cu}_2\text{Te}$  and  $\text{Cu}_{3-x}\text{P}$  NCs by topotactic  $\text{M}^{n+}$  ( $\text{Cd}^{2+}$  and  $\text{In}^{3+}$ , respectively) for  $\text{Cu}^+$  CE. Moreover, ZnS/ $\text{Cu}_2\text{S}$  heteronanocrystals have been prepared by partial  $\text{Zn}^{2+}$  for  $\text{Cu}^+$  CE in  $\text{Cu}_{1.8}\text{S}$  parent NCs, in which a thin slab of  $\text{Cu}_{2-x}\text{S}$  remains between two cation exchanged ZnS portions (Figure 2.12b).<sup>107</sup> Furthermore, we have recently shown that self-limited partial  $\text{In}^{3+}$  for  $\text{Cu}^+$  CE reactions in  $\text{Cu}_{2-x}\text{S}$  QDs can be used to prepare luminescent wurtzite  $\text{CuInS}_2$  QDs<sup>30</sup> and NIR emitting  $\text{CuInSe}_2/\text{CuInS}_2$

heteronanocrystals<sup>31</sup> (discussed in detail in Chapter 6 and 7). Copper chalcogenide NCs are also often used as intermediates in sequential CE reactions, making it possible to synthesize NCs that would otherwise be inaccessible. In this way, PbS nanorods have been prepared from template CdS NRs by sequential ( $\text{Cu}^+$  for  $\text{Cd}^{2+}$  followed by  $\text{Pb}^{2+}$  for  $\text{Cu}^+$ ) CE reactions (Figure 2.12c).<sup>104</sup> Furthermore, wurtzite ZnSe/ZnS core/shell NRs<sup>82</sup> and ultrathin nanoplatelets (NPLs)<sup>83</sup> have been obtained by sequential CE ( $\text{Cu}^+$  for  $\text{Cd}^{2+}$  followed by  $\text{Zn}^{2+}$  for  $\text{Cu}^+$ ) in template CdSe/CdS core/shell NRs (Figure 2.12d) and NPLs, respectively.

### 2.2.3 Ternary Copper Chalcogenides

Unlike the binary copper chalcogenides, ternary I-III-VI materials display tunable photoluminescence, and are therefore promising alternatives to Cd- and Pb-chalcogenide NCs in several applications, such as LEDs,<sup>108–110</sup> photovoltaics,<sup>111,112</sup> luminescent solar concentrators,<sup>113,114</sup> bioimaging,<sup>115,116</sup> and photocatalysis.<sup>117</sup>

#### *Crystal structure of ternary copper chalcogenides*

Ternary copper chalcogenides, with the general formula  $\text{CuXA}_2$  ( $X = \text{In, Sn, Ga, Al}$ ;  $A = \text{S, Se, Te}$ ), exist at room temperature in the chalcopyrite crystal structure, a direct derivative of the binary zinc blende structure (Figure 2.13).<sup>118</sup> Another stable phase is the  $\text{CuA}_5\text{X}_8$  spinel crystal structure, which also has an fcc close-packing of anions. These bulk crystal phases can undergo phase transformations at elevated temperatures or at the nanoscale. For example,  $\text{CuInS}_2$  (CIS) exists in the metastable wurtzite crystal structure (Figure 2.13) at 1045 °C in the bulk,<sup>119</sup> but wurtzite CIS NCs have also been reported.<sup>120</sup>

#### *Colloidal synthesis of ternary copper chalcogenide nanocrystals*

The synthesis of colloidal nanocrystals of ternary copper chalcogenides is still underdeveloped in comparison to that of II-VI and  $\text{Cu}_{2-x}\text{A}$  NCs. This is primarily due to the fact that the control of the nucleation and growth rates of I-III-VI NCs is inherently more challenging, since the reactivities of two cation-precursors and the anion-precursor have to be finely tuned to prevent the formation of binary NCs and to achieve the targeted ternary composition. Therefore, the range of sizes and shapes attainable for I-III-VI NCs is still limited. Furthermore, the exact growth mechanisms of ternary copper chalcogenide NCs are still under debate.

The most widely investigated ternary copper chalcogenide composition is  $\text{CuInS}_2$  (CIS), for which two stable crystal structures have been reported for nanocrystals (Figure 2.13). Small, quasi-spherical CIS NCs with the chalcopyrite crystal structure (roquesite CIS) and visible to NIR tunable PL have been synthesized by direct synthesis protocols.<sup>121–124</sup> The most common synthesis protocol for luminescent CIS NCs with diameters below 10 nm consists of heating-up a mixture of copper iodide, indium acetate and dodecanethiol (DDT).<sup>121</sup> In this case, DDT plays the multiple roles of

sulfur source, ligand and solvent. Large non-luminescent wurtzite CIS nanorods have been synthesized by using *in-situ* nucleated  $\text{Cu}_{2-x}\text{S}$  NCs as seed particles.<sup>11,120</sup> In this case, the hexagonal wurtzite crystal structure of the CIS nanorods is inherited from the  $\text{Cu}_{2-x}\text{S}$  NC seeds, which also have an hexagonal crystal structure. At sufficiently high temperatures, CIS nucleates on the seed NCs, after which further growth of the CIS NCs happens at the hetero-interface of the two materials, consuming the  $\text{Cu}_2\text{S}$  NC seed as a sacrificial Cu(I) and sulfur source. The size of the resulting CIS NCs is largely determined by the size of the  $\text{Cu}_2\text{S}$  seeds, which provides an additional way to control the size of the CIS NCs.

Most synthesis protocols for ternary Cu sulfides use thiolate complexes as sulfur-source. Although thiols are an inexpensive sulfur-source (*e.g.* compared to TOP-S) due to their multiple roles in the synthesis, they also impose additional energy barriers to the nucleation and growth of the NCs, since the C-S bonds of the thiolate molecules must first undergo thermolysis. In this way, a limited amount of monomers are available, resulting in limited control over the size, shape and composition. The protocols to synthesize the Se analogue of CIS,  $\text{CuInSe}_2$  (CISe), are similar to the ones used for CIS, except that Se is typically supplied in its elemental form dissolved in coordinating solvents such as oleylamine,<sup>125</sup> since selenothiols are not readily available. The shapes

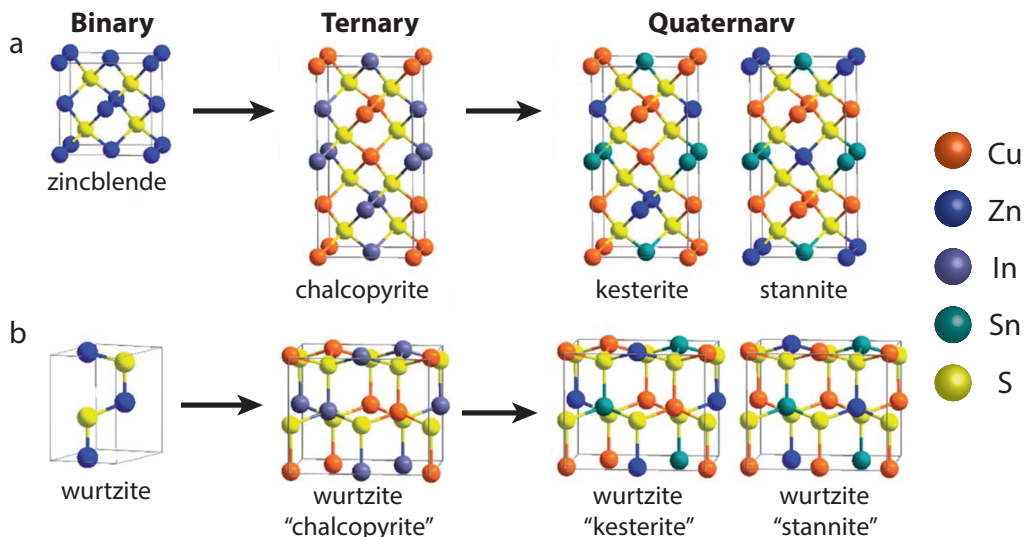


**Figure 2.13. Crystal structures of binary, ternary and quaternary Cu-chalcogenide nanocrystals.** The crystal structures of binary Cu-chalcogenides are directly inherited for the ternary and quaternary Cu-chalcogenides. (a) When the binary NCs have a zinc blende-like crystal structure, the resulting ternary NCs have the chalcopyrite crystal structure. (b) When cation exchange reactions are deployed on wurtzite like Cu-chalcogenides, the resulting ternary and quaternary NCs also have a wurtzite structure. Reproduced with permission from ref 118.

reported for colloidal CISE NCs are trigonal pyramids,<sup>77</sup> bullets,<sup>126</sup> platelets,<sup>125</sup> dot-cuboctahedra,<sup>127</sup> and wires.<sup>128,129</sup>

### *Alternative synthesis routes toward ternary copper chalcogenide nanocrystals*

As illustrated above, the control over size, shape and stoichiometry of ternary copper chalcogenide NCs through direct synthesis protocols is still limited. As discussed in section 2.1.6 above, cation exchange (CE) reactions have emerged as a promising alternative for direct synthesis protocols. In a typical CE reaction, (part) of the cations of the parent NCs are exchanged by different cations, while the anionic sublattice remains unaffected. The efficient extraction of the native cation with concomitant incorporation of the new cation, while preserving the size and shape of the NC, depends on multiple reaction parameters that must be well balanced, since an imbalance may lead to dissolution of the parent NCs or no exchange at all. The most important parameters to control are the chemical potential of the cations in solution and in the NC. This chemical potential can be influenced by the choice of solvent, coordinating ligands and cation precursor salts, for example. The exact balance between these parameters is delicate and different for every system, and therefore often poorly understood. Nevertheless, cation exchange is a powerful and exciting synthesis strategy, which can lead to NCs with unprecedented compositions, shapes, and crystal structures, that would otherwise not be attainable. Below we will discuss some recent examples of partial CE from binary to ternary copper chalcogenide materials. This partial exchange requires either a very precise determination of concentrations, such that only part of the cations can be replaced, or a very good understanding of the mechanism involved, such that the cation exchange is self-limited.

For example, we have recently shown a self-limited partial CE reaction from  $\text{Cu}_{2-x}\text{S}$  NCs to luminescent ternary CIS NCs (discussed in more detail in Chapter 6).<sup>30</sup> We found that the balance between the  $\text{Cu}_{\text{out}}$  and the  $\text{In}_{\text{in}}$  diffusion rates is delicate and could only be balanced at extremely mild reaction conditions (room temperature), resulting in self-limited partial cation exchange, which stops when the ternary composition is reached. In order to proceed until the fully exchanged composition,  $\text{In}_2\text{S}_3$ , a large energy barrier has to be overcome, due to the anionic rearrangement required for this transformation. The template  $\text{Cu}_{2-x}\text{S}$  NCs and the ternary product CIS NCs both have a hexagonal crystal structure with an hcp packing of anions (chalcocite and wurtzite, respectively), whereas  $\text{In}_2\text{S}_3$  has an fcc packing of anions. Although possible, this transformation from hcp to fcc requires a lot of energy, which is not available at the low temperatures used in the reaction.<sup>130</sup>

We extended this knowledge to anisotropic and complex hetero-architectures (discussed in more detail in Chapter 7), by adapting the cation exchange protocol.<sup>31</sup> By effectively coupling the ingoing and outgoing diffusion rates, with the use of a nearly-stoichiometric TOP- $\text{InCl}_3$  complex as both In-source and Cu-extracting agent, ternary

CuInSe<sub>2</sub>/CuInS<sub>2</sub> core/shell heteronanorods were obtained with NIR photoluminescence. This method could also be applied to other ternary compositions, yielding a variety of complex ternary (hetero)structures which are not attainable in a direct fashion, paving the way toward a plethora of ternary NCs with tailor-made size, shape, composition and hetero-architecture.<sup>31</sup>

Similar observations have been reported for other ternary Cu chalcogenide NCs prepared by partial CE reactions. For example, full conversion of Cu<sub>2-x</sub>Se NCs into SnSe NCs was observed for CE with Sn<sup>2+</sup> cations, whereas CE with Sn<sup>4+</sup> cations resulted in self-limited partial CE to Cu<sub>2-x-4y</sub>Sn<sub>y</sub>Se NCs (Figure 2.14).<sup>131</sup> This was explained by the easy diffusion of the Sn<sup>4+</sup> ions through the NC lattice by hopping into copper vacancies, since Sn<sup>4+</sup> and Cu<sup>+</sup> have similar radii.<sup>116</sup> This results in a gradual and isotropic replacement of the cations throughout the lattice and formation of Cu<sub>2-x-4y</sub>Sn<sub>y</sub>Se intermediates. Similarly to the case of the CIS formation from Cu<sub>2-x</sub>S template NCs discussed above, the Sn<sup>4+</sup> for Cu<sup>+</sup> CE reaction is also self-limited due to the stable crystal structures of Cu<sub>2-x</sub>Se (hcp anionic sublattice), Cu<sub>2</sub>SnSe<sub>3</sub> (hcp) and SnSe<sub>2</sub> (fcc), respectively.

#### *Heteronanocrystals and alloys based on ternary copper chalcogenides*

The photoluminescence efficiency of colloidal NCs of semiconductors can be improved by growing a shell of another, wide bandgap, semiconductor (as discussed in section 2.1.5).<sup>1</sup> This passivates surface traps and confines the photoexcited carriers to the core, thereby protecting the NC against oxidation and other unwanted non-radiative relaxation pathways states.<sup>1</sup> Suitable wide bandgap semiconductors for heteroepitaxial shell growth on ternary CIS NCs are ZnS and CdS. Several groups investigated the overgrowth of ZnS and CdS on CIS cores,<sup>121,122</sup> and in all cases a blue shift of the PL has been observed.<sup>121,122</sup> This blue shift has been explained by either alloying of the CIS NC core with the shell cations,<sup>121</sup> or etching of the CIS core prior to growth of

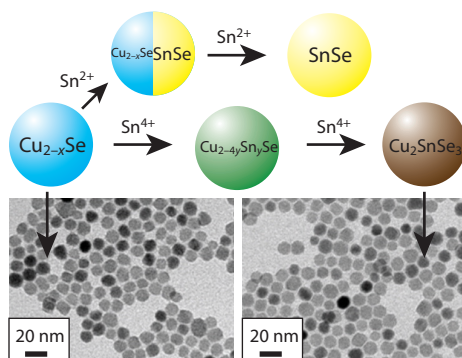


**Figure 2.14. Partial self-limited cation exchange in Cu<sub>2-x</sub>Se NCs.** When Cu<sup>+</sup> is exchanged for Sn<sup>4+</sup>, partial self-limited cation exchange (CE) occurs in Cu<sub>2-x</sub>Se NCs, forming Cu<sub>2</sub>SnSe<sub>3</sub> NCs. CE with Sn<sup>2+</sup> results in Cu<sub>2-x</sub>Se/SnSe hetero-architectures, due to limited diffusion of Sn<sup>2+</sup> within the Cu<sub>2-x</sub>Se host lattice.<sup>131</sup>

the shell.<sup>122</sup> The occurrence of alloying during the shell growth can be explained by the relatively small lattice mismatch between chalcopyrite CIS and zincblende ZnS (1.6%) and the small radius of  $\text{Zn}^{2+}$ , resulting in fast diffusion of the incoming cation into the CIS lattice. The resulting alloyed CIZS NCs show enhancement of the PLQY, which renders them promising materials for implementation into lighting devices or as luminescent probes for bioimaging applications.<sup>115,116</sup> The overgrowth of a shell of a different semiconductor can also be used to control the carrier localization regime in the heteronanocrystal (*i.e.* Type-I, Type-I<sup>1/2</sup> or Type-II, see section 2.1.5 above),<sup>1</sup> thereby allowing the exciton radiative lifetimes and spectral characteristics (*i.e.*, peak position, bandwidth, Stokes shift) of colloidal HNCs to be tailored.<sup>12,22,132</sup> This has been extensively investigated for the prototypical case of HNCs based on Cd-chalcogenides and other II-VI materials,<sup>1</sup> but has yet to be addressed for Cu-chalcogenide based materials.

### Optical properties of ternary copper chalcogenide nanocrystals

The optical properties of ternary copper chalcogenide NCs render them interesting materials for several applications (*e.g.*, light-emitting diodes, luminescent solar concentrators, bioimaging).<sup>41</sup> The most investigated compositions are copper indium chalcogenide NCs ( $\text{CuInA}_2$  NCs, with A = S, Se, CIS and CISE, respectively), which have been shown to exhibit tunable photoluminescence (PL) from the visible to the NIR (Figure 2.15). As will be discussed below, the wide tunability reported in the literature for the optical properties of CIS and CISE NCs is only partially due to quantum confinement effects (exciton Bohr radii are 4.1 nm and 7.5 nm for CIS and CISE,<sup>9,133</sup> respectively), in striking contrast with the II-VI binary analogues, which have been instrumental in the discovery and understanding of quantum confinement effects in

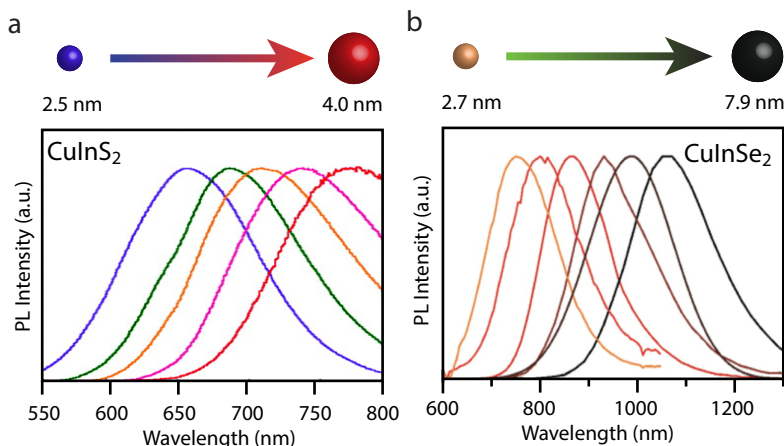


**Figure 2.15. Tunable photoluminescence in ternary  $\text{CuInS(e)}_2$  nanocrystals.** (a)  $\text{CuInS}_2$  nanocrystals of sizes varying between 2.5 and 4.0 nm show photoluminescence (PL) peak positions between 650 and 800 nm. (b)  $\text{CuInSe}_2$  nanocrystals of sizes varying between 2.7 and 7.9 nm show photoluminescence (PL) peak positions between 720 and 1080 nm. Reproduced with permission from ref 41.

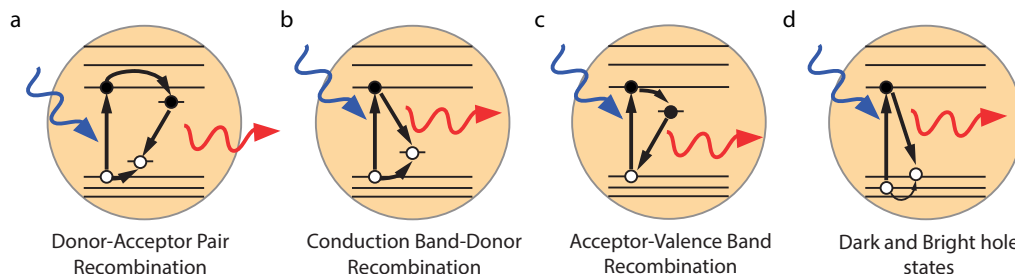


**Figure 2.16. Possible recombination pathways in  $\text{CuInS}_2$  nanocrystals.** The origins of the intriguing optical properties of  $\text{CuInS}_2$  NCs are not yet understood and are still under debate. **(a)** The most often used model is that the PL of CIS NCs is due to a donor-acceptor pair (DAP) recombination involving native point defects such as  $\text{Cu}_{\text{In}}$ ,  $\text{V}_{\text{In}}$  or  $\text{V}_{\text{Cu}}$ . **(b)** Others attributed the PL to recombination of quantized CB electron states with localized holes. **(c)** Some studies proposed that the PL of CIS NCs is due to radiative recombination of quantized VB hole states with electrons localized at native point defects. **(d)** A recent theoretical paper by Efros and coworkers (ref. 137) proposed that the PL of CIS NCs is intrinsic and originates from the  $1\text{S}(\text{e}) \rightarrow 1\text{S}(\text{h})$  exciton transition. Reproduced with permission from ref 41.

semiconductor nanocrystals.<sup>1</sup> Unlike nanocrystals of II-VI (*e.g.* CdSe or CdTe) and IV-VI (*e.g.* PbSe) semiconductors, CIS and CISE NCs typically present essentially featureless absorption spectra and do not exhibit a sharp first absorption transition, even for NCs sufficiently small to be in the quantum confinement regime. Moreover, a low energy tail is usually observed. These characteristics may be due to size and shape inhomogeneities within the NC ensemble, but are also likely to be an intrinsic property of CIS and CISE NCs, since improvements in the preparation methods have resulted in smaller size and shape dispersions, but have not significantly narrowed the observed spectral linewidths.<sup>9</sup> However, CIS can easily accommodate stoichiometry deviations. It is thus possible that ensembles of CIS, CIS/ZnS or CIS/CdS will possess composition inhomogeneities, even if they are monodisperse in size and shape. The same reasoning can be applied to CISE NCs.

The PL of CIS and CISE NCs is also dramatically different from that observed for II-VI and IV-VI quantum dots, and is characterized by a broad band (Full Width at Half Maximum  $\sim 200\text{--}300$  meV), a large ‘global’ Stokes Shift ( $\sim 300$  meV), and multiexponential PL decays with long decay constants (fast component with tens of ns, slow component with hundreds of ns).<sup>9</sup> The PL quantum yields (PLQYs) of bare CIS NCs are typically below 5–10%, while PLQYs as high as 70–85% have been reported for CIS/ZnS or CIS/CdS core/shell HNCs.<sup>121,122</sup> Interestingly, shell overgrowth makes the observed lifetimes even longer, since it reduces the contribution of the fast decay component. Despite a decade of research, the origins of these intriguing optical properties are not yet understood and are still under debate. The most often used model is that the PL of CIS NCs has the same origin as that of bulk CIS,<sup>134</sup> and is thus due

to a donor-acceptor pair (DAP) recombination involving native point defects such as  $\text{Cu}_{\text{In}}$ ,  $\text{V}_{\text{In}}$  or  $\text{V}_{\text{Cu}}$  (Figure 2.16a).<sup>135,136</sup> However, other works attributed the PL to recombination of quantized conduction band (CB) electron states with localized holes (Figure 2.16b), whereas others proposed that the PL of CIS NCs is due to radiative recombination of quantized valence band (VB) hole states with electrons localized at native point defects (Figure 2.16c). Finally, a recent theoretical paper by Efros and coworkers<sup>137</sup> proposed that the PL of CIS NCs is intrinsic and originates from the  $1\text{S}(\text{e}) \rightarrow 1\text{S}(\text{h})$  exciton transition (Figure 2.16d). This clearly illustrates that the nature of the PL is still not well understood, and therefore is still under debate.

#### 2.2.4 Quaternary copper chalcogenides

Quaternary copper chalcogenides ( $\text{Cu}_2\text{-II-IV-VI}_4$ ; with II= Zn, Cd; IV= Ge, Sn, Si; VI= S, Se) have attracted much attention due to the many possibilities they offer of varying the chemical composition, thereby allowing the material band gap (0.8 to 3.3 eV) and functionality to be optimized.<sup>138–140</sup> These materials are thus promising for optics, LEDs and photovoltaics. Especially  $\text{Cu}_2\text{ZnSnS}_4$  (CZTS) has drawn much attention in recent years in the search for earth-abundant and non-toxic photoabsorbers for thin film solar cells.<sup>42,141</sup> CZTS can be seen as an analogue of  $\text{CuInGaS}_2$  (CIGS) in which the rare group III elements (*i.e.* In and Ga) are replaced by earth-abundant and non-toxic elements, while keeping the high stability, large absorption coefficient, and NIR band gap (1.5 eV). CZTS has also been recently proposed as a promising material for high-temperature thermoelectric harvesting.<sup>142</sup>

##### *Crystal structure of quaternary copper chalcogenides*

The most common crystal structures for quaternary copper chalcogenides are kesterite,<sup>143</sup> stannite,<sup>144</sup> and wurtzite,<sup>145</sup> which differ both in the cation positions (kesterite vs. stannite) and in anion distribution within the lattice (kesterite/stannite vs. wurtzite, see Figure 2.13 above).<sup>118</sup> The wurtzite structure is less stable at room temperature for bulk materials but can be obtained for nanocrystals, depending on the synthesis conditions.

##### *Colloidal synthesis of quaternary copper chalcogenide nanocrystals*

As mentioned above, colloidal nanocrystal inks offer an interesting preparation route to inexpensive thin film solar cells.<sup>92,93,146,147</sup> This prospect has provided most of the motivation driving the development of synthesis protocols for monodisperse colloidal nanocrystals of CZTS and related materials, since a large size and shape distribution is detrimental to the quality of the NC film obtained from NC inks. The colloidal synthesis of size- and shape-controlled quaternary Cu-chalcogenide NCs is particularly challenging, since multiple precursor reactivities must be balanced in order to achieve nucleation and growth of a quaternary composition.<sup>148,149</sup> This strongly limits the morphologies that can be obtained.<sup>143,150–152</sup> Typically, mainly large NCs with a broad size and shape distribution have been synthesized (Figure 2.17b,c). However, the

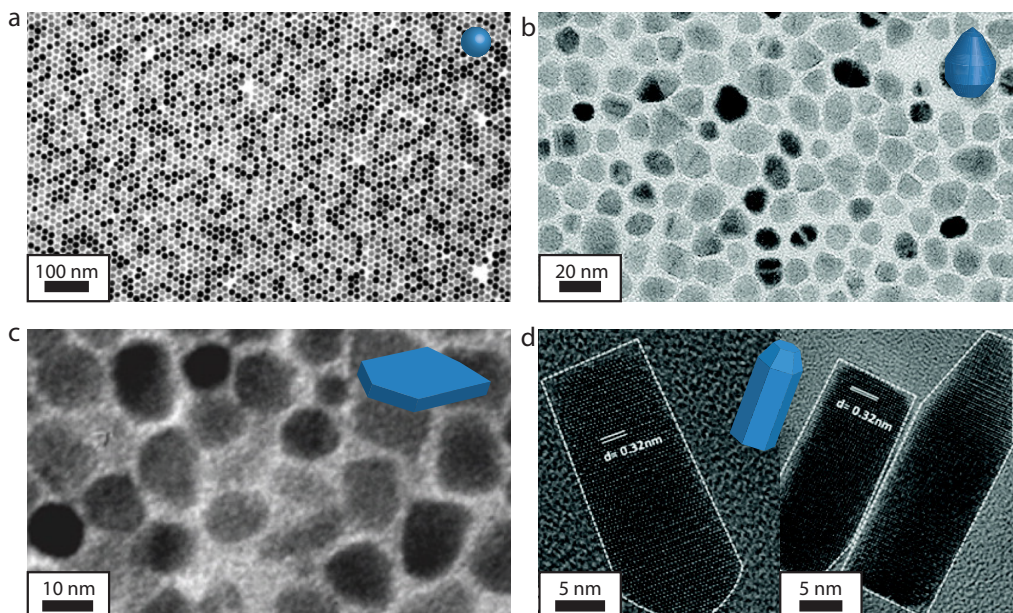


**Figure 2.17. Quaternary  $\text{Cu}_2\text{ZnSnS}_4$  (CZTS) nanocrystals (NCs) with various sizes and shapes.** TEM images of (a) spherical CZTS NCs, (b) anisotropic egg-shaped CZTS NCs, (c) CZTSSe nanoplatelets and (d) wurtzite CZTS nanorods. In order to grow quaternary NCs with control over size and shape, the precursor reactivities have to be precisely balanced. Reproduced with permission from ref 41.

synthesis protocols have become more mature over the last few years, resulting in well-defined spherical NCs with narrow size distribution<sup>153</sup> (Figure 2.17a) and monodisperse bullet-shaped nanorods<sup>152,154</sup> (Figure 2.17d).

Another important parameter in the synthesis of quaternary NCs is the crystal structure of the materials obtained. It has been shown that the crystal structure of the final NCs is strongly influenced by the choice of anion precursor.<sup>148,155</sup> For example, the use of elemental anion sources results in the zinc blende derivative (kesterite or stannite), while NCs with the wurtzite structure are obtained when DDT or bis(dimethylsilyl) sulfide are used as sulfur precursors.<sup>154</sup> A recent study by Ryan and coworkers<sup>152</sup> has investigated the occurrence of polytypism between wurtzite and zinc-blende phases in  $\text{Cu}_2\text{ZnSn}(\text{S},\text{Se})_4$  NCs, showing that the choice of solvents, surfactants and precursors, and the way in which they are introduced, are key factors to control the shape of the NCs from dots to ellipsoids, arrows and rods. Further, the authors showed that the shape evolution is dictated by independently controlling the growth rates of either the wurtzite or the zinc-blende regions in the polytypic system, extending the methodology to the preparation of single-phase wurtzite CZTSSe nanorods.<sup>152</sup>

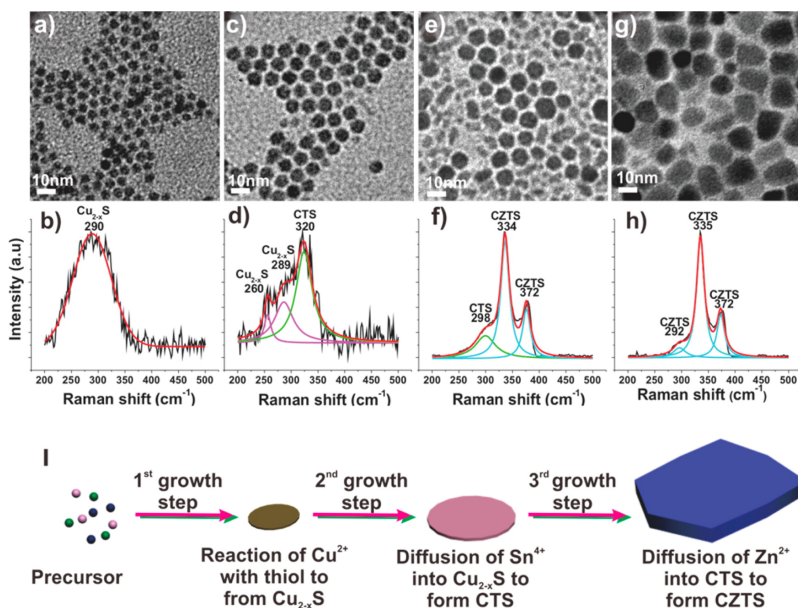


**Figure 2.18. Growth of quaternary CZTS nanocrystals.** (a,b) First,  $\text{Cu}_{2-x}\text{S}$  nanocrystals nucleate as small quasi-spherical clusters. (c,d) In the second step,  $\text{Sn}^{4+}$  diffuses in, resulting in anisotropic CTS nanoplatforms. (e,f) In the third step,  $\text{Zn}^{2+}$  finally diffuses in, (g,h) causing a large increase in lateral dimensions. (i) Schematic representation of the steps involved in the growth of quaternary CZTS nanoplatforms. Reproduced with permission from ref 156.

The growth mechanism of colloidal CZTS nanoplatforms has been recently investigated with TEM and Raman spectroscopy (Figure 2.18).<sup>156</sup> This study showed that the disparity in the reactivities of the different metal precursors causes the nanocrystals to grow in a stepwise fashion:  $\text{Cu}_2\text{S}$  NCs nucleate and grow first, providing seeds into which  $\text{Sn}^{4+}$ , and subsequently  $\text{Zn}^{2+}$ , diffuse.<sup>156</sup> The diffusion is accompanied by reaction with the sulfur precursors (DDT), effectively leading to incorporation of  $\text{SnS}_2$  and  $\text{ZnS}$  units in the growing nanocrystal. This results in particles with broadened size and shape distributions. We note that this growth mechanism is similar to that proposed for the formation of  $\text{Cu}_2\text{SnS}_3$  NCs<sup>157</sup> and CIS wurtzite nanorods,<sup>11</sup> where  $\text{Cu}_2\text{S}$  nucleated first and acted as seed particle into which the second cation ( $\text{Sn}^{4+}$  or  $\text{In}^{3+}$ ) was subsequently incorporated as  $\text{MS}_x$  units, leading to growth of NCs with a ternary composition.

The quest for control over the size and shape of NCs of quaternary copper chalcogenides has been driven not only by the requirements of nanocrystal inks for printable thin-film PV cells, but also by the desire to make NCs sufficiently small to be in the quantum confinement regime. This is of great fundamental interest and is also relevant for potential applications such as LEDs and multi-junction QD solar cells, as it allows

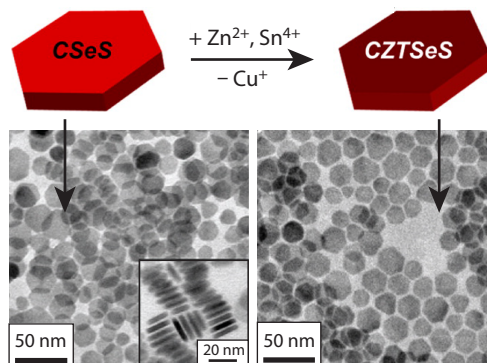


**Figure 2.19.** Cation exchange reactions as possible pathway to produce well-defined CZTSe NCs. Cation exchange reaction in  $\text{Cu}_2(\text{Se,S})$  (CSeS) nanoplatelets, resulting in  $\text{Cu}_2\text{ZnSn}(\text{Se,S})_4$  (CZTSeS) hexagonal nanoplatelets with size and shape preservation. Adapted with permission from ref 161.

quantum confinement effects to be exploited to tune the optoelectronic properties of the NCs. Nevertheless, from this perspective, the synthesis of NCs of quaternary copper chalcogenides is still largely underdeveloped, since there is to date only one report on CZTS NCs sufficiently small to exhibit quantum confinement effects (*viz.*, 2 nm and 2.5 nm in diameter, exciton Bohr diameter is estimated to be 5–6 nm).<sup>158</sup> It is noteworthy that no PL has ever been reported for CZTS NCs at room temperature, regardless of their size, in contrast to NCs of the related ternary copper chalcogenides (*e.g.* CIS and CISE), which typically exhibit size-tunable PL. In fact, CZTS NCs have only been observed to luminesce at low-temperatures (20 K), and even then with relatively low efficiencies.<sup>159</sup> In the study performed by Ryan and coworkers the PL of CZT(S,Se) NCs (*ca.* 11 nm diameter) at 20 K was observed to shift to lower energies, and to become stronger and narrower, with the increase in the Se content.<sup>159</sup> The PL energies are reported to follow the same trend as that of the composition dependent bandgaps, leading the authors to assume the PL was due to near band-edge emission.<sup>159</sup> PL is also unusual for bulk CZTS crystals, and has been reported only once, for slightly S-poor crystals at 25 K, and assigned to D-A recombination.<sup>160</sup>

#### *Alternative synthesis routes to quaternary copper chalcogenide nanocrystals*

As discussed above (section 2.1.6), cation exchange (CE) has emerged as a powerful and versatile tool to circumvent synthetic limitations, and has yielded a variety of novel colloidal NCs, with sizes, shapes and/or compositions that would otherwise not be attainable. Accordingly, CE has been successfully used to obtain nanocrystals of quaternary copper chalcogenides. For example, a one-pot synthesis approach was developed to convert  $\text{Cu}_2(\text{Se,S})$  nanoplatelets into  $\text{Cu}_2\text{ZnSn}(\text{Se,S})_4$  nanoplatelets with size and shape preservation, by using *in-situ* CE reactions (Figure 2.19).<sup>161</sup> It

is interesting to note that *in-situ* CE reactions can be distinguished from the stepwise growth mechanism discussed above ( $\text{Cu}_{2-x}\text{S}$  NCs nucleate first and serve as seeds into which the second and third cations are subsequently incorporated as MS units), because the size and shape of the parent NC is preserved into the product NC, *i.e.* no net growth occurs.

#### *Potential applications of Cu chalcogenide nanocrystals: photovoltaic cells*

As mentioned above, the bandgap of  $\text{Cu}_{2-x}\text{A}$  (with  $\text{A} = \text{S}, \text{Se}, \text{Te}$ ) nanomaterials depends on the number of Cu vacancies, indicated by  $x$ . The combination of a suitable band gap, high absorption coefficient ( $10^4 \text{ cm}^{-1}$ ), and low toxicity has made  $\text{Cu}_{2-x}\text{S}$  a prime candidate for the large scale and sustainable deployment of photovoltaics (PV).<sup>53,87,88</sup> In fact, CdS/ $\text{Cu}_2\text{S}$  heterojunction solar cells were among the earliest thin-film solar cells to be investigated, but their further development was hindered by the low stability of the p/n junction under air, which deteriorated due to formation of Cu vacancies and Cd-Cu interdiffusion.<sup>43,54,89</sup> The possibility to make colloidal dispersions of monodisperse  $\text{Cu}_{2-x}\text{S}$  nanocrystals (NCs) has renewed the interest in  $\text{Cu}_{2-x}\text{S}$  (and other Cu-chalcogenide compositions) for PV,<sup>43,90–96</sup> since it allows the fabrication of solar cells by solution deposition techniques, such as ink-jet printing using nanocrystal inks. Nevertheless, ternary and quaternary copper chalcogenides have superior environmental stability and efficiency compared to their binary analogues, and are therefore preferred in the fabrication of PV devices.

The reported bulk band gap of  $\text{CuInS}_2$  at room temperature varies between 1.52 eV and 1.55 eV,<sup>9</sup> whereas the Se and Te analogues,  $\text{CuInSe}_2$  and  $\text{CuInTe}_2$ , have reported bulk bandgaps of 1.01 eV and 0.97 eV, respectively.<sup>9</sup> Quaternary  $\text{Cu}_2\text{ZnSnS}_4$  (CZTS) has a reported bandgap of 1.5 eV and  $\text{Cu}(\text{In,Ga})\text{Se}_2$  (CIGS) alloys have a band gap that can be tuned from 1.0 to 1.7 eV depending on the Ga content.<sup>76</sup> To date, CIGS thin film PV devices hold the record for highest device efficiency of all thin film solar cells at just over 20%.<sup>162</sup> However, the fabrication of thin-film devices still involves expensive techniques (*e.g.*, chemical vapor deposition), which hinders their widespread deployment. As already briefly mentioned above, one promising approach to low-cost thin-film solar cells is to deposit the absorber layer using a nanocrystal ink and a high-throughput method such as solution coating or printing.<sup>43,90–96</sup> In this way, the production process becomes much cheaper and easier to upscale. CIGS devices prepared from NC inks are still less efficient (*viz.*, 12% after high-temperature sintering) than those manufactured using conventional techniques, but the field is progressing very fast. The main factor limiting the performance of  $\text{Cu}(\text{In,Ga})\text{S}_2$  and CIGS NC solar cells, particularly when unsintered, is poor charge transport.<sup>163</sup> A recent study has shown that the carrier mobility in films of  $\text{CuIn}(\text{Se,S})_2$  QDs can be post-synthetically tuned both by ligand exchange (*i.e.* exchanging the native DDT ligands by shorter ligands, such as 1,2-ethanedithiol) and by composition tailoring through cation exchange, resulting in more than two orders of magnitude increase in the mobilities.<sup>163</sup>

CZTS has attracted increasing attention as an alternative to CIGS as photoabsorber in thin-film solar cells, since it lacks the rare group III elements, but also has high stability, large absorption coefficient, and ideal band gap (1.5 eV). The efficiency of CZT(S,Se) thin film PV devices (*viz.*, 12.6%)<sup>164</sup> is still lower than those of CIGS (20%) and CdTe (16.7%), but already higher than that of amorphous silicon (10%).<sup>165</sup> However, the fabrication techniques used to manufacture the CZT(S,Se) thin-films are still expensive (vacuum deposition) or rely on using toxic and unstable chemicals such as hydrazine. This has motivated extensive research efforts into the development of size- and shape-controlled colloidal CZTS NCs for use in nanocrystal inks. The last few years have witnessed great progress in that direction, and many groups have already reported device efficiencies of up to 7% for CZT(S,Se) (or CZ(Sn,Ge)S) devices prepared from NC inks.<sup>165–167</sup> A recent work investigated the impact of NC size and size distribution, average composition and composition heterogeneity in the properties of CZT(S,Se) thin film devices prepared from CZTS NC inks followed by selenization and sintering at 500 °C.<sup>168</sup> The authors conclude that longer NC synthesis times lead to more efficient devices, probably due to larger crystallite domain sizes after sintering. This implies that further progress will require the development of grain boundary passivation techniques or NC synthesis and sintering methods that lead to better grain growth and more homogeneous inks.<sup>168</sup>

### 2.2.5. Summary and outlook

In conclusion, Cu chalcogenide NCs can be synthesized in a large variety of sizes, shapes and compositions. However, direct synthesis of ternary and quaternary compositions is challenging. These synthetic limitations can be circumvented by deployment of topotactic cation exchange reactions on template binary  $\text{Cu}_{2-x}\text{A}$  NCs, for example resulting in ternary core/shell  $\text{CuInSe}_2/\text{CuInS}_2$  heteronanorods or quaternary  $\text{Cu}_2\text{ZnSn}(\text{Se},\text{S})_4$  nanoplatelets. In this way, high quality, size-, shape- and composition-controlled ternary and quaternary Cu chalcogenide NCs can be prepared, which may prove beneficial for the implementation of these NCs into devices.

## References

- (1) Donega, C. d. M. *Chem. Soc. Rev.* **2011**, *40*, 1512–1546.
- (2) Alivisatos, A. P. *J. Phys. Chem.* **1996**, *100*, 13226–13239.
- (3) Murray, C. B.; Norris, D. J.; Bawendi, M. G. *J. Am. Chem. Soc.* **1993**, *115*, 8706–8715.
- (4) Roduner, E. *Chem. Soc. Rev.* **2006**, *35*, 583–592.
- (5) Shirasaki, Y.; Supran, G.; Bawendi, M.; Bulović, V. *Nat. Photonics* **2012**, *7*, 13–23.
- (6) De Nolf, K.; Capek, R. K.; Abe, S.; Sluydts, M.; Jang, Y.; Martins, J. C.; Cottenier, S.; Lifshitz, E.; Hens, Z. *J. Am. Chem. Soc.* **2015**, *137*, 2495–505.
- (7) Shavel, A.; Ibáñez, M.; Luo, Z.; De Roo, J.; Carrete, A.; Dimitrievska, M.; Genç, A.; Meyns, M.; Pérez-Rodríguez, A.; Kovalenko, M. V.; Arbiol, J.; Cabot, A. *Chem. Mater.* **2016**, *28*, 720–726.
- (8) Hendricks, M. P.; Campos, M. P.; Cleveland, G. T.; Plante, I. J.; Owen, J. S. *Science* **2015**, *348*, 1226–1230.
- (9) Kolny-Olesiak, J.; Weller, H. *ACS Appl. Mater. Interfaces* **2013**, *5*, 12221–12237.
- (10) Carbone, L.; Nobile, C.; De Giorgi, M.; Della Sala, F.; Morello, G.; Pompa, P.; Hych, M.; Snoeck, E.; Fiore, A.; Franchini, I. R. *et al. Nano Lett.* **2007**, *7*, 2942–2950.

- (11) Kruszynska, M.; Borchert, H.; Parisi, J.; Kolny-Olesiak, J. *J. Am. Chem. Soc.* **2010**, *132*, 15976–86.
- (12) Donega, C. d. M. *Phys. Rev. B* **2010**, *81*, 165303.
- (13) De Trizio, L.; Manna, L. *Chem. Rev.* **2016**, acs.chemrev.5b00739.
- (14) Beberwyck, B. J.; Surendranath, Y.; Alivisatos, A. P. *J. Phys. Chem. C* **2013**, *117*, 19759–19770.
- (15) Rivest, J. B.; Jain, P. K. *Chem. Soc. Rev.* **2013**, *42*, 89–96.
- (16) Grodzinska, D.; Pietra, F.; van Huis, M. A.; Vanmaekelbergh, D.; de Mello Donega, C. *J. Mater. Chem.* **2011**, *21*, 11556–11565.
- (17) Gebauer, D.; Kellermeier, M.; Gale, J. D.; Bergström, L.; Cölfen, H. *Chem. Soc. Rev.* **2014**, *43*, 2348–2371.
- (18) Kudera, S.; Carbone, L.; Casula, M. F.; Cingolani, R.; Falqui, A.; Snoeck, E.; Parak, W. J.; Manna, L. *Nano Lett.* **2005**, *5*, 445–449.
- (19) Wang, W.; Banerjee, S.; Jia, S.; Steigerwald, M. L.; Herman, I. P. *Chem. Mater.* **2007**, *19*, 2573–2580.
- (20) Miszta, K.; de Graaf, J.; Bertoni, G.; Dorfs, D.; Brescia, R.; Marras, S.; Ceseracchi, L.; Cingolani, R.; van Roij, R.; Dijkstra, M.; Manna, L. *Nat. Mater.* **2011**, *10*, 872–876.
- (21) Tessier, M. D.; Spinicelli, P.; Dupont, D.; Patriarche, G.; Ithurria, S.; Dubertret, B. *Nano Lett.* **2014**, *14*, 207–213.
- (22) Groeneveld, E.; Donega, C. D. M. *J. Phys. Chem. C* **2012**, *116*, 16240–16250.
- (23) Bouet, C.; Tessier, M. D.; Ithurria, S.; Mahler, B.; Nadal, B.; Dubertret, B. *Chem. Mater.* **2013**, *25*, 1262–1271.
- (24) Ithurria, S.; Tessier, M.; Mahler, B.; Lobo, R.; Dubertret, B.; Efros, A. L. *Nat. Mater.* **2011**, *10*, 936–941.
- (25) Wang, F.; Wang, Y.; Liu, Y.-H.; Morrison, P. J.; Loomis, R. A.; Buhro, W. E. *Acc. Chem. Res.* **2015**, *48*, 13–21.
- (26) Li, H.; Zanella, M.; Genovese, A.; Povia, M.; Falqui, A.; Giannini, C.; Manna, L. *Nano Lett.* **2011**, *11*, 4964–4970.
- (27) van der Stam, W.; Gantapara, A. P.; Akkerman, Q. A.; Soligno, G.; Meeldijk, J. D.; van Roij, R.; Dijkstra, M.; de Mello Donega, C. *Nano Lett.* **2014**, *14*, 1032–1037.
- (28) Pearson, R. G. *Inorg. Chem.* **1988**, *27*, 734–740.
- (29) Mu, L.; Wang, F.; Sadtler, B.; Loomis, R. A.; Buhro, W. E. *ACS Nano* **2015**, *9*, 7419–7428.
- (30) van der Stam, W.; Berends, A. C.; Rabouw, F. T.; Willhammar, T.; Ke, X.; Meeldijk, J. D.; Bals, S.; de Mello Donega, C. *Chem. Mater.* **2015**, *27*, 621–628.
- (31) van der Stam, W.; Bladt, E.; Rabouw, F. T.; Bals, S.; de Mello Donega, C. *ACS Nano* **2015**, *9*, 11430–11438.
- (32) Groeneveld, E.; Witteman, L.; Lefferts, M.; Ke, X.; Bals, S.; Van Tendeloo, G.; de Mello Donega, C. *ACS Nano* **2013**, *7*, 7913–7930.
- (33) Grodzinska, D.; Pietra, F.; van Huis, M. A.; Vanmaekelbergh, D.; de Mello Donega, C. *J. Mater. Chem.* **2011**, *21*, 11556–11565.
- (34) Yin, Y.; Rioux, R. M.; Erdonmez, C. K.; Hughes, S.; Somorjai, G. A.; Alivisatos, A. P. *Science* **2004**, *304*, 711–715.
- (35) Vanmaekelbergh, D. *Nano Today* **2011**, *6*, 419–437.
- (36) van der Stam, W.; Rabouw, F. T.; Vonk, S. J. W.; Geuchies, J. J.; Ligthart, H.; Petukhov, A. V.; de Mello Donega, C. *Nano Lett.* **2016**, acs.nanolett.6b00221.
- (37) Evers, W. H.; De Nijs, B.; Fillion, L.; Castillo, S.; Dijkstra, M.; Vanmaekelbergh, D. *Nano Lett.* **2010**, *10*, 4235–4241.
- (38) Dong, A.; Chen, J.; Vora, P. M.; Kikkawa, J. M.; Murray, C. B. *Nature* **2010**, *466*, 474–477.
- (39) de Nijs, B.; Dussi, S.; Smalenburg, F.; Meeldijk, J. D.; Groenendijk, D. J.; Fillion, L.; Imhof, A.; van Blaaderen, A.; Dijkstra, M. *Nat. Mater.* **2015**, *14*, 56–60.
- (40) Vanmaekelbergh, D.; van Vugt, L. K.; Bakker, H. E.; Rabouw, F. T.; de Nijs, B.; van Dijk-Moes, R. J. A.; van Huis, M. A.; Baesjou, P. J.; van Blaaderen, A. *ACS Nano* **2015**, *9*, 3942–3950.
- (41) van der Stam, W.; Berends, A. C.; de Mello Donega, C. *ChemPhysChem* **2016**, *17*, 559–581.
- (42) Aldakov, D.; Lefrançois, A.; Reiss, P. *J. Mater. Chem. C* **2013**, *1*, 3756–3776.
- (43) Zhao, Y.; Burda, C. *Energy Environ. Sci.* **2012**, *5*, 5564–5576.
- (44) Goel, S.; Chen, F.; Cai, W. *Small* **2014**, *10*, 631–645.
- (45) Luther, J. M.; Jain, P. K.; Ewers, T.; Alivisatos, A. P. *Nat. Mater.* **2011**, *10*, 361–366.
- (46) Abdelhady, A. L.; Ramasamy, K.; Malik, M. A.; O'Brien, P.; Haigh, S. J.; Raftery, J. J. *J. Mater. Chem.* **2011**, *21*, 17888–17895.
- (47) Kuzuya, T.; Tai, Y.; Yamamuro, S.; Sumiyama, K. *Sci. Technol. Adv. Mater.* **2005**, *6*, 84–90.
- (48) Hessel, C. M.; Pattani, V. P.; Rasch, M.; Panthani, M. G.; Koo, B.; Tunnell, J. W.; Korgel, B. A. *Nano Lett.* **2011**, *11*, 2560–2566.
- (49) Wang, S.; Riedinger, A.; Li, H.; Fu, C.; Liu, H.; Li, L.; Liu, T.; Tan, L.; Barthel, M. J.; Pugliese, G.; De Donato, F.; Scotto D'Abbusco, M.; Meng, X.; Manna, L.; Meng, H.; Pellegrino, T. *ACS Nano* **2015**, *9*,

- 1788–1800.
- (50) Reifsnnyder, D. C.; Ye, X.; Gordon, T. R.; Song, C.; Murray, C. B. *ACS Nano* **2013**, *7*, 4307–4315.
- (51) Sigman, M.; Ghezelbash, A.; Hanrath, T.; Saunders, A. E.; Lee, F.; Korgel, B. A. *J. Am. Chem. Soc.* **2003**, *125*, 16050–16057.
- (52) Li, X.; Shen, H.; Niu, J.; Li, S.; Zhang, Y.; Wang, H.; Li, L. S. *J. Am. Chem. Soc.* **2010**, *132*, 12778–12779.
- (53) Li, X.; Wang, M.; Shen, H.; Zhang, Y.; Wang, H.; Li, L. S. *Chem. Eur. J.* **2011**, *17*, 10357–10364.
- (54) Li, W.; Shavel, A.; Guzman, R.; Rubio-Garcia, J.; Flox, C.; Fan, J.; Cadavid, D.; Ibáñez, M.; Arbiol, J.; Morante, J. R.; Cabot, A. *Chem. Commun.* **2011**, *47*, 10332–10334.
- (55) Tang, A.; Qu, S.; Li, K.; Hou, Y.; Teng, F.; Cao, J.; Wang, Y.; Wang, Z. *Nanotechnology* **2010**, *21*, 285602.
- (56) van der Stam, W.; Akkerman, Q. A.; Ke, X.; van Huis, M. A.; Bals, S.; de Mello Donega, C. *Chem. Mater.* **2015**, *27*, 283–291.
- (57) Chakrabarti, D. J.; Laughlin, D. E. *Bull. Alloy Phase Diagrams* **1983**, *4*, 254–271.
- (58) JCPDS cards 00-034-0171 klockmannite, 01-071-0045 umangite, 00-006-0680 berzelianite, 01-071-4325 bellidoite.
- (59) Shen, H.; Wang, H.; Yuan, H.; Ma, L.; Li, L. S. *Cryst. Eng. Commun.* **2012**, *14*, 555–560.
- (60) Deka, S.; Genovese, A.; Zhang, Y.; Miszta, K.; Bertoni, G.; Krahn, R.; Giannini, C.; Manna, L. *J. Am. Chem. Soc.* **2010**, *132*, 8912–8914.
- (61) Lesnyak, V.; Brescia, R.; Messina, G. C.; Manna, L. *J. Am. Chem. Soc.* **2015**, *137*, 9315–9323.
- (62) Li, H.; Brescia, R.; Povia, M.; Prato, M.; Bertoni, G.; Manna, L.; Moreels, I. *J. Am. Chem. Soc.* **2013**, *135*, 12270–12278.
- (63) Li, W.; Zamani, R.; Rivera Gil, P.; Pelaz, B.; Ibáñez, M.; Cadavid, D.; Shavel, A.; Alvarez-Puebla, R. A.; Parak, W. J.; Arbiol, J.; Cabot, A. *J. Am. Chem. Soc.* **2013**, *135*, 7098–7101.
- (64) Han, C.; Li, Z.; Li, W.; Chou, S.; Dou, S. *J. Mater. Chem. A* **2014**, *2*, 11683–11690.
- (65) Xie, Y.; Riedinger, A.; Prato, M.; Casu, A.; Genovese, A.; Guardia, P.; Sottini, S.; Sangregorio, C.; Miszta, K.; Ghosh, S.; Pellegrino, T.; Manna, L. *J. Am. Chem. Soc.* **2013**, *135*, 17630–17637.
- (66) Xie, Y.; Carbone, L.; Nobile, C.; Grillo, V.; D’Agostino, S.; Della Sala, F.; Giannini, C.; Altamura, D.; Oelsner, C.; Kryschi, C.; Cozzoli, P. D. *ACS Nano* **2013**, *7*, 7352–7369.
- (67) Larsen, T. H.; Sigman, M.; Ghezelbash, A.; Doty, R. C.; Korgel, B. A. *J. Am. Chem. Soc.* **2003**, *125*, 5638–5639.
- (68) Chen, Y.-B.; Chen, L.; Wu, L.-M. *Chem. Eur. J.* **2008**, *14*, 11069–11075.
- (69) Nørby, P.; Johnsen, S.; Iversen, B. B. *ACS Nano* **2014**, *8*, 4295–4303.
- (70) Han, W.; Yi, L.; Zhao, N.; Tang, A.; Gao, M.; Tang, Z. *J. Am. Chem. Soc.* **2008**, *130*, 13152–13161.
- (71) Bryks, W.; Wette, M.; Velez, N.; Hsu, S.; Tao, A. R. *J. Am. Chem. Soc.* **2014**, *136*, 6175–6178.
- (72) Kovalenko, M. V.; Bodnarchuk, M. I.; Zausen, J.; Lee, J.-S.; Talapin, D. V. *J. Am. Chem. Soc.* **2010**, *132*, 10085–10092.
- (73) Kovalenko, M. V.; Scheele, M.; Talapin, D. V. *Science* **2009**, *324*, 1417–1420.
- (74) Zanella, M.; Maserati, L.; Pernia Leal, M.; Prato, M.; Lavieville, R.; Povia, M.; Krahn, R.; Manna, L. *Chem. Mater.* **2013**, *25*, 1423–1429.
- (75) Bullen, C.; van Embden, J.; Jasieniak, J.; Cosgriff, J. E.; Mulder, R. J.; Rizzardo, E.; Gu, M.; Raston, C. L. *Chem. Mater.* **2010**, *22*, 4135–4143.
- (76) Dilella, E.; Xie, Y.; Brescia, R.; Prato, M.; Maserati, L.; Krahn, R.; Paoletta, A.; Bertoni, G.; Povia, M.; Moreels, I.; Manna, L. *Chem. Mater.* **2013**, *25*, 3180–3187.
- (77) Koo, B.; Patel, R.; Korgel, B. A. *J. Am. Chem. Soc.* **2009**, *131*, 3134–3135.
- (78) Saldanha, P. L.; Brescia, R.; Prato, M.; Li, H.; Povia, M.; Manna, L.; Lesnyak, V. *Chem. Mater.* **2014**, *26*, 1442–1449.
- (79) Wang, Y.; Zhukovskiy, M.; Tongying, P.; Tian, Y.; Kuno, M. *J. Phys. Chem. Lett.* **2014**, *5*, 3608–3613.
- (80) Zhang, D.; Wong, A. B.; Yu, Y.; Brittan, S.; Sun, J.; Fu, A.; Beberwyck, B.; Alivisatos, A. P.; Yang, P. *J. Am. Chem. Soc.* **2014**, *136*, 17430–17433.
- (81) Kriegel, I.; Rodríguez-Fernández, J.; Wisnet, A.; Zhang, H.; Waurisch, C.; Eychmüller, A.; Dubavik, A.; Govorov, A. O.; Feldmann, J. *ACS Nano* **2013**, *7*, 4367–4377.
- (82) Li, H.; Brescia, R.; Krahn, R.; Bertoni, G.; Alcocer, M. J. P.; D’Andrea, C.; Scotognella, F.; Tassone, F.; Zanella, M.; De Giorgi, M.; Manna, L. *ACS Nano* **2012**, *6*, 1637–1647.
- (83) Bouet, C.; Laufer, D.; Mahler, B.; Nadal, B.; Heuclin, H.; Pedetti, S.; Patriarche, G.; Dubertret, B. *Chem. Mater.* **2014**, *26*, 3002–3008.
- (84) Miszta, K.; Dorfs, D.; Genovese, A.; Kim, M. R.; Manna, L. *ACS Nano* **2011**, *5*, 7176–7183.
- (85) Zhuang, Z.; Peng, Q.; Zhang, B.; Li, Y. *J. Am. Chem. Soc.* **2008**, *130*, 10482–10483.
- (86) Zhao, Y.; Pan, H.; Lou, Y.; Qiu, X.; Zhu, J.; Burda, C. *J. Am. Chem. Soc.* **2009**, *131*, 4253–4261.
- (87) Page, M.; Niitsoo, O.; Itzhaik, Y.; Cahen, D.; Hodes, G. *Energy Environ. Sci.* **2009**, *2*, 220–223.

- (88) Wu, Y.; Wadia, C.; Ma, W.; Sadtler, B.; Alivisatos, A. *Nano Lett.* **2008**, *8*, 2551–2555.
- (89) R. C. Neville, *Solar Energy Conversion: the Solar Cell*, Elsevier **1995**.
- (90) Guo, Q.; Hillhouse, H. W.; Agrawal, R. *J. Am. Chem. Soc.* **2009**, *131*, 4–5.
- (91) Cao, Y.; Denny, M. S.; Caspar, J. V.; Farneth, W. E.; Guo, Q.; Ionkin, A. S.; Johnson, L. K.; Lu, M.; Malajovich, I.; Radu, D.; Rosenfeld, H. D.; Choudhury, K. R.; Wu, W. *J. Am. Chem. Soc.* **2012**, *134*, 15644–15647.
- (92) Mitzi, D. B.; Gunawan, O.; Todorov, T. K.; Wang, K.; Guha, S. *Sol. Energy Mater. Sol. Cells* **2011**, *95*, 1421–1436.
- (93) Todorov, T. K.; Reuter, K. B.; Mitzi, D. B. *Adv. Mater.* **2010**, *22*, E156–E159.
- (94) Steinhagen, C.; Panthani, M. G.; Akhavan, V.; Goodfellow, B.; Koo, B.; Korgel, B. A. *J. Am. Chem. Soc.* **2009**, *131*, 12554–12555.
- (95) Guo, Q.; Kim, S.; Kar, M.; Shafarman, W.; Birkmire, R. W.; Stach, E. A.; Agrawal, R.; Hillhouse, H. W. *Nano Lett.* **2008**, *8*, 2982–2987.
- (96) Otelaja, O. O.; Ha, D.; Zhang, H.; Robinson, R. D. *ACS Appl. Mater. Interfaces* **2014**, *6*, 18911–18920.
- (97) Lukashev, P.; Lambrecht, W. R. L.; Kotani, T.; van Schilfgaarde, M. *Phys. Rev. B* **2007**, *76*, 195202.
- (98) Kriegel, I.; Jiang, C.; Rodriguez-Fernandez, J.; Schaller, R. D.; Talapin, D. V.; Da Como, E.; Feldmann, J. *J. Am. Chem. Soc.* **2012**, *134*, 1583–1590.
- (99) Dorfs, D.; Härtling, T.; Miszta, K.; Bigall, N. C.; Kim, M. R.; Genovese, A.; Falqui, A.; Povia, M.; Manna, L. *J. Am. Chem. Soc.* **2011**, *133*, 11175–11180.
- (100) Wang, X.; Swihart, M. T. *Chem. Mater.* **2015**, *27*, 1786–1791.
- (101) Hsu, S.; Bryks, W.; Tao, A. R. *Chem. Mater.* **2012**, *24*, 3765–3771.
- (102) Hsu, S.-W.; On, K.; Tao, A. R. *J. Am. Chem. Soc.* **2011**, *133*, 19072–19075.
- (103) Liu, Y.; Deng, Y.; Sun, Z.; Wei, J.; Zheng, G.; Asiri, A. M.; Khan, S. B.; Rahman, M. M.; Zhao, D. *Small* **2013**, *9*, 2702–2708.
- (104) Luther, J. M.; Zheng, H.; Sadtler, B.; Alivisatos, A. P. *J. Am. Chem. Soc.* **2009**, *131*, 16851–16857.
- (105) Sadtler, B.; Demchenko, D. O.; Zheng, H.; Hughes, S. M.; Merkle, M. G.; Dahmen, U.; Wang, L.-W.; Alivisatos, A. P. *J. Am. Chem. Soc.* **2009**, *131*, 5285–5293.
- (106) De Trizio, L.; Gaspari, R.; Bertoni, G.; Kriegel, I.; Moretti, L.; Scotognella, F.; Maserati, L.; Zhang, Y.; Messina, G. C.; Prato, M.; Marras, S.; Cavalli, A.; Manna, L. *Chem. Mater.* **2015**, *27*, 1120–1128.
- (107) Ha, D.; Caldwell, A. H.; Ward, M. J.; Honrao, S.; Mathew, K.; Hovden, R.; Koker, M. K. A.; Muller, D. A.; Hennig, R. G.; Robinson, R. D. *Nano Lett.* **2014**, *14*, 7090–7099.
- (108) Yoon, H. C.; Oh, J. H.; Ko, M.; Yoo, H.; Do, Y. R. *ACS Appl. Mater. Interfaces* **2015**, *7*, 7342–7350.
- (109) Demir, N.; Oner, I.; Varlikli, C.; Ozsoy, C.; Zafer, C. *Thin Solid Films* **2015**, *589*, 153–160.
- (110) Park, S. H.; Hong, A.; Kim, J.-H.; Yang, H.; Lee, K.; Jang, H. S. *ACS Appl. Mater. Interfaces* **2015**, *7*, 6764–6771.
- (111) Chang, J.-Y.; Su, L.-F.; Li, C.-H.; Chang, C.-C.; Lin, J.-M. *Chem. Commun.* **2012**, *48*, 4848–4850.
- (112) Pan, Z.; Shen, Q.; Zhang, H.; Li, Y.; Zhao, K.; Wang, J.; Zhong, X.; Bisquert, J. *J. Am. Chem. Soc.* **2014**, *136*, 9203–9210.
- (113) Meinardi, F.; Colombo, A.; Velizhanin, K. A.; Simonutti, R.; Lorenzon, M.; Beverina, L.; Viswanatha, R.; Klimov, V. I.; Brovelli, S. *Nat. Photonics* **2014**, *8*, 392–399.
- (114) Knowles, K. E.; Kilburn, T. B.; Alzate, D. G.; McDowall, S.; Gamelin, D. R. *Chem. Commun.* **2015**, *51*, 9129–9132.
- (115) Chen, C.-W.; Wu, D.-Y.; Chan, Y.-C.; Lin, C. C.; Chung, P.-H.; Hsiao, M.; Liu, R.-S. *J. Phys. Chem. C* **2015**, *119*, 2852–2860.
- (116) Guo, W.; Sun, X.; Jacobson, O.; Yan, X.; Min, K.; Srivatsan, A.; Niu, G.; Kiesewetter, D. O.; Chang, J.; Chen, X. *ACS Nano* **2015**, *9*, 488–495.
- (117) Singh, V.; Castellanos Beltran, I. J.; Casamada Ribot, J.; Nagpal, P. *Nano Lett.* **2014**, *14*, 597–603.
- (118) Chang, J.; Waclawik, E. R. *CrystEngComm* **2013**, *15*, 5612–5619.
- (119) Binsma, J. J. M.; Giling, L. J.; Bloem, J. J. *Cryst. Growth* **1980**, *50*, 429–436.
- (120) Lu, X.; Zhuang, Z.; Peng, Q.; Li, Y. *CrystEngComm* **2011**, *13*, 4039–4045.
- (121) de Trizio, L.; Prato, M.; Genovese, A.; Casu, A.; Povia, M.; Simonutti, R.; Alcocer, M. J. P.; D’Andrea, C.; Tassone, F.; Manna L. *Chem. Mater.* **2012**, *24*, 2400–2406.
- (122) Li, L.; Pandey, A.; Werder, D.; Khanal, B. P.; Pietryga, J. M.; Klimov, V. I. *J. Am. Chem. Soc.* **2011**, *133*, 1176–1179.
- (123) Xia, C.; Cao, L.; Liu, W.; Su, G.; Gao, R.; Qu, H.; Shi, L.; He, G. *CrystEngComm* **2014**, *16*, 7469–7477.
- (124) Zhong, H.; Bai, Z.; Zou, B. *J. Phys. Chem. Lett.* **2012**, *3*, 3167–3175.
- (125) Tang, J.; Hinds, S.; Kelley, S.; Sargent, E. *Chem. Mater.* **2008**, *20*, 6906–6910.
- (126) Bao, N.; Qiu, X.; Wang, Y.-H. A.; Zhou, Z.; Lu, X.; Grimes, C. A.; Gupta, A. *Chem. Commun.* **2011**, *47*, 9441–9443.

- (127) Yarema, O.; Bozyigit, D.; Rousseau, I.; Nowack, L.; Yarema, M.; Heiss, W.; Wood, V. *Chem. Mater.* **2013**, *25*, 3753–3757.
- (128) Xu, J.; Lee, C.; Tang, Y.; Chen, X.; Chen, Z. *ACS Nano* **2010**, *4*, 1845–1850.
- (129) Wark, S. E.; Hsia, C.-H.; Luo, Z.; Son, D. H. *J. Mater. Chem.* **2011**, *21*, 11618–11625.
- (130) Huang, X.; Li, S.; Huang, Y.; Wu, S.; Zhou, X.; Li, S.; Gan, C. L.; Boey, F.; Mirkin, C. A.; Zhang, H. *Nat. Commun.* **2011**, *2*, 292.
- (131) De Trizio, L.; Li, H.; Casu, A.; Genovese, A.; Sathya, A.; Messina, G. C.; Manna, L. *J. Am. Chem. Soc.* **2014**, *136*, 16277–16284.
- (132) Groeneveld, E.; van Berkum, S.; van Schooneveld, M. M.; Gloter, A.; Meeldijk, J. D.; van den Heuvel, D. J.; Gerritsen, H. C.; de Mello Donega, C. *Nano Lett.* **2012**, *12*, 749–757.
- (133) Yakushev, M. V.; Luckert, F.; Faugeras, C.; Karotki, A. V.; Mudryi, A. V.; Martin, R. W. *Appl. Phys. Lett.* **2010**, *97*, 152110.
- (134) Debnath, T.; Maiti, S.; Maity, P.; Ghosh, H. N. *J. Phys. Chem. Lett.* **2015**, *6*, 3458–3465.
- (135) Binsma, J.; Giling, L.; Bloem, J. *J. Lumin.* **1982**, *27*, 35–53.
- (136) Binsma, J.; Giling, L.; Bloem, J. *J. Lumin.* **1982**, *27*, 55–72.
- (137) Shabaev, A.; Mehl, M. J.; Efros, Al. L. *Phys. Rev. B* **2015**, *92*, 035431.
- (138) Scragg, J. J.; Dale, P. J.; Peter, L. M.; Zoppi, G.; Forbes, I. *Phys. Status Solidi* **2008**, *245*, 1772–1778.
- (139) Persson, C. *J. Appl. Phys.* **2010**, *107*, 053710.
- (140) Matsushita, H.; Ichikawa, T.; Katsui, A. *J. Mater. Sci.* **2005**, *40*, 2003–2005.
- (141) Zhou, H.; Hsu, W.-C.; Duan, H.-S.; Bob, B.; Yang, W.; Song, T.-B.; Hsu, C.-J.; Yang, Y. *Energy Environ. Sci.* **2013**, *6*, 2822–2838.
- (142) Yang, H.; Jauregui, L. A.; Zhang, G.; Chen, Y. P.; Wu, Y. *Nano Lett.* **2012**, *12*, 540–545.
- (143) Shavel, A.; Cadavid, D.; Ibáñez, M.; Carrete, A.; Cabot, A. *J. Am. Chem. Soc.* **2012**, *134*, 1438–1441.
- (144) Rath, T.; Haas, W.; Pein, A.; Saf, R.; Maier, E.; Kunert, B.; Hofer, F.; Resel, R.; Trimmel, G. *Sol. Energy Mater. Sol. Cells* **2012**, *101*, 87–94.
- (145) Lu, X.; Zhuang, Z.; Peng, Q.; Li, Y. *Chem. Commun.* **2011**, *47*, 3141–3143.
- (146) Collord, A. D.; Hillhouse, H. W. *Chem. Mater.* **2015**, *27*, 1855–1862.
- (147) Larramona, G.; Bourdais, S.; Jacob, A.; Choné, C.; Muto, T.; Cuccaro, Y.; Delatouche, B.; Moisan, C.; Péré, D.; Dennler, G. *J. Phys. Chem. Lett.* **2014**, *5*, 3763–3767.
- (148) Jiang, C.; Liu, W.; Talapin, D. V. *Chem. Mater.* **2014**, *26*, 4038–4043.
- (149) Zou, Y.; Su, X.; Jiang, J. *J. Am. Chem. Soc.* **2013**, *135*, 18377–18384.
- (150) Coughlan, C.; Singh, A.; Ryan, K. *Chem. Mater.* **2013**, *25*, 653–661.
- (151) Singh, A.; Coughlan, C.; Laffir, F.; Ryan, K. M. *ACS Nano* **2012**, *6*, 6977–6983.
- (152) Singh, S.; Liu, P.; Singh, A.; Coughlan, C.; Wang, J.; Lusi, M.; Ryan, K. M. *Chem. Mater.* **2015**, *27*, 4742–4748.
- (153) Yu, X.; Shavel, A.; An, X.; Luo, Z.; Ibáñez, M.; Cabot, A. *J. Am. Chem. Soc.* **2014**, *136*, 9236–9239.
- (154) Singh, A.; Geaney, H.; Laffir, F.; Ryan, K. M. *J. Am. Chem. Soc.* **2012**, *134*, 2910–2913.
- (155) Jiang, C.; Lee, J.; Talapin, D. *J. Am. Chem. Soc.* **2012**, *134*, 5010–5013.
- (156) Tan, J. M. R.; Lee, Y. H.; Pedireddy, S.; Baikie, T.; Ling, X. Y.; Wong, L. H. *J. Am. Chem. Soc.* **2014**, *136*, 6684–6692.
- (157) Kruszynska, M.; Parisi, J.; Kolny-Olesiak, J. *Zeitschrift für Naturforsch. A* **2014**, *69*, 2–6.
- (158) Khare, A.; Wills, A. W.; Ammerman, L. M.; Norris, D. J.; Aydil, E. S. *Chem. Commun.* **2011**, *47*, 11721–11723.
- (159) Singh, A.; Singh, S.; Levchenko, S.; Unold, T.; Laffir, F.; Ryan, K. M. *Angew. Chem. Int. Ed.* **2013**, *52*, 9120–9124.
- (160) Tanaka, K.; Miyamoto, Y.; Uchiki, H.; Nakazawa, K.; Araki, H. *Phys. Status Solidi* **2006**, *203*, 2891–2896.
- (161) Lesnyak, V.; George, C.; Genovese, A.; Prato, M.; Casu, A.; Ayyappan, S.; Scarpellini, A.; Manna, L. *ACS Nano* **2014**, *8*, 8407–8418.
- (162) Green, M. A.; Emery, K.; Hishikawa, Y.; Warta, W.; Dunlop, E. D. *Prog. Photovoltaics Res. Appl.* **2013**, *21*, 606–614.
- (163) Draguta, S.; McDaniel, H.; Klimov, V. I. *Adv. Mater.* **2015**, *27*, 1701–1705.
- (164) Wang, W.; Winkler, M. T.; Gunawan, O.; Gokmen, T.; Todorov, T. K.; Zhu, Y.; Mitzi, D. B. *Adv. Energy Mater.* **2014**, *4*, 1301465.
- (165) Stolle, C. J.; Harvey, T. B.; Korgel, B. A. *Curr. Opin. Chem. Eng.* **2013**, *2*, 160–167.
- (166) Guo, Q.; Ford, G.; Yang, W.; Walker, B. C.; Stach, E. A.; Hillhouse, H. W.; Agrawal, R. *J. Am. Chem. Soc.* **2010**, *132*, 17384–17386.
- (167) Ford, G. M.; Guo, Q.; Agrawal, R.; Hillhouse, H. W. *Chem. Mater.* **2011**, *23*, 8–11.
- (168) Collord, A. D.; Hillhouse, H. W. *Sol. Energy Mater. Sol. Cells* **2015**, *141*, 383–390.



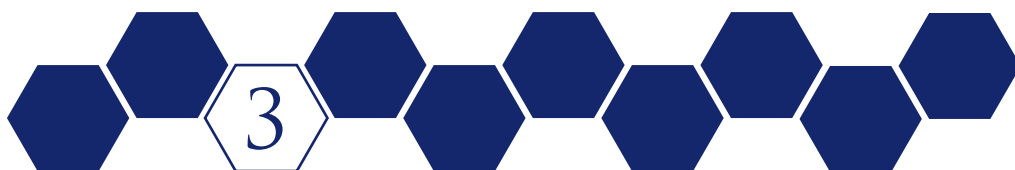


# PART A

## SHAPE TAILORING



# Shape Control of Colloidal $\text{Cu}_{2-x}\text{S}$ Polyhedral Nanocrystals by Tuning the Nucleation Rates



## ABSTRACT

Synthesis protocols for colloidal nanocrystals (NCs) with narrow size and shape distributions are of particular interest for the successful implementation of these nanocrystals into devices. Besides, the preparation of NCs with well-defined crystal phases is of key importance. In this chapter, we show that Sn(IV)-thiolate complexes formed *in-situ* strongly influence the nucleation and growth rates of colloidal  $\text{Cu}_{2-x}\text{S}$  polyhedral NCs, thereby dictating their final size, shape, and crystal structure. This allowed us to successfully synthesize hexagonal bifrustums and hexagonal bipyramid NCs with the low-chalcocite crystal structure, and hexagonal nanoplatelets with various thicknesses and aspect ratios with the djurleite crystal structure, by solely varying the concentration of Sn(IV)-additives (*viz.*,  $\text{SnBr}_4$ ) in the reaction medium. Solution and solid-state  $^{119}\text{Sn}$ -NMR measurements show that  $\text{SnBr}_4$  is converted *in-situ* to Sn(IV)-thiolate complexes, which increase the  $\text{Cu}_{2-x}\text{S}$  nucleation barrier, without affecting the precursor conversion rates. This influences both the nucleation and growth rates in a concentration dependent fashion, and leads to a better separation between nucleation and growth. Our approach of tuning the nucleation and growth rates with *in-situ* generated Sn-thiolate complexes might have a more general impact, due to the availability of various metal-thiolate complexes, possibly resulting in polyhedral NCs of a wide variety of metal-sulfide compositions.

Based on

**Shape Control of Colloidal  $\text{Cu}_{2-x}\text{S}$  Polyhedral Nanocrystals by Tuning the Nucleation Rates**

W. van der Stam, S. Gradmann, T. Altantzis, X. Ke, M. Baldus, S. Bals and C. de Mello Donega, 2016, submitted.

### 3.1 Introduction

In recent years, the scientific community has achieved a high level of mastery over the size, shape and composition of colloidal nanocrystals (NCs) and heteronanocrystals (HNCs) of Cd- and Pb-chalcogenide compositions.<sup>1-4</sup> However, their further deployment into applications has been hindered by toxicity concerns.<sup>5-8</sup> The properties of copper chalcogenides ( $\text{Cu}_{2-x}\text{A}$ , with A = S, Se and Te) make them attractive alternatives for Cd- and Pb-based semiconductors for several applications.<sup>6,8-10</sup> For instance,  $\text{Cu}_{2-x}\text{S}$  is a direct p-type semiconductor with a band gap that depends on its stoichiometry (1.1 – 1.4 eV for  $x = 0 - 0.04$ ; 1.5 eV for  $x = 0.2$ ; 2.0 eV for  $x = 1$ ).<sup>11-13</sup> The combination of a suitable band gap, high absorption coefficient ( $10^4 \text{ cm}^{-1}$ ), and low toxicity has made  $\text{Cu}_{2-x}\text{S}$  a promising candidate for large scale and sustainable implementation into photovoltaic (PV) devices.<sup>14,15</sup> Moreover,  $\text{Cu}_{2-x}\text{A}$  NCs can hold both excitons and tunable localized surface plasmon resonances on demand.<sup>9,13,16-18</sup> This makes  $\text{Cu}_{2-x}\text{A}$  NCs promising materials for photovoltaics,<sup>15</sup> photocatalysis,<sup>19</sup> sensing<sup>20</sup> and nanoplasmonics.<sup>9,11,17,21,22</sup>

The application of colloidal NCs in photovoltaic and nanoplasmonic devices requires strict control over the size, shape and polydispersity of the NC ensemble, since these characteristics are of crucial importance not only for the optoelectronic properties of the NCs themselves, but also for the quality of the NC thin films obtained by solution based deposition techniques.<sup>23-25</sup>  $\text{Cu}_{2-x}\text{S}$  NCs are of particular interest, since a variety of shapes not attainable for other semiconductor NCs can easily be synthesized with narrow size and shape distributions. For example, hexagonal nanodisks, nanoplatelets and nanosheets, among other polyhedral shapes, have been successfully synthesized.<sup>6,26-29</sup> Shape control over  $\text{Cu}_{2-x}\text{S}$  NCs may also have a more general impact, since  $\text{Cu}^+$  ions in copper chalcogenides have been shown to be easily exchangeable by other cations.<sup>6,30-37</sup> This opens up the possibility of using (partial) topotactic cation exchange reactions to convert  $\text{Cu}_{2-x}\text{A}$  NCs into other compositions, while preserving the size and shape of the parent NCs, thereby making NCs with novel functionalities.<sup>33,36,37</sup> However, the methods currently available to control the size and shape of  $\text{Cu}_{2-x}\text{S}$  NCs lack flexibility, since different sets of physical-chemical parameters (concentrations, ligands, reaction temperatures, reaction times) have to be used for each different shape.<sup>6,26,28</sup>

In this chapter, a novel methodology for the size and shape control of colloidal  $\text{Cu}_{2-x}\text{S}$  NCs is developed, which relies on changing just one single reaction variable: the concentration of Sn(IV)-complexes that are used to control the nucleation and growth rates of  $\text{Cu}_{2-x}\text{S}$  NCs. In this way, hexagonal bifrustums, hexagonal bipyramids and hexagonal nanoplatelets of various aspect ratios are synthesized with narrow size and shape distributions. Solid-state  $^{119}\text{Sn}$ -NMR measurements indicate that Sn-thiolate complexes formed *in-situ* control the nucleation and growth rates, which results in various polyhedral  $\text{Cu}_{2-x}\text{S}$  NCs. Our study provides insights into the formation

of polyhedral Cu<sub>2-x</sub>S NCs and possibly paves the way toward the development of synthetic protocols for polyhedral NCs of various compositions by deployment of *in-situ* nucleation and growth controlling agents, such as Sn(IV)-thiolates.

## 3.2 Methods

**Materials.** Copper(I) chloride (CuCl, 97%), tin(IV) tetrabromide (SnBr<sub>4</sub>, 99%), 1-dodecanethiol (DDT, ≥98%), oleylamine (OLAM, 70%), anhydrous methanol (MeOH), butanol (BuOH), toluene and chloroform were purchased from Sigma Aldrich and used as delivered, except for OLAM, which was degassed at 120 °C under vacuum for 2 hours.

*Colloidal hexagonal bipyramid-shaped Cu<sub>2-x</sub>S NCs* were synthesized based on the protocol described by Kuzuya *et al.*,<sup>38</sup> which was modified by adding SnBr<sub>4</sub> to the reaction mixture. In a typical synthesis, 1.0 mmol CuCl (99 mg) and 0.5 mmol SnBr<sub>4</sub> (219 mg) were mixed in 8 mL (33.6 mmol) of 1-dodecanethiol (DDT) and 2 mL (6 mmol) of oleylamine (OLAM). The flask was purged with N<sub>2</sub> and the solution was gradually heated to 225 °C. At first, a creamy white substance was present, but around 80 °C the solution turned slightly yellow. When further heated, a clear yellow solution was obtained around 130 °C. Nucleation and growth of Cu<sub>2-x</sub>S started when the temperature had reached 200 °C. Finally, the particles were allowed to grow at 225 °C for one hour and subsequently the nanoparticles were precipitated by the repeated addition of a methanol/butanol solution and redispersion in toluene.

*Colloidal polyhedral Cu<sub>2-x</sub>S NCs of various morphologies* were synthesized based on the same method as described above, only the amount of SnBr<sub>4</sub> was varied (Cu:Sn ratio of 2:3 for low aspect ratio hexagonal nanoplatelets, 1:2 for high aspect ratio hexagonal nanoplatelets, 30:1 for small hexagonal bipyramids and 1:1 for large hexagonal bipyramids).

**Transmission Electron Microscopy (TEM) and Energy Dispersive X-Ray Spectroscopy (EDS).** TEM and EDS measurements were performed on a Tecnai20F (FEI) microscope equipped with a Field Emission Gun, a Gatan 694 CCD camera and an EDAX spectrometer. The microscope was operated at 200 kV. Acquisition time for EDS measurements was 30 s. Samples for TEM imaging were prepared by dripping a diluted nanocrystal solution in toluene on a carbon coated polymer film copper grid (300 mesh). The solvent (toluene) was allowed to evaporate prior to imaging.

**High-resolution (Scanning) Transmission Electron Microscopy** was performed on a double aberration corrected cubed FEI Titan 50-80 electron microscope operated at 120 kV. High-resolution Transmission Electron Microscopy was performed on a FEI Osiris electron microscope operated at 200 kV. The Selected Area Electron Diffraction (SAED) Patterns were acquired using a FEI Tecnai G2 electron microscope operated at 200kV. Electron tomography measurements were performed in High-Angle Annular Dark-Field Scanning Transmission Electron Microscopy (HAADF-STEM) mode, in order to get rid of any unwanted diffraction contrast present in TEM, by using an aberration-corrected cubed FEI Titan 60-300 electron microscope and a double aberration-corrected cubed FEI Titan 50-80 electron microscope operated at 200 and 300 kV. The acquisition of all the series was performed manually over a tilt range from -74° to +74° and a tilt increment of 2° by using a Fischione model 2020 single tilt tomography holder. The alignment of all the acquired series was performed by using cross-correlation and the reconstruction by using the Simultaneous Iterative Reconstruction Technique (SIRT) as implemented in ASTRA toolbox.<sup>69</sup>

**Solid-state <sup>119</sup>Sn-NMR & solution <sup>1</sup>H-NMR** experiments were performed using a Bruker Avance III spectrometer equipped with a 4 mm double resonance probehead at 11.7 T static magnetic field. All experiments on precipitated and dry nanocrystals were measured at room temperature and on solution samples at 308 K. Tin and proton field strengths for 90° pulses were 50 kHz and 71 kHz, respectively. Spectral referencing was done using SnBr<sub>4</sub> for tin and adamantane for protons.

*X-Ray Diffraction* (XRD) patterns were obtained by using a PW 1729 Philips diffractometer, equipped with a Cu K $\alpha$  X-ray source ( $\lambda = 1.5418 \text{ \AA}$ ). Samples for XRD analysis were prepared by depositing purified NCs in chloroform on a Si wafer substrate under inert atmosphere. The concentrated solution of NCs was dropcasted on the Si wafer and the chloroform was allowed to evaporate at RT, resulting in a concentrated NC solid.

### 3.3 Results and Discussion

#### 3.3.1 Shape control of anisotropic Cu $_{2-x}$ S NCs by SnBr $_4$ addition

Colloidal Cu $_{2-x}$ S nanocrystals (NCs) were synthesized by heating up a solution of CuCl in 1-dodecanethiol (DDT) and oleylamine (OLAM) to 225 °C (see Methods for details). In this protocol, DDT has the combined roles of ligand, solvent and sulfur source.<sup>38–40</sup> In the absence of SnBr $_4$  large polydisperse nanoplatelets (~100 nm lateral dimensions) are obtained (Figure 3.1a). The addition of SnBr $_4$  to the reaction mixture has a dramatic impact on the size and shape of the product NCs, leading to a variety of polyhedral shapes (hexagonal bifrustums, hexagonal bipyramids, low and high aspect ratio hexagonal nanoplatelets) with small polydispersity, depending on the SnBr $_4$  concentration (Figure 3.1).

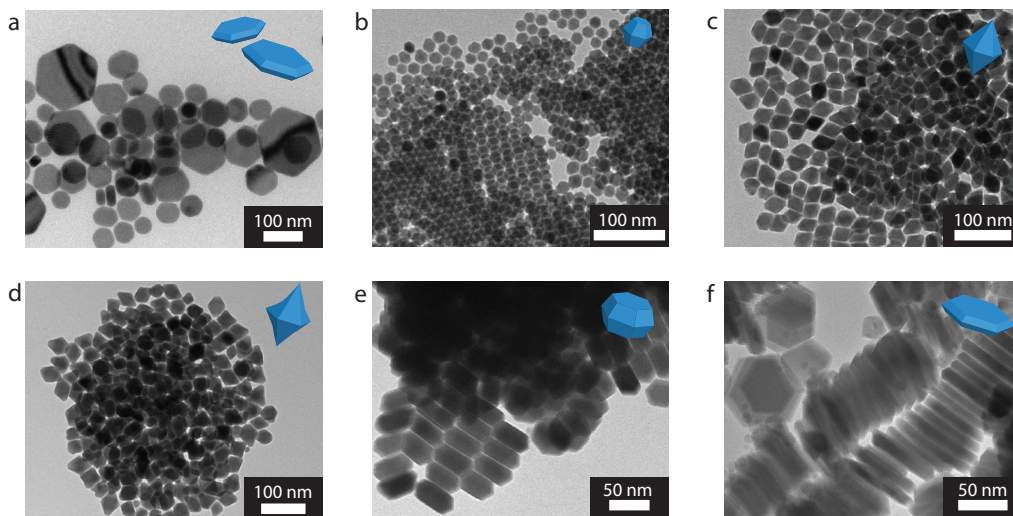


**Figure 3.1. Representative Transmission Electron Microscopy (TEM) images of Cu $_{2-x}$ S nanocrystals synthesized with varying SnBr $_4$  concentration under otherwise constant reaction conditions.** The amount of SnBr $_4$  was the only variable, all other reaction parameters were kept constant (see experimental section for details). (a) Polydisperse Cu $_{2-x}$ S nanoplatelets synthesized in the absence of SnBr $_4$ . (b) Monodisperse Cu $_{2-x}$ S bifrustum NCs (diameter: 17 nm) are obtained when a small amount of SnBr $_4$  is added (Cu:Sn 30:1). (c) A Cu:Sn ratio of 2:1 yields hexagonal bipyramids (28 nm wide, 38 nm long). (d) Cu $_{2-x}$ S NCs synthesized under Cu:Sn = 1:1. (e) Hexagonal nanoplatelets (25 nm thick, 50 nm wide) are obtained under Cu:Sn = 2:3. (f) Further increase of the Cu:Sn ratio to 1:2 leads to wider and thinner hexagonal nanoplatelets (80 nm by 10 nm).

High-Resolution Transmission Electron Microscopy (HRTEM) (Figure 3.2), Electron Diffraction (Appendix A3.1) and X-ray Diffractometry (Appendix A3.2) measurements revealed that the product Cu<sub>2-x</sub>S nanoplatelets have the djurleite crystal structure (Cu<sub>31</sub>S<sub>16</sub>, Cu<sub>1.96</sub>S),<sup>41</sup> whereas the product Cu<sub>2-x</sub>S bipyramids have the low-chalcocite (Cu<sub>2</sub>S) crystal structure. This is evident in the HRTEM images and the corresponding Fast Fourier Transform (FFT) patterns of hexagonal bipyramid NCs viewed along the [010] zone axis (Figure 3.2a,d), and of low aspect ratio nanoplatelets (Figure 3.2b,c,e,f). The observed spacings are in agreement (within a 1% error margin) with the djurleite crystal structure (lattice parameters  $a = 26.89 \text{ \AA}$ ,  $b = 15.74 \text{ \AA}$  and  $c = 13.57 \text{ \AA}$ )<sup>41</sup> for the nanoplatelets and with the low-chalcocite crystal structure (lattice parameters  $a = 11.92 \text{ \AA}$ ,  $b = 27.34 \text{ \AA}$  and  $c = 13.44 \text{ \AA}$ )<sup>41</sup> for the bipyramid NCs.

The morphology of the NCs was investigated by carrying out electron tomography measurements in High-Angle Annular Dark Field Scanning Transmission Electron Microscopy (HAADF-STEM) mode (Figure 3.3). By combining the electron tomography results concerning the shape of the NCs, with the crystal structure

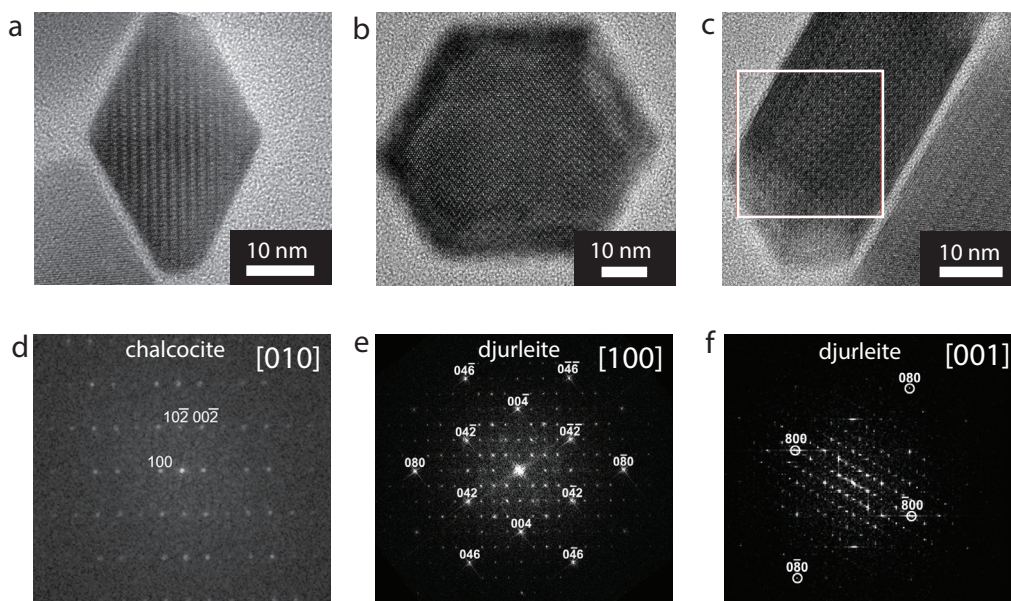


**Figure 3.2. Structural analysis of the product Cu<sub>2-x</sub>S nanocrystals.** (a) High-Resolution Transmission Electron Microscopy (HRTEM) images of hexagonal bipyramid Cu<sub>2-x</sub>S NCs and (b) low aspect ratio hexagonal Cu<sub>2-x</sub>S nanoplatelets viewed along the [100] direction and (c) along the [001] direction. The white square in c indicates the area of which the FFT pattern is displayed in panel g. (d) FFT pattern of the bipyramid NC displayed in panel a, showing characteristic atomic reflections of low-chalcocite Cu<sub>2</sub>S viewed along the [010] zone axis. (e) FFT pattern of the NC displayed in panel b, showing characteristic atomic reflections of hexagonal djurleite Cu<sub>1.96</sub>S viewed along the [100] zone axis. (f) FFT pattern of a selected area (white square) of the NC displayed in panel c, showing characteristic atomic reflections of hexagonal djurleite Cu<sub>1.96</sub>S, viewed along the [001] direction.

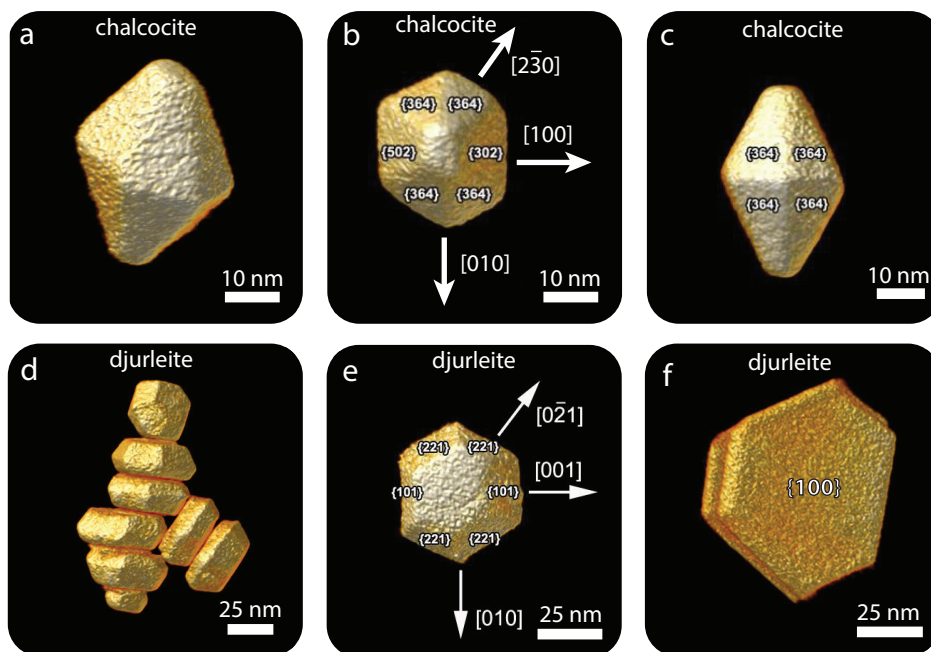


**Figure 3.3. Electron tomography reconstructions of polyhedral  $\text{Cu}_{2-x}\text{S}$  nanocrystals.** (a) Electron tomography reconstruction of a single hexagonal  $\text{Cu}_2\text{S}$  bipyramid nanocrystal. (b) Facets indexation of a low-chalcocite  $\text{Cu}_2\text{S}$  hexagonal bipyramid. (c) Tomographic reconstruction of a single hexagonal bipyramid viewed along the  $[010]$  direction, showing four equivalent  $\{364\}$  facets. (d) Tomographic reconstruction of the low aspect ratio hexagonal djurleite  $\text{Cu}_{1.96}\text{S}$  nanoplatelets, viewed along the  $[100]$  direction, and of (e) low aspect ratio hexagonal  $\text{Cu}_{1.96}\text{S}$  nanoplatelets viewed from the top and (f) two high aspect ratio nanoplatelets viewed from the top.

determined from the HRTEM measurements (Figure 3.2 above), the different facets can be indexed according to the low-chalcocite (for bipyramids) and djurleite (for nanoplatelets) crystal structures.<sup>41</sup> In this way, the lateral facets of the low-chalcocite  $\text{Cu}_2\text{S}$  bipyramids are indexed as  $\{364\}$  (8 facets),  $\{502\}$  (2 facets) and  $\{302\}$  (2 facets) (Figure 3.3b,c). A different indexation holds for the low and high aspect ratio hexagonal nanoplatelets, which have the djurleite  $\text{Cu}_{1.96}\text{S}$  crystal structure. The side facets of the nanoplatelets are formed by 8 trapezoidal  $\{221\}$  and 4  $\{101\}$  facets, and the top and bottom facets are the hexagonal  $\{100\}$  facets. It is thus evident that the addition of  $\text{SnBr}_4$  alters the size and crystal structure, and hence, the faceting, of  $\text{Cu}_{2-x}\text{S}$  NCs in a concentration dependent fashion. At the lowest Sn:Cu ratio (1:30) small ( $d = 17$  nm) hexagonal bifrustums are obtained with the low-chalcocite crystal structure, in which the top and bottom  $\{100\}$  facets and the  $\{364\}$  and  $\{302\}/\{502\}$  side facets have similar areas. Increase of the Sn:Cu ratio to 2:1 leads to large (28 nm by 38 nm), hexagonal bipyramidal low-chalcocite NCs in which the  $\{100\}$  facets are almost absent. Further

increase of the Sn:Cu ratio results in djurleite hexagonal nanoplatelets of which the relative area of the {100} facets, the lateral dimensions and the aspect ratio grow with the Sn:Cu ratio (25 nm thick, 50 nm wide, for Sn:Cu = 3:2; and 10 nm thick, 80 nm wide, for Sn:Cu = 2:1). The formation mechanism for low-chalcocite bipyramids and djurleite nanoplatelets will be discussed in detail below.

As will be discussed in Chapter 4, the addition of SnBr<sub>4</sub> to synthesis protocols for Cu<sub>2-x</sub>S NCs dramatically affects the size and shape of the product NCs, yielding ultrathin (2 nm thick) Cu<sub>2-x</sub>S nanosheets with well-defined shape and size (triangular or hexagonal, 100 nm to 3 μm wide), instead of nearly spherical small (9 nm diameter) NCs.<sup>29</sup> The effect was clearly shown to be due to the halides, so that Sn(IV) tetrahalides were only relevant as sources of sufficiently high halide concentrations in the growth solution.<sup>29</sup> To investigate the roles of the halide and Sn(IV) in the present case, we carried out control experiments, in which either SnBr<sub>4</sub> was replaced by Sn(OAc)<sub>4</sub> or additional halides were added in the form of CuBr in the absence of any Sn(IV) compound. The results clearly show that, in contrast to our study on the formation of ultrathin Cu<sub>2-x</sub>S nanosheets (Chapter 4),<sup>29</sup> the effect in the present case is due to the Sn(IV) (Appendix A3.3), since additional halides yield polydisperse nanoplatelets similar to those obtained under the standard reaction conditions (*i.e.*, SnBr<sub>4</sub> absent, Figure 3.1a above), while addition of Sn(OAc)<sub>4</sub> resulted in polyhedral NCs similar to those obtained upon addition of SnBr<sub>4</sub> (Sn:Cu= 1:2, Figure 3.1c above). The larger polydispersity observed when using Sn(OAc)<sub>4</sub> instead of SnBr<sub>4</sub> can be ascribed to the fact that Sn(OAc)<sub>4</sub> is less reactive toward DDT molecules than SnBr<sub>4</sub>, since acetate and Sn<sup>4+</sup> are a strong Lewis base and acid, respectively, and are better matched in terms of hardness (both hard) than bromide and Sn<sup>4+</sup> (soft and hard, respectively).<sup>42</sup> This suggests that the active Sn(IV) species responsible for the observed morphological changes are formed *in-situ*. This also explains the different roles observed for Sn(IV) in the present work (active species) and in our previous study on the formation of Cu<sub>2-x</sub>S nanosheets (*viz.*, halide carrier),<sup>29</sup> since in the latter case a smaller excess of DDT (10-fold with respect to Cu) was injected in the reaction mixture, while in the present case a large excess of DDT is used (30-fold with respect to Cu), allowing the formation of both Cu-DDT and Sn-DDT complexes, despite the lower reactivity of Sn(IV) towards DDT. As will become clear below (NMR Spectroscopy section), another important chemical difference in the present reaction system is the presence of oleylamine, which deprotonates DDT, thereby further facilitating its reaction with SnBr<sub>4</sub>.

To gain further insight into the role of SnBr<sub>4</sub> in the shape control of the product Cu<sub>2-x</sub>S NCs, Energy Dispersive X-ray spectroscopy (EDS) chemical mapping was used to quantify and locate the elements present in the NCs. The Cu:Sn:S ratio was found to be 1.81±0.14 : 0.02±0.01 : 1.00, regardless of the Cu:Sn ratio used in the reaction. Bromide was not detected in any sample. Elemental mapping shows that Sn is not homogeneously distributed across the ensemble of NCs, but is concentrated on

a few NCs that appear morphologically distinct from the majority of the ensemble (Appendices A3.4 and A3.5). The Sn distribution in the Sn-poor NCs does not indicate any preference for a particular facet, regardless of the shape of the NC (*i.e.*, bipyramids or nanoplatelets). The signal from individual NCs was too low to allow the composition of the Sn-rich NCs to be reliably established, but their different shapes imply that they no longer have the hexagonal crystal structure of djurleite or low-chalcocite,<sup>41</sup> and may have adopted the cubic crystal structures characteristic of ternary  $\text{Cu}_x\text{Sn}_y\text{S}_z$  phases (*e.g.*, zinc blende for  $\text{Cu}_2\text{SnS}_3$ , cubic spinel for  $\text{Cu}_2\text{Sn}_3\text{S}_7$ ).<sup>43–46</sup> The Cu-Sn-S phase diagram is however quite rich (16 different phases, 13 of them metastable),<sup>46</sup> and therefore the range of possible compositions for the Sn-rich NCs is very wide (from  $\text{Cu}_9\text{Sn}_2\text{S}_9$  to  $\text{Cu}_2\text{Sn}_{3.75}\text{S}_8$ ). Nevertheless, it is clear that in these NCs some degree of Sn(IV) inter-diffusion has taken place, inducing crystal structure and morphology changes. Considering that only a very small fraction of the NCs is observed to be Sn-rich (< 5%), we can conclude that the Sn(IV)-diffusion rates in the  $\text{Cu}_{2-x}\text{S}$  NCs were negligible under the conditions prevalent in our experiments. This is consistent with previous studies in which significant Sn(IV) inter-diffusion in  $\text{Cu}_{2-x}\text{S}$  NCs was only observed at temperatures as high as 240 °C.<sup>45</sup>

The results presented above demonstrate that the dramatic impact of  $\text{SnBr}_4$  in the size and shape evolution of  $\text{Cu}_{2-x}\text{S}$  NCs synthesized by heating-up a solution of  $\text{CuCl}$  in DDT is due to *in-situ* generated Sn(IV) species, and rules out Sn(IV) incorporation as the cause for the observed changes. Tin(IV) compounds (*viz.*,  $\text{SnCl}_4$  and  $\text{Sn}(\text{acetylacetonate})\text{Cl}_2$ ) have been previously reported to affect the shape of  $\text{Cu}_{2-x}\text{S}$  NCs obtained by heating-up  $\text{Cu}(\text{II})\text{acetylacetonate}$  in DDT, leading to the formation of either nanosheets or nanodisks, under conditions that would otherwise yield spherical NCs.<sup>47–49</sup> This effect has been tentatively ascribed to *in-situ* generated  $[\text{Sn}_x\text{S}_y]$  species (*e.g.*,  $[\text{Sn}_2\text{S}_6]^{4-}$ ) that would presumably act as selective surfactants, thereby influencing the relative growth rates of different facets and thus altering the NC morphology.<sup>47–49</sup> However, no evidence was provided for the presence of such species, either in the reaction medium or at the surface of the product  $\text{Cu}_{2-x}\text{S}$  NCs. Therefore, in order to verify the validity of this hypothesis and to uncover the nature of the Sn(IV)-complexes that were formed *in-situ* in the present study, we carried out  $^1\text{H}$  and  $^{119}\text{Sn}$  NMR spectroscopic measurements.

### 3.3.2 Solution and solid-state $^{119}\text{Sn}$ NMR Spectroscopy

Solid-state and solution  $^{119}\text{Sn}$  NMR spectroscopy is particularly suited to elucidate the nature of the Sn-complexes in solution and on the surface of the NCs. Overall, the fairly high natural abundance of  $^{119}\text{Sn}$  nuclei as well as the large range of isotropic chemical shifts (around 6500 ppm) that leads to clearly separated chemical shift regions in the spectra, makes  $^{119}\text{Sn}$  NMR a promising tool for characterizing tin compounds. Combined with novel NMR methods like dynamic nuclear polarization (DNP)  $^{119}\text{Sn}$  NMR also has a great potential for the investigation of nanomaterial surfaces.<sup>50</sup> Furthermore, former studies have shown that the chemical shift tensor parameters of

tin sulfides are highly sensitive to coordination numbers and symmetry in the local environment of the tin atom.<sup>51</sup> Therefore, probing the chemical shift anisotropy (CSA) *via* solid-state NMR provides an opportunity to detect structural details.

In the following, three of our Cu<sub>2-x</sub>S NC morphologies were analyzed with solid-state <sup>119</sup>Sn NMR, namely the hexagonal bipyramids (Cu:Sn 2:1), the low aspect ratio nanoplatelets (Cu:Sn 2:3) and the high aspect ratio nanoplatelets (Cu:Sn 1:2). The reference for solid-state <sup>119</sup>Sn NMR measurements was SnBr<sub>4</sub>, with a sharp peak at chemical shift  $\delta$  -638 ppm. None of the measured NC samples showed a detectable amount of SnBr<sub>4</sub> in the spectra. Instead, in the cases of an excess of Sn compared to Cu, the spectra were dominated by a sharp signal at +144 ppm under static conditions as well as magic angle spinning (MAS) at 5 kHz (black lines in Figure 3.4b, signal at 144 ppm indicated with a red star). The absence of line narrowing after spinning at 5 kHz indicates that these compounds have a symmetrical surrounding, meaning they are not on the NC surface. Additionally, less intense and broader signals in the chemical shift range between 0–80 ppm were observed for the high aspect ratio Cu<sub>2-x</sub>S NPs, obtained by mixing Cu(I) and Sn(IV) salts in a 1:2 ratio (Figure 3.4b, indicated with blue stars). In the presence of a higher Cu amount compared to Sn (Cu:Sn 2:1), one broad peak centered at -208 ppm was detected (top of Figure 3.4b, indicated with a black star). Here, 5 kHz spinning resulted in significant line narrowing (top of Figure 4b), indicating an asymmetrical surrounding. This signal was therefore assigned to a Sn-compound bound to the NC surface. Comparison with the chemical shift values reported by Kovalenko *et al.*<sup>52,53</sup> for Sn-sulfocomplexes ([Sn<sub>2</sub>S<sub>6</sub>]<sup>4-</sup> and [SnS<sub>4</sub>]<sup>4-</sup> at  $\delta$  = +56.3 ppm and  $\delta$  = 70–75 ppm, respectively) lead to the conclusion that the Sn(IV) species formed *in-situ* in our experiments are of a different nature. This is further supported by the fact that the anisotropic line broadening (around 60 ppm, top of Figure 3.4b) of the <sup>119</sup>Sn NMR spectrum obtained for hexagonal bipyramids (Cu:Sn of 2:1) is far less pronounced than reported in literature for salts containing [Sn<sub>2</sub>S<sub>6</sub>]<sup>4-</sup> ions.<sup>54</sup>

We thus propose a mechanism where thiol molecules replace bromides from SnBr<sub>4</sub> in order to form Sn-thiolate complexes. This replacement is a stepwise process, where one Br is replaced by a thiol in each step (Figure 3.4a). Tin(IV) methylthiolate, (MeS)<sub>4</sub>Sn, is known to show a sharp signal at +160 ppm.<sup>55,56</sup> A shift to slightly lower ppm values is expected if the methylthiolate groups are replaced by thiolate-groups containing longer alkyl chains,<sup>55,56</sup> as dodecylthiolate in the present work. The sharp signal at +144 ppm is thus assigned to (C<sub>12</sub>H<sub>25</sub>S)<sub>4</sub>Sn (indicated by a red star in panel a). This interpretation is supported by earlier findings that related sharp signals with a lack of prominent sidebands under slow spinning speeds (around 3 kHz) and low magnetic fields correspond to salts containing [SnS<sub>4</sub>]<sup>4-</sup> compounds.<sup>51</sup> The clear contribution of anisotropic chemical shielding interactions (CSA) to the broad signal at -208 ppm indicates a non-isotropic environment of the central tin atom (Figure 3.4a, indicated by a black star). The lower ppm value compared to the sharp peak at +144 ppm suggests

the presence of remaining Br atoms, since the quadrupolar nature of  $^{79}\text{Br}$  and  $^{81}\text{Br}$  would further contribute to the line broadening. Previous studies have shown that a successive replacement of Br *via* alkyls in tin compounds leads to a large, non-linear shift towards higher ppm values (*e.g.*  $\text{MeSnBr}_3$   $-165$  ppm,  $\text{Me}_2\text{SnBr}_2$   $+70$  ppm,  $\text{Me}_3\text{SnBr}$   $+128$  ppm).<sup>55</sup> Bearing these values in mind, we attribute the signal at  $-208$  ppm to the intermediate compound  $(\text{C}_{12}\text{H}_{25}\text{S})\text{SnBr}_3$ .

Further,  $^{119}\text{Sn}$  NMR was also used to analyze the compounds present in solution prior to the onset of  $\text{Cu}_{2-x}\text{S}$  NC nucleation (Figure 3.4c). To this end, all possible  $\text{CuCl}$  and  $\text{SnBr}_4$  combinations of the three main NC samples (hexagonal bipyramids, low and high aspect ratio hexagonal NPs) in their corresponding Cu:Sn ratio were mixed in a DDT/OLAM solution and heated to  $180$  °C. This temperature is slightly below the onset of  $\text{Cu}_{2-x}\text{S}$  NC nucleation, which is clearly evidenced by the change in the color of the reaction medium from light yellow to brown. This gives rise to the formation of all precursors, without (significant) formation of  $\text{Cu}_{2-x}\text{S}$  nuclei. The dominating peak at  $144$  ppm is present in solution as well (indicated by a red star in Figure 3.4c) and a

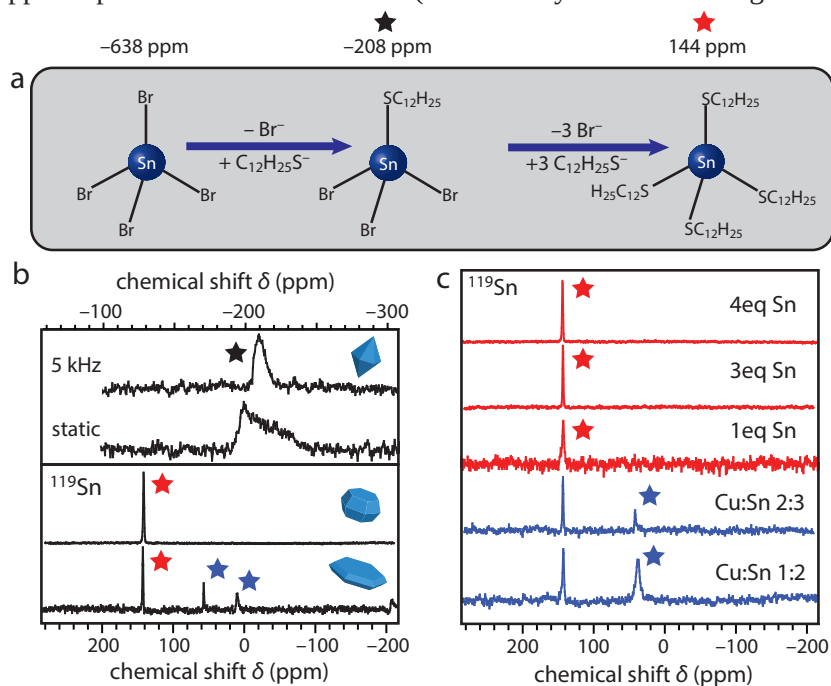


**Figure 3.4. Solid-state and solution  $^{119}\text{Sn}$  NMR spectra of polyhedral  $\text{Cu}_{2-x}\text{S}$  nanocrystals and pre-nucleation reaction products.** (a) Schematic representation of the Sn(IV)-thiolate complexes formed by the stepwise replacement of bromide for deprotonated thiols. (b) Solid-state  $^{119}\text{Sn}$  NMR spectra of hexagonal  $\text{Cu}_{2-x}\text{S}$  bipyramids (with and without  $5$  kHz MAS), low aspect ratio  $\text{Cu}_{2-x}\text{S}$  nanoplatelets and high aspect ratio  $\text{Cu}_{2-x}\text{S}$  nanoplatelets. (c) Solution  $^{119}\text{Sn}$  NMR spectra. Blue lines,  $\text{CuCl}$  and  $\text{SnBr}_4$  mixed in the same concentration and ratio used to synthesize the nanoplatelets. Red lines, different equivalents of  $\text{SnBr}_4$  in DDT/OLAM. The insets denote the nanocrystal morphology and the Cu:Sn ratio in the reaction mixture.

second Sn-complex is observed around 80 ppm (indicated with blue stars). Furthermore, solution samples without Cu<sup>+</sup> ions (red lines in Figure 3.4c) show the same signal at 144 ppm. This finding demonstrates that the formation of the compound responsible for the peak at 144 ppm is independent of the presence of Cu<sup>+</sup> or NCs, so this peak can be unambiguously ascribed to unbound (C<sub>12</sub>H<sub>25</sub>S)<sub>4</sub>Sn. However, additional peaks in the range of 80–0 ppm show a clear dependency on the presence of Cu<sup>+</sup> (blue lines in Figure 3.4c, signals indicated with blue stars). This suggests that a thiolate complex containing both Sn(IV) and Cu(I) is present prior to the onset of Cu<sub>2-x</sub>S nucleation. Heterometallic polynuclear Sn(IV)-Cu(I) complexes in which thiolates act as ligands are known to be stable both in solution and as crystalline solids.<sup>57,58</sup> It is thus plausible that similar complexes are also formed during the heating-up of the reaction medium to the reaction temperature. Although the chemical shift values are slightly different, the signals observed in the pre-nucleation solutions at 80 ppm and in the solid-state samples of high aspect ratio nanoplatelets (Cu:Sn ratio 1:2) at 80–0 ppm might have the same origin. Different packing in the solid-state and different coordination modes in solution could be a possible explanation for the differences, as it has already been reported for other tin(IV) compounds before.<sup>59</sup>

For further investigation, we performed <sup>1</sup>H NMR measurements on the solution samples. All three spectra show huge proton density at chemical shift areas characteristic for alkyl chains (3.5–0 ppm) and a peak at around 5 ppm, which typically corresponds to R-NH<sub>3</sub><sup>+</sup> species (Figure 3.5). This implies that the amine group of OLAM deprotonates the thiol head group of DDT, resulting in nucleophiles (C<sub>12</sub>H<sub>25</sub>S<sup>-</sup>) that are more reactive toward both Sn(IV) and Cu(I). This is consistent with our experimental observation that

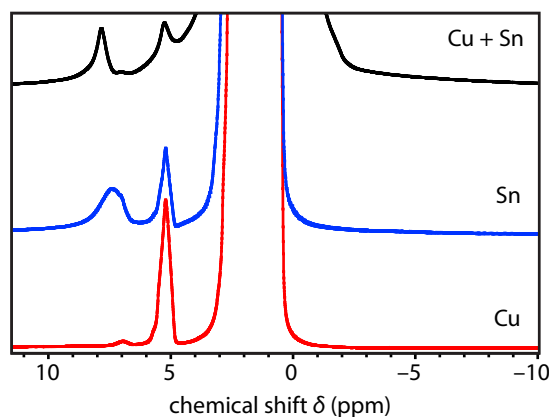


**Figure 3.5.** <sup>1</sup>H NMR spectra of three solution based samples, where all combinations of metal salts were mixed in a DDT/OLAM mixture, just below the nucleation temperature (~180 °C), to ensure that all precursors are formed without nucleation of Cu<sub>2-x</sub>S NCs. The peak at 5 ppm stems from R-NH<sub>3</sub><sup>+</sup> compounds formed after deprotonation of thiol molecules by amines. The broad peak at 2 ppm is characteristic for alkyl chains. A peak at 7.8 ppm is observed, corresponding to a proton in close proximity to a Sn-atom.

the presence of OLAM increases the reaction rates. Furthermore, a peak is observed around 7.5–8 ppm, which can be ascribed to the presence of Sn, since it is absent in the case of the Cu-DDT/OLAM solution.

### 3.3.3 Mechanism

Based on the findings discussed above, we propose a mechanism for the impact of SnBr<sub>4</sub> and other Sn(IV) salts (*e.g.*, Sn(OAc)<sub>4</sub>, SnCl<sub>4</sub>, Sn(acetylacetonate)Cl<sub>2</sub>) on the size and shape evolution of Cu<sub>2-x</sub>S NCs formed by heating up Cu salts in DDT. First, the thiolate complexes of both Cu(I) and Sn(IV) (Cu(DDT) and Sn(DDT)<sub>4</sub>, respectively) are formed by replacement of the native anions by DDT. This reaction is facilitated by amines (OLAM in the present case), which deprotonate the thiol, forming a nucleophile that is sufficiently reactive to displace the native ligands bound to Sn(IV). Our results show that the replacement of Br by DDT occurs in a stepwise fashion, one Br at a time, until the fully substituted (C<sub>12</sub>H<sub>25</sub>S)<sub>4</sub>Sn complex is formed. The stability of Cu(I)-DDT is known to be higher than that of Cu(II)-DDT<sup>60</sup> and therefore, when Cu(II) salts are used, the formation of the Cu-DDT complex is preceded by the reduction of Cu(II) to Cu(I) by oxidation of DDT to didodecyl disulfide.<sup>40</sup>

Copper(I) thiolates are very useful as single-source precursors for the synthesis of Cu<sub>2-x</sub>S NCs, and have been extensively used for that purpose, both in solventless and solution based routes using either hot-injection or heating-up protocols.<sup>6,26,29,38–40,61,62</sup> The rate limiting step in the formation of Cu<sub>2-x</sub>S NCs from Cu(I)-thiolates has been shown to be the thermally induced cleavage of the C-S bond,<sup>40</sup> which is catalyzed by the Cu(I) atoms,<sup>63</sup> so that only DDT molecules directly bound to Cu undergo thermolysis. In order for [Cu-S] monomers to be formed, several C-S bonds must be cleaved, since each Cu-atom is coordinated to four DDT molecules.<sup>60</sup>

It is interesting to note that the observations discussed above imply that the reaction temperature used in our study (225°C) is sufficiently high to lead to thermolysis of Cu-thiolate followed by nucleation and growth of Cu<sub>2-x</sub>S NCs, but is too low to induce significant thermolysis of the C-S bonds of the Sn(IV) thiolate complexes, since Sn<sub>x</sub>S<sub>y</sub> species are not observed. The high thermal stability of Sn(DDT)<sub>4</sub> is in line with the high decomposition temperatures reported for tin(IV) thiolates and dithiocarbamates, which require temperatures ranging from 250 to 375 °C to yield SnS<sub>2</sub>.<sup>64</sup> Therefore, the hypothesis proposed in refs. 47–49 (*viz.*, shape control by *in-situ* generated [Sn<sub>2</sub>S<sub>6</sub>]<sup>4-</sup> surfactants) is unlikely, since the reaction temperatures used in those studies were even lower (*viz.* 200° C) than that used in the present work. Instead, our study unambiguously demonstrates that the active species are Sn(DDT)<sub>4</sub> and/or the partially substituted complexes, such as Sn(DDT)Br<sub>3</sub>.

To understand how the Sn(DDT)<sub>x</sub>Br<sub>y</sub> (*x*= 1–4; *y*= 0–3) complexes generated *in-situ* affect the size and shape evolution of the Cu<sub>2-x</sub>S NCs, we have to consider the formation

mechanism of colloidal Cu<sub>2-x</sub>S NCs upon heating-up of a solution of CuCl in excess DDT. As discussed above, Cu-DDT is initially formed, which is followed at sufficiently high temperatures by thermolysis of the C-S bonds of the Cu-DDT complex, thereby forming [Cu-S] monomers. As a result of the high activation energies associated with the C-S bond cleavage, the precursor to monomer formation becomes the rate-limiting step in the formation of Cu<sub>2-x</sub>S NCs from Cu-DDT.<sup>6,40</sup> This is in line with the general mechanism proposed for the formation of colloidal NCs of several metal chalcogenides (e.g., CdSe, PbSe, PbS),<sup>1,65-67</sup> and implies that tuning the precursor conversion kinetics can dramatically affect the nucleation and growth rates, allowing the size of the nanocrystals to be controlled. This size control strategy has been recently illustrated by Owen and coworkers,<sup>68</sup> who used the reactivity of substituted thiourea precursors to tune the size of NCs of a number of metal sulfides, including Cu<sub>2-x</sub>S. The authors demonstrated that increasing the thiourea reactivity produces a higher concentration of smaller NCs, as a result of faster monomer formation rates and, consequently, faster nucleation rates.

We propose that the dramatic impact of the Sn(DDT)<sub>x</sub>Br<sub>y</sub> complexes on the formation of Cu<sub>2-x</sub>S NCs is also due to changes in the nucleation rates. However, in contrast to the examples discussed above, in the present case the nucleation is directly affected by the Sn(DDT)<sub>x</sub>Br<sub>y</sub> complexes, which make it more difficult by increasing the activation energy for nucleation (Figure 3.6a). This additional nucleation barrier is imposed by the interaction between the Sn(DDT)<sub>x</sub>Br<sub>y</sub> complexes and the [Cu-S] monomers, which transiently forms heterometallic polynuclear Sn(IV)-Cu(I) thiolate complexes, as observed in the NMR measurements discussed above. This also implies that the higher

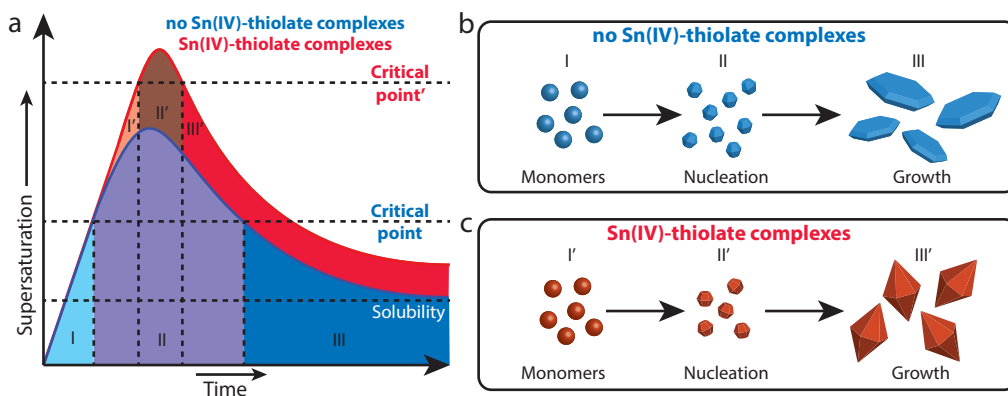


**Figure 3.6. Tuning the nucleation and growth rates of Cu<sub>2-x</sub>S NCs by Sn(IV)-thiolate complexes.** (a) La Mer plots of nucleation and growth of Cu<sub>2-x</sub>S nanocrystals (NCs) without (blue) and with Sn(IV)-additives (red). The addition of Sn(IV)-thiolate complexes to a Cu<sub>2-x</sub>S NC synthesis, results in an increase of the nucleation barrier and, as a result, nucleation and growth are well separated, resulting in polyhedral NCs with narrow size and shape distributions. (b,c) Schematic representations of the two Cu<sub>2-x</sub>S formation mechanisms. (b) Without Sn-additives, polydisperse Cu<sub>2-x</sub>S nanoplatelets are obtained and (c) with Sn-additives, well-defined polyhedral Cu<sub>2-x</sub>S nanocrystals are formed.

the concentration of  $\text{Sn}(\text{DDT})_x\text{Br}_y$  complexes, the higher the nucleation barrier (Figure 3.6a). The monomer formation rates are not affected since they depend only on the thermolysis rates of the C-S bonds of the Cu-thiolate complexes. As a result, nucleation becomes the rate-limiting step, which impacts on both the size and shape of the product  $\text{Cu}_{2-x}\text{S}$  NCs.

In the absence of  $\text{Sn}(\text{DDT})_x\text{Br}_y$  complexes, the activation energy for nucleation is low, but the monomer supply is limited by the C-S thermolysis rates. The polydisperse ensemble of relatively large nanoplatelets obtained in the absence of  $\text{SnBr}_4$  (Figure 3.1a) suggests that the heating rates employed in our experiments are not sufficiently fast to induce a sudden burst of C-S thermolysis and monomer formation, thereby resulting in relatively few nucleation events spread over a wide temperature range. The addition of a small concentration of  $\text{SnBr}_4$  (which is converted *in-situ* to  $\text{Sn}(\text{DDT})_x\text{Br}_y$  complexes) already significantly increases the activation energy for nucleation, delaying it until sufficiently high temperatures have been reached. The concentration of monomers produced by thermolysis of the Cu-DDT complexes will then be high, and a burst of nucleation followed by fast growth and depletion of the monomers becomes possible, leading to a high concentration of relatively small and monodisperse NCs (Figure 3.1b, 17 nm hexagonal bifrustums). Further increase in the concentration of added  $\text{SnBr}_4$  leads to a higher concentration of *in-situ* generated  $\text{Sn}(\text{DDT})_x\text{Br}_y$  complexes, which make the nucleation rates increasingly lower, while keeping the monomer formation rates unaffected. As a result, the size of the product  $\text{Cu}_{2-x}\text{S}$  NCs increases with increasing  $\text{Sn}(\text{DDT})_x\text{Br}_y$  (Figure 3.1), since fewer nuclei are formed under a constant monomer supply (Figure 3.6b,c). This also affects the morphology of the NCs, since facet development during growth and the final shape adopted by a colloidal NC are dictated by a balance between several driving forces.<sup>1</sup>

The growth rate of a given NC facet depends on its free-energy and on the total concentration of monomers available for growth. At low monomer activities the overall growth rates are slow, and therefore the difference between different crystallographic facets are not significant (thermodynamically controlled growth regime).<sup>1</sup> Consequently, the NC will grow toward an equilibrium shape that minimizes the most its total free-energy, which implies that a relatively isotropic shape exposing low free-energy facets will be favored. In contrast, at high monomer activities the overall growth rates become fast, allowing the high free-energy facets to grow faster than the low free-energy ones, outcompeting them for the monomer supply. This leads to anisotropic morphologies (kinetically controlled growth regime).<sup>1</sup> Surfactants (ligands) modify the free-energy of specific facets through preferential binding, thereby depressing their growth rates relative to the facets that are less densely capped. This affects the shape evolution under both growth regimes.

Colloidal  $\text{Cu}_{2-x}\text{S}$  NCs synthesized by thermolysis of Cu-DDT complexes have been

shown to adopt a nearly spherical morphology at early growth stages or under slow growth conditions, and a hexagonal nanoplatelet morphology under fast growth conditions (*i.e.*, high concentrations and/or high temperatures).<sup>6,26,29,38–40,61,62</sup> This implies that the free-energies of the facets in the [010] and [001] directions (*viz.*, {101} and {221} for djurleite) are higher than that of the {100} facet. The different shapes of the Cu<sub>2-x</sub>S NCs obtained in the presence of different concentrations of added SnBr<sub>4</sub> can thus be understood as a direct consequence of the impact of the *in-situ* generated Sn(DDT)<sub>x</sub>Br<sub>y</sub> complexes on the nucleation rates. As discussed above, the nucleation rates decrease with increasing concentration of Sn(DDT)<sub>x</sub>Br<sub>y</sub> complexes, which leads to an increasingly higher concentration of monomers available for growth, thereby enhancing the growth rates and favoring the formation of nanoplatelets with increasingly larger aspect ratios.

It is possible that the Sn(DDT)<sub>x</sub>Br<sub>y</sub> complexes also act as surfactants, but the NMR spectroscopy and elemental mapping results discussed above do not provide any evidence supporting the notion that the formation of nanoplatelets is induced by selective binding of these complexes to the {100} facet, since Sn was detected at very low concentrations and randomly distributed, regardless of the NC shape, and no Sn compounds were observed bound to the surface of the nanoplatelets. Surface bound Sn(DDT)Br<sub>3</sub> complexes were however observed in the solid-state <sup>119</sup>Sn NMR spectra of the bipyramid-shaped Cu<sub>2-x</sub>S NCs. This suggests that Sn(DDT)<sub>x</sub>Br<sub>y</sub> complexes preferentially bind to the {302}/{502} and {364} facets, possibly because these facets have a higher free-energy and are less densely capped with DDT molecules than the {100} facet. This adsorption is however not strong enough to significantly depress the growth rates of the {302}/{502} and {364} facets, but slows it sufficiently down with respect to the {100} facets to allow the formation of bipyramid NCs, which require growth both in the [100] direction and in the [010] and [001] directions. This mild down-modulation of the {302}/{502} and {364} growth is nevertheless insufficient to counteract the dramatic increase in the growth rates brought about by further increase of the concentration of the Sn(DDT)<sub>x</sub>Br<sub>y</sub> complexes, since this results in a large increase of the monomer concentrations.

### 3.4 Conclusions

In this chapter, We have shown that *in-situ* formed Sn(IV)-thiolate complexes can be used as shape directing agents that modulate the nucleation and growth rates of polyhedral Cu<sub>2-x</sub>S NCs. Several anisotropic polyhedral NCs were obtained with narrow size and shape distributions (*e.g.* hexagonal bipyramids and bipyramids, and hexagonal nanoplatelets with various aspect ratios), by solely changing the concentration of the additive SnBr<sub>4</sub>, which is converted *in-situ* to Sn(IV)-thiolate complexes through a stepwise replacement of bromide by deprotonated thiols. The crystal structure of the product Cu<sub>2-x</sub>S NCs is observed to depend on the concentration of Sn(IV)-thiolate

complexes, resulting in monoclinic low-chalcocite and monoclinic djurleite in the low- and high-concentration limits, respectively. Our results rule out that the impact of the Sn(IV)-thiolate complexes on the formation of  $\text{Cu}_{2-x}\text{S}$  NCs is due to Sn incorporation in the growing NCs or to a surfactant effect. Instead, the Sn(IV)-thiolate complexes increase the  $\text{Cu}_{2-x}\text{S}$  nucleation barrier, without affecting the precursor conversion rates. This influences both the nucleation and growth rates, and leads to a better separation between nucleation and growth, thereby decreasing the ensemble polydispersity. It also dictates the final shape and structure of the product  $\text{Cu}_{2-x}\text{S}$  NCs by affecting the balance between the nucleation and growth rates under constant monomer formation rates. In the low-concentration limit, the nucleation rates are relatively fast, leading to a high concentration of nuclei and a low concentration of monomers available for growth. This results in slow growth under thermodynamic control. The nucleation rates decrease with increasing concentration of Sn(IV)-thiolate complexes, which leaves an increasingly higher concentration of monomers available for growth. This progressively enhances the growth rates, thereby shifting the growth to the kinetically controlled regime. The use of inorganic ligands as shape directing agents has not been extensively studied yet, and could possibly lead to novel NC morphologies and improved size control strategies. This could be beneficial for implementation of NCs in *i.e.* photovoltaic and photonic devices, for which well-defined building blocks are required to form highly-ordered thin layers of individual NCs. In combination with topotactic cation exchange reactions, this could boost the importance of the synthetic strategy developed in this work, giving rise to tailor-made NCs and NC solids with novel functionalities, which may prove beneficial for a number of applications.

## References

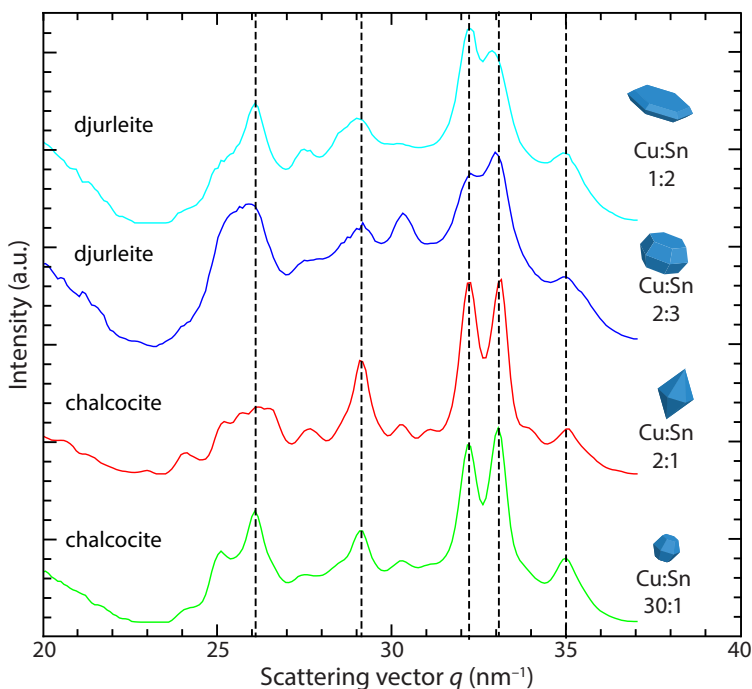
- (1) Donega, C. d. M. *Chem. Soc. Rev.* **2011**, *40*, 1512–1546.
- (2) Kovalenko, M. V; Manna, L.; Cabot, A.; Hens, Z.; Talapin, D. V; Kagan, C. R.; Klimov, X. V. I.; Rogach, A. L.; Reiss, P.; Milliron, D. J.; *et al.* *ACS Nano* **2015**, *9*, 1012–1057.
- (3) Talapin, D. V.; Lee, J. S.; Kovalenko, M. V.; Shevchenko, E. V. *Chem. Rev.* **2010**, *110*, 389–458.
- (4) Grim, J. Q.; Manna, L.; Moreels, I. *Chem. Soc. Rev.* **2015**, *44*, 5897–5914.
- (5) Shirasaki, Y.; Supran, G.; Bawendi, M. G.; Bulović, V. *Nat. Photonics* **2012**, *7*, 13–23.
- (6) van der Stam, W.; Berends, A. C.; Donega, C. d. M. *ChemPhysChem* **2016**, *17*, 559–581.
- (7) Zhang, Y.; Xie, C.; Su, H.; Liu, J.; Pickering, S.; Wang, Y.; Yu, W. W.; Wang, J.; Wang, Y.; Hahm, J.; *et al.* *Nano Lett.* **2011**, *11*, 329–332.
- (8) Kolny-Olesiak, J.; Weller, H. *ACS Appl. Mater. Interfaces* **2013**, *5*, 12221–12237.
- (9) Luther, J. M.; Jain, P. K.; Ewers, T.; Alivisatos, A. P. *Nat. Mater.* **2011**, *10*, 361–366.
- (10) Burda, C.; Chen, X.; Narayanan, R.; El-Sayed, M. A. *Chem. Rev.* **2005**, *105*, 1025–1102.
- (11) Zhao, Y.; Pan, H.; Lou, Y.; Qiu, X.; Zhu, J.; Burda, C. *J. Am. Chem. Soc.* **2009**, *131*, 4253–4261.
- (12) Zhuang, Z.; Peng, Q.; Zhang, B.; Li, Y. *J. Am. Chem. Soc.* **2008**, *130*, 10482–10483.
- (13) Xie, Y.; Riedinger, A.; Prato, M.; Casu, A.; Genovese, A.; Guardia, P.; Sottini, S.; Sangregorio, C.; Miszta, K.; Ghosh, S.; *et al.* *J. Am. Chem. Soc.* **2013**, *135*, 17630–17637.
- (14) Page, M.; Niitsoo, O.; Itzhaik, Y.; Cahen, D.; Hodes, G. *Energy Environ. Sci.* **2009**, *2*, 220–223.
- (15) Wu, Y.; Wadia, C.; Ma, W.; Sadtler, B.; Alivisatos, A. P. *Nano Lett.* **2008**, *8*, 2551–2555.
- (16) Xie, Y.; Carbone, L.; Nobile, C.; Grillo, V.; D’Agostino, S.; Della Sala, F.; Giannini, C.; Altamura, D.; Oelsner, C.; Kryschi, C.; *et al.* *ACS Nano* **2013**, *7*, 7352–7369.
- (17) Kriegel, I.; Rodríguez-Fernández, J.; Wisnet, A.; Zhang, H.; Waurisch, C.; Eychmüller, A.; Dubavik, A.; Govorov, A. O.; Feldmann, J. *ACS Nano* **2013**, *7*, 4367–4377.

- (18) Dorfs, D.; Härtling, T.; Miszta, K.; Bigall, N. C.; Kim, M. R.; Genovese, A.; Falqui, A.; Povia, M.; Manna, L. *J. Am. Chem. Soc.* **2011**, *133*, 11175–11180.
- (19) Liu, Y.; Deng, Y.; Sun, Z.; Wei, J.; Zheng, G.; Asiri, A. M.; Khan, S. B.; Rahman, M. M.; Zhao, D. *Small* **2013**, *9*, 2702–2708.
- (20) Vinokurov, K.; Elimelech, O.; Millo, O.; Banin, U. *ChemPhysChem* **2016**, *17*, 675–680.
- (21) Hsu, S.; Bryks, W.; Tao, A. R. *Chem. Mater.* **2012**, *24*, 3765–3771.
- (22) Wolf, A.; Härtling, T.; Hinrichs, D.; Dorfs, D. *ChemPhysChem* **2016**, *17*, 717–723.
- (23) van der Stam, W.; Rabouw, F. T.; Vonk, S. J. W.; Geuchies, J. J.; Ligthart, H.; Petukhov, A. V.; Donega, C. d. M. *Nano Lett.* **2016**, acs.nanolett.6b00221.
- (24) Reifsnnyder, D. C.; Ye, X.; Gordon, T. R.; Song, C.; Murray, C. B. *ACS Nano* **2013**, *7*, 4307–4315.
- (25) van der Stam, W.; Gantapara, A. P.; Akkerman, Q. A.; Soligno, G.; Meeldijk, J. D.; van Roij, R.; Dijkstra, M.; Donega, C. d. M. *Nano Lett.* **2014**, *14*, 1032–1037.
- (26) Kruszynska, M.; Borchert, H.; Bachmatiuk, A.; Rümmele, M. H.; Büchner, B.; Parisi, J.; Kolny-Olesiak, J. *ACS Nano*, **2012**, *6*, 5889–5896.
- (27) Sigman, M.; Ghezlbash, A.; Hanrath, T.; Saunders, A. E.; Lee, F.; Korgel, B. A. *J. Am. Chem. Soc.* **2003**, *125*, 16050–16057.
- (28) Li, W.; Shavel, A.; Guzman, R.; Rubio-Garcia, J.; Flox, C.; Fan, J.; Cadavid, D.; Ibañez, M.; Arbiol, J.; Morante, J. R.; Cabot, A. *Chem. Commun.* **2011**, *47*, 10332–10334.
- (29) van der Stam, W.; Akkerman, Q. A.; Ke, X.; van Huis, M. A.; Bals, S.; Donega, C. d. M. *Chem. Mater.* **2015**, *27*, 283–291.
- (30) Beberwyck, B. J.; Surendranath, Y.; Alivisatos, A. P. *J. Phys. Chem. C* **2013**, *117*, 19759–19770.
- (31) Gupta, S.; Kershaw, S. V.; Rogach, A. L. *Adv. Mater.* **2013**, *25*, 6923–6944.
- (32) Li, H.; Zanella, M.; Genovese, A.; Povia, M.; Falqui, A.; Giannini, C.; Manna, L. *Nano Lett.* **2011**, *11*, 4964–4970.
- (33) van der Stam, W.; Berends, A. C.; Rabouw, F. T.; Willhammar, T.; Ke, X.; Meeldijk, J. D.; Bals, S.; Donega, C. d. M. *Chem. Mater.* **2015**, *27*, 621–628.
- (34) Ha, D.-H.; Caldwell, A. H.; Ward, M. J.; Honrao, S.; Mathew, K.; Hovden, R.; Koker, M. K. A.; Muller, D. A.; Hennig, R. G.; Robinson, R. D. *Nano Lett.* **2014**, *14*, 7090–7099.
- (35) Luther, J. M.; Zheng, H.; Sadtler, B.; Alivisatos, A. P. *J. Am. Chem. Soc.* **2009**, *131*, 16851–16857.
- (36) van der Stam, W.; Bladt, E.; Rabouw, F. T.; Bals, S.; Donega, C. d. M. *ACS Nano* **2015**, *9*, 11430–11438.
- (37) de Trizio, L.; Manna, L. *Chem. Rev.* **2016**, acs.chemrev.5b00739.
- (38) Kuzuya, T.; Tai, Y.; Yamamuro, S.; Sumiyama, K. *Sci. Technol. Adv. Mater.* **2005**, *6*, 84–90.
- (39) Bryks, W.; Wette, M.; Velez, N.; Hsu, S.; Tao, A. R. *J. Am. Chem. Soc.* **2014**, *136*, 6175–6178.
- (40) Nørby, P.; Johnsen, S.; Iversen, B. B. *ACS Nano* **2014**, *8*, 4295–4303.
- (41) Evans, H. *Nature* **1971**, *232*, 69–70.
- (42) Pearson, R. G. *Inorg. Chem.* **1988**, *27*, 734–740.
- (43) Chang, J.; Waclawik, E. R. *CrystEngComm* **2013**, *15*, 5612–5619.
- (44) Wang, J.; Liu, P.; Seaton, C. C.; Ryan, K. M. *J. Am. Chem. Soc.* **2014**, *136*, 7954–7960.
- (45) Tan, J. M. R.; Lee, Y. H.; Pedireddy, S.; Baikie, T.; Ling, X. Y.; Wong, L. H. *J. Am. Chem. Soc.* **2014**, *136*, 6684–6692.
- (46) Fiechter, S.; Martinez, M.; Schmidt, G.; Henrion, W.; Tomm, Y. *J. Phys. Chem. Solids* **2003**, *64*, 1859–1862.
- (47) Li, X.; Shen, H.; Niu, J.; Li, S.; Zhang, Y.; Wang, H.; Li, L. S. *J. Am. Chem. Soc.* **2010**, *132*, 12778–12779.
- (48) Li, X.; Wang, M.; Shen, H.; Zhang, Y.; Wang, H.; Li, L. S. *Chemistry* **2011**, *17*, 10357–10364.
- (49) Yi, L.; Gao, M. *Cryst. Growth Des.* **2011**, *11*, 1109–1116.
- (50) Protesescu, L.; Rossini, A. J.; Kriegner, D.; Valla, M.; de Kergommeaux, A.; Walter, M.; Kravchyk, K. V.; Nachttegaal, M.; Stangl, J.; Malaman, B.; et al. *ACS Nano* **2014**, *8*, 2639–2648.
- (51) Mundus, C.; Taillades, G.; Pradel, A.; Ribes, M. *Sol. State Nucl. Magn. Reson.* **1996**, *7*, 141–146.
- (52) Kovalenko, M. V.; Bodnarchuk, M. I.; Zaumseil, J.; Lee, J.-S.; Talapin, D. V. *J. Am. Chem. Soc.* **2010**, *132*, 10085–10092.
- (53) Kovalenko, M. V.; Scheele, M.; Talapin, D. V. *Science* **2009**, *324*, 1417–1420.
- (54) Rangan, K. K.; Trikalitis, P. N.; Canlas, C.; Bakas, T.; Weliky, D. P.; Kanatzidis, M. G. *Nano Lett.* **2002**, *2*, 513–517.
- (55) Gielen, M. *Tin Chemistry: Fundamentals, Frontiers and Applications*. Wiley, **2008**, ISBN: 978-0-470-51771-0
- (56) Günther, H. *NMR Spectroscopy: Basic Principles, Concepts and Applications in Chemistry*. Wiley, **2013**, ISBN: 978-3-527-33004-1.
- (57) Wang, X.; Sheng, T.-L.; Fu, R.-B.; Hu, S.-M.; Xiang, S.-C.; Wang, L.-S.; Wu, X.-T. *Inorg. Chem.* **2006**, *45*,

- 5236–5238.
- (58) Wang, L.-S.; Sheng, T.-L.; Wang, X.; Chen, D.-B.; Hu, S.-M.; Fu, R.-B.; Xiang, S.-C.; Wu, X.-T. *Inorg. Chem.* **2008**, *47*, 4054–4059.
- (59) Jiao, J.; Lee, M.; Barnes, E.; Hagaman, E. W. *Magn. Reson. Chem.* **2008**, *46*, 690–692.
- (60) Espinet, P.; Lequerica, M. C.; Martín-Alvarez, J. M. *Chem. Eur. J.* **1999**, *5*, 1982–1986.
- (61) Han, W.; Yi, L.; Zhao, N.; Tang, A.; Gao, M.; Tang, Z. *J. Am. Chem. Soc.* **2008**, *130*, 13152–13161.
- (62) Li, S.; Wang, H.; Xu, W.; Si, H.; Tao, X.; Lou, S.; Du, Z.; Li, L. S. *J. Colloid Interface Sci.* **2009**, *330*, 483–487.
- (63) Wang, L.; He, W.; Yu, Z. *Chem. Soc. Rev.* **2013**, *42*, 599–621.
- (64) Barone, G.; Chaplin, T.; Hibbert, T. G.; Kana, A. T.; Mahon, M. F.; Molloy, K. C.; Worsley, I. D.; Parkin, I. P.; Price, L. S. *J. Chem. Soc. Dalton Trans.* **2002**, *6*, 1085–1092.
- (65) Owen, J. S.; Chan, E. M.; Liu, H.; Alivisatos, A. P. *J. Am. Chem. Soc.* **2010**, *132*, 18206–18213.
- (66) Abe, S.; Čapek, R. K.; Geyter, B. De; Hens, Z. *ACS Nano* **2012**, *6*, 42–53.
- (67) Rempel, J. Y.; Bawendi, M. G.; Jensen, K. F. *J. Am. Chem. Soc.* **2009**, *131*, 4479–4489.
- (68) Hendricks, M. P.; Campos, M. P.; Cleveland, G. T.; Plante, I. J.; Owen, J. S. *Science* **2015**, *348*, 1226–1230.
- (69) Palenstijn, W. J.; Batenburg, K. J.; Sijbers, J. *J. Struct. Biol.* **2011**, *176*, 250–253.

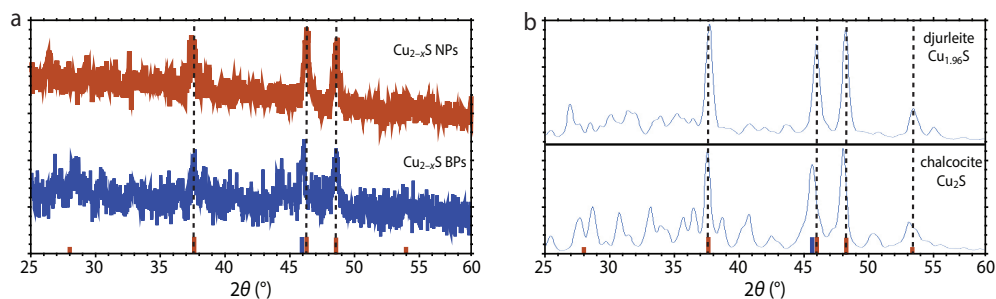
## Appendices

### A3.1 Electron Diffraction



**Figure A3.1.** Figure S1. Electron Diffraction. In the case of excess Cu compared to Sn, polyhedral  $\text{Cu}_{2-x}\text{S}$  NCs with the low-chalcocite crystal structure are formed. An increase of the Sn concentration results in  $\text{Cu}_{2-x}\text{S}$  nanoplatelets with the djurleite crystal structure. 1D PXRD patterns were obtained by radially integrating 2D Electron Diffraction patterns.

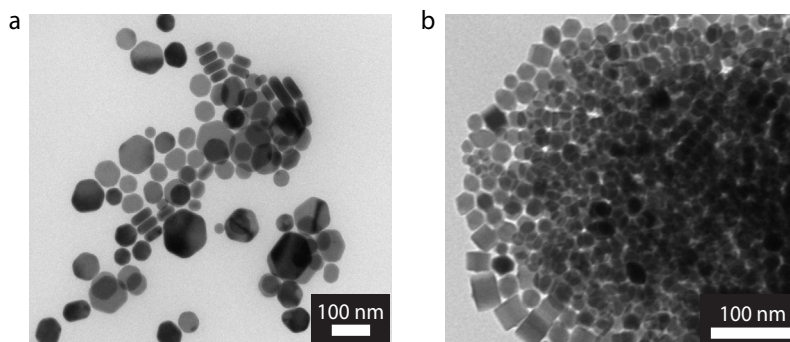
## A3.2 X-Ray Diffractometry



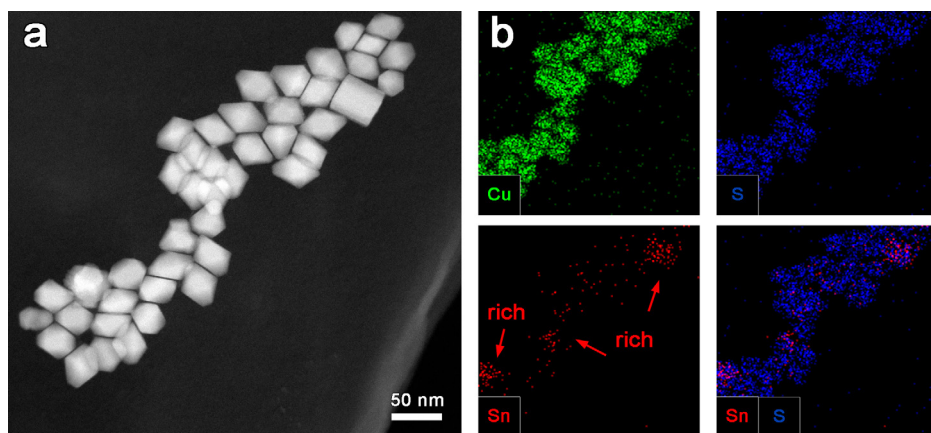
**Figure A3.1.** (a) X-ray Diffractograms of high aspect ratio  $\text{Cu}_{2-x}\text{S}$  nanoplatelets (red line) and hexagonal  $\text{Cu}_{2-x}\text{S}$  bipyramids (blue line). (b) Calculated XRD patterns for djurleite and low-chalcocite. Red bars in both panels denote the XRD pattern for the djurleite  $\text{Cu}_{1.96}\text{S}$  crystal structure, while the blue bars denote the XRD pattern for low-chalcocite  $\text{Cu}_2\text{S}$ . The patterns are very similar, but the djurleite peak at around  $46^\circ$  is shifted toward smaller angles in low-chalcocite. The bipyramid NCs closely match the stoichiometric chalcocite  $\text{Cu}_2\text{S}$  phase, while the nanoplatelets match the djurleite  $\text{Cu}_{1.96}\text{S}$  phase.

3

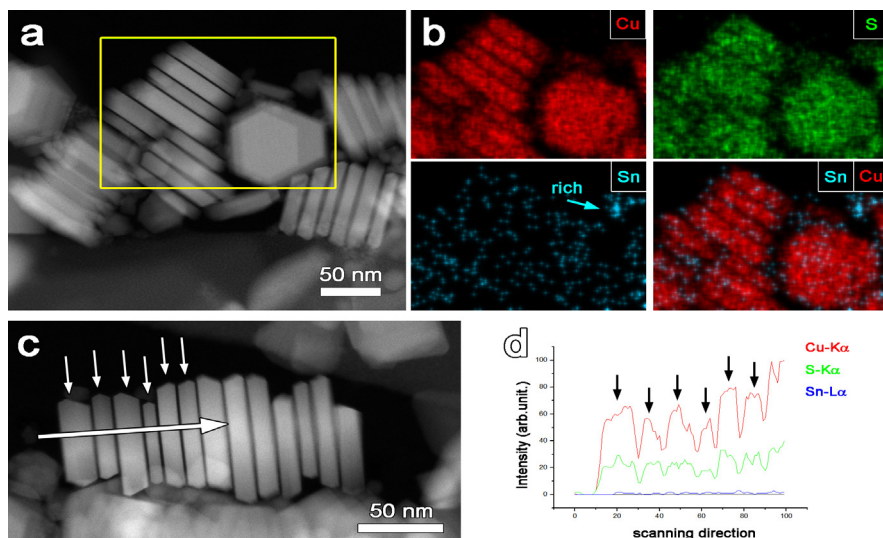
## A3.3 Influence of other Sn-compounds



**Figure A3.2.** Transmission Electron Microscopy images of  $\text{Cu}_{2-x}\text{S}$  NCs synthesized after (a) the addition of halides in the form of  $\text{CuBr}$  and after (b) the addition of  $\text{Sn}(\text{OAc})_4$ . Concentrations of  $\text{Cu}:\text{halide}$  and  $\text{Cu}:\text{Sn}$  are the same as in the synthesis protocol for hexagonal  $\text{Cu}_{2-x}\text{S}$  bipyramids, *i.e.*  $\text{Cu}:\text{halide}$  1:2 in (a) and  $\text{Cu}:\text{Sn}$  2:1 in (b). Scale bars correspond to 100 nm.

A3.4 Energy Dispersive X-ray Spectroscopy mapping of  $\text{Cu}_{2-x}\text{S}$  bipyramids

**Figure A3.3.** (a) High-Angle Annular Dark Field Scanning Transmission Electron Microscopy image of hexagonal  $\text{Cu}_{2-x}\text{S}$  bipyramids. (b) Energy-Dispersive X-ray spectroscopy (EDS) chemical mapping of the hexagonal  $\text{Cu}_{2-x}\text{S}$  bipyramids shown in (a). Sn is present at low concentrations (2–3%) and is not homogeneously distributed, but is concentrated on nanocrystals that appear larger and morphologically distinct from the majority of the ensemble.

A3.5 Energy Dispersive X-ray Spectroscopy mapping of  $\text{Cu}_{2-x}\text{S}$  nanoplatelets

**Figure A3.4.** (a) High-Angle Annular Dark Field Scanning Transmission Electron Microscopy image of an ensemble of hexagonal  $\text{Cu}_{2-x}\text{S}$  nanoplatelets. (b) Energy-Dispersive X-ray spectroscopy (EDS) Elemental maps of high aspect ratio hexagonal  $\text{Cu}_{2-x}\text{S}$  nanoplatelets. (c,d) EDS linescan along a stack of nanoplatelets, showing no preferred position of Sn across the nanocrystals.





# Solution-Processable Ultrathin Size- and Shape-Controlled Colloidal $\text{Cu}_{2-x}\text{S}$ Nanosheets



## ABSTRACT

Ultrathin 2-dimensional (2D) nanosheets (NSs) possess extraordinary properties that are attractive for both fundamental studies and technological devices. Solution-based “bottom-up” methods are emerging as promising routes to produce free-standing NSs, but the synthesis of colloidal NSs with well-defined size and shape has remained a major challenge. In this chapter we discuss a novel method that yields 2 nm thick colloidal  $\text{Cu}_{2-x}\text{S}$  NSs with well-defined shape (triangular or hexagonal) and size (100 nm to 3  $\mu\text{m}$ ). The key feature of our approach is the use of a synergistic interaction between halides (Br or Cl) and copperthiolate metal-organic frameworks to create a template that imposes 2D constraints on the Cu-catalyzed C-S thermolysis, resulting in nucleation and growth of colloidal 2D  $\text{Cu}_{2-x}\text{S}$  NSs. Moreover, the NS composition can be post-synthetically tailored by exploiting topotactic cation exchange reactions. This is illustrated by converting the  $\text{Cu}_{2-x}\text{S}$  NSs into ZnS and CdS NSs while preserving their size and shape. The method presented here thus holds great promise as a route to solution-processable compositionally diverse ultrathin colloidal NSs with well-defined shape and size.

### Based on

#### **Solution-Processable Ultrathin Size- and Shape-Controlled Colloidal $\text{Cu}_{2-x}\text{S}$ Nanosheets**

W. van der Stam, Q. A. Akkerman, X. Ke, M. A. van Huis, S. Bals and C. de Mello Donega, *Chem. Mater.*, **2015**, 27, 283–291.

## 4.1 Introduction

Ultrathin 2-dimensional (2D) nanomaterials (nanosheets, NSs) are attracting increasing research efforts due to their extraordinary electronic, phononic, optical and mechanical properties.<sup>1–9</sup> Well-known examples are graphene and transition-metal dichalcogenides (*e.g.*, MoS<sub>2</sub>).<sup>1–9</sup> An essential feature of ultrathin NSs is that they are just a few atomic monolayers thick ( $w \leq 2.5$  nm), but have lateral dimensions ( $L$ ) of at least 100 nm. This creates a strong 1D quantum confinement, which results in unique properties.<sup>1–9</sup> NSs offer compelling opportunities for fundamental studies in 2D physics and hold an immense potential for spintronic devices, field-effect transistors, nanoscale sensors, and as building blocks for batteries, photodetectors, and LEDs.<sup>1–9</sup> NSs are typically obtained by exfoliation of bulk materials or grown on substrates by MBE or CVD.<sup>1–9</sup> These methods are however not suitable to produce large amounts of free-standing NSs and lack control over their shape and lateral dimensions.

Solution-based “bottom-up” colloidal chemical methods offer an appealing alternative, and are emerging as promising routes to free-standing colloidal inorganic NSs, due to their versatility in terms of composition, size, shape and surface control. Nevertheless, ultrathin colloidal NSs of inorganic semiconductors are still restricted to just a few materials.<sup>10–27</sup> The most investigated ones are CdX ( $X = S, Se, Te$ ) nanoplatelets ( $w = 1.2 - 2.1$  nm;  $L = 10 - 700$  nm, square or rectangular with irregular edges)<sup>10–13</sup> and nanoribbons ( $L \leq 1$   $\mu\text{m}$ , tens of nm wide),<sup>14–17</sup> which have been shown to possess remarkable optical properties.<sup>10,14,16,18–20</sup> Despite advances in the colloidal synthesis of 2D NSs of various compositions,<sup>21–27</sup> full control over the shape and dimensions of the NSs remains a challenge. In this chapter, we demonstrate a synthesis method that yields free-standing ultrathin (2 nm) Cu<sub>2–x</sub>S NSs with well-defined shape (triangular or hexagonal) and sizes tunable from 100 nm to 3  $\mu\text{m}$ . Moreover, these NSs do not easily fold or entangle themselves, and readily self-assemble into ordered stacks. The key feature of our approach is the use of a synergistic interaction between halides (Br or Cl) and copper-thiolate metal-organic frameworks to create a template that imposes 2D constraints on the Cu-catalyzed C-S thermolysis, resulting in nucleation and growth of colloidal Cu<sub>2–x</sub>S NSs.

Cu<sub>2–x</sub>S is a direct p-type semiconductor with a bandgap that depends on its stoichiometry (1.1 – 1.4 eV for  $x = 0 - 0.04$ ; 1.5 eV for  $x = 0.2$ ; 2.0 eV for  $x = 1$ ).<sup>28,29</sup> Copper chalcogenide nanocrystals (NCs) have been shown to possess the unique property of holding quantum confined excitons and highly tunable localized surface plasmons on demand, opening up the way to create coupled plasmon-excitons in the same NC.<sup>30–32</sup> This creates a number of exciting possibilities, such as ultrafast optical switching or plasmon-enhanced photovoltaics.<sup>30</sup> Cu<sub>2–x</sub>S NCs also hold promise for biomedical applications<sup>33</sup> and as electrodes for Li-ion batteries.<sup>28</sup> The availability of ultrathin size-

and shape-controlled colloidal Cu<sub>2-x</sub>S NSs may thus prove beneficial for a number of fundamental studies and potential applications. Furthermore, monovalent copper cations have a high solid state mobility due to their small size and low charge, and are therefore easily exchanged by other cations *via* topotactic place exchange reactions, which allow the shape and size of the parent NC to be preserved in the product NC.<sup>34,35</sup> This has made copper chalcogenide NCs a versatile nanoscale template for the preparation of NCs that cannot be synthesized by direct routes.<sup>34,35</sup> We demonstrate the potential of topotactic cation exchange reactions to post-synthetically tailor the composition of the ultrathin colloidal Cu<sub>2-x</sub>S NSs by converting them into ZnS and CdS, while preserving their well-defined shape, lateral dimensions and thickness.

## 4.2 Methods

**Materials.** Copper(I) acetate (CuAc, 97%), tin(IV) tetrabromide (SnBr<sub>4</sub>, 99%), tin(II) dibromide (SnBr<sub>2</sub>), tin(IV) tetrachloride pentahydrate (SnCl<sub>4</sub>·5H<sub>2</sub>O, 98%), tin(IV) acetate (SnAc<sub>4</sub>), copper(I) chloride (CuCl, 97%), copper(I) bromide (CuBr, 98%), copper(I) iodide (CuI, 98%), sodium bromide (NaBr, ≥99%), sodium chloride (NaCl, 99.999%), potassium iodide (KI, 99.99%), cadmium nitrate tetrahydrate (Cd(NO<sub>3</sub>)<sub>2</sub>·4H<sub>2</sub>O, 98%), zinc chloride (ZnCl<sub>2</sub>, reagent grade, ≥98%), tributylphosphine (TBP, 97%), trioctylphosphine (TOP, 90%), 1-dodecanethiol (DDT, ≥98%), 1-octadecene (ODE, tech., 90%), trioctylphosphine oxide (TOPO, 99%), anhydrous toluene, methanol (MeOH) and butanol (BuOH) were purchased from Sigma Aldrich. Sulfur powder was obtained from Strem Chemicals. All chemicals were used without any further purification, except for ODE and TOPO, which were degassed at 120 °C for 2 h prior to synthesis.

**Synthesis of ultrathin Cu<sub>2-x</sub>S nanosheets.** The method developed here to synthesize Cu<sub>2-x</sub>S NSs is based on a synthesis protocol reported in the literature,<sup>36</sup> which was modified by adding SnBr<sub>4</sub> (or SnCl<sub>4</sub>) to the reaction mixture. Typically, 27.3 mg (0.22 mmol) CuAc, 32.85 mg (0.075 mmol) SnBr<sub>4</sub>, and 0.55 g (1.42 mmol) TOPO were dispersed in 12.5 mL ODE. This mixture was degassed for 30 min at 100 °C, and subsequently heated to 160 °C. At this temperature, 0.5 mL (2.1 mmol) DDT was swiftly injected. The solution was then purged with N<sub>2</sub> and further heated to 220 °C. The reaction was maintained at this temperature for 40 min. Aliquots were extracted during the synthesis in order to monitor the evolution of the reaction. The Cu<sub>2-x</sub>S NSs were precipitated by adding a methanol:butanol mixture and centrifuging at 3000 rpm for 15 min. Afterwards, the NSs were redispersed in toluene. These washing steps were repeated three times.

**Cation Exchange.** The Cd<sup>2+</sup> or Zn<sup>2+</sup> for Cu<sup>+</sup> cation exchange in Cu<sub>2-x</sub>S NSs was performed by using a modification of the method described by Son *et al.*<sup>37</sup> The metal salts that were used were Cd(NO<sub>3</sub>)<sub>2</sub> and ZnCl<sub>2</sub>, which were chosen due to the relatively weak bond between the cation and anion, ensuring availability of the cations. 0.14 mmol of metal salt was dissolved in 1 mL MeOH in the presence of a small amount of TBP (100 μL). The NSs solution was diluted by adding 2 mL toluene to 1 mL of NSs solution. The M<sup>2+</sup>/Cu<sup>+</sup> molar ratio in the reaction mixture was ~3. This ratio is a lower limit estimate, since it assumes a 100% yield and no purification losses in the synthesis of the Cu<sub>2-x</sub>S NSs. After addition of the cation-precursor in MeOH, the solution was stirred vigorously for several days at room temperature. The cation exchanged NSs were precipitated by adding 1:1 MeOH:BuOH, isolated by centrifugation at 3000 rpm (10 min), and redispersed in ~2 mL toluene.

**Optical spectroscopy.** Samples for optical measurements were prepared by directly dissolving the crude reaction mixture in anhydrous toluene under nitrogen and stored in sealed cuvettes. Absorption spectra were measured on a double beam Perkin-Elmer Lambda 16 UV/Vis spectrometer. PL and PL excitation

spectra were recorded by an Edinburgh Instruments FLS920 Spectrofluorimeter equipped with a 450 W Xenon lamp as excitation source and double grating monochromators. PL decay curves were obtained by time-correlated single-photon counting *via* time-to-amplitude conversion. A pulsed diode laser (EPL-445 Edinburgh Instruments, 441 nm, 55 ps pulse width, 0.2–20 MHz repetition rate) was used as the excitation source.

**Transmission Electron Microscopy (TEM).** TEM and Energy Dispersive X-Ray Spectroscopy (EDS) measurements were performed using a FEI Tecnai-12 microscope operating at 120 kV and a FEI Tecnai-20F microscope operating at 200 kV. Samples for TEM imaging were prepared by drop-casting a toluene solution of NSs onto a carbon-coated copper (400-mesh) TEM grid. The excess liquid was removed by blotting using filter paper. EDS measurements were performed using a dedicated low background holder and Cu-free Ni TEM grids. Acquisition time for EDS measurements was  $\sim 30$  s –  $\sim 1$  min. To ensure that the elemental concentrations were statistically valid and representative of the whole NS ensemble, EDS analyses were performed on wide areas ( $\sim 10^4$  –  $10^5$  nm<sup>2</sup>), encompassing several hundreds of NSs. High-resolution (Scanning) Transmission Electron Microscopy (HRTEM), High-Angle Annular Dark-Field (HAADF) Scanning Transmission Electron Microscopy (STEM) and Electron Diffraction (ED) measurements were performed on a FEI Titan 50-80 cubed microscope equipped with an aberration-corrector for the image forming lens, operated at 120 kV.

**X-Ray Diffraction (XRD).** XRD diagrams were obtained by using a PW 1729 Philips diffractometer, equipped with a Cu K $\alpha$  X-ray source ( $\lambda = 1.5418$  Å). Samples for XRD analysis were prepared by depositing a concentrated solution of purified NSs on a Si single crystalline substrate (100 orientation) under inert atmosphere.

## 4.3 Results and Discussion

### 4.3.1. Solution synthesis of ultrathin colloidal Cu<sub>2-x</sub>S nanosheets with well-defined size and shape

Figure 4.1 shows that SnBr<sub>4</sub> has a dramatic impact on the morphology and dimensions of colloidal Cu<sub>2-x</sub>S nanocrystals (NCs) produced by hot-injection of 1-dodecanethiol (DDT) into a solution of copper(I) acetate and trioctylphosphine oxide (TOPO) in octadecene (ODE), inducing the formation of ultrathin hexagonal Cu<sub>2-x</sub>S nanosheets (NSs, 2 nm thick, 110 nm lateral size, Figure 4.1b,c). In the absence of SnBr<sub>4</sub>, nearly spherical Cu<sub>2-x</sub>S NCs ( $\sim 9$  nm in diameter) are obtained (Figure 4.1a). Owing to their uniformity in thickness, the NSs readily self-assemble into ordered stacks (Figure 4.1c) that give rise to a series of low-angle XRD peaks (Figure 4.1d), which can be ascribed to successive diffraction orders from a periodic superstructure. The peak separation (*viz.*,  $\sim 2.49^\circ$ ) corresponds to a periodicity of  $\sim 36.7$  Å, indicating that the stacks consist of 2 nm thick Cu<sub>2-x</sub>S nanosheets separated by one DDT monolayer (the length of a fully extended DDT molecule is 17.7 Å, including the thiol headgroup).<sup>38</sup> This is corroborated by HRTEM images, which show  $\sim 2.0$  nm thick NSs separated by a ligand layer of  $\sim 1.6$  nm (Figure 4.2b,d). The fact that the inter-NS separation is similar to the length of one DDT molecule implies that the capping monolayers of neighboring NSs fully interpenetrate each other. This is consistent with the results reported by Pileni and co-workers for alkanethiol capped Ag and Ag<sub>2</sub>S nanocrystals,<sup>38</sup> where alkyl chains

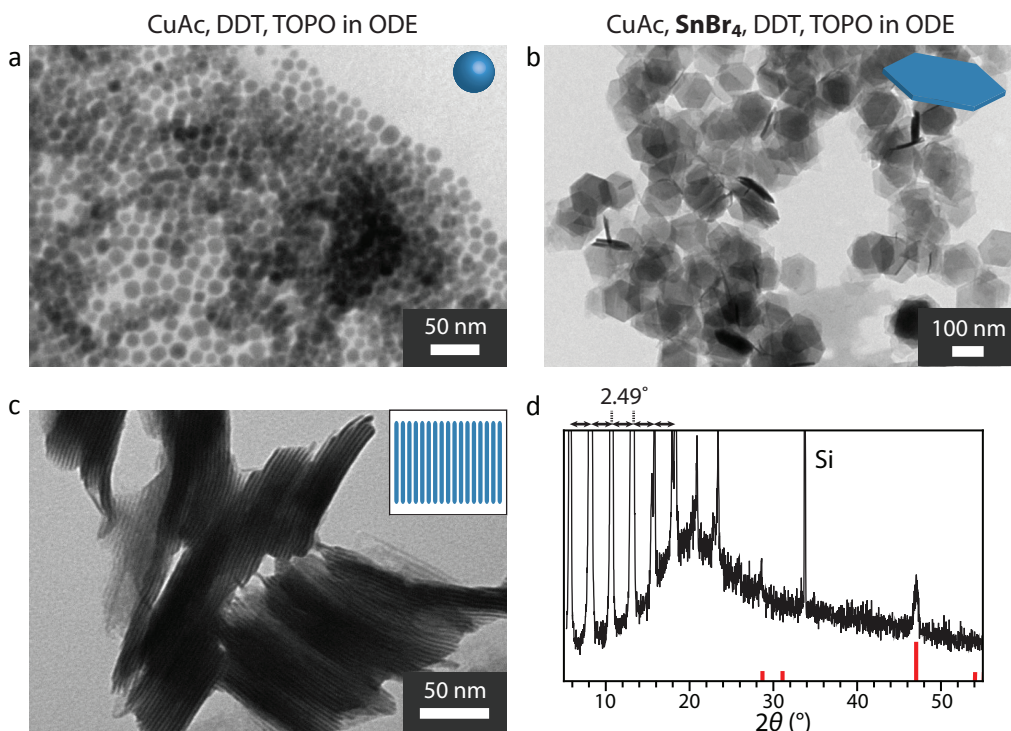


**Figure 4.1. Transmission Electron Microscopy (TEM) images of colloidal  $\text{Cu}_{2-x}\text{S}$  nanocrystals** synthesized in the absence (a) and in the presence (b,c) of  $\text{SnBr}_4$ , under otherwise identical conditions, showing that stacks of ultrathin 2D  $\text{Cu}_{2-x}\text{S}$  nanosheets (NSs) form in the presence of  $\text{SnBr}_4$ . (d) X-ray Diffractometry (XRD) pattern of a sample of  $\text{Cu}_{2-x}\text{S}$  NSs. The sharp reflections between  $6^\circ$  and  $24^\circ$  originate from stacking of NSs. The XRD pattern of digenite  $\text{Cu}_{1.8}\text{S}$  (JCPDS card no. [47-1748]) is shown as reference (red bars).

on adjacent nanocrystals were observed to fully interdigitate for carbon chain lengths equal to or longer than 12 carbon atoms.

The crystallinity of the nanosheets is clearly evident in the XRD pattern (Figure 4.1d), in the HRTEM images (Figure 4.2d), and in the electron diffraction (ED) patterns (Figure 4.2c). The binary Cu-S system has a very rich phase diagram,<sup>39</sup> and therefore  $\text{Cu}_{2-x}\text{S}$  can crystallize in various equilibrium crystal structures (*viz.*, monoclinic low-chalcocite  $\text{Cu}_2\text{S}$ , djurleite  $\text{Cu}_{1.96}\text{S}$  and roxbyite  $\text{Cu}_{1.78}\text{S}$ , hexagonal high-chalcocite  $\text{Cu}_2\text{S}$ , digenite  $\text{Cu}_{1.8}\text{S}$ , and covellite  $\text{CuS}$ , orthorhombic djurleite  $\text{Cu}_{1.96}\text{S}$  and anilite  $\text{Cu}_{1.75}\text{S}$ ).<sup>39,40</sup> These crystal structures are characterized by either hexagonal or cubic close-packing of S atoms, with Cu atoms positioned at the interstices. Transformations involving rearrangement of S atoms from cubic to hexagonal (and *vice versa*) are extremely slow, leading to a number of metastable phases (*e.g.*, low-digenite  $\text{Cu}_{1.8}\text{S}$ , tetragonal  $\text{Cu}_{2-x}\text{S}$  with  $x = 0.03 - 0.15$ ).<sup>39</sup>

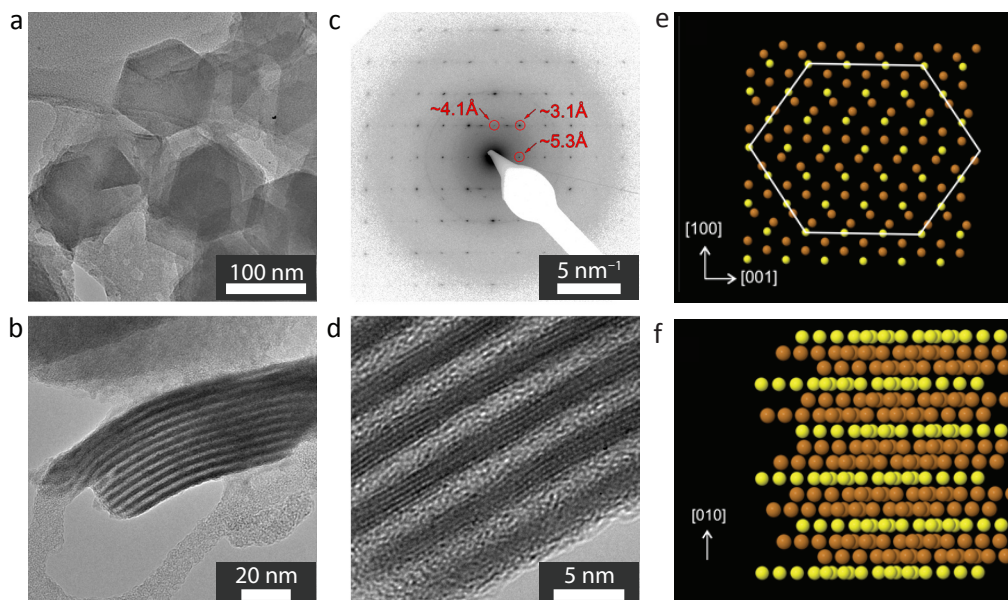


**Figure 4.2. TEM characterization of ultrathin colloidal  $\text{Cu}_{2-x}\text{S}$  nanosheets (NSs).** (a) Overview of NSs lying flat on the TEM grid. (b) Side view of a NS stack, highlighting the uniformity of both the NS thickness and the inter-NS separation. (c) Diffraction pattern (DP) taken from a single NS. (d) High-resolution TEM image, showing a detail of the stack presented in (b). The crystallinity of the NSs is clearly observed in this projection. (e,f) Atomic model of the tetragonal  $\text{Cu}_2\text{S}$  structure. The brown and yellow spheres depict Cu and S atoms, respectively. (e) Projection along the  $b$ -axis of the tetragonal structure. The tetragonal  $a$  and  $c$  axes are indicated. It now becomes clear why the outer morphology of the NSs can be hexagonal, whereas the crystal structure is tetragonal. (f) Perspective view of the atomic structure with the  $b$ -axis pointing upward. The buckled Cu layers are visible, corresponding to the atomic layers with dark contrast in the HRTEM image shown in (d).

The XRD pattern in Figure 4.1d also shows a peak at higher angles ( $47^\circ$ ), which corresponds to a lattice spacing of  $2.0 \text{ \AA}$ . This peak may be assigned to the (1 0 20) reflection of the hexagonal digenite crystal structure (see reference XRD pattern in Figure 4.1d). However, the ED patterns obtained from single, flat lying NSs are not hexagonal, but tetragonal (Figure 4.2c). Moreover, HRTEM images of stacks of NSs in a side projection (Figure 4.2d) reveal an interlayer distance of approximately  $3.9 \pm 0.2 \text{ \AA}$ . From a comparison of the experimental structural data (XRD, HRTEM, and ED) with the phase diagram of  $\text{Cu}_{2-x}\text{S}$ ,<sup>39</sup> we infer that the crystal structure of the NSs is likely the metastable tetragonal  $\text{Cu}_{2-x}\text{S}$  phase, with approximate lattice parameters  $a = b = 4.0 \text{ \AA}$ ,  $c = 11.0 \text{ \AA}$  (Figure 4.2e,f). Assuming this structure, the spots observed in the ED pattern (Figure 4.2c) can be assigned to the (100) and (002) lattice spacings, with the  $a$  and  $c$  axes lying in the plane of the NS and the  $b$  axis perpendicular to it. The  $a$  and  $b$  axes are equivalent and could be interchanged. The interlayer distance observed in the HRTEM

images (Figure 4.2d) can then be taken to correspond to the 4.0 Å spacing between the buckled Cu atomic layers along the  $b$ -axis in the tetragonal  $\text{Cu}_{2-x}\text{S}$  crystal structure (Figure 4.2e,f). This analysis indicates that the peak observed in the XRD pattern (Figure 4.1d) actually corresponds to the (200) reflection of a metastable tetragonal polymorph of digenite. We suggest the tetragonal phase as the most plausible crystal structure as the beam sensitivity of the sample prohibits a profound determination of the crystal structure.

Energy-Dispersive X-ray Spectroscopy (EDS) was used to analyze the sample, confirming that the NSs are made of  $\text{Cu}_{2-x}\text{S}$ . Intriguingly, the NSs also contain a significant amount of Br, but are devoid of Sn (average Cu : S : Sn : Br elemental ratios are  $2.0\pm 0.2 : 1.0 : 0 : 0.30\pm 0.06$ ), even if the nanocrystals are taken directly from the diluted crude reaction mixture and analyzed without any washing. This implies that Sn and Br play very different roles in the formation of ultrathin  $\text{Cu}_{2-x}\text{S}$  NSs, despite their common origin (*i.e.*,  $\text{SnBr}_4$ ).

#### 4.3.2 Unraveling the roles of Br, Sn and DDT

To clarify the influence of the different components of the reaction system, a series of control experiments was carried out. The results are summarized in Figure 4.3. As shown above (Figures 4.1 and 4.2) and in Figure 4.3a, ultrathin hexagonal  $\text{Cu}_{2-x}\text{S}$  NSs are obtained if  $\text{SnBr}_4$  is added to a reaction system that would otherwise yield spherical  $\text{Cu}_{2-x}\text{S}$  NCs. In contrast, if  $\text{SnAc}_4$  is used instead of  $\text{SnBr}_4$ , the reaction still yields small spherical NCs (Figure 4.3b). The use of  $\text{SnBr}_2$  instead of  $\text{SnBr}_4$  yields only irregularly shaped and aggregated sheets.

The impact of  $\text{SnBr}_4$  is clearly concentration dependent, since co-existing hexagonal NSs and irregularly shaped thin material are obtained if the concentration of  $\text{SnBr}_4$  is halved (Figure 4.3c). Interestingly, the elemental composition of the irregularly shaped thin material significantly differs from that of the hexagonal NSs (Cu : S : Br ratios are  $1.41\pm 0.14 : 1.0 : 0.03\pm 0.01$  and  $2.0\pm 0.2 : 1.0 : 0.30\pm 0.06$ , respectively, Appendix A4.1). If the concentration of  $\text{SnBr}_4$  is further reduced to a quarter of that originally used, nanosheets are no longer formed, but instead small  $\text{Cu}_{2-x}\text{S}$  nanodisks (aspect ratio  $\sim 2$ ) are obtained (Figure 4.3d), which readily self-assemble into corn cob superlattices. Co-existing hexagonal NSs and irregularly shaped thin material are also obtained in the absence of  $\text{SnBr}_4$ , provided  $\text{CuAc}$  is replaced by  $\text{CuBr}$  (Figure 4.3e). Remarkably, if  $\text{CuBr}$  is used in combination with  $\text{NaBr}$  only well-defined ultrathin hexagonal  $\text{Cu}_{2-x}\text{S}$  NSs are obtained (Figure 4.3f).

These observations unambiguously demonstrate that Br plays a pivotal role in the formation of  $\text{Cu}_{2-x}\text{S}$  NSs, while Sn(IV) has only the adjuvant role of ensuring that a sufficiently high concentration of Br is readily available in solution. The failure of  $\text{SnBr}_2$  to yield well-formed NSs can be attributed to the lower availability of Br, since

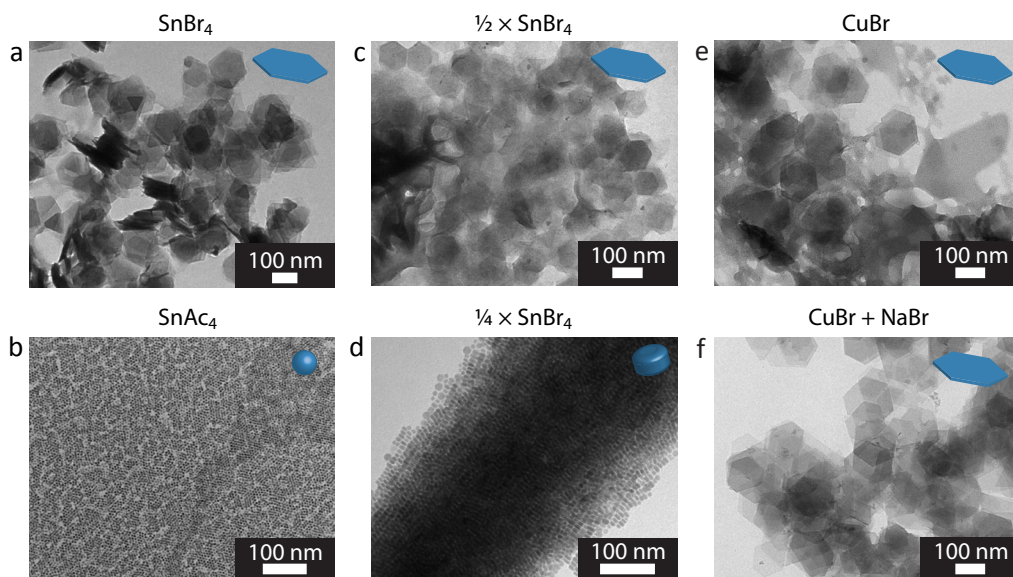


**Figure 4.3.** TEM images of colloidal  $\text{Cu}_{2-x}\text{S}$  NCs obtained with different additives. The composition of the reaction medium and reaction conditions are identical in all cases, except for the additive. (a)  $\text{SnBr}_4$ . (b)  $\text{SnAc}_4$ . (c)  $\text{SnBr}_4$ , but its concentration is  $\frac{1}{2}$  of that used in (a). (d)  $\text{SnBr}_4$ , but its concentration is  $\frac{1}{4}$  of that used in (a). (e) No additive, but  $\text{CuAc}$  is replaced by  $\text{CuBr}$ . (f)  $\text{NaBr}$  as additive and  $\text{CuBr}$  instead of  $\text{CuAc}$ .

$\text{Br}$  (a soft Lewis base) forms a much stronger bond with  $\text{Sn(II)}$  (a soft Lewis acid) than with  $\text{Sn(IV)}$  (a hard Lewis acid). Furthermore, experiments in which dodecanethiol was replaced by other sulfur sources, clearly demonstrate that well-defined  $\text{Cu}_{2-x}\text{S}$  NSs can be formed only when long chain alkanethiols (DDT and octadecanethiol) are used (Appendix A4.2). For example, phenylethanethiol (a bulky and short thiol) yields only irregularly shaped and aggregated thin material, while elemental sulfur leads to small and polydisperse nanocrystals. In contrast, 1-octadecanethiol (ODT) yields hexagonal NSs similar to those formed using 1-DDT, except for the larger inter-NS separation in the stacks (*viz.*, 2 nm compared to  $\sim 1.6$  nm). The longer inter-NS separation is consistent with the increase in length of the alkyl chain from 1.77 nm to 2.5 nm from 1-DDT to 1-ODT.<sup>38</sup>

#### 4.3.3 Size and shape control

The lateral dimensions of the NSs can be increased up to  $\sim 400$  nm, while preserving their shape, by diluting the reaction system with ODE (Figure 4.4a,b). The lateral dimensions of the hexagonal NSs can also be increased by decreasing the concentration of the coordinating ligand TOPO (Figure 4.4d), allowing the synthesis of  $2 \mu\text{m}$  wide hexagonal NSs. In contrast, the total absence of TOPO changes both the lateral

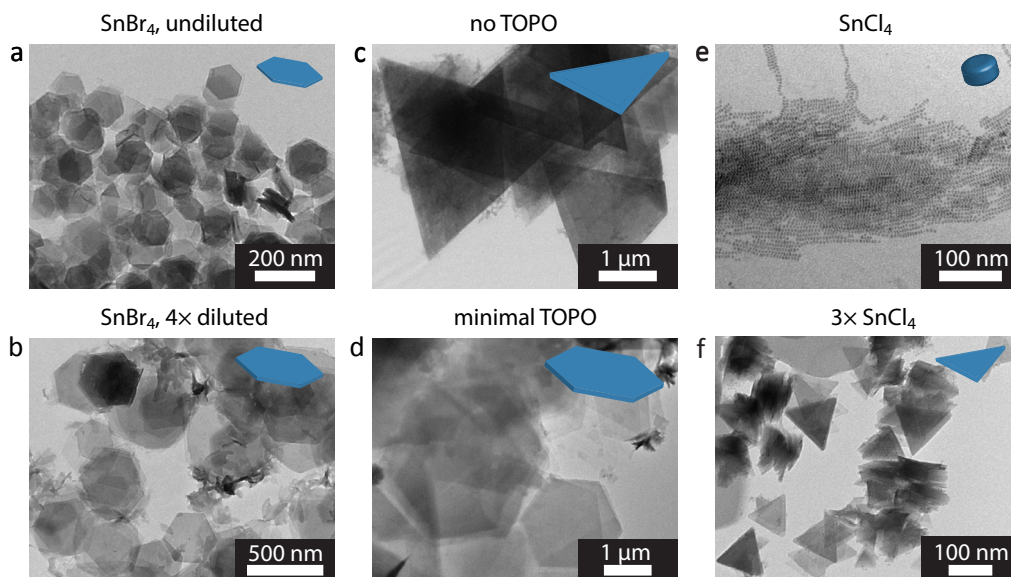


**Figure 4.4.** TEM images of colloidal  $\text{Cu}_{2-x}\text{S}$  NCs obtained under different reaction conditions. (a) 17 mM CuAc, 5.8 mM  $\text{SnBr}_4$  and 0.1 M TOPO in ODE; injection of 2.1 mmol DDT. (b) Same as (a), but diluted by a factor 4 with ODE. (c) Same as (a) but without TOPO. (d) Same as (a) but TOPO concentration reduced to 20 mM. (e)  $\text{SnCl}_4$  instead of  $\text{SnBr}_4$ , while keeping all concentrations unchanged. (f)  $\text{SnCl}_4$  instead of  $\text{SnBr}_4$ , but  $\text{SnCl}_4$  concentration increased by a factor 3.

dimensions and shape of the NSs, yielding large (3–4  $\mu\text{m}$ ) triangular NSs (Figure 4.4c). These experiments clearly demonstrate that TOPO affects the shape of the NSs, converting them from triangular to hexagonal, while simultaneously decreasing the lateral growth rates. The thickness of the nanosheets is not affected, as confirmed by XRD measurements, resulting in well-defined 2 nm-thick hexagonal nanosheets with aspect ratios up to 1000 (Appendix A4.3).

The size and shape of the NSs can also be tailored by using  $\text{SnCl}_4$  instead of  $\text{SnBr}_4$ , although a higher concentration of  $\text{SnCl}_4$  is required to produce ultrathin NSs (Figure 4.4e,f). It is noteworthy that the use of  $\text{SnCl}_4$  instead of  $\text{SnBr}_4$  changes the NS shape from hexagonal to triangular. The effect is clearly due to the Cl, since a similar result is obtained by replacing CuAc and  $\text{SnCl}_4$  by CuCl and NaCl, respectively, in the absence of any other additive (Appendix A4.4). The fact that a higher concentration of  $\text{SnCl}_4$  is needed to form NSs can be ascribed to the lower Cl availability due to the stronger Sn-Cl bond.

#### 4.3.4 Formation Mechanism

Several mechanisms have been proposed for the formation of ultrathin colloidal NSs

of semiconductors: 2D oriented attachment of PbS NCs,<sup>20</sup> self-assembly of  $(\text{CdX})_n$  ( $X = \text{S}, \text{Se}$ ) magic-size clusters (MSCs) within 2D lamellar templates,<sup>11–14</sup> 2D growth by monomer addition to  $(\text{CdX})_n$  MSC seeds,<sup>8,9</sup> and 2D-constrained growth of CdSe nanodisks within soft-templates formed by close-packed fatty acid layers.<sup>10</sup> It is interesting to note that work by Buhro and co-workers has provided compelling evidence that the formation of PbS nanosheets by 2D oriented attachment of small PbS nanoparticles is directed by lamellar-mesophase templates.<sup>21</sup> A soft-template mechanism has also been proposed to explain the formation of slightly thicker ( $w = 3.2$  nm) covellite CuS nanosheets.<sup>38</sup> To investigate whether a soft template mechanism is also involved in the formation of the ultrathin  $\text{Cu}_{2-x}\text{S}$  NSs reported in the present work, we followed the evolution of the reaction by TEM and optical spectroscopy.

Directly after DDT injection, irregularly shaped thin sheets form (Figure 4.5a). As the reaction progresses, the irregular thin sheets gradually disappear, while hexagonal  $\text{Cu}_{2-x}\text{S}$  NSs form and increase in concentration, eventually becoming the only nanostructure present (Figure 4.5). The temporal evolution observed in Figure 4.5 bears similarities with that previously reported for the reaction between Cu(I) salts and DDT in solution at high temperatures (185–220 °C),<sup>33,39</sup> where irregularly shaped thin sheets are also observed at early reaction times and gradually disappear as  $\text{Cu}_{2-x}\text{S}$  NCs are formed.<sup>33,39</sup> Nevertheless, in these cases ultrathin NSs are not formed, but instead the reaction yields either spherical NCs (5–18 nm)<sup>33,39</sup> or small nanodisks (9 by 13–17 nm),<sup>33</sup> in striking contrast with the present results. This difference is remarkable, and is clearly due to the presence of tin tetrahalides. Tin(IV) compounds (*viz.*,  $\text{SnCl}_4$  and  $\text{Sn}(\text{acetylacetonate})_2\text{Cl}_2$ ) have been previously shown to affect the shape of  $\text{Cu}_{2-x}\text{S}$  NCs obtained by reacting Cu(II)acetylacetonate and neat DDT, leading to the formation of either aggregated ultrathin  $\text{Cu}_{1.96}\text{S}$  NSs ( $w = 0.65$  nm,  $L = 200$  nm, hexagonal or triangular without shape selectivity)<sup>24</sup> or  $\text{Cu}_{2-x}\text{S}$  nanodisks ( $w = 3.2$ –6 nm;  $L = 13$ –84 nm),<sup>40</sup> under conditions that would otherwise yield spherical NCs. This has been tentatively ascribed to *in-situ* generated  $[\text{Sn}_x\text{S}_y]$  species (*e.g.*,  $[\text{Sn}_2\text{S}_6]^{4-}$ ),<sup>24,40</sup> but the results presented above unambiguously demonstrate that the effect is actually due to the halides and that Sn(IV) is important only to the extent that it ensures the

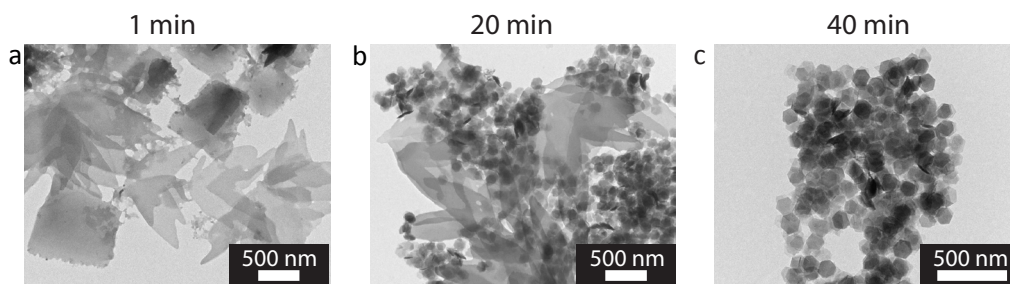


**Figure 4.5. Precursor evolution.** TEM images of samples collected at different time points after the injection of DDT into a solution of Cu(I) acetate,  $\text{SnBr}_4$  and TOPO in ODE at 220 °C.

availability of sufficiently high halide concentrations in the growth solution. It is also clear that the formation of ultrathin Cu<sub>2-x</sub>S NSs results from a synergistic interaction between halides and Cu-alkanethiolate complexes that are formed *in-situ*, since the use of sulfur sources other than alkanethiols does not yield nanosheets (see above and Appendix A4.2).

Copper-thiolates have been extensively used as single source precursors to produce Cu<sub>2-x</sub>S NCs, both by solventless and solution based routes.<sup>33,37,39-43</sup> These synthetic protocols have yielded a wealth of different nanocrystal shapes (quasi-spheres, hexagonal bipyramids and bifrustums, hexagonal nanodisks and nanoplatelets),<sup>33,37,39-43</sup> but ultrathin nanosheets are rare, and have been observed only when halides were present in the reaction medium. The reaction mechanisms are not yet well-understood, although an *in-situ* synchrotron powder X-ray diffraction study has demonstrated that the C-S bond cleavage is the limiting step in the formation and growth of colloidal Cu<sub>2-x</sub>S NCs by thermolysis of [Cu(DDT)] in solution.<sup>41</sup> Cu-alkanethiolates form a metal-organic framework (MOF) that is stable as a lamellar solid up to 143.5 °C (for Cu-DDT), when it undergoes a phase transition to a mesogenic liquid crystal.<sup>44</sup> The structure of this liquid crystal phase is particularly relevant for the present discussion, as it consists of a hierarchically self-assembled hexagonal columnar mesophase, in which each column is made of a stack of tetranuclear [Cu<sub>4</sub>(DDT)<sub>4</sub>] disks that are kept together by weaker Cu-S inter-disk interactions. The irregularly shaped sheets observed at early reaction stages in this and other works<sup>33,39</sup> can thus be tentatively ascribed to intact Cu-thiolate frameworks. However, the inter-column and inter-disk interactions break at sufficiently high temperatures (*e.g.*, 205.6 °C for neat Cu-DDT) leading to an isotropic liquid,<sup>44</sup> which, upon further heating, will undergo Cu-catalyzed C-S thermolysis, producing independent [Cu<sub>4</sub>S<sub>4</sub>] nuclei that further grow into spherical NCs or nanodisks by monomer addition.<sup>33,39</sup> The different fate of the irregular sheets in the present work suggests that halides have a stabilizing effect on the Cu-thiolate framework, keeping its 2D-structural integrity at temperatures that are sufficiently high to sustain C-S thermolysis. Interestingly, work by Tao and co-workers has demonstrated that the ordered liquid crystalline mesophase plays an essential role in templating the nanocrystal morphology obtained by solventless thermolysis of Cu-thiolates, so that hexagonal Cu<sub>2-x</sub>S nanodisks and nanoplatelets are only obtained for Cu-thiolates that adopt an inverse columnar mesophase at the reaction temperature.<sup>42</sup> It is thus likely that the 2D-constrained growth observed in the present work is due to a templating framework formed by halides and the Cu-thiolate MOF.

Our experiments show that halides have a dramatic impact on both the optical spectra and the morphology of the Cu-thiolate precursor complexes formed upon heating of a mixture of Cu(I) salts and DDT in ODE to 190 °C (Appendix A4.5). This temperature is just below the onset of C-S thermolysis, and therefore also below the nucleation threshold. The measurements shown in Appendix A4.5 thus reflect the properties of the

precursor complexes formed in the reaction mixture. The presence of Br clearly affects the morphology of the Cu-thiolate precursor complex at room temperature, converting it from a 3D gel network to irregularly shaped thin sheets. A 3D Cu-DDT gel has been observed before by Han and co-workers,<sup>39</sup> by cooling a solution of Cu-DDT in DDT from 200 °C to room temperature. It is interesting to note that this implies that the Cu-thiolate lamellar structure does not form under these conditions, suggesting that the inter-column Van der Waals interactions are weakened by the presence of the solvent molecules (ODE or DDT). The inter-disk Cu-S interactions are however sufficiently strong to keep the columns intact, allowing the formation of a 3D gel network of interconnected strings. The observation of 2D sheets in the presence of Br can thus be interpreted as evidence that the inter-column interaction is reinforced by halides, allowing the formation of lamellar frameworks. Halides may be expected to have a large impact on MOFs based on Cu(I) as connectors, since they are capable of binding as poly-coordinated bridging atoms between multiple (up to 4) Cu(I) atoms, often forming  $[(\text{CuX})\text{L}]_n$  (L = sulfur-donor ligand) coordination polymers with highly variable structures, ranging from 2D to 3D.<sup>46</sup> As will be discussed below, the pronounced changes observed in the optical spectra of the precursor complexes in the presence of halides clearly demonstrate the formation of direct bonds between halides and Cu(I) atoms in the Cu-thiolate complexes.

#### 4.3.5 Optical spectroscopy

Optical spectroscopy is thus particularly useful to unravel the role of the halides, since it allows the formation of  $\text{Cu}_{2-x}\text{S}$  NCs to be followed, while simultaneously signaling the presence of precursors and intermediate reaction compounds. The optical spectra of samples collected during the synthesis (Figure 4.6) clearly show that halides have no effect on the identity of the complexes present prior to DDT injection, but dramatically affect the electronic structure of the Cu-thiolate complex formed immediately after the injection (Figure 4.6c). When no halides are added, an absorption transition is observed at 325 nm (Figure 4.6a), while in the presence of Br this absorption transition shifts to 375 nm (Figure 4.6b). We note that these spectra are identical to those obtained by heating up the reaction mixture to 190 °C, indicating that the same precursor complexes are formed. The photoluminescence (PL) of the Cu-thiolate precursor complexes also changes dramatically upon addition of halides (Figure 4.6a,b). It is evident that these precursor complexes are consumed as the reaction progresses, since both the absorption and PL peaks associated with them decrease, while the characteristic absorption of  $\text{Cu}_{2-x}\text{S}$  increases (Figure 4.6a,b). This is consistent with the TEM observations discussed above (Figure 4.5).

The optical properties of the precursor complexes formed upon DDT injection are typical of polynuclear Cu(I) complexes with halides and sulfur-donor ligands.<sup>45,46</sup> Multinuclear Cu(I) complexes with sulfur or halide donors typically show efficient PL at room temperature, peaking at wavelengths ranging from 500 – 700 nm, depending

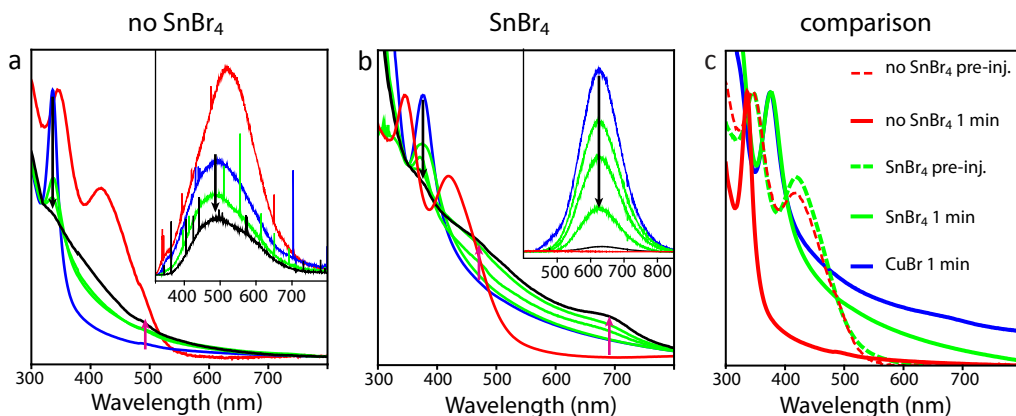


**Figure 4.6. Optical spectroscopy.** (a,b) Temporal evolution of the absorption and PL (insets) spectra of samples collected at different time points during  $\text{Cu}_{2-x}\text{S}$  NC syntheses performed without (a) and with  $\text{SnBr}_4$  (b). The reaction conditions and composition of the reaction mixture were identical in both cases, except for the presence or absence of  $\text{SnBr}_4$ . Red and blue lines give, respectively, the spectra prior to and 1 min after DDT injection. Black lines correspond to the final samples, collected at 15 min for (a) (9 nm  $\text{Cu}_{2-x}\text{S}$  NCs), and 80 min for (b) (ultrathin hexagonal  $\text{Cu}_{2-x}\text{S}$  NSs). Intermediate time points are given by green lines (4, 10 min in a; 4, 15, 33 min in b). The arrows indicate the evolution of the peak intensities, and show that Cu-thiolate (black arrow) is consumed as  $\text{Cu}_{2-x}\text{S}$  (purple arrow) forms. (c) Comparison of the absorption of samples collected prior to and 1 min after injection.

on the ligands and the structure of the complex or coordination polymer.<sup>45</sup> The PL is often characterized by two independent bands, where the high energy PL peak originates from a Cu/halide-to-ligand charge transfer triplet state and the low energy PL peak originates from a  $\text{Cu}_4\text{X}_4$  (X = donor atom, *i.e.* sulfur or halide) centered triplet state, which is a combination of X to Cu(I) charge-transfer and *d-s* transitions.<sup>45</sup> The low energy PL has larger Stokes shifts and longer lifetimes than the high energy PL. Moreover, the quantum yield of the high energy PL is lower, making it often absent at room temperature. The peak position, Stokes shift and lifetime (*viz.*, 7.8  $\mu\text{s}$  with a faster initial component of 1.8  $\mu\text{s}$ , Appendix A4.6) observed for the Br-modified Cu-thiolate precursor complex are consistent with emission from the low energy state. The large shifts induced in both the absorption and PL spectra by the presence of Br (*viz.*, 0.34 eV and 0.48 eV, respectively) thus provide compelling evidence that Br atoms coordinate directly to Cu(I) atoms in the Cu-DDT precursor complexes. This is further supported by the dramatic increase observed in the PL QY in the presence of Br, since shorter Cu-Cu distances are known to lead to more efficient PL at RT.<sup>45</sup> It should be noted that the optical spectra provide no signatures of MSCs or stepwise growth,<sup>47,48</sup> thereby excluding mechanisms involving MSCs.

We propose that in the present case binding between halides (Br or Cl) and Cu(I) atoms in the Cu-thiolate precursor complexes forms a soft 2D template that remains structurally

intact beyond the onset of the C-S bond thermolysis. The thermally induced C-S bond cleavage is catalyzed by the Cu(I) atoms,<sup>49</sup> and therefore only DDT molecules directly involved in the Cu-thiolate framework will undergo thermolysis. Since the C-S bond cleavage is the limiting step in the formation of colloidal Cu<sub>2-x</sub>S NCs by thermolysis of [Cu(DDT)] in solution,<sup>41</sup> the soft template will impose 2D constraints on the nucleation and growth of the Cu<sub>2-x</sub>S NSs, thereby leading to the formation of ultrathin colloidal Cu<sub>2-x</sub>S nanosheets. This mechanism is analogous to the nucleation and growth of colloidal NCs in solution,<sup>50</sup> except for the fact that it is two-dimensionally constrained. The impact of TOPO and of the overall concentration of the reaction system on the lateral dimensions and shape of the NSs can easily be understood from this perspective, since coordinating ligands are well-known to modulate the growth rates of colloidal NCs by competing with the monomers (*i.e.*, [CuS] units) for the binding sites, in a strongly facet-dependent fashion.<sup>50</sup> It is thus likely that both the final shape and the crystal structure of the NSs are determined by the interplay between the constraints imposed by the 2D soft template, the C-S thermolysis rates, and coordination by TOPO, halides and intact DDT molecules. This mechanism will be investigated in more detail in Chapter 5, by using *in-situ* Small-Angle X-ray Scattering. It is interesting to note that the mechanism proposed in this chapter may be applicable also to the preparation of ultrathin 2D nanocrystals of other compositions, since lamellar metal thiolate complexes are widely used as single source precursors in the synthesis of nanocrystals of a variety of transition metal sulfides (*e.g.*, Fe, Ni, Cu, Co, Cd, Zn, Pd, Pt, Ag, Au, Pb and Bi).<sup>51-55</sup>

#### 4.3.6 Composition tailoring by cation exchange

Nanoscale cation exchange (CE) provides a versatile strategy for synthesizing colloidal NCs with compositions and morphologies that are not accessible by conventional methods (see also Chapters 2, 6 and 7).<sup>31,32,48,56-62</sup> Very often the anionic sublattice is not affected by the cation exchange, leading to a topotactic reaction, through which the size and shape of the parent NCs are preserved in the product NCs, despite the compositional change.<sup>31,56</sup> Interestingly, the degree of cation exchange can be controlled, leading to partial or total replacement of the native cation.<sup>31,56</sup> In the case of partial exchange, the elemental profile distribution within the product NC can also be controlled, so that core/shell heteronanocrystals,<sup>59,60</sup> homogeneous or gradient alloy nanocrystals,<sup>60</sup> and doped nanocrystals<sup>61,62</sup> can be obtained, depending on the chemical system and reaction conditions.<sup>31,56,59-62</sup> Topotactic CE reactions in which Cu<sup>+</sup> is exchanged for other cations have been extensively investigated in copper chalcogenides, yielding NCs with metastable shapes and structures that would otherwise not be attainable.<sup>31,32,56-58</sup>

In the present work, CE reactions were exploited to convert Cu<sub>2-x</sub>S NSs into CdS and ZnS NSs (Figure 4.7). The results show that the Cd<sup>2+</sup> or Zn<sup>2+</sup> for Cu<sup>+</sup> exchange reactions in Cu<sub>2-x</sub>S NSs are topotactic, thereby preserving the shape and size (both lateral dimensions and thickness) of the parent NSs in the product NSs. This is

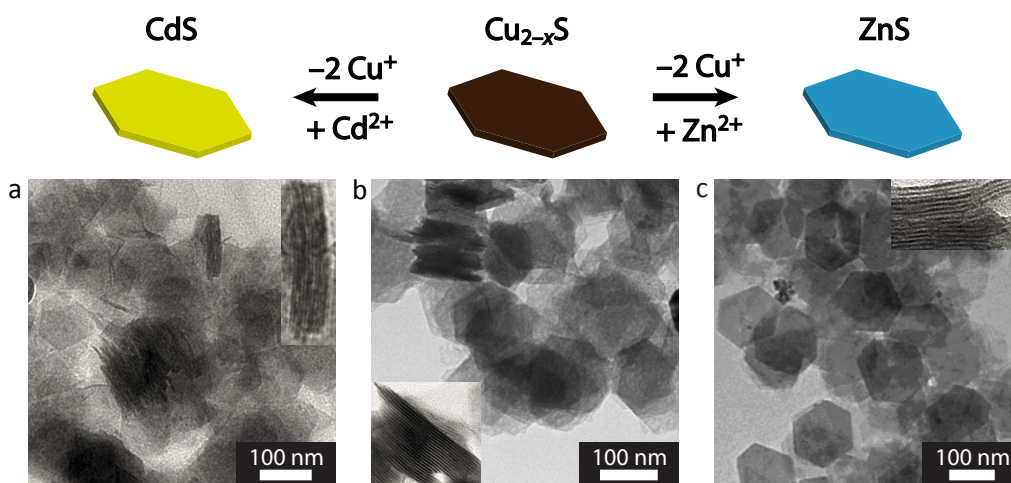


**Figure 4.7. Cation exchange reaction on ultrathin  $\text{Cu}_{2-x}\text{S}$  nanosheets.** Top: Schematic representation of the cation exchange reactions with  $\text{Cu}_{2-x}\text{S}$  nanosheets (NSs) as parent nanocrystals, resulting in CdS and ZnS NSs. Bottom: TEM images of ultrathin colloidal nanosheets (NSs) of various compositions (insets show stacks of NSs). (a) NSs obtained after  $\text{Cd}^{2+}$  for  $\text{Cu}^+$  exchange in  $\text{Cu}_{2-x}\text{S}$  NSs (ratio Cd: S: Cu: Br=  $0.90\pm 0.04$ :  $1.0$ :  $0.06\pm 0.01$ :  $0.03\pm 0.01$ ) (b)  $\text{Cu}_{2-x}\text{S}$  NSs used as parent NCs for the NSs shown in a and c (ratio S: Cu: Br=  $1.0$ :  $2.0\pm 0.2$ :  $0.30\pm 0.06$ ); (c) NSs obtained after  $\text{Zn}^{2+}$  for  $\text{Cu}^+$  exchange in  $\text{Cu}_{2-x}\text{S}$  NSs (ratio Zn: S: Cu: Br=  $0.97\pm 0.04$ :  $1.0$ :  $0.30\pm 0.06$ :  $0.10\pm 0.02$ ).

remarkable considering the ultrathin dimensions of the parent NSs, and implies that the sulfide anionic framework is very robust and can readily accommodate and relax the local strain induced by the exchange of two  $\text{Cu}^+$  ions by one  $\text{Cd}^{2+}$  or  $\text{Zn}^{2+}$  cation. This is in line with the crystal structure proposed for the  $\text{Cu}_{2-x}\text{S}$  NSs (Figure 4.2e,f). However, the cation exchange did not reach completion, yielding Cu-doped CdS NSs and ZnS NSs. The doping level in the CdS NSs is sufficiently low to allow observation of efficient PL associated with exciton recombination in the  $\text{Cu}^+$  dopants (Appendix A4.7).<sup>63</sup> These results demonstrate that the  $\text{Cu}_{2-x}\text{S}$  NSs developed here can be used as well-defined morphological templates for the preparation of compositionally diverse NSs, thus allowing access to novel ultrathin colloidal NSs that cannot be synthesized by direct routes.

#### 4.4 Conclusions

The novel “bottom-up” solution-based synthesis method developed in this chapter yields 2 nm thick colloidal  $\text{Cu}_{2-x}\text{S}$  NSs with well-defined size and shape (hexagonal or triangular). The lateral dimensions of these ultrathin NSs can be tuned from 100 nm to 3  $\mu\text{m}$ . These NSs are very robust and do not easily fold or aggregate, and therefore offer excellent solution processability. They can also be used as building blocks for

self-organized superstructures. Moreover, we demonstrate that the composition of the NSs can be post-synthetically tailored by exploiting topotactic cation exchange reactions, while preserving their well-defined shape, lateral dimensions and thickness. The method presented here thus holds great promise as a route to solution-processable compositionally diverse ultrathin colloidal NSs with well-defined shape and size. It should be noted that combined control over surface, size, shape and composition can be used to modify the properties of the NSs or to bestow them with novel functionalities, paving the way towards tailor-made NSs for a myriad of potential applications.

## Acknowledgments

Financial support from the EU FP7-Integrated Infrastructure Initiative-I3 program ESTEEM2(312483) is gratefully acknowledged.

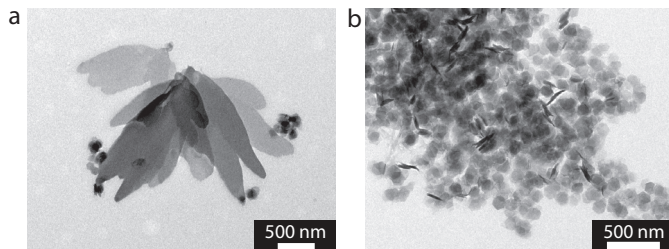
## References

- (1) Butler, S. Z.; Hollen, S. M.; Cao, L.; Cui, Y.; Gupta, J. A.; Gutie, H. R.; Heinz, T. F.; Hong, S. S.; Huang, J.; Ismach, A. F.; *et al.* *ACS Nano* **2013**, *7*, 2898–2926.
- (2) Wang, Q. H.; Kalantar-Zadeh, K.; Kis, A.; Coleman, J. N.; Strano, M. S. *Nat. Nanotechnol.* **2012**, *7*, 699–712.
- (3) Xu, M.; Liang, T.; Shi, M.; Chen, H. *Chem. Rev.* **2013**, *113*, 3766–3798.
- (4) Chhowalla, M.; Shin, H. S.; Eda, G.; Li, L.-J.; Loh, K. P.; Zhang, H. *Nat. Chem.* **2013**, *5*, 263–275.
- (5) Rao, C. N. R.; Ramakrishna Matte, H. S. S.; Maitra, U. *Angew. Chem. Int. Ed.* **2013**, *52*, 13162–13185.
- (6) Rogers, J. A.; Lagally, M. G.; Nuzzo, R. G. *Nature* **2011**, *477*, 45–53.
- (7) Narita, A.; Feng, X.; Hernandez, Y.; Jensen, S. A.; Bonn, M.; Yang, H.; Verzhbitskiy, I. A.; Casiraghi, C.; Hansen, M. R.; Koch, A. H. R. *et al.* *Nat. Chem.* **2014**, *6*, 126–132.
- (8) Yin, Z.; Zhu, J.; He, Q.; Cao, X.; Tan, C.; Chen, H.; Yan, Q.; Zhang, H. *Adv. Energy Mater.* **2014**, *4*, 1300574.
- (9) Huang, X.; Tan, C.; Yin, Z.; Zhang, H. *Adv. Mater.* **2014**, *26*, 2185–2204.
- (10) Bouet, C.; Tessier, M. D.; Ithurria, S.; Mahler, B.; Nadal, B.; Dubertret, B. *Chem. Mater.* **2013**, *25*, 1262–1271.
- (11) Ithurria, S.; Bousquet, G.; Dubertret, B. *J. Am. Chem. Soc.* **2011**, *133*, 3070–3077.
- (12) Li, Z.; Peng, X. *J. Am. Chem. Soc.* **2011**, *133*, 6578–6586.
- (13) Hutter, E. M.; Bladt, E.; Goris, B.; Pietra, F.; van der Bok, J. C.; Boneschanscher, M. P.; de Mello Donega, C.; Bals, S.; Vanmaekelbergh, D. *Nano Lett.* **2014**, *14*, 6257–6262.
- (14) Yang, J.; Son, J. S.; Yu, J. H.; Joo, J.; Hyeon, T. *Chem. Mater.* **2013**, *25*, 1190–1198.
- (15) Son, J. S.; Park, K.; Kwon, S. G.; Yang, J.; Choi, M. K.; Kim, J.; Yu, J. H.; Joo, J.; Hyeon, T. *Small* **2012**, *8*, 2394–2402.
- (16) Yu, J. H.; Liu, X.; Kweon, K. E.; Joo, J.; Park, J.; Ko, K.-T.; Lee, D. W.; Shen, S.; Tivakornsasithorn, K.; Son, J. S. *et al.* *Nat. Mater.* **2010**, *9*, 47–53.
- (17) Liu, Y. H.; Wang, F. D.; Wang, Y. Y.; Gibbons, P. C.; Buhro, W. E. *J. Am. Chem. Soc.* **2011**, *133*, 17005–17013.
- (18) Ithurria, S.; Tessier, M. D.; Mahler, B.; Lobo, R. P. S. M.; Dubertret, B.; Efros, A. L. *Nat. Mater.* **2011**, *10*, 936–941.
- (19) Pelton, M.; Ithurria, S.; Schaller, R. D.; Dolzhnikov, D. S.; Talapin, D. V. *Nano Lett.* **2012**, *12*, 6158–6163.
- (20) Tessier, M. D.; Mahler, B.; Nadal, B.; Heuclin, H.; Peditti, S.; Dubertret, B. *Nano Lett.* **2013**, *13*, 3321–3328.
- (21) Malakooti, R.; Cademartiri, L.; Migliori, A.; Ozin, G. A. *J. Mater. Chem.* **2008**, *18*, 66–69.
- (22) Li, L.; Chen, Z.; Hu, Y.; Wang, X.; Zhang, T.; Chen, W.; Wang, Q. *J. Am. Chem. Soc.* **2013**, *135*, 1213–1216.
- (23) Schliehe, C.; Juarez, B. H.; Pelletier, M.; Jander, S.; Greshnykh, D.; Nagel, M.; Meyer, A.; Foerster, S.; Kornowski, A.; Klinke, C. *et al.* *Science* **2010**, *329*, 550–553.
- (24) Morrison, P. J.; Loomis, R. A.; Buhro, W. E. *Chem. Mater.* **2014**, *26*, 5012–5019.
- (25) Park, H.; Chung, H.; Kim, W. *Mater. Lett.* **2013**, *99*, 172–175.
- (26) Park, K. H.; Jang, K.; Son, S. U. *Angew. Chem. Int. Ed.* **2006**, *45*, 4608–4612.
- (27) Yi, L.; Gao, M. *Cryst. Growth Des.* **2011**, *11*, 1109–1116.

- (28) Zhao, Y.; Burda, C. *Energy Environ. Sci.* **2012**, *5*, 5564–5576.
- (29) Wadia, C.; Alivisatos, A. P.; Kammen, D. M. *Environ. Sci. Technol.* **2009**, *43*, 2072–2077.
- (30) Luther, J. M.; Jain, P. K.; Ewers, T.; Alivisatos, A. P. *Nat. Mater.* **2011**, *10*, 361–366.
- (31) Kriegel, I.; Jiang, C.; Rodríguez-Fernández, J.; Schaller, R. D.; Talapin, D. V.; da Como, E.; Feldmann, J. *J. Am. Chem. Soc.* **2012**, *134*, 1583–1590.
- (32) Hsu, S. W.; Ngo, C.; Tao, A. R. *Nano Lett.* **2014**, *14*, 2372–2380.
- (33) Goel, S.; Chen, F.; Cai, W. *Small* **2014**, *10*, 631–645.
- (34) Beberwyck, B. J.; Surendranath, Y.; Alivisatos, A. P. *J. Phys. Chem. C* **2013**, *117*, 19759–19770.
- (35) Li, H.; Brescia, R.; Povia, M.; Prato, M.; Bertoni, G.; Manna, L.; Moreels, I. *J. Am. Chem. Soc.* **2013**, *135*, 12270–12278.
- (36) Wang, Y.; Hu, Y.; Zhang, Q.; Ge, J.; Lu, Z.; Hou, Y.; Yin, Y. *Inorg. Chem.* **2010**, *49*, 6601–6608.
- (37) Son, D. H.; Hughes, S. M.; Yin, Y.; Alivisatos, A. P. *Science* **2004**, *306*, 1009–1012.
- (38) Pileni, M. P. *J. Phys. Chem. B* **2001**, *105*, 3358–3371.
- (39) Chakrabarti, D. J.; Laughlin, D. E. *Bull. Alloy Phase Diagrams* **1983**, *4*, 254–270.
- (40) Li, W.; Shavel, A.; Guzman, R.; Rubio-Garcia, J.; Flox, C.; Fan, J.; Cadavid, D.; Ibáñez, M.; Arbiol, J.; Morante, J. R.; Cabot, A. *Chem. Commun.* **2011**, *47*, 10332–10337.
- (41) Du, Y.; Yin, Z.; Zhu, J.; Huang, X.; Wu, X.-J.; Zeng, Z.; Yan, Q.; Zhang, H. *Nat. Commun.* **2012**, *3*, 1177.
- (42) Han, W.; Yi, L.; Zhao, N.; Tang, A.; Gao, M.; Tang, Z. *J. Am. Chem. Soc.* **2008**, *130*, 13152–13161.
- (43) Li, X.; Shen, H.; Niu, J.; Li, S.; Zhang, Y.; Wang, H.; Li, L. S. *J. Am. Chem. Soc.* **2010**, *132*, 12778–12779.
- (44) Noerby, P.; Johnsen, S.; Iversen, B. B. *ACS Nano* **2014**, *8*, 4295–4303.
- (45) Bryks, W.; Wette, M.; Velez, N.; Hsu, S.-W.; Tao, A. R. *J. Am. Chem. Soc.* **2014**, *136*, 6175–6178.
- (46) Sigman, M. B.; Ghezlbash, A.; Hanrath, T.; Saunders, A. E.; Lee, F.; Korgel, B. A. *J. Am. Chem. Soc.* **2003**, *125*, 16050–16057.
- (47) Espinet, P.; Lequerica, M. C.; Martín-Alvarez, J. M. *Chem. Eur. J.* **1999**, *5*, 1982–1986.
- (48) Ford, P. C.; Cariati, E.; Bourassa, J. *Chem. Rev.* **1999**, *99*, 3625–3648.
- (49) Lapprand, A.; Bonnot, A.; Knorr, M.; Rousselin, Y.; Kubicki, M. M.; Fortin, D.; Harvey, P. D. *Chem. Commun.* **2013**, *49*, 8848–8850.
- (50) Groeneveld, E.; van Berkum, S.; Meijerink, A.; de Mello Donega, C. *Small* **2011**, *7*, 1247–1256.
- (51) Groeneveld, E.; van Berkum, S.; van Schooneveld, M. M.; Gloter, A.; Meeldijk, J. D.; van den Heuvel, D. J.; Gerritsen, H. C.; de Mello Donega, C. *Nano Lett.* **2012**, *12*, 749–757.
- (52) Wang, L.; He, W.; Yu, Z. *Chem. Soc. Rev.* **2013**, *42*, 599–621.
- (53) de Mello Donega, C. *Chem. Soc. Rev.* **2011**, *40*, 1512–1546.
- (54) Zhuang, Z.; Lu, X.; Peng, Q.; Li, Y. *Chem. Eur. J.* **2011**, *17*, 10445–10452.
- (55) Tang, A.; Wang, Y.; Ye, H.; Zhou, C.; Yang, C.; Li, X.; Peng, H.; Zhang, F.; Hou, Y.; Teng, F. *Nanotechnology* **2013**, *24*, 355602.
- (56) Wang, Y.; Tang, A.; Li, K.; Yang, C.; Wang, M.; Ye, H.; Hou, Y.; Teng, F. *Langmuir* **2012**, *28*, 16436–16443.
- (57) Busupalli, B.; Kummara, S.; Kumaraswamy, G.; Prasad, B. L. V. *Chem. Mater.* **2014**, *26*, 3436–3442.
- (58) Shi, W.; Zhu, J.; Rui, X.; Cao, X.; Chen, C.; Zhang, H.; Hng, H. H.; Yan, Q. *ACS Appl. Mater. Interfaces* **2012**, *4*, 2999–3006.
- (59) Chen, J.; Wu, L. M.; Chen, L. *Inorg. Chem.* **2007**, *46*, 586–591.
- (60) Xu, C.; Zeng, Y.; Rui, X.; Xiao, N.; Zhu, J.; Zhang, W.; Chen, J.; Liu, W.; Tan, H.; Hng, H. H.; *et al.* *ACS Nano* **2012**, *6*, 4713–4721.
- (61) Wu, W. Y.; Chakraborty, S.; Chang, C. K. L.; Guchhait, A.; Lin, M.; Chan, Y. *Chem. Mater.* **2014**, *26*, 6120–6126.
- (62) Rivest, J. B.; Jain, P. K. *Chem. Soc. Rev.* **2013**, *42*, 89–96.
- (63) Li, H.; Zanella, M.; Genovese, A.; Povia, M.; Falqui, A.; Giannini, C.; Manna, L. *Nano Lett.* **2011**, *11*, 4964–4970.
- (64) van der Stam, W.; Gantapara, A. P.; Akkerman, Q. A.; Soligno, G.; Meeldijk, J. D.; van Roij, R.; Dijkstra, M.; de Mello Donega, C. *Nano Lett.* **2014**, *14*, 1032–1037.
- (65) Casavola, M.; van Huis, M. A.; Bals, S.; Lambert, K.; Hens, Z.; Vanmaekelbergh, D. *Chem. Mater.* **2012**, *24*, 294–302.
- (66) Groeneveld, E.; Witteman, L.; Lefferts, M.; Ke, X.; Bals, S.; van Tendeloo, G.; de Mello Donega, C. *ACS Nano* **2013**, *7*, 7913–7930.
- (67) Eilers, J.; Groeneveld, E.; de Mello Donega, C.; Meijerink, A. *J. Phys. Chem. Lett.* **2012**, *3*, 1663–1667.
- (68) Sahu, A.; Kang, M. S.; Kompch, A.; Notthoff, C.; Wills, A. W.; Deng, D.; Winterer, M.; Frisbie, C. D.; Norris, D. J. *Nano Lett.* **2012**, *12*, 2587–2594.
- (69) Tang, A.; Yi, L.; Han, W.; Teng, F.; Wang, Y.; Hou, Y.; Gao, M. *Appl. Phys. Lett.* **2010**, *97*, 033112.

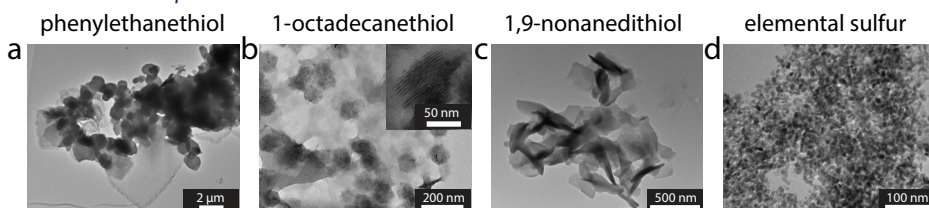
## Appendices

### A4.1 Composition of Cu-thiolate precursors and $Cu_{2-x}S$ nanosheets



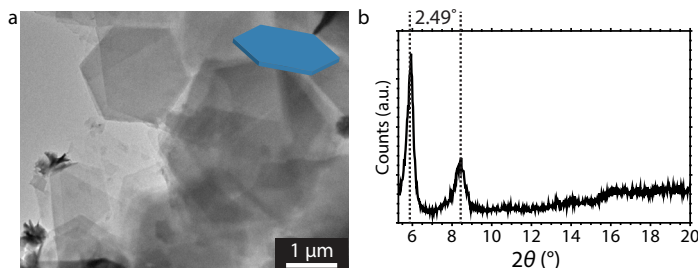
**Figure A4.1.** TEM images of (a) irregularly shaped thin material (EDS ratio Cu : S : Br =  $1.41 \pm 0.14 : 1.0 : 0.03 \pm 0.01$ ) and (b) well-defined hexagonal NSs (EDS ratio Cu : S : Br =  $2.0 \pm 0.2 : 1.0 : 0.30 \pm 0.06$ ) obtained when the concentration of  $SnBr_4$  in the reaction medium is halved.

### A4.2 Other sulfur sources

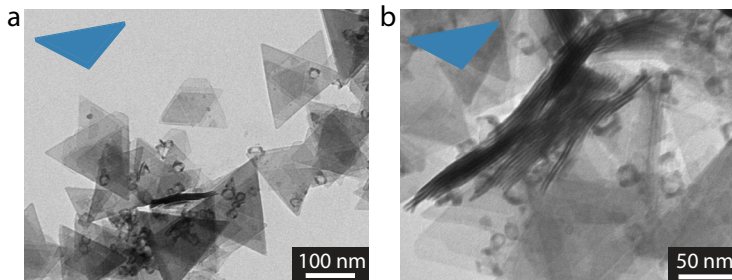


**Figure A4.2.** TEM images of the reaction products obtained using different sulfur sources. All other reaction parameters and chemicals are identical. (a) Phenylethanethiol (a bulky and short thiol) yields irregularly shaped and aggregated thin material. (b) 1-Octadecanethiol yields hexagonal NSs similar to those formed using 1-DDT, except for the inter-NS separation in the stacks (2 nm, see inset). The longer inter-NS separation is consistent with the increase in length of the alkyl chain from 1.77 nm to 2.5 nm from DDT to ODT. (c) 1,9-Nonanedithiol yields irregularly shaped thin material, often rolled up in nanoscrolls. (d) Elemental sulfur yields small and polydisperse nanocrystals.

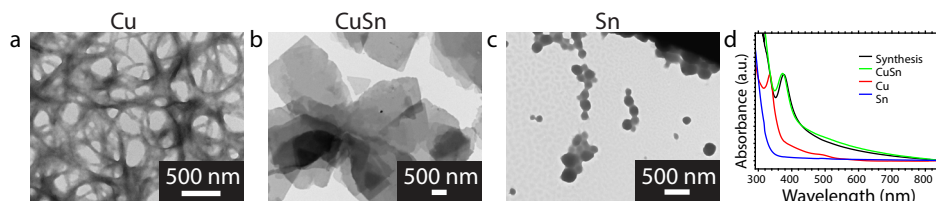
### A4.3 XRD of $3 \mu m$ $Cu_{2-x}S$ nanosheets



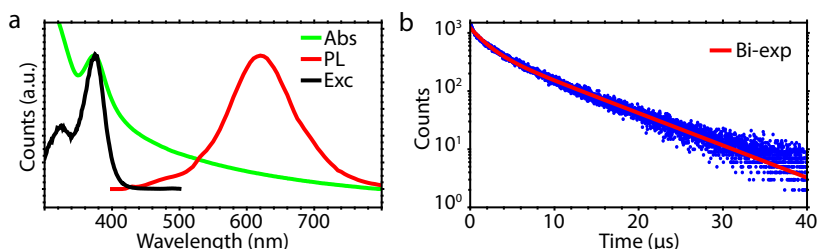
**Figure A4.3.** (a) Representative TEM image of large ( $\sim 3 \mu m$  wide) ultrathin hexagonal  $Cu_{2-x}S$  nanosheets and (b) low-angle X-ray diffraction (XRD) pattern of the same sample. The low-angle reflections are ascribed to successive diffraction orders from a periodic superstructure formed by nanosheet stacks. The separation between the peaks ( $2.49^\circ$ ) corresponds to a periodicity of  $36.7 \text{ \AA}$ , which is the same as that observed for the stacks of smaller ( $110 \text{ nm}$  wide) hexagonal  $Cu_{2-x}S$  nanosheets. This shows that the large triangular  $Cu_{2-x}S$  nanosheets are also 2 nm thick and are coated by DDT.

A4.4 *CuCl and NaCl as halide source*

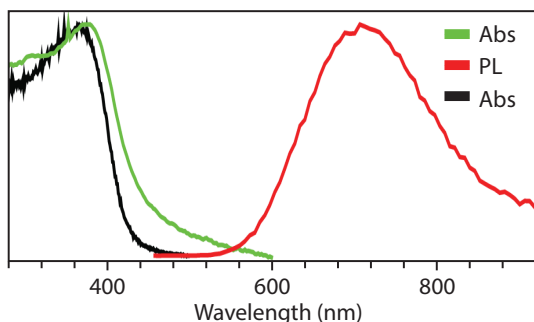
**Figure A4.4.** TEM images of  $\text{Cu}_{2-x}\text{S}$  NSs obtained using CuCl (instead of CuAc and NaCl (instead of  $\text{SnCl}_4$ )). Ultrathin triangular NSs are obtained, indicating that Cl induces NSs formation.

A4.5 *Morphology and optical properties of the metal-thiolate precursors*

**Figure A4.5.** TEM images of samples prepared by dissolving metal salts in a solution of 1-DDT in ODE, followed by heating to 190 °C. (a) Cu(I)acetate only; (b) mixed Cu(I)acetate and  $\text{SnBr}_4$ ; (c)  $\text{SnBr}_4$  only. The samples were taken directly from the reaction mixture and diluted in toluene. The presence of Br clearly affects the long-range morphology and topology of the Cu-thiolate precursor complex at room temperature, converting it from a 3D gel network (a) to irregularly shaped thin sheets (b).  $\text{SnBr}_4$  and DDT alone are not capable of forming polymeric frameworks (c). (d) Comparison between the absorption spectra of the three samples shown in (a–c) with that of a sample collected 1 min after DDT injection in a solution of Cu(I)acetate,  $\text{SnBr}_4$  and TOPO in ODE at 190 °C. It is clear that the absorption peak observed at 375 nm in samples collected during the synthesis of ultrathin  $\text{Cu}_{2-x}\text{S}$  NSs can be ascribed to a Br-modified Cu-thiolate precursor complex.

A4.6 *Optical properties of Br-modified Cu-thiolate precursor*

**Figure A4.6.** (a) Absorption (Abs), photoluminescence (PL), PL excitation (PLE) spectra and (b) PL decay curve of a sample collected 1 min after DDT injection in a solution of Cu(I)acetate,  $\text{SnBr}_4$  and TOPO in ODE at 190 °C. The red line in (b) is a bi-exponential fit to the decay curve. The PLE spectrum unambiguously shows that the PL band at 620 nm and the absorption peak at 375 nm originate from the same compound. The PL lifetime for the Br-modified Cu-thiolate precursor complex is long (7.8  $\mu\text{s}$ ) with a faster initial component of 1.8  $\mu\text{s}$ .

A4.7 Optical properties of Cu-doped CdS NSs obtained by  $\text{Cd}^{2+}$  for  $\text{Cu}^+$  cation exchange

**Figure A4.7.** Absorption, PL and PLE spectra of ultrathin colloidal CdS NSs obtained by  $\text{Cd}^{2+}$  for  $\text{Cu}^+$  exchange in  $\text{Cu}_{2-x}\text{S}$  NSs. The cation exchange was not complete, leaving a small concentration of  $\text{Cu}^+$  in the NSs (ratio Cd : S : Cu : Br =  $0.90 \pm 0.04$  :  $1.0$  :  $0.06 \pm 0.01$  :  $0.03 \pm 0.01$ ). The remaining Br is probably at the surface of the NSs. The absorption spectrum is in good agreement with that previously reported by Ithurria *et al.* for CdS NSs with a thickness of 5 monolayers.<sup>18</sup> This confirms the size and shape preservation of the cation exchange, since the parent  $\text{Cu}_{2-x}\text{S}$  NSs also consisted of 5 monolayers. Interestingly, the PL of the CdS NSs obtained in the present work is very efficient, but is strongly red shifted with respect to the band edge absorption. This emission can be ascribed to radiative recombination of the exciton in the  $\text{Cu}^+$  dopants. The good correspondence between the PLE spectrum and the absorption spectrum shows that the  $\text{Cu}^+$  dopants are populated by exciton transitions in the CdS NSs.





# *In-situ* Probing of Stack-Templated Growth of Ultrathin $\text{Cu}_{2-x}\text{S}$ Nanosheets



## ABSTRACT

Ultrathin 2D nanomaterials have attracted intense research efforts due to their extraordinary optoelectronic properties. However, the nucleation and growth mechanisms of 2D colloidal nanosheets are still poorly understood. In the previous chapter we showed that the formation of ultrathin 2D  $\text{Cu}_{2-x}\text{S}$  nanosheets can be tailored by halides. In this chapter, we study the formation of ultrathin 2D  $\text{Cu}_{2-x}\text{S}$  nanosheets *in-situ* with Small-Angle X-ray Scattering. While thermal decomposition of Cu-dodecanethiolates produces spheroidal  $\text{Cu}_{2-x}\text{S}$  nanocrystals, the addition of chloride to the reaction mixture results in 2 nm thick  $\text{Cu}_{2-x}\text{S}$  nanosheets with well-defined shape and size. We follow the precursor decomposition and product formation for both procedures, and show that chloride stabilizes stacks of lamellar Cu-thiolate supramolecular complexes, so that they remain intact beyond the onset of  $\text{Cu}_{2-x}\text{S}$  nucleation at 230 °C, leading to 2D-constrained stack-templated nucleation and growth. The face-to-face stacking of the nanosheets inhibits growth in the thickness direction and allows only for lateral growth. Our results provide valuable insights into the formation mechanism of ultrathin colloidal nanosheets, which may be exploited for other metal-sulfide compositions.

### Based on

#### ***In-situ* Probing of Stack-Templated Growth of Ultrathin $\text{Cu}_{2-x}\text{S}$ Nanosheets**

W. van der Stam, F. T. Rabouw, J. J. Geuchies, A. C. Berends, S. O. M. Hinterding, R. G. Geitenbeek, J. van der Lit, S. Prévost, A. V. Petukhov and C. de Mello Donega, *Chem. Mater.* **2016**, doi: 10.1021/acs.chemmater.6b02787

## 5.1 Introduction

The electronic properties of colloidal nanocrystals (NCs) depend not only on their chemical composition, but also on their size and shape.<sup>1</sup> By a proper choice of the reaction conditions and chemicals used in the synthesis, different sizes and shapes can be obtained, ranging from 0D quantum dots<sup>2</sup> to 1D nanorods<sup>3</sup> and 2D nanosheets.<sup>4</sup> Ultrathin 2D nanosheets (NSs) possess extraordinary properties that are attractive for both fundamental studies and technological devices.<sup>4-8</sup> To date, colloidal NSs of a variety of compositions have been prepared (*e.g.* CdX with X = S, Se, Te;<sup>9</sup> PbS;<sup>10,11</sup> SnX, with X = S, Se;<sup>12,13</sup> In<sub>2</sub>S<sub>3</sub>;<sup>14</sup> Cu<sub>2-x</sub>S;<sup>15</sup> Cu<sub>2-x</sub>Se;<sup>6</sup> WS<sub>2</sub><sup>16</sup>), but their formation mechanism remains poorly understood, possibly due to the scarcity of *in-situ* studies. *In-situ* Transmission Electron Microscopy (TEM), Powder X-ray Diffraction (PXRD) and Small-Angle X-ray Scattering (SAXS) have emerged as promising techniques to probe the nucleation and growth of nanomaterials. Liquid cell TEM is a direct-space imaging technique that can record the growth of individual (or a few) nanocrystals, and has for example been used to analyze the formation of Pt and Pt<sub>3</sub>Fe nanoparticles.<sup>17,18</sup> *In-situ* PXRD can provide a more statistical picture of nanocrystal growth by probing an entire ensemble. It is sensitive to the nucleation, transformation and growth of crystalline domains, and has been used to follow the growth of spherical Cu<sub>2-x</sub>S NCs<sup>19</sup> and TiO<sub>2</sub> nanoparticles.<sup>20</sup>

*In-situ* SAXS provides access to statistically-averaged structural information on superatomic scale such as the nanocrystal shape and their self-organization into larger structures.<sup>21</sup> High-temperature *in-situ* SAXS studies of NC nucleation and growth have until now, however, been limited to spherical NCs.<sup>22</sup> As will be shown below, SAXS is especially suitable for studying the size and (anisotropic) shape of nanomaterials,<sup>22</sup> and is therefore the technique of choice to elucidate the growth mechanism of ultrathin 2D nanosheets.

In this chapter, we follow the formation of both colloidal spheroidal Cu<sub>2-x</sub>S NCs and colloidal ultrathin 2D Cu<sub>2-x</sub>S NSs in real-time by performing *in-situ* Small-Angle X-ray Scattering (SAXS) experiments. Both syntheses are based on the thermal decomposition of Cu-thiolate complexes, but the addition of chloride ions results in ultrathin Cu<sub>2-x</sub>S NSs with well-defined shape (triangular) and size (thickness: 2 nm, lateral dimensions: ~110 nm, aspect ratio: 55), rather than quasi-spherical Cu<sub>2-x</sub>S NCs (as described in the previous chapter).<sup>15</sup> Our results show that Cu-thiolate complexes form lamellar stacks that are thermally stabilized by bonds with chloride ions in solution, so that they remain structurally intact up to the onset of Cu<sub>2-x</sub>S nucleation at 230 °C, leading to 2D templated nucleation and growth. The face-to-face stacking of the NSs inhibits growth in the thickness direction and allows only for lateral growth, resulting in large aspect ratios and constant thicknesses. Our model of growing NSs confined in stacks accurately reproduces the entire scattering pattern, including the

structure factor peak arising from stacking NSs in solution at large  $q$ -values, as well as the form factor contributions at small  $q$ -values (explained in more detail in section 5.2). Our work provides the first example of an *in-situ* X-ray scattering study of the synthesis of colloidal 2D nanomaterials (aspect ratio: 55) and unravels the formation mechanism that governs the formation of size- and shape-controlled colloidal 2D  $\text{Cu}_{2-x}\text{S}$  NSs. This knowledge may prove useful in the development of methods to synthesize NSs of a variety of metal sulfides, by exploiting the rich library of lamellar metal-thiolate complexes.

## 5.2 X-ray Scattering

### 5.2.1 Synchrotron radiation

There are different types of electromagnetic waves that are commonly used to study objects of various sizes. In order to study objects with very small dimensions, such as nanocrystals, high energy waves are necessary, *i.e.* X-rays (Figure 5.1a).<sup>23</sup> X-rays were first discovered by Röntgen in 1895 in his famous experiment where he imaged the bones of the hand of his wife (including wedding ring)<sup>24</sup> and ever since, X-rays have been extensively used in bioimaging applications. In order to also study molecules and atoms with X-rays, a synchrotron radiation source is necessary to produce X-rays with high energy (10 – 120 keV) and brilliance. A synchrotron radiation source typically

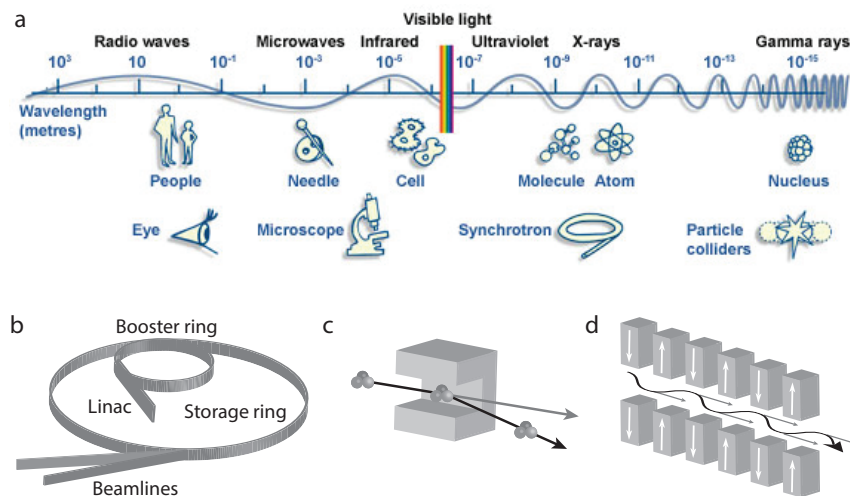


**Figure 5.1. Synchrotron radiation.** (a) The electromagnetic spectrum, indicating the wavelength of the various electromagnetic waves (top), what can be imaged with the corresponding waves (middle) and what instrument must be used to image these objects (bottom). (b) Schematic representation of a synchrotron. (c) Schematic representation of a bending magnet, which redirects the electron bunch (black arrow), resulting in an X-ray beam (grey arrow). (d) Schematic representation of an undulator/insertion device, in which the electron bunch (black arrow) wobbles due to alternating magnets. At each wobble, X-rays are produced (grey arrows), which interfere and produce a narrow X-ray beam with high brilliance. Panel a was reproduced from ref 23.

consists of four parts: the linear accelerator (Linac), the booster ring, the storage ring and the experimental beamlines (Figure 5.1b). The first part, the Linac, creates the high energy electrons necessary for the production of high-energy X-rays. These electrons are then injected into the booster ring, where the electrons are accelerated to an energy of 6 GeV before being injected into the larger storage ring. Inside the storage ring, several magnets are placed in order to let the electrons travel in circles. The magnets redirect the electrons, after which part of the energy of the electrons is lost as X-rays (Figure 5.1c,d). These X-rays are then collected and collimated into a narrow, intense X-ray beam, called the beamline.

There are three types of magnets inside the storage ring: focusing magnets, bending magnets and undulator/insertion devices.<sup>23</sup> The focusing magnets ensure that the electrons stay inside the desired path, whereas the bending magnets bend the electrons into the desired direction. When the electrons are deflected by the bending magnets, they emit X-rays (Figure 5.1c). The synchrotron light produced by a bending magnet is not very focused, due to the spread of X-ray energies produced.<sup>23</sup> An undulator, or insertion device, produces much more focused and brilliant X-rays (Figure 5.1d). An undulator is a complex array of small magnets, which results in an oscillation of the electrons (undulating). At each bend, radiation is emitted, which interferes with that from other bends, resulting in a very focused and brilliant beam. Besides, the gap between the rows of magnets can be changed to fine-tune the wavelength of the X-rays in the beam for the envisioned application in an X-ray scattering experiment.

### 5.2.2 Small-Angle X-ray Scattering

In a typical X-ray scattering experiment, a collimated X-ray hits the sample, which scatters the X-ray beam (Figure 5.2a). If the scatterer is aperiodic, the X-ray beam is scattered in all directions, whereas in the case of a periodic scatterer, the X-ray beam is scattered to very precise directions (azimuthal angles  $\varphi$ ). Bragg's law states that constructive interference of X-rays occurs when the following condition is met:<sup>25,26</sup>

$$n\lambda = 2d\sin\theta \quad (5.1)$$

in which the angle of scattering is defined as  $\theta$ , the distance of scattering planes (periodic arrangement of identical objects, *i.e.* atomic crystal planes) is given as  $d$  and  $\lambda$  denotes the wavelength of the X-ray. In reciprocal space, often called Fourier space or  $q$ -space, Bragg's law is rewritten as

$$q = 2\pi/d = (4\pi\sin\theta)/\lambda \quad (5.2)$$

From Bragg's law it follows that small objects scatter at large angles (or  $q$ -values) and large objects scatter at small angles (or  $q$ -values). A lot of information can be derived from a SAXS experiment. Typically, a SAXS pattern consists of three regions: the

Porod region, the Debye region and the Guinier region (Figure 5.2b).<sup>27,28</sup> The Porod region is located at the largest  $q$ -values, *i.e.* smallest objects in real space, and gives a first indication of the size and shape of the scatterers ( $q \sim 1/d$  for any particle size). The Debye region provides information about the size distribution within the ensemble of scatterers, as well as the shape of the scatterers, since the slope of the scattering pattern in this region is directly related to the shape of the objects (Figure 5.2b–d). For example, a slope of  $q^{-4}$  denotes spherical scatterers, but a slope of  $q^{-2}$  indicates platelike objects.<sup>27,28</sup> Before the Debye region lies the Guinier region, which is typically independent of  $q$ , meaning the curve is flat, which gives information about the total volume of scattering objects in the ensemble. Next to form factor contributions, SAXS patterns can also contain structure factor contributions, which arise from periodic arrangement of large objects, such as nanocrystals in a self-assembled superstructure or stacks of platelike objects (as will be discussed in more detail in section 5.4 below). The integrated intensity of a SAXS pattern consists of form factor and structure factor contributions, as given by:<sup>28</sup>

$$I(q) = F(q)S(q) \quad (5.3)$$

where  $I(q)$  denotes the scattering intensity as a function of scattering vector  $q$ ,  $F(q)$  is the cross-section form factor of the particle, which is the Fourier transform (FT) of

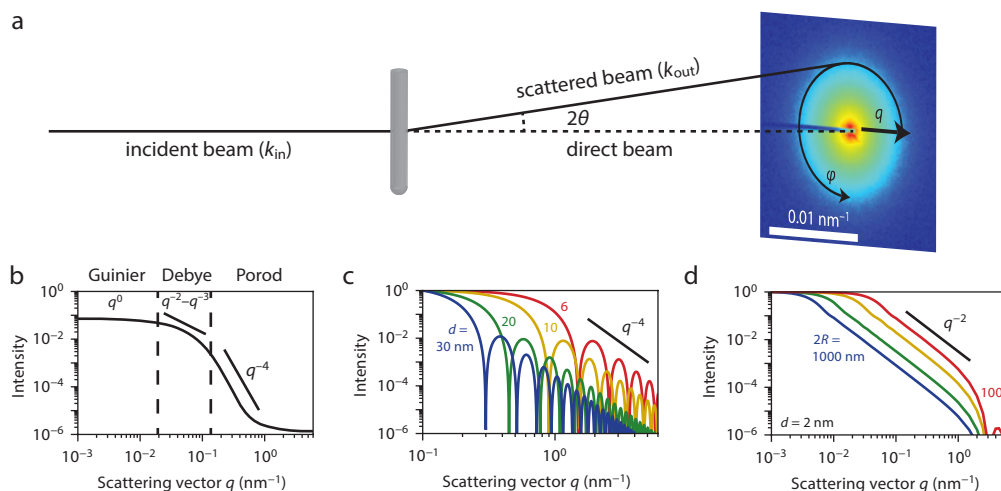


**Figure 5.2. SAXS experiments: Form factor and structure factor contributions.** (a) Schematic representation of a X-ray scattering experiment, where an incident beam is scattered at an angle of  $2\theta$ , which corresponds to a distance of  $q$  in reciprocal space. After integration over all azimuthal angles  $\varphi$ , 1D SAXS patterns are obtained. (b) Three regions are defined in a SAXS pattern: Guinier, Debye and Porod. All regions have a different dependency on  $q$  and provide information about size, shape and volume of the scattering objects.<sup>27</sup> (c) Form factor scattering for different sizes of spherical scatterers. (d) Form factor scattering for different sizes of platelike scatterers with a fixed thickness  $d = 2$  nm. Patterns in c and d were plotted according to the formulas for spherical and platelike objects in ref 28.

the nanostructure shape, and  $S(q)$  is the structure factor contribution, *i.e.* the FT of the nanostructure position with respect to each other. As can be seen in Figure 5.2c, the SAXS pattern of spheres contains multiple minima, so-called shape modulations. The position of the first minimum roughly represents the diameter of the nanostructure, and moves to smaller  $q$ -values when the scattering object becomes larger. For platelike scatterers, this local minimum is less defined (Figure 5.2d), but by fitting the entire SAXS pattern, the diameter of the scatterers is obtained. Growth of the scattering objects is directly evident from the SAXS pattern when looking at the transition from the plateau (Guinier region) to  $q^{-2}$  dependence (Debye region), which moves to smaller  $q$ -values in the case of larger scatterers. Therefore, careful analysis of the SAXS patterns is required in order to obtain all the information present.

### 5.3 Methods

**Materials.** Copper(I) acetate (CuAc, 97%), copper(I) chloride (CuCl, 97%), 1-dodecanethiol (DDT,  $\geq 98\%$ ), 1-octadecene (ODE, tech., 90%), trioctylphosphine oxide (TOPO, 99%), anhydrous toluene, methanol (MeOH) and butanol (BuOH) were purchased from Sigma Aldrich. All chemicals were used without any further purification.

**Spheroidal  $\text{Cu}_{2-x}\text{S}$  nanocrystals** were synthesized according to our previously reported method.<sup>15</sup> Typically, a stock solution was prepared, which contained 27.3 mg (0.22 mmol) CuAc, 0.55 g (1.42 mmol) TOPO and 0.5 mL (2.1 mmol) DDT, dispersed in 12.5 mL ODE. A small portion of this mixture was loaded in a 1 mm capillary and mounted in a Linkam heating stage. The capillary was rapidly heated to 230 °C with a heating rate of 80 °C/min. The reaction was maintained at this temperature for 30 min. The final  $\text{Cu}_{2-x}\text{S}$  NCs were removed from the capillary and precipitated by adding a methanol:butanol mixture, followed by centrifugation at 3000 rpm for 15 min. Afterwards, the NCs were redispersed in toluene.

**Ultrathin  $\text{Cu}_{2-x}\text{S}$  nanosheets** were synthesized in the same way as described above for spheroidal  $\text{Cu}_{2-x}\text{S}$  NCs, with the sole difference that CuAc was replaced by CuCl in the preparation of the stock solution.

**Small-Angle X-ray Scattering (SAXS)** experiments were performed at the ID02 beamline at ESRF, Grenoble, France. The SAXS detector was a Rayonix MX-170HS mounted on a rail inside a vacuum chamber, which allowed us to probe the entire  $q$ -range from  $10^{-3} \text{ nm}^{-1}$  to  $6 \text{ nm}^{-1}$ . The wavelength of the collimated X-ray beam was 0.1 nm (12.4 keV).

**Transmission Electron Microscopy (TEM)** images were acquired using a FEI Tecnai-10 microscope operating at 100 kV. Samples for TEM imaging were prepared by drop-casting a toluene solution of NCs onto a carbon-coated copper (400-mesh) TEM grid.

**Powder X-ray Diffraction measurements** were performed with a PW 1729 Philips diffractometer, equipped with a Cu  $K\alpha$  X-ray source ( $\lambda = 1.5418 \text{ \AA}$ ). Samples for XRD analysis were prepared by depositing a concentrated solution of purified NSs in chloroform on a Si(100) substrate.

## 5.4 Results & Discussion

### 5.4.1 Formation of $\text{Cu}_{2-x}\text{S}$ NCs followed by in-situ SAXS

$\text{Cu}_{2-x}\text{S}$  NCs were prepared by thermolysis of Cu-dodecanethiolate single-source precursors at 230 °C in octadecene in the presence of trioctylphosphine oxide (see Methods for details). The Cu-thiolate complex was formed *in-situ* by mixing a Cu(I) salt (acetate or chloride) and dodecanethiol (DDT). In a typical experiment, the reaction mixture was loaded in a 1 mm diameter quartz capillary and mounted in a Linkam heating stage. The mixture was then heated to 230 °C at a rate of 80 °C/min and kept at the final temperature for ~30 min, after which the NCs were isolated and analyzed *ex-situ* with TEM. The setup has a variable distance between sample and the SAXS detector located in a vacuum tube (Figure 5.3a). Each experiment was performed *in triplo*, at three different detector-to-sample distances (Figure 5.3a). In this way, scattering could be recorded over a range of scattering vectors  $q$  from  $10^{-3} \text{ nm}^{-1}$  to  $6 \text{ nm}^{-1}$  (Figure 5.3a). Such a large range is necessary to capture scattering from stacks of NSs or lamellar precursors separated by a few nm (large  $q$ ),<sup>15,29</sup> as well as form factor scattering due to the  $>100 \text{ nm}$  lateral dimensions of the NSs (small  $q$ ).<sup>22,28</sup> The scattering signal was collected on a 2D SAXS detector at three detector-to-sample distances (Figure 5.3b–d) and after azimuthal integration (Figure 5.3d), a 1D scattering curve is obtained that covers the entire  $q$ -space (Figure 5.4b,e).

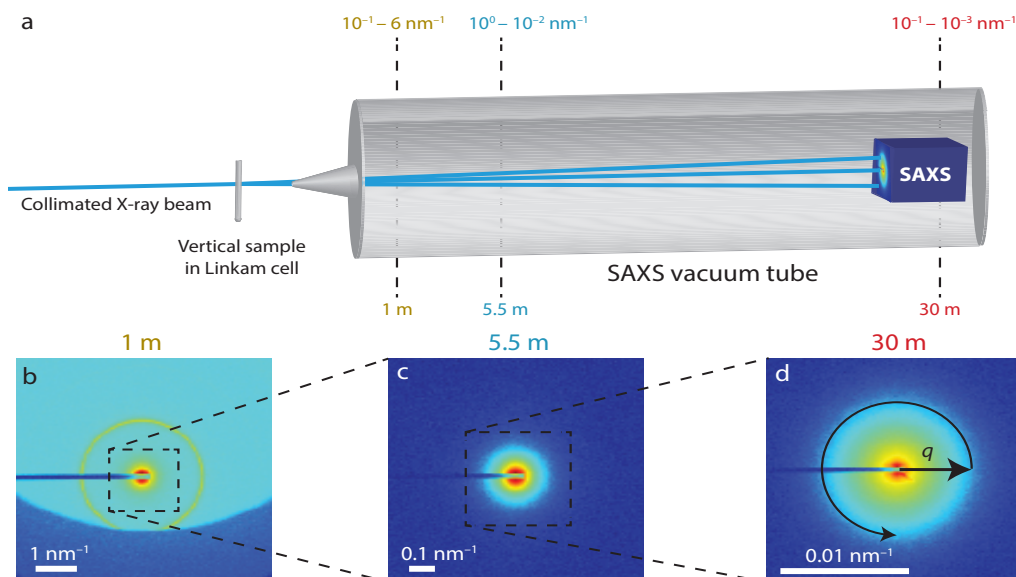


**Figure 5.3. In-situ SAXS experiments.** (a) Schematic representation of the experimental setup at beamline ID02, ESRF, Grenoble. The large SAXS vacuum tube allows for coverage of the entire  $q$ -space from  $10^{-3} \text{ nm}^{-1}$  up to  $6 \text{ nm}^{-1}$ . A collimated X-ray beam is scattered by the sample and results in a 2D scattering pattern at different detector-to-sample distances; (b) 1 m, (c) 5.5 m, (d) 30 m.

### 5.4.2 Nanocrystal morphology and the model to analyze the SAXS data

The final products formed in the capillaries were isolated and imaged with TEM (Figure 5.4a,d). The NC sizes and shapes obtained from the reaction in the capillaries (with only convective mixing and inhomogeneous heating, under air) closely match the morphologies obtained in larger scale reactions under optimized conditions (13 mL volumes, under stirring, homogenous heating, under N<sub>2</sub> atmosphere):<sup>15</sup> spheroidal NCs in the absence of chlorides (Figure 5.4a), and ultrathin (2 nm thick) triangular NSs in the presence of chlorides (Figure 5.4d). This indicates that the NC formation studied is robust to changes in reaction conditions and is therefore ideally suited for *in-situ* X-ray scattering measurements. Furthermore, the crystallinity of the *in-situ* formed Cu<sub>2-x</sub>S NSs is evident from X-ray scattering at wider angles (Appendix A5.1 and Chapter 4), which shows the same reflection as in *ex-situ* powder XRD experiments (*d*-spacing = 1.95 Å), corresponding to a tetragonal polymorph of the digenite (Cu<sub>1.8</sub>S) crystal structure, as studied in detail in the previous chapter.<sup>15</sup> Figure 5.4b,e shows the scattering patterns in the presence of chlorides (panel e) and in the absence of chlorides (panel b) 12 min after the temperature had reached 230 °C. The scattering patterns were obtained by combining the scattering of experiments at three sample-to-detector distances. The most prominent feature in the *in-situ* scattering patterns in the presence of chlorides is a structure factor peak at  $q = 1.45 \text{ nm}^{-1}$  (4.35 nm in real space) arising from stacked NSs in solution (Figure 5.4e). A structure factor peak is absent for the spheroidal NCs, but a plateau is observed with a first minimum at  $1 \text{ nm}^{-1}$  (Figure 5.4b). The patterns can be accurately fitted to simple models (solid lines in Figure 5.4b,e, Appendix A5.2 and A5.3, and Figure A5.2). The spheroidal NCs are modeled as polydisperse spheres with mean radius  $R$  (Figure 5.4c). The low- $q$  ( $< 2 \times 10^{-2} \text{ nm}^{-1}$ ) scattering is ascribed to clustering of the NCs (see Figure 5.4b and Appendix A5.3). The stacks of NSs are modeled as platelets with thickness  $h = 2 \text{ nm}$  (determined from TEM) and circular cross-section of polydisperse diameter  $D$ , with inter-NS stacking distance  $d$  and a distributed number  $N$  of platelets per stack with total length  $L$  (Figure 5.4f and Appendix A5.2 and Figure A5.2).

### 5.4.3 Formation of spheroidal colloidal Cu<sub>2-x</sub>S nanocrystals

Supramolecular species and metal-organic frameworks, such as the Cu-alkylthiolates used here, have emerged as single-source precursors for the growth of semiconductor NCs by thermolysis.<sup>30–33</sup> Cu-alkylthiolates are known to form a lamellar phase, which melts into a columnar mesophase at low temperatures (143.5 °C for Cu-DDT) and an isotropic liquid at higher temperatures (205.6 °C for Cu-DDT).<sup>28</sup> In SAXS experiments, these ordered superstructures should give rise to structure factor peaks at large  $q$ -values (between 1 and 2 nm<sup>-1</sup>), allowing their existence to be monitored over time. Indeed, our *in-situ* SAXS experiments show one set of structure factor peaks at regular intervals for the reaction in the absence of chlorides (Figure 5.5a). From the structure factor peak positions, the inter-lamellae separation is deduced ( $2\pi/q = 3.6 \text{ nm}$ ), consistent with the reported values for 1D stacks of Cu-DDT lamellar complexes.<sup>15,28</sup> At 150

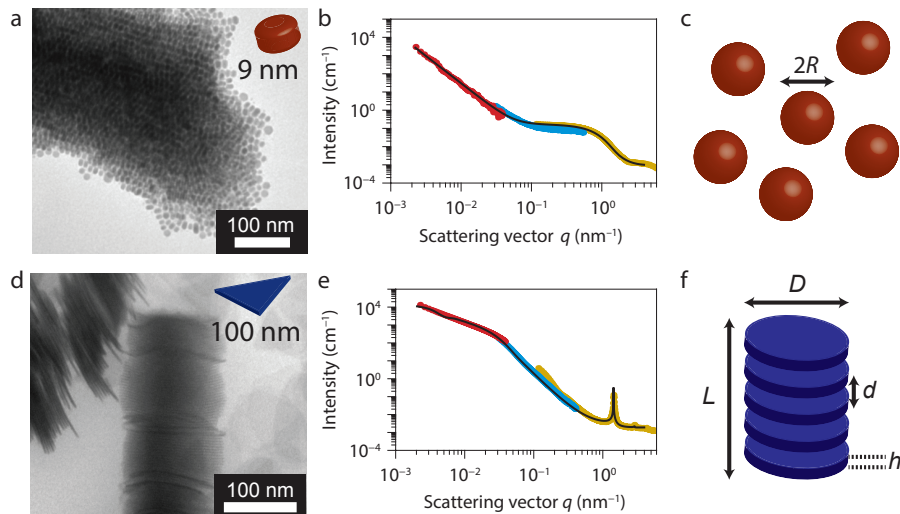


**Figure 5.4. Representative TEM image and SAXS pattern for spheroidal  $\text{Cu}_{2-x}\text{S}$  nanocrystals and ultrathin  $\text{Cu}_{2-x}\text{S}$  nanosheets.** (a) TEM image of spheroidal  $\text{Cu}_{2-x}\text{S}$  NCs obtained in a capillary when a reaction solution containing CuAc was heated to 230 °C for 30 min. (b) The *in-situ* SAXS pattern of the reaction mixture containing spheroidal NCs after 12 min at 230 °C, measured at three detector-to-sample distances (yellow: 1 m, blue: 5.5 m, red: 30 m). The black line shows the fit (see Appendix A5.2). (c) Schematic of the dimensions of the spheroidal NCs used in the model. (d) TEM image of ultrathin  $\text{Cu}_{2-x}\text{S}$  NSs obtained in a capillary when a solution of CuCl, TOPO, and DDT in ODE was heated to 230 °C for 30 min. (e) The *in-situ* SAXS pattern of the reaction mixture containing NSs after 12 min at 230 °C, measured at three detector-to-sample distances (yellow: 1 m, blue: 5.5 m, red: 30 m). The black line shows the fit (see Appendix A5.1). (f) Schematic of the dimensions of the NSs and the NS stacks used in the model (described in more detail in Figure A5.2).

°C, the structure factor peaks disappear, since the lamellar structure melts. We find no evidence for the presence of a liquid columnar mesophase. It is likely that the columnar mesophase is not stable when the Cu-DDT complex is diluted in a solvent, and instead an isotropic solution is formed. After nucleation ( $T = 230$  °C, evidenced by a color change from yellow to brown), a broad scattering signal is observed with minimum scattering intensity around  $3 \text{ nm}^{-1}$  (red line in Figure 5.5b). The minimum in scattering intensity moves toward smaller  $q$ -values over time, indicating growth of NCs. This is form factor scattering typical for nearly-spherical NCs,<sup>29,34,35</sup> consistent with the TEM observations in Figure 5.4. The scattering patterns were fitted to the form factor of polydisperse spheres, from which the growth in diameter of the NCs is obtained (Figure 5.5c and Appendix A5.3). We find that the mean diameter of the NCs increases from 1 nm to a final value of 8 nm over a duration of 17 min. After these 17 min of growth at 230 °C, sharp peaks appear in the SAXS pattern (Figure 5.5a,d), which can be ascribed to structure factor peaks of an ordered superstructure, formed by self-organization of the NCs. The peaks can be matched to a columnar structure of NCs (Figure 5.5e). The slightly oblate NCs are stacked face-to-face in columns (blue dotted lines in Figure 5.5d,

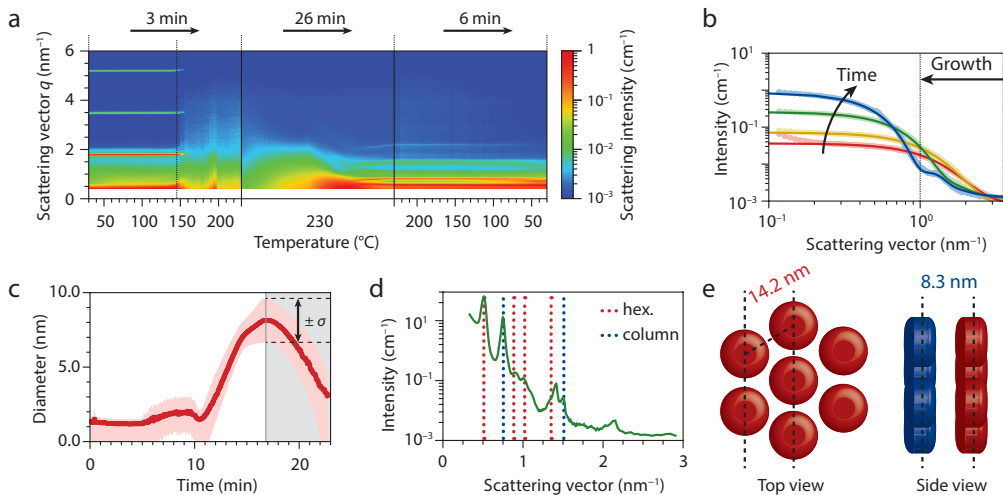


**Figure 5.5. Small-Angle X-ray Scattering (SAXS) during the formation of spheroidal  $\text{Cu}_{2-x}\text{S}$  nanocrystals.**

(a) SAXS structure factor peaks of lamellar Cu-thiolate precursors and form factor scattering of  $\text{Cu}_{2-x}\text{S}$  nanocrystals (NCs), followed over the course of the entire experiment. (b) Four representative SAXS patterns (data points) with their corresponding fits (solid lines), showing close agreement between the experiment and the model. (c) The NCs grow over time to a final size of  $\sim 8$  nm in diameter, in agreement with the *ex-situ* TEM measurements. The shaded area (after  $t = 17$  min) denotes the period in which the NCs form ordered 3D superstructures, which disrupts the fits to determine the NC diameter. (d) After 17 min of growth, the NCs form ordered 3D superstructures, consistent with *ex-situ* TEM in Figure 5.4a. The pattern matches with a columnar phase of NCs stacked in columns at a stacking distance of 8.3 nm (blue dotted lines), and the columns packed hexagonally with inter-column separation of 14.2 nm (red dotted lines). (e) Schematic of the top and side view of the columnar superstructure, indicating the separation between the NCs (14.2 nm) within the plane, as well as between the columns (8.3 nm).

stacking distance 8.3 nm), with the columns in hexagonal order<sup>36,37</sup> (red dotted lines in Figure 5.5d, inter-NC separation 14.2 nm). The 3D ordered superstructure of oblate NCs remains intact when the reaction mixture is cooled down to room temperature (RT). Indeed, ordered superstructures of NCs are observed with *ex-situ* TEM after the reaction had reached completion (see Figure 5.4a).

#### 5.4.4 Formation of ultrathin colloidal $\text{Cu}_{2-x}\text{S}$ nanosheets: the effect of chloride

We now discuss the precursor decomposition, and the nucleation and growth of the reaction products in the presence of chlorides, which results in ultrathin colloidal  $\text{Cu}_{2-x}\text{S}$  NSs. Figure 5.6a shows the time evolution of the scattering at high  $q$ -values ( $0.5 - 6 \text{ nm}^{-1}$ ) over the course of the entire experiment. As above, scattering peaks from stacks of lamellar precursor complexes are observed below  $150^\circ\text{C}$ . However, when chlorides are present, there are three sets of peaks originating from lamellar stacks with different inter-lamellae separations (Figure 5.6b). Clearly, the presence of chloride alters the structure of the precursor, such that three different phases appear. Two of

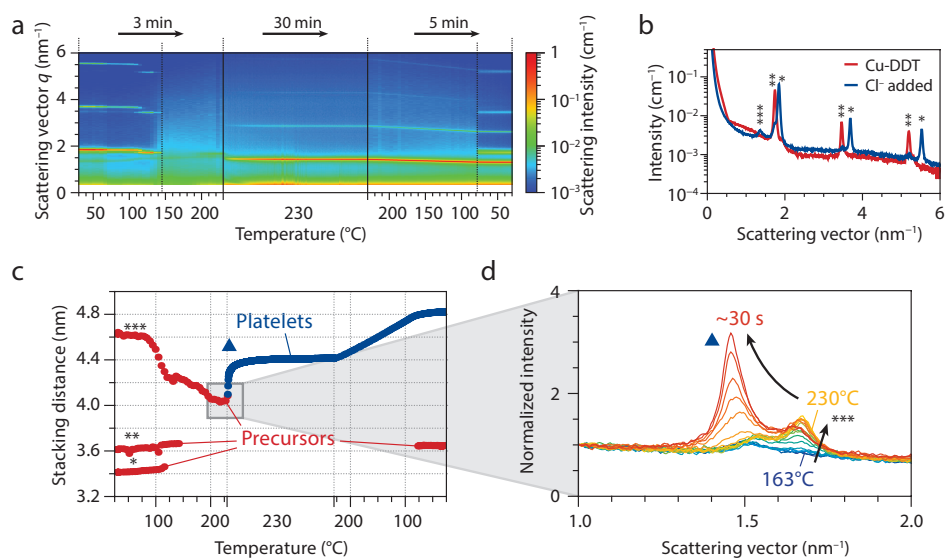


**Figure 5.6. Small-Angle X-ray Scattering (SAXS) of Cu-thiolate lamellar precursors in the presence of chloride.** (a) SAXS structure factor peaks of lamellar Cu-thiolate precursors, Cu<sub>2-x</sub>S NS stacks, and form factor scattering of Cu<sub>2-x</sub>S NSs followed over the course of the entire experiment. (b) Snapshots of the SAXS patterns at the start of the experiments, showing structure factor peaks associated with lamellar Cu-thiolate precursors in the presence of chlorides (blue line) and in the absence of chlorides (red line). The asterisks denote the structure factor peaks and their corresponding overtones. (c) From the position of the stacking peaks in the range  $q = 1 - 2 \text{ nm}^{-1}$  we deduce the time-evolution of the stacking distance of precursor complexes (red, denoted with asterisks for different species) and NSs (blue, denoted with a triangle). It can be seen that directly after the nucleation threshold is reached ( $\sim 230 \text{ }^\circ\text{C}$ ), NS stacks are already present in the reaction medium (blue line). (d) A zoom of the precursor evolution around the nucleation threshold shows a direct transition from the low-intensity precursor peak ( $q = 1.65 \text{ nm}^{-1}$ , three asterisks) toward the structure factor peak associated with stacking NSs ( $q = 1.45 \text{ nm}^{-1}$ , blue triangle). The structure factor peak eventually grows in intensity and becomes the only peak present within the first 30 s after nucleation.

those phases melt at  $150 \text{ }^\circ\text{C}$ , but chloride stabilizes one phase beyond the onset of Cu<sub>2-x</sub>S nucleation ( $230 \text{ }^\circ\text{C}$ , Figure 5.6c). The red data points in Figure 5.6c denote the stacking distance of the lamellar precursors as a function of temperature in the presence of chloride. At the nucleation threshold temperature of  $230 \text{ }^\circ\text{C}$  (evidenced by the color change of the solution inside the capillary from yellow to brown), the remaining stacked precursor phase directly evolves into Cu<sub>2-x</sub>S NS stacks (blue line in Figure 5.6c and sharp peak at  $q = 1.45 \text{ nm}^{-1}$  in Figure 5.6d). Prior to nucleation, the stabilized precursor phase shrinks from a stacking distance of  $4.6 \text{ nm}$  at  $100 \text{ }^\circ\text{C}$  to  $4.0 \text{ nm}$  at  $230 \text{ }^\circ\text{C}$  (Figure 5.6c). This shrinking may be due to reorganization of the thiolate chains, but may also indicate the onset of the thermolysis of the C-S bonds and the formation of the Cu-S bonds, which would be accompanied by loss of the alkyl chains. The structure factor peak arising from stacking NSs in solution (at  $q = 1.45 \text{ nm}^{-1}$ ) then increases rapidly in

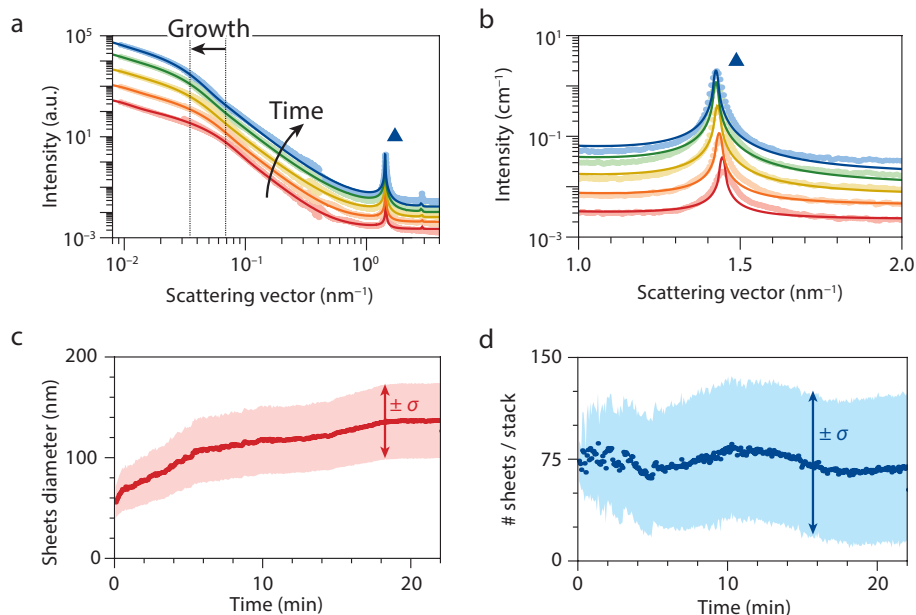


**Figure 5.7. Small-Angle X-ray Scattering (SAXS) during the formation of ultrathin  $\text{Cu}_{2-x}\text{S}$  nanosheets.** (a) Five representative SAXS patterns (data points) with their corresponding fits (solid lines), showing close agreement between the experiment and the model. The nanosheets grow over time, as indicated by the shift of the transition from  $q^{-1}$  dependence to  $q^{-3}$  dependence in the SAXS patterns. (b) Zoom of the structure factor peak associated with stacks of NSs, showing a small shift to smaller  $q$ -values, *i.e.* larger inter-NS separation, over the first 30 s. (c) The SAXS patterns were fitted with our model (see Appendices), from which we deduce the diameter of the NSs and find final lateral dimensions of  $\sim 130$  nm ( $\sigma = 40$  nm), consistent with the TEM data. (d) From the fits of the structure factor peak at  $q = 1.45$   $\text{nm}^{-1}$ , the number of NSs in a stack is obtained, which remains constant over the course of the entire experiment, at a value of 75 NSs per stack.

intensity, until, 30 s after nucleation, it becomes the only species present (Figure 5.6d). After the growth time of 30 min, the capillaries were allowed to cool to RT, which leads to reappearance of the structure factor peak at  $q = 1.75$   $\text{nm}^{-1}$ , indicating that one phase of stacked Cu-thiolate complexes reforms upon cooling, *i.e.* the overall reaction is not stoichiometric.

From these high- $q$  measurements we conclude that the  $\text{Cu}_{2-x}\text{S}$  NSs are already stacked when they nucleate at 230 °C, implying that they form directly from the stacks of chloride-stabilized Cu-thiolate lamellae. In other words, the precursor stacks act as templates, being directly converted into stacked  $\text{Cu}_{2-x}\text{S}$  NSs upon thermolysis followed by 2D constrained nucleation and growth. Afterward, the thickness of the NSs remains constant as evidenced by the fixed position of the NS stacking peak at  $q = 1.45$   $\text{nm}^{-1}$ . We follow the lateral growth of the NSs by fitting the full scattering patterns with the

model introduced above (Figure 5.4 and Appendix A5.2 and A5.3). Figure 5.7a shows five representative SAXS patterns (data points) and their corresponding fits (solid lines). Figure 5.7b is a zoom of the structure factor peak associated with the 1D order of the NS stacks. From the model, the evolution of the diameter  $D$  of the NSs is determined, showing an increase in average diameter from 60 nm ( $\sigma = 15$  nm) to 130 nm ( $\sigma = 40$  nm, Figure 5.7c), in close agreement with the TEM measurement in Figure 5.4d (diameter 110 nm). The lateral growth is also visible from the SAXS patterns in Figure 5.7a, where a shift of the transition from  $q^{-1}$  ( $10^{-2} - 4 \times 10^{-2}$  nm<sup>-1</sup>) to  $q^{-3}$  ( $7 \times 10^{-2} - 7 \times 10^{-1}$  nm<sup>-1</sup>) dependency is observed. Meanwhile, the number of NSs per stack remains constant at on average 75 NSs/stack during the entire growth period (Figure 5.7d). Clearly, the NSs are formed directly from the precursor stacks, and remain stacked while growing. This stacking is likely the reason for the strongly anisotropic growth, resulting in high aspect ratio NSs (AR = 55), by allowing growth solely in the lateral direction.

#### 5.4.5 Mechanism for the formation of ultrathin colloidal Cu<sub>2-x</sub>S NSs

The results discussed above show that chlorides increase the thermal stability of lamellar stacks of Cu-DDT complexes, so that the structural integrity of the superstructures is preserved beyond the onset of the Cu-catalyzed thermolysis of the C-S bonds (Figure 5.8a), confirming the model proposed in Chapter 4. This leads to two-dimensionally constrained nucleation and growth of Cu<sub>2-x</sub>S, resulting in ultrathin Cu<sub>2-x</sub>S NSs. Growth by [Cu-S] monomer addition occurs solely in the lateral direction, since the face-to-face stacking of the chloride-stabilized precursor lamellae inhibits growth in the thickness direction. As a result, the thickness of the NSs remains constant throughout the growth process, while the lateral dimensions increase. In the absence of chlorides, the lamellar stacks of Cu-DDT complexes disassemble at temperatures below the onset of the C-S thermolysis, forming an isotropic liquid, which results in free [Cu-S] monomers and Cu<sub>2-x</sub>S nucleation in solution (Figure 5.8b). Growth then results in the formation of spheroidal NCs, which eventually self-organize in 3D superstructures. Typically, the limited growth in thickness for colloidal 2D NSs is ascribed to surface ligands and soft-templating effects.<sup>10,38,39</sup> Our work provides the first evidence for NS stacking as a thickness-determining mechanism, leading to the formation of ultrathin NSs with well-defined thickness. Furthermore, we show the first example of *in-situ* X-ray scattering experiments to follow the growth of anisotropic colloidal nanocrystals in real-time, which provides valuable insights in the formation of 2D colloidal nanomaterials from Cu-thiolate precursors. Our approach of adding stabilizing species to lamellar metal-sulfide complexes may be further exploited to produce NSs of various metal sulfide compositions, by taking advantage of the rich library of lamellar M-thiolate complexes that is currently available (with M = Fe, Ni, Cu, Co, Cd, Zn, Pd, Pt, Ag, Au, Pb and Bi).<sup>40-45</sup> Moreover, as demonstrated in the previous chapter, different halides lead to different NS shapes, and the NS composition can be post-synthetically tailored by using topotactic cation exchange reactions. The insights provided here may thus prove beneficial in the development of synthetic

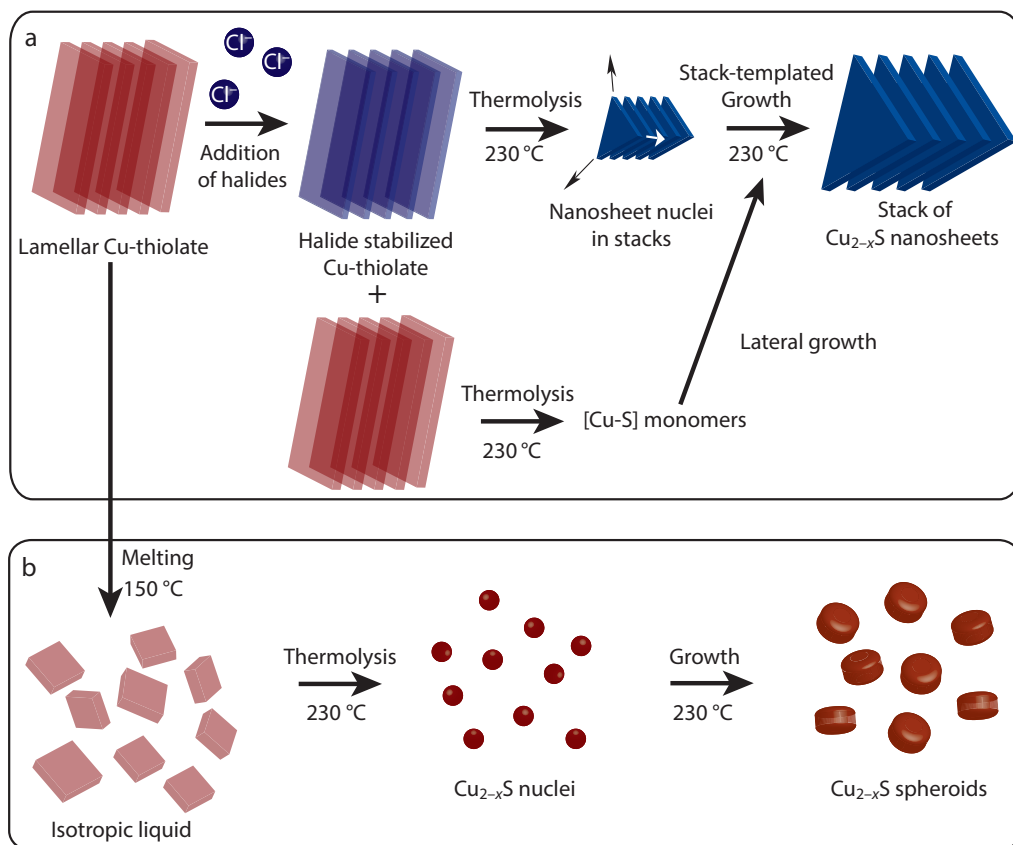


**Figure 5.8. Schematic representation of the formation mechanism of  $\text{Cu}_{2-x}\text{S}$  NCs under different conditions.** (a) Formation of ultrathin  $\text{Cu}_{2-x}\text{S}$  NSs: stacks of lamellar Cu-thiolate precursors, in the presence of coordinating chloride ions, are stabilized to temperatures above the nucleation threshold. After thermolysis of the C-S bonds, this results in 2D-constrained stack-templated nucleation and growth of  $\text{Cu}_{2-x}\text{S}$  NSs, which remain stacked while growing. (b) Formation of spheroidal  $\text{Cu}_{2-x}\text{S}$  NCs: in the absence of halides, the lamellar Cu-thiolate complexes melt and form an isotropic liquid, which after C-S thermolysis produces free Cu-S monomers in solution, eventually resulting in nucleation and growth of spheroidal  $\text{Cu}_{2-x}\text{S}$  NCs.

routes to a myriad of solution processable ultrathin colloidal NSs with well-defined composition, size and shape.

## 5.5 Conclusions

In conclusion, our *in-situ* SAXS study reveals the stack-templated formation mechanism of the complex multiscale nucleation and growth of 2D colloidal  $\text{Cu}_{2-x}\text{S}$

NSs. We show that chloride forms direct bonds with lamellar Cu-thiolate complexes, which ensures that their structural integrity remains intact beyond the onset of Cu<sub>2-x</sub>S nucleation. We effectively followed the lamellar Cu-thiolate precursor transformations and the size and shape evolution of 2D colloidal Cu<sub>2-x</sub>S NSs using *in-situ* SAXS at three detector-to-sample distances. Our results show that lamellar stacks of Cu-thiolate precursor complexes melt into an isotropic liquid around 150 °C in the absence of chloride, but persist until above the nucleation threshold (230 °C) in the presence of chlorides. In this way, the Cu-catalyzed thermolysis of the C-S bond results in 2D-constrained stack-templated nucleation and growth of Cu<sub>2-x</sub>S NSs. The stacking of the NSs precludes growth in the thickness direction, thereby effectively limiting the thickness to 2 nm. Furthermore, we find that the lateral growth of colloidal 2D Cu<sub>2-x</sub>S nanosheets is mainly limited by the slow precursor to monomer conversion. Our work provides important insights in the formation of 2-dimensional nanomaterials from lamellar Cu-thiolate complexes, and may prove beneficial for the design of synthetic strategies for other 2D metal sulfide nanosheets by deploying metal-thiolates lamellar complexes as precursors.

## Acknowledgments

Beamline ID02, ESRF, Grenoble, France, is acknowledged for the granted beamtime under proposal number CH-4389. The authors would like to thank Giuseppe Portale and Daniel Hermida Merino from the DUBBLE beamline at ESRF, Grenoble, France, for their technical assistance with exploratory measurements, which were supported by NWO under grant number 195.068.854.

## References

- (1) de Mello Donegá, C. *Chem. Soc. Rev.* **2011**, *40*, 1512–1546.
- (2) Murray, C. B.; Norris, D.; Bawendi, M. G. *J. Am. Chem. Soc.* **1993**, *115*, 8706–8715.
- (3) Carbone, L.; Nobile, C.; De Giorgi, M.; Della Sala, F.; Morello, G.; Pompa, P.; Hytch, M.; Snoeck, E.; Fiore, A.; Franchini, I. R.; *et al.* *Nano Lett.* **2007**, *7*, 2942–2950.
- (4) Ithurria, S.; Tessier, M.; Mahler, B.; Lobo, R. P. S. M.; Dubertret, B.; Efron, Al. L. *Nat. Mater.* **2011**, *10*, 936–941.
- (5) Lhuillier, E.; Pedetti, S.; Ithurria, S.; Nadal, B.; Heuclin, H.; Dubertret, B. *Acc. Chem. Res.* **2015**, *48*, 22–30.
- (6) Chhowalla, M.; Shin, H. S.; Eda, G.; Li, L.-J.; Loh, K. P.; Zhang, H. *Nat. Chem.* **2013**, *5*, 263–75.
- (7) Wu, X.-J.; Huang, X.; Liu, J.; Li, H.; Yang, J.; Li, B.; Huang, W.; Zhang, H. *Angew. Chem. Int. Ed.* **2014**, *53*, 5083–5087.
- (8) Zhang, H. *ACS Nano* **2015**, *9*, 9451–9469.
- (9) Bouet, C.; Tessier, M. D.; Ithurria, S.; Mahler, B.; Nadal, B.; Dubertret, B. *Chem. Mater.* **2013**, *25*, 1262–1271.
- (10) Schliehe, C.; Juarez, B. H.; Pelletier, M.; Jander, S.; Greshnykh, D.; Nagel, M.; Meyer, A.; Foerster, S.; Kornowski, A.; Klinke, C.; Weller, H. *Science* **2010**, *329*, 550–553.
- (11) Bhandari, G. B.; Subedi, K.; He, Y.; Jiang, Z.; Leopold, M.; Reilly, N.; Lu, H. P.; Zayak, A. T.; Sun, L. *Chem. Mater.* **2014**, *26*, 5433–5436.
- (12) Liu, X.; Li, Y.; Zhou, B.; Wang, X.; Cartwright, A. N.; Swihart, M. T.; *Chem. Mater.* **2014**, *26*, 3515–3521.
- (13) Vaughn, D.; In, S.; Schaak, R. *ACS Nano* **2011**, *5*, 8852–8860.
- (14) Park, K. H.; Jang, K.; Son, S. U. *Angew. Chem. Int. Ed.* **2006**, *45*, 4608–4612.

- (15) van der Stam, W.; Akkerman, Q. A.; Ke, X.; van Huis, M. A.; Bals, S.; de Mello Donega, C. *Chem. Mater.* **2015**, *27*, 283–291.
- (16) Mahler, B.; Hoepfner, V.; Liao, K.; Ozin, G. *J. Am. Chem. Soc.* **2014**, *136*, 14121–14127.
- (17) Liao, H.-G.; Zherebetsky, D.; Xin, H.; Czarnik, C.; Ercius, P.; Elmlund, H.; Pan, M.; Wang, L.-W.; Zheng, H. *Science* **2014**, *345*, 916–919.
- (18) Liao, H.-G.; Cui, L.; Whitelam, S.; Zheng, H. *Science* **2012**, *336*, 1011–1014.
- (19) Nørby, P.; Johnsen, S.; Iversen, B. B. *ACS Nano* **2014**, *8*, 4295–4303.
- (20) Søndergaard, M.; Dalgaard, K. J.; Bøjesen, E. D.; Wonsyld, K.; Dahl, S.; Iversen, B. B. *J. Mater. Chem. A* **2015**, *3*, 18667–18674.
- (21) Gordon, T. R.; Diroll, B. T.; Paik, T.; Doan-Nguyen, V. V. T.; Gaulding, E. A.; Murray, C. B. *Chem. Mater.* **2015**, *27*, 2502–2506.
- (22) Abécassis, B.; Bouet, C.; Garnero, C.; Constantin, D.; Lequeux, N.; Ithurria, S.; Dubertret, B.; Pauw, B. R.; Pontoni, D. *Nano Lett.* **2015**, *15*, 2620–2626.
- (23) <http://www.esrf.eu/about/synchrotron-science/synchrotron-light>
- (24) Röntgen, W. K. *Science* **1896**, *3*, 227–231.
- (25) Bragg, W. H. *Proc. Soc. London A* **1913**, *89*, 246–248.
- (26) Laue, M.; Friedrich, P.; Knipping, W. *Sitz.ber. Bayer. Akademie d. Wiss.* **1912**, *8*, 303–322.
- (27) Pauw, B. R. *J. Phys. Condens. Matter* **2013**, *25*, 383201.
- (28) Renaud, G.; Lazzari, R.; Leroy, F. *Surf. Sci. Rep.* **2009**, *64*, 255–380.
- (29) Espinet, P.; Lequerica, M. C.; Martín-Alvarez, J. M. *Chem. Eur. J.* **1999**, *5*, 1982–1986.
- (30) Larsen, T. H.; Sigman, M.; Ghezelbash, A.; Doty, R. C.; Korgel, B. A. *J. Am. Chem. Soc.* **2003**, *125*, 5638–5639.
- (31) Chen, L.; Chen, Y.-B.; Wu, L.-M. *J. Am. Chem. Soc.* **2004**, *126*, 16334–16335.
- (32) Sigman, M.; Ghezelbash, A. *J. Am. Chem. Soc.* **2003**, *125*, 16050–16057.
- (33) Wang, Y.; Hu, Y.; Zhang, Q.; Ge, J.; Lu, Z.; Hou, Y.; Yin, Y. *Inorg. Chem.* **2010**, *49*, 6601–6608.
- (34) Murray, C.; Kagan, C.; Bawendi, M. *Science* **1995**, *270*, 1335–1338.
- (35) Guinier, A.; Fournet, G. Small angle scattering of X-rays. *J. Polym. Sci.* **1956**, *19*, 594.
- (36) Pietra, F.; Rabouw, F. T.; Evers, W. H.; Byelov, D. V.; Petukhov, A. V.; de Mello Donegá, C.; Vanmaekelbergh, D. *Nano Lett.* **2012**, *12*, 5515–5523.
- (37) Heitsch, A. T.; Patel, R. N.; Goodfellow, B. W.; Smilgies, D.-M.; Korgel, B. A. *J. Phys. Chem. C* **2010**, *114*, 14427–14432.
- (38) Wang, Z.; Schliehe, C.; Wang, T.; Nagaoka, Y.; Cao, Y. C.; Bassett, W. A.; Wu, H.; Fan, H.; Weller, H. *J. Am. Chem. Soc.* **2011**, *133*, 14484–14487.
- (39) Wang, F.; Wang, Y.; Liu, Y.-H.; Morrison, P. J.; Loomis, R. A.; Buhro, W. E. *Acc. Chem. Res.* **2015**, *48*, 13–21.
- (40) Zhuang, Z.; Lu, X.; Peng, Q.; Li, Y. *Chemistry* **2011**, *17*, 10445–10452.
- (41) Busupalli, B.; Kummara, S.; Kumaraswamy, G.; Prasad, B. L. V. *Chem. Mater.* **2014**, *26*, 3436–3442.
- (21) Xu, C.; Zeng, Y.; Rui, X.; Xiao, N.; Zhu, J.; Zhang, W.; Chen, J.; Liu, W.; Tan, H.; Hng, H. H.; Yan, Q. *ACS Nano* **2012**, *6*, 4713–4721.
- (43) Wu, W.-Y.; Chakraborty, S.; Chang, C. K. L.; Guchhait, A.; Lin, M.; Chan, Y. *Chem. Mater.* **2014**, *26*, 6120–6126.
- (44) Wang, Y.; Tang, A.; Li, K.; Yang, C.; Wang, M.; Ye, H.; Hou, Y.; Teng, F. *Langmuir* **2012**, *28*, 16436–16443.
- (45) Chen, J.; Wu, L. M.; Chen, L. *Inorg. Chem.* **2007**, *46*, 586–591.
- (46) Lindner, P.; Zemb, Th. *Neutrons, X-rays and Light: Scattering Methods Applied to Soft Condensed Matter*; Elsevier: North-Holland, **2002**, p. 407.
- (47) Teixeira, J. *J. Appl. Cryst.* **1988**, *21*, 781–785.

## Appendices

### A5.1 Crystallinity of *ex-situ* and *in-situ* formed $\text{Cu}_{2-x}\text{S}$ NSs: PXRD and WAXS

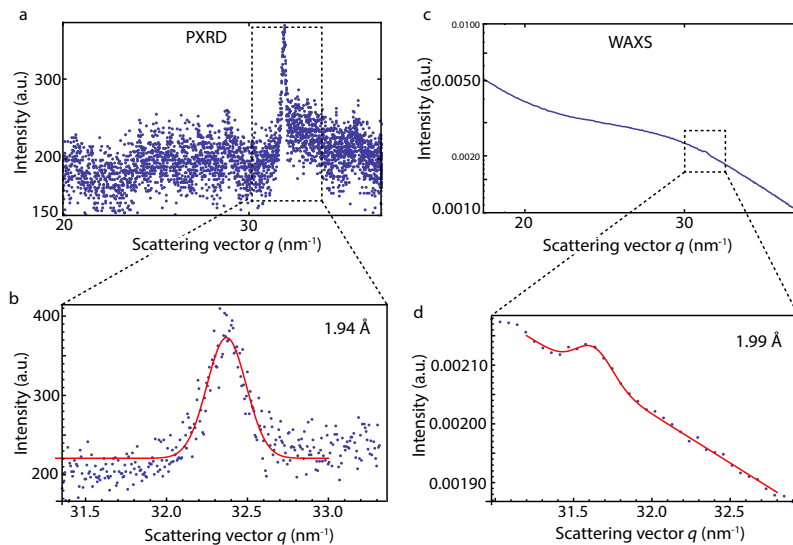


**Figure A5.1.** (a) PXRD pattern of  $\text{Cu}_{2-x}\text{S}$  nanosheets synthesized in the lab and (b) a zoom of the dominant reflection and its corresponding fit (red line). (c) *In-situ* WAXS pattern of  $\text{Cu}_{2-x}\text{S}$  nanosheets synthesized in a capillary and (d) a zoom of the reflection and its corresponding fit (red line).

## A5.2 SAXS model for the nanosheet stacks

The rotationally averaged scattering pattern of a dispersion of anisotropic particles, like stacks of nanosheets, can be approximated as:<sup>46</sup>

$$I(q) = \phi \Delta\rho^2 P(q) F(q) \quad (1)$$

where  $I(q)$  denotes the scattering intensity as a function of scattering vector  $q$ ,  $\phi$  is the volume fraction of sheets in the solution, and  $\Delta\rho$  is the scattering contrast of the particles with the surrounding solvent.  $P(q)$  is the cross-section form factor of the particle, and  $F(q)$  is the shape factor for the stacking direction.

Here, for the sake of simplicity, we model the nanosheets as disks with a circular cross section of radius  $R$ , so that:<sup>28</sup>

$$P(q) = A^2 \left[ \frac{2J_1(qR)}{qR} \right]^2 \quad (2)$$

where  $A$  is the cross-sectional area of the nanosheets, and  $J_1(x)$  is the first-order Bessel function. In the model we assume that there is polydispersity in the nanosheet radius such that the contribution of a particular radius to the scattering intensity is Gaussian distributed with maximum at the intensity-weighted average radius  $\langle R \rangle$ :

$$\langle P(q) \rangle_R = \frac{\langle A^2 \rangle}{\sqrt{2\pi} \sigma_R} \int_0^\infty e^{-\frac{1}{2} \left( \frac{R-\langle R \rangle}{\sigma_R} \right)^2} \left[ \frac{2J_1(qR)}{qR} \right]^2 dR \quad (3)$$

where  $\langle A^2 \rangle$  is the average cross-sectional area, and  $\sigma_R$  the standard deviation in radius.

The shape factor  $F(q)$  is the Fourier transform of the electron density profile  $n(z)$  in the stacking direction. The electron density profile of a stack of  $N$  sheets of thickness  $D$  at a center-to-center separation of  $d$  is the convolution of the shape factor of an individual sheet

$$f(z) = \begin{cases} 1 & ; |z| < D/2 \\ 0 & ; \text{otherwise} \end{cases} \quad (4)$$

with a finite series of  $N$  delta-peaks at regular intervals

$$g(z) = \sum_{j=1}^N \delta(z - jd) \quad (5)$$

The shape factor therefore becomes

$$F(q) = \tilde{f}(q) \tilde{g}(q) = \frac{\sin(qD/2)}{qD/2} \frac{\sin(qNd/2)}{\sin(qd/2)} \quad (6)$$

where  $\tilde{f}(q)$  and  $\tilde{g}(q)$  are the Fourier transforms of  $f(z)$  and  $g(z)$ , respectively.

In the fits we fix the nanosheet width  $D$  to a value of 2.0 nm, as determined from *ex-situ* TEM. The stacking distance  $d$  is determined from fitting the peak position  $q_1$  of the scattering peak (around  $1.4 \text{ nm}^{-1}$ ). Subsequently, the value of  $d$  is fixed at  $2\pi/q_1$ . We assume a Gaussian polydispersity in  $N$ , the number of

sheets per stack, with mean  $\langle N \rangle$  and standard deviation  $\sigma_N$ :

$$\langle F(q) \rangle_N = \frac{1}{\sqrt{2\pi} \sigma_N} \int_0^\infty e^{-\frac{1}{2} \left( \frac{N - \langle N \rangle}{\sigma_N} \right)^2} \frac{\sin(qD/2)}{qD/2} \frac{\sin(qNd/2)}{\sin(qd/2)} d. \quad (7)$$

The total model scattering pattern, including polydispersity in radius  $R$  and number of sheets  $N$ , becomes

$$I(q) = \phi \Delta \rho^2 \langle P(q) \rangle_R \langle F(q) \rangle_N \quad (8)$$

which we fit to each individual pattern to follow the growth of the nanosheets.

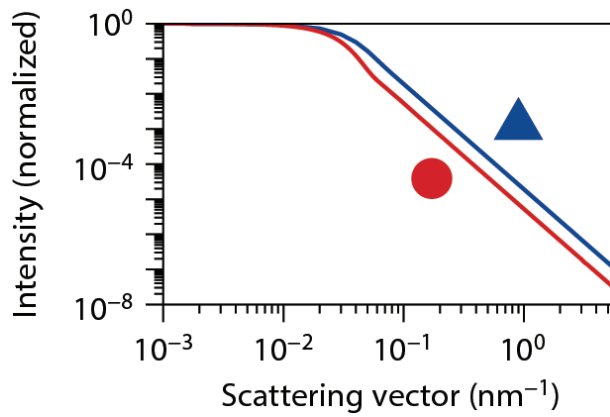


**Figure A5.2.** The cross-section form factor  $P(q)$  for polydisperse circular sheets with a mean radius of 50 nm and a polydispersity of  $\sigma = 20$  nm in red, and  $P(q)$  for polydisperse triangular sheets with equal surface area and averaged over orientation in blue.

## A5.2 SAXS model for spheroidal nanocrystals

Scattering by the quasi-spherical NCs formed in the absence of chloride, is fitted to a model of polydisperse spheres. We assume a Gaussian distribution of radii with mean  $\langle R \rangle$  and standard deviation  $\sigma_R$ :

$$I(q) = \phi \Delta \rho^2 \langle P(q) \rangle_R S(q) \quad (9)$$

with the form factor of a sphere, averaged over the size distribution is<sup>28</sup>

$$\langle P(q) \rangle_R = \frac{1}{\sqrt{2\pi} \sigma_R} \int_0^\infty e^{-\frac{1}{2} \left( \frac{R - \langle R \rangle}{\sigma_R} \right)^2} 3V \left[ \frac{\sin(qR) - qR \cos(qR)}{(qR)^3} \right]^2 dR \quad (10)$$

where  $V$  is the volume of a NC with radius  $R$ . With this model we neglect that the NCs are slightly elongated (TEM image in Figure 5.4a), because the signature of such elongation would not be observable in the scattering pattern of a polydisperse sample.

To extract the growth of the NCs from the analysis of the time-resolved scattering patterns (Figure 5.3b), we use the above equation with  $S(q) = 1$  on the wave vector range between  $0.2 \text{ nm}^{-1}$  and  $4 \text{ nm}^{-1}$ . However, in the full pattern (Figure 5.4b) we observe some additional scattering at  $q < 0.1 \text{ nm}^{-1}$  that is not described by  $\langle P(q) \rangle_R$ . This contribution can be reproduced with a model that some of the NCs are clustered in loosely packed aggregates. We use the expression of the structure factor  $S(q)$  for a fractal aggregate:<sup>47</sup>

$$S(q) = 1 + \frac{1}{(q \langle R \rangle)^D} \frac{D \Gamma(D - 1) \sin[(D - 1) \tan^{-1} q \xi]}{(1 + 1/q^2 \xi^2)^{(D-1)/2}} \quad (11)$$

with  $\Gamma(x)$  the gamma function,  $\langle R \rangle$  the mean NC radius,  $D$  the fractal dimension, and  $\xi$  the typical length scale of the aggregate. We fit the data of Figure 5.4b to a combination of 22% free NC, and 78% NCs in aggregates with  $D = 3$  and  $\xi = 20 \text{ }\mu\text{m}$ . Such aggregates would be the pre-stage to the ordered clusters that form after 20 min of NC growth (Figure 5.5d).





# PART B

## COMPOSITION TAILORING



# Luminescent CuInS<sub>2</sub> Quantum Dots by Partial Cation Exchange in Cu<sub>2-x</sub>S Nanocrystals



## ABSTRACT

In this chapter, we show successful partial cation exchange reactions in Cu<sub>2-x</sub>S nanocrystals (NCs) yielding luminescent ternary CuInS<sub>2</sub> (CIS) NCs. Our approach of mild reaction conditions ensures slow Cu extraction rates, which results in a balance with the slow In incorporation rate. With this method, we obtain CIS NCs with photoluminescence (PL) far in the near-infrared (NIR), which cannot be directly synthesized by currently available synthesis protocols. We discuss the factors that favor partial, self-limited cation exchange from Cu<sub>2-x</sub>S to CIS NCs, rather than complete cation exchange to In<sub>2</sub>S<sub>3</sub>. The product CIS NCs have the wurtzite crystal structure, which is understood in terms of conservation of the hexagonal close packing of the anionic sublattice of the parent NCs into the product NCs. These results are an important step toward the design of CIS NCs with sizes and shapes that are not attainable by direct synthesis protocols and may thus impact a number of potential applications.

Based on

**Luminescent CuInS<sub>2</sub> Quantum Dots by Partial Cation Exchange in Cu<sub>2-x</sub>S Nanocrystals**

W. van der Stam, A. C. Berends, F. T. Rabouw, T. Willhammar, X. Ke, J. D. Meeldijk, S. Bals and C. de Mello Donega, *Chem. Mater.*, **2015**, *27*, 621–628.

## 6.1 Introduction

Colloidal semiconductor nanocrystals (NCs) have attracted increasing attention due to their exciting and tunable optical properties, which render them promising materials for several applications.<sup>1-4</sup> For example, NCs can be used as luminescent probes for *in vivo* bio-imaging,<sup>5,6</sup> as well as light converters in displays and LEDs.<sup>7,8</sup> However, the presence of heavy metals such as cadmium and lead is an increasing concern, which limits the applicability of colloidal NCs.<sup>8,9</sup>

Copper indium dichalcogenide ( $\text{CuInE}_2$ , with  $E = \text{S}$  and/or  $\text{Se}$ ) NCs have optical properties that can be tuned in the visible to the near-infrared (potentially up to 855 nm for  $\text{CuInS}_2$ , CIS, and up to 1215 nm for  $\text{CuInSe}_2$ , CISE) spectral range, which makes them promising alternatives for the well-known heavy metal based NCs ( $\text{CdE}$  and  $\text{PbE}$ , with  $E = \text{S}, \text{Se}, \text{Te}$ ).<sup>10-14</sup> For example, the direct bandgap of 1.45 eV and large absorption coefficients make CIS a suitable alternative absorber material for quantum dot and thin film photovoltaics (PV).<sup>15-17</sup> Additionally, the small self-absorption cross-section<sup>10</sup> makes CIS NCs very interesting materials as luminophores in luminescent solar concentrators.<sup>18,19</sup>

However, the currently available protocols for the direct colloidal synthesis of luminescent ternary NCs such as CIS and CISE produce only small quasi-spherical NCs.<sup>10-12</sup> Larger and anisotropic NCs with a homogeneous composition are difficult to obtain because multiple precursor reactivities need to be balanced for simultaneous thermolysis of the cationic precursors.<sup>20</sup> Otherwise, it is favorable for the reaction system to form instead binary NCs, such as  $\text{Cu}_{2-x}\text{S}$ .<sup>21</sup> Pure phase luminescent quasi-spherical CIS NCs have only been obtained with photoluminescence (PL) peak between 550 and 750 nm,<sup>22-24</sup> whereas large non-luminescent CIS nanorods are obtained when  $\text{Cu}_{2-x}\text{S}$  NCs are used *in-situ* as nucleation seeds.<sup>25</sup> Hence, there is a wide range of sizes and shapes that have not yet been explored for CIS NCs.

Here, we present a synthetic pathway toward ternary  $\text{CuInS}_2$  NCs from binary  $\text{Cu}_{2-x}\text{S}$  parent NCs by exploiting cation exchange (CE) reactions.<sup>26-30</sup> Nonluminescent  $\text{Cu}_{2-x}\text{S}$  NCs are converted into luminescent CIS NCs, where the PL peak position of the product CIS NCs is determined by the size of the parent  $\text{Cu}_{2-x}\text{S}$  NCs. This method allows us to synthesize CIS NCs with PL in the near-infrared (NIR) centered at 870 nm, which are not attainable in a direct fashion. Since colloidal  $\text{Cu}_{2-x}\text{S}$  NCs can be synthesized with large control over size and shape (*e.g.*, nearly spherical NCs, hexagonal bipyramids, bipyramids and nanoplatelets, and ultrathin nanosheets),<sup>30-34</sup> the method described in this chapter may provide a pathway to prepare colloidal CIS NCs of as yet unexplored morphologies and functionalities.

## 6.2 Methods

**Materials.** Copper(I) acetate (CuAc, 97%), Copper sulfate pentahydrate (CuSO<sub>4</sub>·5H<sub>2</sub>O, ≥98%), Copper iodide (CuI, 99.999%), Indium nitrate hydrate (In(NO<sub>3</sub>)<sub>3</sub>·H<sub>2</sub>O, 99.99%), Indium acetate (InAc<sub>3</sub>, 99.99%), 1-dodecanethiol (DDT, ≥98%), 1-octadecene (ODE, 90%), trioctylphosphine oxide (TOPO, 99%), trioctylphosphine (TOP, 90%), oleic acid (OA, 90%), anhydrous toluene, methanol and butanol were purchased from Sigma Aldrich. ODE and TOPO were degassed for 2 h at 120 °C prior to synthesis, all other materials were used as received.

**Synthesis of 2.5 nm Cu<sub>2-x</sub>S NCs.** The Cu<sub>2-x</sub>S NCs (size: 2.5 nm) were synthesized according to the method described by Wang *et al.*<sup>34</sup> In a round-bottom flask, 0.3 mmol CuAc and 1.1 g TOPO were dissolved in 25 mL previously degassed ODE. After additional degassing for one hour at 100 °C, the reaction mixture was further heated to 160 °C and 1 mL DDT was swiftly injected into the dark green solution under N<sub>2</sub> atmosphere. The NCs were allowed to grow for 90 minutes. Subsequently, the NCs were cooled to room temperature. They were washed by adding methanol and butanol (1:1 ratio), centrifugation at 3000 rpm for 5 min, and redispersion in 2 mL toluene. This cycle was repeated 3 times.

**Synthesis of 4 nm Cu<sub>2-x</sub>S NCs.** For the synthesis of 4 nm sized Cu<sub>2-x</sub>S nanocrystals, the same procedure as described above was followed, only the NCs were allowed to grow for an additional 2 hours (overall growth time; 3.5 hours). The same washing steps were performed.

**Synthesis of 11 nm Cu<sub>2-x</sub>S NCs.** The 11 nm sized Cu<sub>2-x</sub>S nanocrystals were synthesized according to an adaptation of the method described by Lu *et al.*<sup>25</sup> In a round-bottom flask, 0.8 mmol CuSO<sub>4</sub>·5H<sub>2</sub>O (203 mg), 7.5 mL DDT and 6 mL OA were mixed and gradually heated to 200 °C. Total heating time was 15 minutes, after which the solution was maintained at 200 °C for 2 hours. The crude reaction mixture was purified in the same way as described above and redispersed in ~5 mL toluene.

**Cation exchange (CE) reactions of Cu<sup>+</sup> for In<sup>3+</sup>.** The cation exchange reactions were performed according to an adaptation of the method described by Son *et al.* for Cd<sup>2+</sup> for Ag<sup>+</sup> exchange reactions.<sup>27</sup> 1 mL Cu<sub>2-x</sub>S NCs (~10<sup>-8</sup> M) in toluene was diluted three times and 0.14 mmol In(NO<sub>3</sub>)<sub>3</sub>·H<sub>2</sub>O dissolved in 1 mL methanol was added. The In:Cu molar ratio was ~1 for all NC sizes. This ratio was estimated by assuming quantitative reaction and no purification losses. Finally, 100 μL TOP was added as Cu-extracting ligand and the solution was stirred for several days. The NCs were thoroughly washed to remove excess precursor and ligands by adding methanol and butanol (1:1 ratio) and centrifugation at 3000 rpm for 10 min. Subsequently, the NCs were redispersed in 2 mL toluene.

**Direct synthesis of 2.5 nm CuInS<sub>2</sub> NCs.** For comparison, CIS NCs were directly synthesized following the method described by Li *et al.*<sup>35</sup> In a round-bottom flask, 0.4 mmol of CuI, 0.4 mmol of InAc<sub>3</sub>, and 5 mL of DDT were mixed and degassed under vacuum at 100 °C for 1 h. Subsequently, the temperature was raised to 230 °C, and the NCs were allowed to grow for 11 min. The solution was cooled to room temperature, and the NCs were precipitated by addition of a methanol/butanol solution (1:1 volume ratio) and centrifugation at 3000 rpm. The supernatant was discarded and the NCs were redispersed in ~5 mL toluene. The washing steps were repeated twice.

**Optical spectroscopy.** Samples for optical measurements were prepared by diluting the washed NCs (10x dilution) with anhydrous toluene and the samples were stored under nitrogen in sealed cuvettes. Absorption spectra were measured on a double beam Perkin-Elmer Lambda 16 UV/Vis spectrometer. Photoluminescence (PL) and PL excitation spectra were recorded by an Edinburgh Instruments FLS920 Spectrofluorimeter equipped with a 450 W Xenon lamp as excitation source and double grating monochromators. PL decay curves were obtained by time-correlated single-photon counting *via* time-to-amplitude conversion. A pulsed diode laser (EPL-445 Edinburgh Instruments, 441 nm, 55 ps pulse width, 0.2–0.5 MHz repetition rate) was used as the excitation source.

**Transmission Electron Microscopy (TEM) and Energy Dispersive X-Ray Spectroscopy (EDS) experiments**

were performed using a FEI Tecnai-12 microscope operating at 120 kV and a FEI Tecnai-20F microscope operating at 200 kV. Samples for TEM imaging were prepared by dropcasting a toluene solution of NCs onto a carbon-coated copper (400-mesh) TEM grid. The excess liquid was removed by blotting using filter paper.

*Energy Dispersive X-ray Spectroscopy mapping.* Scanning TEM EDS measurements were performed on a FEI Tecnai-20F microscope operating at 200 kV. EDS measurements were performed using a dedicated low background holder and Cu-free Ni TEM grids. Acquisition time for EDS measurements was  $\sim 30$  s –  $\sim 1$  min. To ensure that the elemental concentrations were statistically valid and representative of the whole NC ensemble, EDS analyses were performed on wide areas ( $10^4 - 10^5$  nm<sup>2</sup>), encompassing several thousands of NCs. The EDS-signal is acquired with an EDAX Si(Li) detector and processed in Tecnai Imaging and Analysis software (TIA), using the following lines: S-K at 2.3 keV, In-L at 3.3 keV and Cu-K at 8.0 keV. The S-K and In-L are well resolved but Cu-K is partially overlapping with the Ni-K $\beta$  peak at 8.26 keV (originating from the nickel TEM grid). The software deconvoluted these two peaks. The automatically acquired background subtraction was adjusted manually where necessary in order to quantitatively deconvolute the peaks.

*High-Resolution Scanning Transmission Electron Microscopy (HRSTEM)* images of the CIS NCs were acquired using an FEI Titan3 operated at an accelerating voltage of 120 kV. The images were collected using a high angle annular dark field (HAADF) detector. The samples were prepared by adding a droplet of the toluene dispersion to a carbon coated copper grid. The lattice averaging were performed by calculating a Fast Fourier transform (FFT) from the area of interest, extracting one Fourier component from each of the lattice points of the FFT and perform an inverse Fourier transform to create the final map. The image processing was performed using the software CRISP.<sup>36</sup>

*X-ray Diffractometry.* X-ray Diffraction (XRD) measurements were performed with a Bruker D2 Phaser, equipped with a Co K $\alpha$  X-ray source with X-ray wavelength of 1.79026 Å. Thin solid film NC samples for XRD were prepared by drop-casting a concentrated NC solution in chloroform on a Si wafer and evaporating the solvent.

## 6.3 Results & Discussion

### 6.3.1 2.5 nm CIS NCs by partial cation exchange in Cu<sub>2-x</sub>S NCs

Non-luminescent 2.5 nm Cu<sub>2-x</sub>S nanocrystals (NCs), with a first absorption transition around 500 nm (dashed line in Figure 6.1a), are converted into NCs that show efficient photoluminescence (PL) both in the visible (peak at 650 nm) and in the NIR (peak at 900 nm, solid red line in Figure 6.1a). The position of the first PL peak is in close agreement with that expected for directly synthesized CuInS<sub>2</sub> (CIS) NCs of 2.5 nm (*viz.*, 665 nm). Further, PL lifetime measurements on the CIS NCs obtained by cation exchange (CE) yields lifetime values of  $\tau_1 = 36$  ns and  $\tau_2 = 206$  ns (Figure 6.1c), which are comparable to those obtained on directly synthesized CIS NCs of comparable size and shape ( $\tau_1 = 26$  ns and  $\tau_2 = 205$  ns, Figure 6.1b). Hence, the recombination pathways in the product CIS NCs obtained by CE in Cu<sub>2-x</sub>S NCs are essentially the same as those in standard CIS NCs. This also indicates that the PLQYs of the CIS NCs obtained by CE reactions are comparable to those of the directly synthesized CIS NCs, which are in the 5 to 10% range, depending on the sample. We note that these PLQYs are comparable to the highest values reported in the literature for CIS NCs.<sup>11,37</sup> Higher PLQYs (as high as 85%) have been reported only for CIS/CdS and CIS/ZnS core/shell

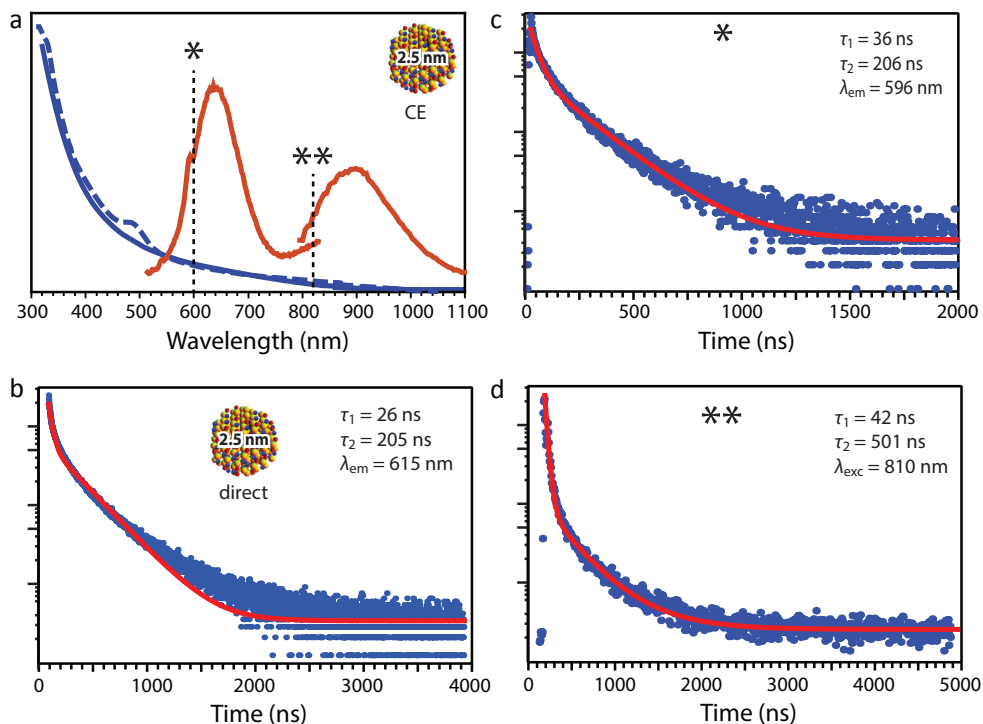


**Figure 6.1. Optical spectroscopy of 2.5 nm Cu<sub>2-x</sub>S and CuInS<sub>2</sub> nanocrystals.** (a) Absorption (blue solid line) and photoluminescence (PL, red solid line) spectra of 2.5 nm CIS NCs obtained by partial cation exchange in Cu<sub>2-x</sub>S NCs. Two PL spectra are plotted due to the change of detector necessary to obtain a good signal in the NIR region. The absorption spectrum of the parent 2.5 nm Cu<sub>2-x</sub>S NCs is also shown (blue dashed line). The asterisks denote the emission wavelengths at which the PL decay curves were measured. (b) PL decay of CIS NCs of ~2.5 nm obtained by direct synthesis. Fitting a bi-exponential to the data (red curve) yields a fast component with  $\tau_1 = 26$  ns and a slow component with  $\tau_2 = 205$  ns (although the fit is off between 1000 and 2000 ns). (c) PL decay curve of CIS NCs (2.5 nm) obtained by partial CE reaction, monitoring the higher energy PL (denoted with an asterisk in panel a). Fitting a biexponential to the data (red curve) yields a fast component with  $\tau_1 = 36$  ns and a slow component with  $\tau_2 = 206$  ns. (d) PL decay curve of CIS NCs (2.5 nm) obtained by partial CE reaction, monitoring the lower energy PL (denoted with two asterisks in panel a). Fitting a biexponential to the data (red curve) yields a fast component with  $\tau_1 = 42$  ns and a slow component with  $\tau_2 = 501$  ns.

or graded alloy NCs.<sup>11,35,38</sup>

CIS NCs typically exhibit a single broad PL band located several hundred meV below the apparent absorption edge, which is usually ascribed to donor-acceptor pair (DAP) recombination, by analogy to bulk CIS.<sup>11,23</sup> This explains the large global Stokes shift and relatively slow decay dynamics.<sup>23</sup> The observation of two bands in the PL spectrum of the 2.5 nm CIS NCs obtained by CE (Figure 6.1a) is thus remarkable. As discussed

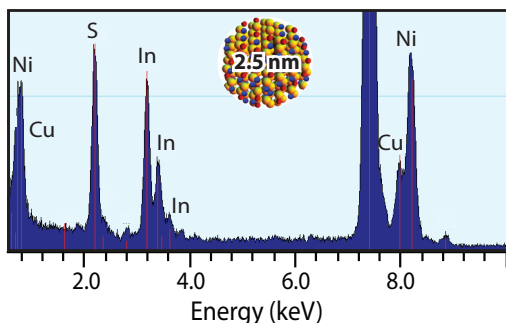


**Figure 6.2. Energy Dispersive X-ray Spectroscopy (EDS) measurement on ~2.5 nm CuInS<sub>2</sub> (CIS) nanocrystals (NCs)** obtained by partial cation exchange reaction, indicating successful conversion of Cu<sub>2-x</sub>S nanocrystals into ternary CuInS<sub>2</sub> nanocrystals, evidenced by the peaks corresponding to In at 3.2 keV. The Ni peaks originate from the Ni TEM grid. The Ni and Cu peaks were deconvoluted by the imaging software prior to quantification, which yields a Cu:In:S ratio of 1.0±0.12 : 1.4±0.16 : 2.0.

above, the higher energy peak can be ascribed to DAP recombination pathways that are essentially the same as those present in directly synthesized CIS NCs. In contrast, the PL lifetime measured while monitoring the lower energy band is much longer than that observed in similar sized CIS NCs obtained by direct synthesis (*viz.*,  $\tau_1 = 42$  ns and  $\tau_2 = 501$  ns, Figure 6.1d). This is consistent with exciton recombination involving more localized states, such as those associated with surface and/or internal defects. Considering the large surface/volume ratio of such small NCs and the fact that CE is essentially a surface process (see mechanism section below), it is likely that part of the CIS NC ensemble contains surface defects that give rise to additional recombination pathways. The limited resolution of the FEI Tecnai-12 TEM for particles smaller than 3 nm did not allow us to clearly visualize the 2.5 nm NCs. The formation of CIS NCs by partial cation exchange in Cu<sub>2-x</sub>S NCs (2.5 nm diameter) is however confirmed by Energy Dispersive X-ray Spectroscopy (EDS) which reveals a Cu:In:S ratio of 1.0±0.12 : 1.4±0.16 : 2.0 (Figure 6.2). It is noteworthy that this ratio is consistent with the observed optical properties, since the highest PLQYs are typically associated with In-rich (or Cu-poor) CIS NCs.<sup>11,37</sup>

### 6.3.2 4 nm CIS NCs by partial cation exchange in Cu<sub>2-x</sub>S NCs

The partial CE reaction was also exploited to convert larger Cu<sub>2-x</sub>S parent NCs (4 nm in diameter) into CIS NCs. In this case, the product NCs show a single PL peak at 870 nm (Figure 6.3a). This clearly demonstrates that the NC size is inherited from the parent Cu<sub>2-x</sub>S NCs since this emission wavelength is consistent with CIS NCs of 4 nm in diameter. Considering that the optical properties are determined by the size of the CIS NCs, we can conclude that the method presented here provides a pathway to synthesize CIS NCs with efficient PL in the NIR, which have not yet been synthesized by direct synthesis protocols. Compared to the smaller NCs (2.5 nm), quantum confinement is relaxed leading to PL at lower energies. The PL decay of these larger (*viz.*, 4 nm) CIS NCs can be well described by a biexponential fit, with a fast component  $\tau_1 = 68$  ns and slow component  $\tau_2 = 408$  ns (Figure 6.3b). These decay constants are slower than those usually observed in small CIS NCs. This difference is qualitatively explained by Fermi's golden rule,<sup>39</sup> according to which the spontaneous emission rate scales with the

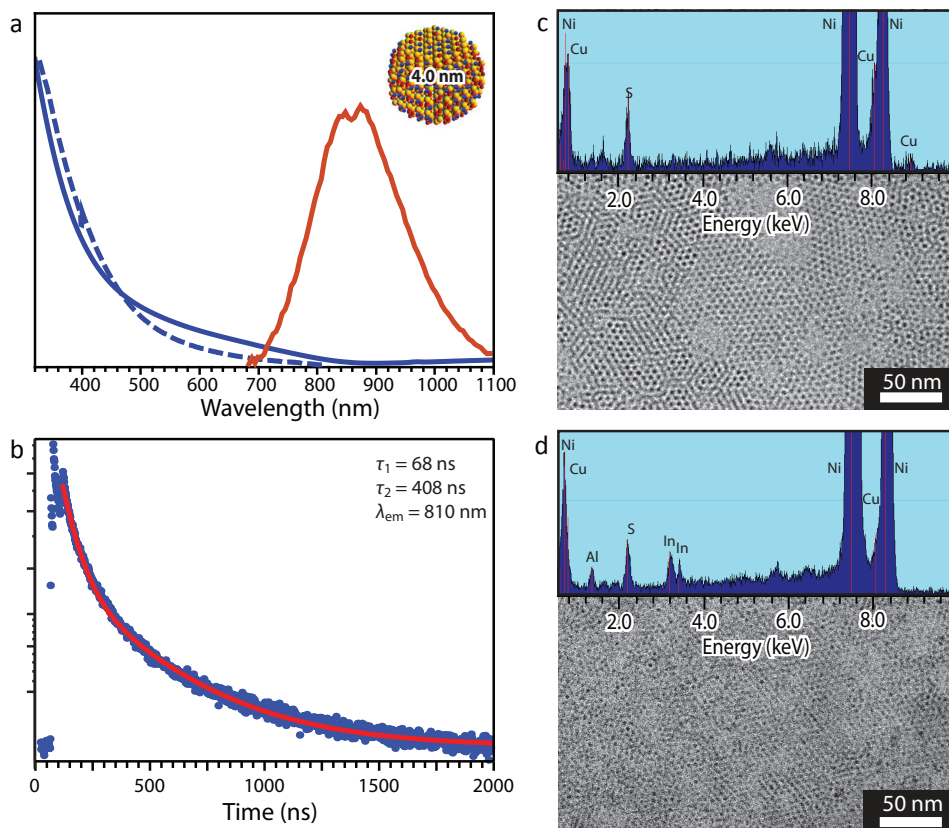


**Figure 6.3. Optical spectroscopy and electron microscopy measurements of 4 nm CuInS<sub>2</sub> nanocrystals obtained by partial cation exchange reactions.** (a) Absorption (blue solid line) and photoluminescence (PL, red solid line) spectra of CIS NCs obtained by partial cation exchange in 4 nm diameter Cu<sub>2-x</sub>S NCs. The absorption spectrum of the parent Cu<sub>2-x</sub>S NCs is also shown (blue dotted line). (b) PL decay of 4 nm diameter CIS NCs obtained from Cu<sub>2-x</sub>S NCs by CE reactions. Fitting a bi-exponential to the data (red curve) yields a fast component with  $\tau_1 = 68$  ns and a slow component with  $\tau_2 = 408$  ns. (c) Transmission Electron Microscopy (TEM) image of 4 nm Cu<sub>2-x</sub>S parent NCs. Inset displays the Energy Dispersive X-ray Spectroscopy (EDS) spectrum of the parent Cu<sub>2-x</sub>S NCs (d) TEM image of 4 nm CIS NCs, obtained from Cu<sub>2-x</sub>S NCs by partial CE. Inset displays the EDS spectrum of the CIS NCs.

transition energy. More precisely, for excitonic transitions in NCs of varying sizes the radiative lifetime should scale linearly with the emission wavelength.<sup>40</sup> The difference between the PL lifetimes of the two sizes of CIS NCs investigated here is, however, larger than predicted by Fermi's golden rule (emission wavelength ratio is 1.3, while the lifetime ratio is 1.9). This indicates that the emission transitions in CIS NCs are not excitonic in nature but instead involve DAP recombination,<sup>23</sup> in agreement with the assignment presented above for the smaller NCs. Although the PLQYs of the larger CIS NCs could not be directly determined due to limitations of our setup in the NIR,

the similarity of the PL decay curves suggests that they are at least of the same order of magnitude as those observed for the smaller NCs, since pronounced PL quenching should result in faster decays due to increased nonradiative recombination rates.

TEM measurements revealed that the size of the parent  $\text{Cu}_{2-x}\text{S}$  NCs is preserved in the product CIS NCs (Figure 6.3c,d). The product NCs no longer form self-assembled superstructures on the TEM grid, suggesting that the size dispersion has slightly increased. It is also possible that the NC self-assembly is prevented by the presence of reaction by-products that were not completely removed by the washing procedure. The successful transformation of the parent  $\text{Cu}_{2-x}\text{S}$  NCs into product CIS NCs is clearly reflected in EDS measurements, where In peaks around 3.2 keV are observed in the product NCs (Figure 6.3d). Quantification of the EDS measurements gives a Cu:S ratio of  $2 \pm 0.16 : 1$  for the parent  $\text{Cu}_{2-x}\text{S}$  NCs (Figure 6.3c) and a Cu:In:S ratio of  $1.1 \pm 0.14 : 1.6 \pm 0.21 : 2.0$  for the product CIS NCs (Figure 6.3d). It should be noted that this Cu/In ratio is consistent with the observation of efficient PL,<sup>11,37</sup> in line with the results obtained for the smaller NCs.

X-Ray Diffraction (XRD) measurements suggest that the  $\text{In}^{3+}$  for  $\text{Cu}^+$  cation exchange in  $\text{Cu}_{2-x}\text{S}$  NCs is accompanied by a crystal structure transformation from low-chalcocite  $\text{Cu}_{2-x}\text{S}$  to wurtzite CIS (Figure 6.4). The peaks are however severely broadened due to finite size effects, precluding a definite assignment of the observed reflections. Nevertheless, the formation of pure phase wurtzite CIS is unambiguously confirmed by High-Resolution Scanning Transmission Electron Microscopy (HRSTEM) measurements (Figure 6.5). The 4 nm CIS product NCs were imaged along two crystallographic directions, viz. [100] and [101]. The images reveal the expected atomic arrangement for wurtzite CIS NCs. In Figure 6.5a, the NC viewed along the [100] direction is indicated by the red circle, whereas the NC viewed along the [101] direction is indicated by the blue circle. In the other panels, the same colors are used for the two directions, red for [100] (Figure 6.5b,d,e) and blue for [101] (Figure 6.5c,f,g). When Fast Fourier Transformation (FFT) is calculated from the circled areas, the characteristic lattice of wurtzite CIS is directly evident in both cases (Figure 6.5b,c). When the images of the NCs from panel a are

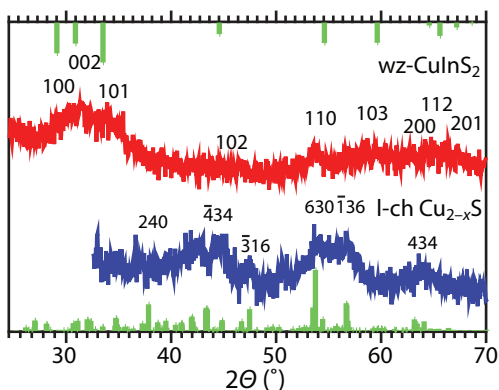


**Figure 6.4. X-ray Diffraction (XRD) measurements**

(Co  $K\alpha$  X-ray source) on small 4 nm NCs. The reflections are severely broadened, making it hard to distinguish separate peaks, but a transition can be observed when comparing the XRD patterns before (blue line) and after cation exchange (red line). Reference bars for the expected crystal structures are added for clarity (green bars) for low-chalcocite (l-ch)  $\text{Cu}_{2-x}\text{S}$  NCs (blue line) and wurtzite (wz)  $\text{CuInS}_2$  NCs (red line). Reference bars are from PDF-card R120113-9 for low-chalcocite  $\text{Cu}_{2-x}\text{S}$  and JCPDS card 01-077-9459 for wurtzite  $\text{CuInS}_2$ .

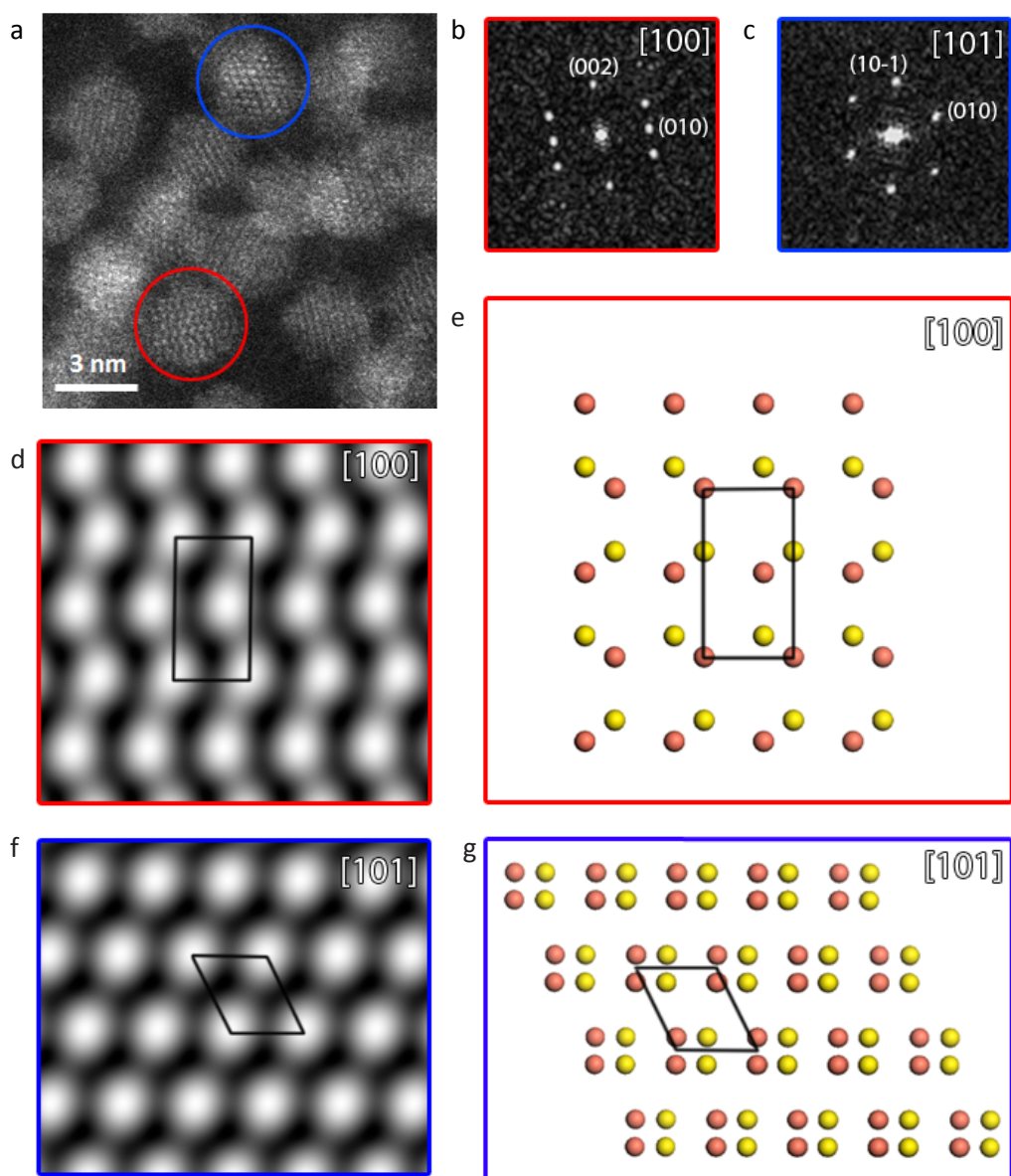


**Figure 6.5. Crystal structure determination.** (a) High-Resolution Scanning Transmission Electron Microscopy (HRSTEM) image of the 4 nm product CIS NCs viewed along the [100] direction with respect to the electron beam (red circle) and along the [101] direction (blue circle) (b,c) Calculated FFTs from the areas indicated by the red circle (b) and by the blue circle (c). (d) Lattice averaged image from the red area in (a) reveals the atomic arrangement along the [100] direction. (e) The atomic arrangement fits well with the wurtzite CIS crystal structure. (f) Lattice averaged image of the blue area in (a) shows the atomic arrangement along the [101] direction. (g) The atomic arrangement fits well with the wurtzite CIS crystal structure. The yellow spheres denote the sulfur atoms and the orange spheres the Cu/In atoms in (e) and (g).

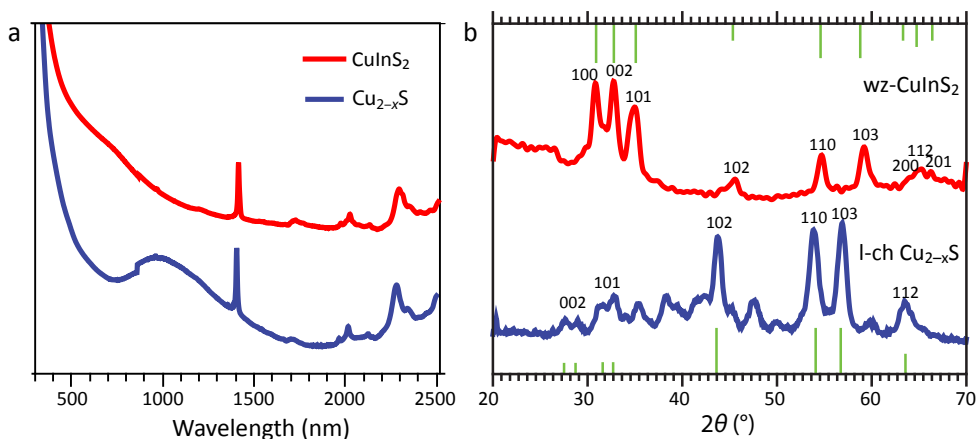


**Figure 6.6. Absorption and XRD measurements on 11 nm  $\text{Cu}_{2-x}\text{S}$  and  $\text{CuInS}_2$  nanocrystals.** (a) Absorption spectrum of 11 nm CIS NCs obtained by cation exchange from  $\text{Cu}_{2-x}\text{S}$  NCs (red line). The absorption spectrum of the parent 11 nm  $\text{Cu}_{2-x}\text{S}$  NCs is also shown (blue line). (b) XRD patterns (Co  $\text{K}\alpha$  source) of 11 nm CIS NCs obtained by cation exchange from  $\text{Cu}_{2-x}\text{S}$  NCs (wurtzite, wz, red line) and of the parent  $\text{Cu}_{2-x}\text{S}$  NCs (low-chalcocite, l-ch, blue line). Reference bars (green lines) are from JCPDS PDF-card 01-077-9459 for wurtzite CIS and R120113-9 for low-chalcocite.<sup>41</sup>

lattice averaged, clear atomic positions are obtained (Figure 6.5d,f). The observed atomic arrangement fits well with the wurtzite CIS crystal structure in both directions, as can be seen in the models depicted in Figure 6.5e,g, confirming the wurtzite crystal structure of the product 4 nm CIS NCs. Note that the contrast of the HAADF-STEM images is related to the atomic number so the contribution of In and Cu will dominate over S. The resolution of the HRSTEM images is less than 3 Å which further prevents resolving the S atoms from the Cu/In atoms. The low resolution is due to poor beam stability of the material and severe contamination.

### 6.3.3 11 nm CIS NCs by partial cation exchange in $\text{Cu}_{2-x}\text{S}$ NCs

To demonstrate that our method can also yield CIS NCs of unprecedented sizes, we performed CE in  $\text{Cu}_{2-x}\text{S}$  NCs of 11 nm. Although the product CIS NCs are non-luminescent due to their large size, the outcome of the CE reaction is more easily analysed with TEM and XRD. The UV-VIS absorption spectrum of the product NCs shows an absorption onset that is close to the bulk bandgap of CIS (1.4 eV, Figure 6.6a). It is also interesting to note that the NIR plasmon band associated with Cu vacancies in  $\text{Cu}_{2-x}\text{S}$  NCs disappeared after the CE. Moreover, XRD measurements reveal a clear transition from the hexagonal low-chalcocite  $\text{Cu}_{2-x}\text{S}$  crystal structure to the hexagonal wurtzite CIS crystal structure (Figure 6.6b), consistent with the observations discussed above for the 4 nm CIS NCs. The structural change is also clear in the electron diffraction patterns. However, the size dispersion of the product CIS NCs is much larger than that of the parent  $\text{Cu}_{2-x}\text{S}$  NCs, suggesting that in this case CE was accompanied by partial

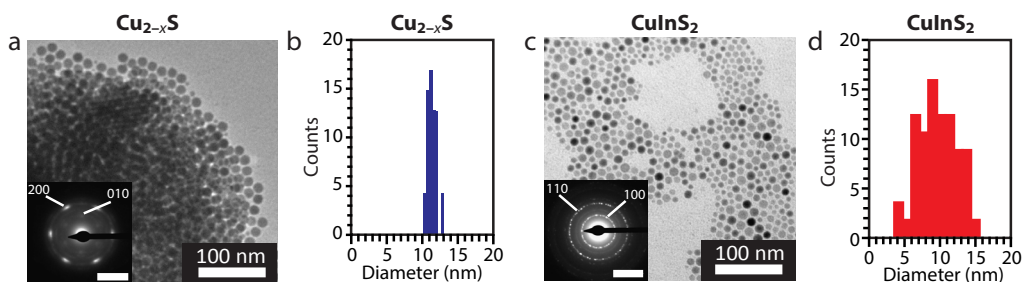


**Figure 6.7. Size and shape of 11 nm Cu<sub>2-x</sub>S and CuInS<sub>2</sub> nanocrystals.** (a) Transmission Electron Microscopy (TEM) measurements show that the Cu<sub>2-x</sub>S parent nanocrystals (NCs) self-assemble into 3D clusters, with atomic orientation of the NCs, evidenced by the electron diffraction (ED) pattern displayed in the inset (scale bar: 5 nm<sup>-1</sup>). (b) The Cu<sub>2-x</sub>S NCs have a narrow size distribution. (c) The product CuInS<sub>2</sub> (CIS) NCs have ripened after cation exchange reactions and display a wurtzite CuInS<sub>2</sub> crystal structure, evidenced by the ED pattern in the inset (scale bar: 5 nm<sup>-1</sup>). (d) The product CIS NCs have a broad size distribution, due to ripening of the NCs.

dissolution and ripening (Figure 6.7). As will be discussed below, this indicates that there was a slight imbalance between the Cu<sup>+</sup> outgoing and the In<sup>3+</sup> incoming rates.

### 6.3.4 Mechanism

Cation exchange reactions consist of a chain of inherently linked elementary kinetic steps, which must proceed in a concerted manner.<sup>26,42</sup> The driving force for the reaction is determined by the energy balance of the overall reaction, and therefore depends on the relative stabilities of the incoming and outgoing cations in solution and in the NC. It should also be noted that the cation exchange would not proceed beyond the surface in the absence of solid state diffusion fluxes in the NC,<sup>43</sup> allowing the native cations to diffuse outward and the new cations to diffuse inward. The overall energy balance is thus also strongly dependent on the activation energies for diffusion of both the incoming and outgoing cations in the NC.

Figure 6.8 schematically depicts the elementary steps that can be identified in the In<sup>3+</sup> for Cu<sup>+</sup> exchange in Cu<sub>2-x</sub>S NCs. It is interesting to note that the Cu<sup>+</sup> extraction and the In<sup>3+</sup> incorporation proceed by separate chemical pathways, in contrast to other well-known nanoscale cation exchange reactions (*e.g.*, Cd<sup>2+</sup> for Zn<sup>2+</sup> exchange in ZnSe NCs using Cd(oleate)<sub>2</sub>), in which the place exchange is mediated by a single ligand.<sup>43</sup> In the present case, Cu<sup>+</sup> (a soft Lewis acid with absolute hardness  $\eta = 6.28$  eV)<sup>44</sup> is extracted from the Cu<sub>2-x</sub>S NCs by trioctylphosphine (a soft Lewis base with  $\eta \approx 6$  eV),<sup>26</sup> while In<sup>3+</sup> (a hard Lewis acid with  $\eta = 13$  eV)<sup>44</sup> is transported to the NC surface as a complex with the solvent molecules (methanol) and is subsequently incorporated in the Cu<sup>+</sup> vacancies. It should be noted that the off-stoichiometry of the parent Cu<sub>2-x</sub>S NCs is due to native Cu vacancies. These vacancies are not compensated by the formation of Cu<sup>2+</sup> ions, but instead lead to free charge carriers (holes) in the valence band, effectively

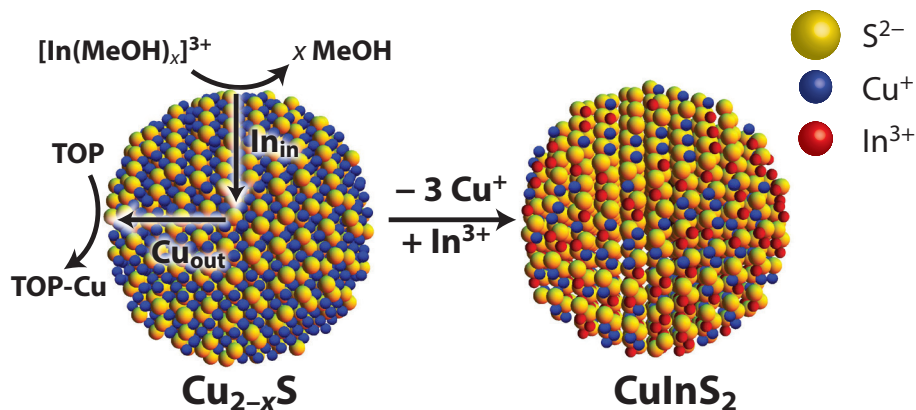


**Figure 6.8.** Schematic illustration of the elementary kinetic steps involved in conversion of  $\text{Cu}_{2-x}\text{S}$  nanocrystals into  $\text{CuInS}_2$  nanocrystals by  $\text{In}^{3+}$  for  $\text{Cu}^+$  cation exchange.  $\text{Cu}^+$  extraction (mediated by trioctylphosphine, TOP) and  $\text{In}^{3+}$  incorporation into  $\text{Cu}^+$  vacancies take place at the NC surface and set in motion two solid state cation diffusion fluxes (inward diffusion of  $\text{In}^{3+}$ ,  $\text{In}_{\text{in}}$ , and outward diffusion of  $\text{Cu}^+$ ,  $\text{Cu}_{\text{out}}$ ), effectively converting binary  $\text{Cu}_{2-x}\text{S}$  nanocrystals into ternary  $\text{CuInS}_2$  nanocrystals.

keeping the Cu atoms in the +1 valency and changing the valency of some S atoms from  $-2$  to  $-1$ .<sup>45</sup> The free holes give rise to a localized plasmon resonance, which becomes stronger with decreasing Cu content (*i.e.*, increasing density of free holes).<sup>45</sup> Interestingly, the extraction of Cu atoms from the NCs by TOP does not increase the plasmon resonance, but rather causes its disappearance (see *e.g.*, Figure 6.6a above). This is consistent with the fact that the Cu atoms are extracted as  $\text{Cu}^+$ , thereby removing also the excess holes since the CIS NCs obtained after the cation exchange are  $\text{In}^{3+}$ -rich. The removal of the excess holes by extraction of  $\text{Cu}^{2+}$  ions instead of  $\text{Cu}^+$  is unlikely since the binding energies for  $\text{TOP-Cu}^{2+}$  are much smaller than those for  $\text{TOP-Cu}^+$  ( $\text{Cu}^{2+}$  is a harder Lewis acid, with  $\eta = 8.27$  eV).<sup>44</sup>

As a consequence of the separate chemical pathways for Cu extraction and In incorporation, the extraction rate of the  $\text{Cu}^+$  ions ( $\text{Cu}_{\text{out}}$ ) and the incorporation rate of the  $\text{In}^{3+}$  ions ( $\text{In}_{\text{in}}$ ) must be precisely balanced, otherwise the NCs will either dissolve ( $\text{Cu}_{\text{out}}$  faster than  $\text{In}_{\text{in}}$ ) or the CE reaction will simply not proceed ( $\text{Cu}_{\text{out}}$  too slow). Several CE experiments were carried out with small variations in the reaction conditions (*i.e.*, higher temperatures of 50–100 °C, higher concentration, different CE precursors, and Cu-extracting ligands), but these conditions failed to effectively convert  $\text{Cu}_{2-x}\text{S}$  NCs into CIS NCs because the  $\text{Cu}^+$  extraction rate was too fast compared to the  $\text{In}^{3+}$  incorporation rate, resulting in dissolution of the NCs. This highlights the sensitivity of the cation exchange process toward external synthetic conditions.

CE reactions are very often topotactic, preserving the crystal structure of the parent

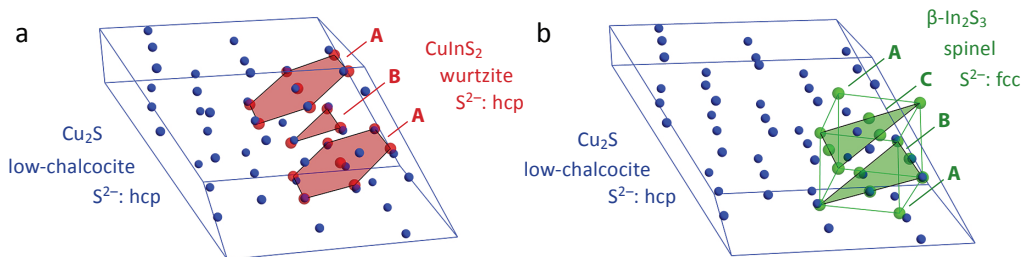


**Figure 6.9. Anionic sublattice comparison.** (a) Comparison of the anionic sublattice of low-chalcocite  $\text{Cu}_{2-x}\text{S}$  with wurtzite CIS, showing that the anionic sublattice of low-chalcocite  $\text{Cu}_{2-x}\text{S}$  (blue spheres) is compatible with wurtzite CIS (red spheres), since both anionic sublattices have an hcp arrangement. (b) Comparison of low-chalcocite unit cell (blue spheres) with  $\text{In}_2\text{S}_3$  (green spheres). The spinel  $\text{In}_2\text{S}_3$  structure has an fcc anionic sublattice, where layer C has to dislocate by 58% of a S-S distance in order to fit in the low-chalcocite lattice.

NCs into the product NCs.<sup>26–30</sup> More precisely, the anionic sublattice is conserved, while the cations are exchanged. In this way, metastable crystal structures can be obtained, *e.g.*, wurtzite  $\text{ZnS}$  starting from  $\text{Cu}_{2-x}\text{S}$ .<sup>28–30</sup> The present case is special since partial CE is required in order to form the ternary CIS crystal structure rather than fully exchanged  $\text{In}_2\text{S}_3$  (in principle, the In/Cu molar ratio of the CE reaction does allow full exchange to occur). This requires strict control over the incorporation and extraction rates of the cations.  $\text{Cu}_{2-x}\text{S}$  exists in multiple crystal structures, determined by the anionic arrangement and the concentration of Cu vacancies indicated by  $x$  (*i.e.*, monoclinic low-chalcocite  $\text{Cu}_2\text{S}$ , djurleite  $\text{Cu}_{1.96}\text{S}$ , and roxbyite  $\text{Cu}_{1.78}\text{S}$ , as well as hexagonal low and high-chalcocite  $\text{Cu}_2\text{S}$ , digenite  $\text{Cu}_{1.8}\text{S}$ , and covellite  $\text{CuS}$ ).<sup>46</sup> An *in-situ* X-ray study showed that small  $\text{Cu}_{2-x}\text{S}$  NCs (diameter < 7 nm) typically have the near-stoichiometric hexagonal high-chalcocite structure.<sup>47</sup> Our XRD measurements reveal a low-chalcocite crystal structure for  $\text{Cu}_{2-x}\text{S}$  particles of 11 nm in diameter (Figure 6.6b) and indicate a low-chalcocite crystal structure for 4 nm NCs. The main difference between hexagonal low and high-chalcocite is in the atomic positions of the Cu atoms, whereas the anions lie in a hexagonally close packed (hcp) arrangement in both cases.<sup>41,48,49</sup> Nanocrystalline CIS can attain two crystal structures, *viz.* roquesite and wurtzite. Roquesite is a zinc blende derivative where the sulfide anions are on a face centered cubic (fcc) sublattice, while wurtzite CIS is a hexagonal structure with an hcp anionic sublattice. CE reactions with djurleite and low- and high-chalcocite  $\text{Cu}_{2-x}\text{S}$  NCs as parent NCs are expected to result in wurtzite products, due to the hexagonal symmetry of the starting crystal structure. Hence, in our CE reaction, wurtzite CIS NCs are favored over roquesite CIS since the transformation of  $\text{Cu}_{2-x}\text{S}$  into the latter would require a substantial restructuring of the anionic sublattice.<sup>41,50</sup> This is also confirmed by XRD and HRSTEM measurements discussed above.

$\text{In}_2\text{S}_3$  exists in three crystal structures, denoted as  $\alpha$ ,  $\beta$ , and  $\gamma$ , where  $\beta\text{-In}_2\text{S}_3$  is the stable structure up to 693 K.<sup>51</sup> All  $\text{In}_2\text{S}_3$  crystal structures have an fcc stacking of  $\text{S}^{2-}$  anions, but differ in the ordering of the  $\text{In}^{3+}$  cations. Hence, the anion sublattice is intrinsically different from hexagonal  $\text{Cu}_{2-x}\text{S}$  and wurtzite CIS, which is an important feature in avoiding full exchange from  $\text{Cu}_{2-x}\text{S}$  into  $\text{In}_2\text{S}_3$ . Figure 6.9 compares the rearrangement of the anion sublattice required for the partial conversion of hexagonal low-chalcocite  $\text{Cu}_{2-x}\text{S}$  into wurtzite CIS (Figure 6.9a) to the full conversion of hexagonal low-chalcocite  $\text{Cu}_{2-x}\text{S}$  into  $\beta\text{-In}_2\text{S}_3$  (Figure 6.9b). Low-chalcocite  $\text{Cu}_{2-x}\text{S}$  and wurtzite CIS both have an hcp anion sublattice, with the hexagonal layers of  $\text{S}^{2-}$  anions ABAB stacked. This conversion requires a mere 1.4% contraction within the layers and 6.4% between the layers. The anions in  $\beta\text{-In}_2\text{S}_3$ , however, are ABC stacked. Hence, the conversion from low-chalcocite to  $\beta\text{-In}_2\text{S}_3$  would require that four of every six anion layers shift over 58% of a S–S distance. Although such rearrangements from an hcp to an fcc anion sublattice have been demonstrated before,<sup>52</sup> they have high activation barriers and require high reaction temperatures. Consequently, the low reaction temperatures employed here limit the CE to the extent that only partial exchange occurs, with luminescent ternary CIS as final product.

## 6.4 Conclusions

We show successful partial, self-limited cation exchange (CE) reactions from binary low-chalcocite  $\text{Cu}_{2-x}\text{S}$  NCs to luminescent ternary wurtzite  $\text{CuInS}_2$  (CIS) NCs. With this method, large CIS NCs of 4 nm can be obtained with photoluminescence (PL) in the near-infrared (NIR), which is not possible by direct synthesis protocols. Slow extraction of  $\text{Cu}^+$  is essential, due to the balance between the Cu-extraction rate and the slow incorporation rate of  $\text{In}^{3+}$ . This slow  $\text{Cu}_{\text{out}}$  rate is achieved by choosing mild reaction temperatures. Furthermore, low reaction temperatures ensure that the CE is partial and prevent the formation of fully exchanged  $\text{In}_2\text{S}_3$ . The method presented here may prove beneficial for several applications where shape selective deposition techniques are used to fabricate assembled 2D layers, for example in the field of photovoltaics or nanophotonics. The combination of multiple morphologies attainable for  $\text{Cu}_{2-x}\text{S}$  NCs and the post-synthetic control over the composition towards CIS can thus result in the successful implementation of luminescent CIS NCs in several devices and in further tunability of the optoelectronic properties of CIS NCs. The problems arising from Cd-based luminescent NCs, such as toxicity, can be circumvented with this approach, which will prove beneficial for several applications in the field of photovoltaics, bio-imaging and lighting.

## Acknowledgments

The authors also appreciate financial support from the European Union under the

Seventh Framework Program (Integrated Infrastructure Initiative No. 262348 European Soft Matter Infrastructure, ESMI). The authors thank Josine Bulle for the synthesis of 4 nm Cu<sub>2-x</sub>S NCs, Gang Wang for XRD measurements and Joost van der Lit for image processing assistance.

## References

- (1) Rogach, A. L.; Talapin, D. V.; Shevchenko, E. V.; Kornowski, A.; Haase, M.; Weller, H. *Adv. Funct. Mater.* **2002**, *12*, 653–664.
- (2) Donega, C. d. M. *Chem. Soc. Rev.* **2011**, *40*, 1512–1546.
- (3) Skrabalak, S. E.; Xia, Y. *ACS Nano* **2009**, *3*, 10–15.
- (4) Talapin, D. V.; Murray, C. B. *Science* **2005**, *310*, 86–89.
- (5) Zhao, Y.; van Rooy, I.; Hak, S.; Fay, F.; Tang, J.; de Lange Davies, C.; Skobe, M.; Allen Fisher, E.; Radu, A.; Fayad, Z. A.; de Mello Donega, C.; Meijerink, A.; Mulder, W. J. M. *ACS Nano* **2013**, *7*, 10362–10370.
- (6) Li, L.; Daou, T.; Texier, I.; Chi, T. K. *Chem. Mater.* **2009**, *21*, 2422–2429.
- (7) Bourzac, K. *Nature* **2013**, *493*, 283.
- (8) Shirasaki, Y.; Supran, G.; Bawendi, M.; Bulović, V. *Nat. Photonics* **2012**, *7*, 13–23.
- (9) Zhang, Y.; Xie, C.; Su, H.; Liu, J.; Pickering, S.; Wang, Y.; Yu, W. W.; Wang, J.; Wang, Y.; Hahm, J.; Dellas, N.; Mohnney, S. E.; Xu, J. *Nano Lett.* **2011**, *11*, 329–332.
- (10) Kruszynska, M.; Borchert, H.; Parisi, J.; Kolny-Olesiak, J. *J. Am. Chem. Soc.* **2010**, *132*, 15976–15986.
- (11) Kolny-Olesiak, J.; Weller, H. *ACS Appl. Mater. Interfaces* **2013**, *5*, 12221–12237.
- (12) Yarema, O.; Bozyigit, D.; Rousseau, I.; Nowack, L.; Yarema, M.; Heiss, W.; Wood, V. *Chem. Mater.* **2013**, *5*, 3753–3757.
- (13) Reifsnnyder, D. C.; Ye, X.; Gordon, T. R.; Song, C.; Murray, C. B. *ACS Nano* **2013**, *7*, 4307–4315.
- (14) Kim, S.; Kang, M.; Kim, S.; Heo, J.-H.; Noh, J. H.; Im, S. H.; Seok, S. I.; Kim, S.-W. *ACS Nano* **2013**, *7*, 4756–4763.
- (15) Meillaud, F.; Shah, A.; Droz, C.; Vallat-Sauvain, E.; Miazza, C. *Sol. Energy Mater. Sol. Cells* **2006**, *90*, 2952–2959.
- (16) Shockley, W.; Queisser, H. J. *J. Appl. Phys.* **1961**, *32*, 510.
- (17) Panthani, M. G.; Stolle, C. J.; Reid, D. K.; Rhee, D. J.; Harvey, T. B.; Akhavan, V. A.; Yu, Y.; Korgel, B. A. *J. Phys. Chem. Lett.* **2013**, *4*, 2030–2034.
- (18) Krumer, Z.; Pera, S. J.; van Dijk-Moes, R. J. A.; Zhao, Y.; de Brouwer, A. F. P.; Groeneveld, E.; van Sark, W. G. J. H. M.; Schropp, R. E. I.; de Mello Donega, C. *Sol. Energy Mater. Sol. Cells* **2013**, *111*, 57–65.
- (19) Erickson, C. S.; Bradshaw, L. R.; McDowall, S.; Gilbertson, J. D.; Gamelin, D. R.; Patrick, D. L. *ACS Nano* **2014**, *8*, 3461–3467.
- (20) Tan, J. M. R.; Lee, Y. H.; Pedireddy, S.; Baikie, T.; Ling, X. Y.; Wong, L. H. *J. Am. Chem. Soc.* **2014**, *136*, 6684–6692.
- (21) Kruszynska, M.; Borchert, H.; Parisi, J.; Kolny-Olesiak, J. *J. Nanoparticle Res.* **2011**, *13*, 5815–5824.
- (22) Panthani, M. G.; Akhavan, V.; Goodfellow, B.; Schmidtke, J. P.; Dunn, L.; Dodabalapur, A.; Barbara, P. F.; Korgel, P. A. *J. Am. Chem. Soc.* **2008**, *130*, 16770–16777.
- (23) Zhong, H.; Zhou, Y.; Ye, M.; He, Y.; Ye, J.; He, C.; Yang, C.; Li, Y. *Chem. Mater.* **2008**, *20*, 6434–6443.
- (24) Xia, C.; Cao, L.; Liu, W.; Su, G.; Gao, R.; Qu, H.; Shi, L.; He, G. *CrystEngComm* **2014**, *16*, 7469–7477.
- (25) Lu, X.; Zhuang, Z.; Peng, Q.; Li, Y. *CrystEngComm* **2011**, *13*, 4040–4045.
- (26) Beberwyck, B. J.; Surendranath, Y.; Alivisatos, A. P. *J. Phys. Chem. C* **2013**, *117*, 19759–19770.
- (27) Son, D. H.; Hughes, S. M.; Yin, Y.; Alivisatos, A. P. *Science* **2004**, *306*, 1009–1012.
- (28) van der Stam, W.; Gantapara, A. P.; Akkerman, Q. A.; Soligno, G.; Meeldijk, J. D.; van Roij, R.; Dijkstra, M.; de Mello Donega, C. *Nano Lett.* **2014**, *14*, 1032–1037.
- (29) Li, H.; Zanella, M.; Genovese, A.; Povia, M.; Falqui, A.; Giannini, C.; Manna, L. *Nano Lett.* **2011**, *11*, 4964–4970.
- (30) van der Stam, W.; Akkerman, Q. A.; Ke, X.; van Huis, M. A.; Bals, S.; de Mello Donega, C. *Chem. Mater.* **2015**, *27*, 283–291.
- (31) Luther, J. M.; Zheng, H.; Sadtler, B.; Alivisatos, A. P. *J. Am. Chem. Soc.* **2009**, *131*, 16851–16857.
- (32) Bryks, W.; Wette, M.; Velez, N.; Hsu, S.-W.; Tao, A. R. *J. Am. Chem. Soc.* **2014**, *136*, 6175–6178.
- (33) Li, W.; Shavel, A.; Guzman, R.; Rubio-Garcia, J.; Flox, C.; Fan, J.; Cadavid, D.; Ibáñez, M.; Arbiol, J.;

- Morante, J. R.; Cabot, A. *Chem. Commun.* **2011**, 47, 10332–10334.
- (34) Wang, Y.; Hu, Y.; Zhang, Q.; Ge, J.; Lu, Z.; Hou, Y.; Yin, Y. *Inorg. Chem.* **2010**, 49, 6601–6608.
- (35) Li, L.; Pandey, A.; Werder, D. J.; Khanal, B. P.; Pietryga, J. M.; Klimov, V. I. *J. Am. Chem. Soc.* **2011**, 133, 1176–1179.
- (36) Hövmöller, S. *Ultramicroscopy* **1992**, 41, 121–135.
- (37) Chen, B.; Zhong, H.; Zhang, W.; Tan, Z.; Li, Y.; Yu, C.; Zhai, T.; Bando, Y.; Yang, S.; Zou, B. *Adv. Funct. Mater.* **2012**, 22, 2081–2088.
- (38) De Trizio, L.; Prato, M.; Genovese, A.; Casu, A.; Povia, M.; Simonutti, R.; Alcocer, M. J. P.; D’Andrea, C.; Tassone, F.; Manna, L. *Chem. Mater.* **2012**, 24, 2400–2406.
- (39) Delerue, C.; Lannoo, M. *Nanostructures: Theory and Modeling, 1st ed*; Springer: New York, **2004**.
- (40) de Mello Donega, C.; Koole, R. *J. Phys. Chem. C* **2009**, 113, 6511–6520.
- (41) (a) JCPDS card R120113-9, low-chalcocite Cu<sub>2</sub>S. (b) JCPDS card 01-077-9459, wurtzite CuInS<sub>2</sub>. (c) JCPDS card 00-032-0456, β-In<sub>2</sub>S<sub>3</sub>.
- (42) Rivest, J. B.; Jain, P. K. *Chem. Soc. Rev.* **2013**, 42, 89–96.
- (43) Groeneveld, E.; Witteman, L.; Lefferts, M.; Ke, X.; Bals, S.; van Tendeloo, G.; de Mello Donega, C. *ACS Nano* **2013**, 7, 7913–7930.
- (44) Pearson, R. G. *Inorg. Chem.* **1988**, 27, 734–740.
- (45) Xie, Y.; Riedinger, A.; Prato, M.; Casu, A.; Genovese, A.; Guardia, P.; Sottini, S.; Sangregorio, C.; Miszta, K.; Ghosh, S.; Pellegrino, T.; Manna, L. *J. Am. Chem. Soc.* **2013**, 135, 17630–17637.
- (46) Chakrabarti, D. J.; Laughlin, D. E. *Bull. Alloy Phase Diagrams* **1983**, 4, 254–270.
- (47) Noerby, P.; Johnsen, S.; Iversen, B. B. *ACS Nano* **2014**, 8, 4295–4303.
- (48) Buerger, M. J.; Wuensch, B. J. *Science* **1963**, 141, 276–277.
- (49) Evans, H. T. *Nature* **1971**, 232, 69–70.
- (50) Wyckoff, R. W. G. *Structure of Crystals; American Chemical Society Monograph Series; American Chemical Society: Washington, DC, 1935*.
- (51) Diehl, R.; Nitsche, R. J. *Cryst. Growth* **1975**, 28, 306–310.
- (52) Huang, X.; Li, S.; Huang, Y.; Wu, S.; Zhou, X.; Li, S.; Gan, C. L.; Boey, F.; Mirkin, C. A.; Zhang, H. *Nat. Commun.* **2011**, 2, 292.





# Near-Infrared Emitting $\text{CuInSe}_2/\text{CuInS}_2$ Core/Shell Heteronanorods by Sequential Cation Exchange



## ABSTRACT

In this chapter, we report a sequential topotactic cation exchange (CE) pathway that yields  $\text{CuInSe}_2/\text{CuInS}_2$  dot core/rod shell nanorods with near-infrared luminescence. In our novel approach, the  $\text{Cu}^+$  extraction rate is coupled to the  $\text{In}^{3+}$  incorporation rate by the use of a stoichiometric trioctylphosphine- $\text{InCl}_3$  complex, which fulfills the roles of both In-source and Cu-extracting agent. This is in contrast to the method described in the previous chapter, in which the balance between the in- and outgoing rate proved to be delicate and needed to be precisely balanced for successful cation exchange (CE) to occur. In our new CE protocol,  $\text{Cu}^+$  ions can only be extracted by trioctylphosphine ligands when the In-P bond is broken. This results in readily available  $\text{In}^{3+}$  ions at the same surface site from which the  $\text{Cu}^+$  is extracted, making the process a direct place exchange reaction and shifting the overall energy balance in favor of the CE. Consequently, controlled cation exchange can occur even in large and anisotropic heterostructured nanocrystals with preservation of the size, shape and hetero-structuring of the template NCs into the product NCs. The method is very versatile, successfully yielding a variety of luminescent  $\text{CuInX}_2$  ( $X = \text{S}, \text{Se}$  and  $\text{Te}$ ) quantum dots, nanorods, and heteronanocrystals, by using Cd-chalcogenide NCs and HNCs as templates.

### Based on

**Near-Infrared Emitting  $\text{CuInSe}_2/\text{CuInS}_2$  Dot Core/Rod Shell Heteronanorods by Sequential Cation Exchange**

*W. van der Stam, E. Bladt, F. T. Rabouw, S. Bals and C. de Mello Donega, ACS Nano, 2015, 9, 11430–11438.*

## 7.1 Introduction

The unique size- and shape-dependent properties of colloidal semiconductor nanocrystals (NCs), combined with their easy solution processability, have turned them into promising materials for a variety of technologies.<sup>1</sup> Colloidal NCs consisting of two (or more) different semiconductors (*i.e.*, heteronanocrystals, HNCs) offer even more possibilities regarding property engineering, since the carrier localization regime in these materials can be tailored by controlling the composition, size and shape of each component, and the architecture of the HNC (see also Chapter 2).<sup>1</sup> Over the last decades, a remarkable degree of precision has been achieved in the synthesis of NCs and core/shell HNCs based on Cd- and Pb-chalcogenides (CdX and PbX, with X = S, Se, Te),<sup>1-4</sup> leading to materials with exceptional properties (*e.g.*, high quantum yields,<sup>3</sup> reduced blinking,<sup>5,6</sup> reduced threshold for lasing<sup>7</sup>). However, the large scale deployment of these NCs is limited by the toxicity of Pb and Cd. This has stimulated a worldwide research effort on alternative materials that possess comparable properties and are less toxic.

Nanocrystals based on ternary I-III-VI semiconductors such as  $\text{CuInX}_2$  are an attractive option, since their photoluminescence (PL) can be tuned from the visible to the near-infrared (NIR), which is relevant for applications such as light-emitting devices or biomedical imaging.<sup>8-12</sup> Moreover, they are also promising for applications in solar energy conversion (PV and photocatalysis).<sup>9</sup> However, the synthesis of ternary NCs is challenging, since multiple precursor reactivities must be simultaneously controlled. As a result, direct synthesis protocols for colloidal  $\text{CuInX}_2$  NCs are still largely underdeveloped,<sup>13-18</sup> and do not offer the same degree of control available for Cd-based NCs. To date, it has not been possible to grow luminescent anisotropic ternary NCs, or to combine two different  $\text{CuInX}_2$  compounds into a single HNC by hetero-epitaxial overgrowth. Here, we report a novel method that yields luminescent  $\text{CuInSe}_2/\text{CuInS}_2$  (CISe/CIS) dot core/rod shell heteronanorods by applying sequential ( $\text{Cu}^+$  for  $\text{Cd}^{2+}$  followed by self-limited partial  $\text{In}^{3+}$  for  $\text{Cu}^+$ ) topotactic cation exchange (CE) reactions to template Cd-chalcogenide HNCs. The generality of our approach is demonstrated by converting a variety of Cd-chalcogenide (H)NCs into luminescent CuIn-chalcogenide (H)NCs, with preservation of the size, shape and hetero-architecture of the template NCs.

## 7.2 Methods

**Materials.** Cadmium oxide (CdO, 99.5%, trace metal basis), tetrakisacetonitrile copper(I) hexafluorophosphate ( $[\text{Cu}(\text{CH}_3\text{CN})_4]\text{PF}_6$ ), Indium chloride ( $\text{InCl}_3$ , 99.999%), trioctylphosphine oxide (TOPO, tech., 90%), trioctylphosphine (TOP, 90%), octadecyl phosphonic acid (ODPA, 97%), 1-octadecene (ODE, tech., 90%), sulfur powder (S, 99.98%, trace metal basis), chloroform, anhydrous methanol and anhydrous toluene were purchased from Sigma-Aldrich and used as delivered, except for TOPO and ODE,

which were degassed prior to use by applying vacuum at 120 °C for 2 h. Selenium powder (Se, ~200 mesh, 99.999%) was bought from Brunschwig Chemie and used as supplied.

*The CdSe nanocrystals (NCs)* used as seeds were synthesized according to the method reported by Carbone *et al.*<sup>2</sup> In a typical synthesis, 0.060 g CdO, 3.0 g TOPO and 0.290 g ODPa were mixed in a 50 mL three-neck flask and heated to 150 °C under vacuum in a Schlenk line. After 2 h, the solution was heated to 330 °C under nitrogen until it became transparent. 1.5 g TOP was then injected, followed by heating to 370 °C and injection of TOP-Se (0.058 g Se in 0.360 g TOP). The NCs were allowed to grow for 7 min, after which the reaction was quenched by removal of the heating source. 5 mL toluene was injected when the temperature had dropped below 70 °C. In order to remove excess reactants, the CdSe NCs were washed three times by precipitation with methanol from a solution in toluene. The purified NCs were redispersed in toluene.

*CdSe/CdS dot core/rod shell nanorods* were synthesized using a seeded growth approach.<sup>2</sup> 0.090 g CdO, 3.0 g TOPO and 0.330 g ODPa were mixed in a 100 mL three-neck flask and degassed at 150 °C under vacuum for 2 h in a Schlenk line. The reaction mixture was subsequently heated to 350 °C. When a transparent solution was obtained, 1.5 g TOP was first injected, followed by the injection of a TOP-S solution (0.12 g S in 1.5 g TOP) and 200 µL CdSe NC seeds in TOP (400 µM). After 12 min, the reaction was quenched by removal of the heating source and the NRs were washed by precipitation/redispersion with 5 mL methanol and 5 mL toluene.

*Cu<sup>+</sup> for Cd<sup>2+</sup> cation exchange* was performed following the method reported by Li *et al.*<sup>51</sup> In a typical synthesis, 15 mg (0.04 mmol) [Cu(CH<sub>3</sub>CN)<sub>4</sub>]PF<sub>6</sub> was dissolved into 2 mL of methanol and added to 4 mL of a CdSe/CdS NRs solution in toluene (~2×10<sup>-9</sup> M). To ensure full exchange, a 10-fold excess of Cu<sup>+</sup> ions was used. The solution was stirred at room temperature for 5 min, after which the NRs were separated from the reaction solution by centrifuging at 3000 rpm for 5 min. Finally, the Cu<sub>2</sub>Se/Cu<sub>2</sub>S NRs were redispersed in 1 mL toluene.

*In<sup>3+</sup> for Cu<sup>+</sup> cation exchange* was performed using an adaptation of our recently reported method (discussed in the previous chapter).<sup>26</sup> 100 µL of a 2M TOP-InCl<sub>3</sub> precursor in ODE (1 mmol InCl<sub>3</sub> in 0.5 mL TOP, diluted with 3 mL ODE) was added to 0.5 mL of a diluted NCs solution (10<sup>-9</sup> M) in toluene at 100 °C. The solution was stirred for 4 h, after which the excess precursor was removed by precipitation with ~5 mL methanol followed by redispersion in ~5 mL toluene. This washing cycle was repeated twice.

*Optical spectroscopy.* Samples for optical spectroscopy measurements were prepared by diluting the stock solution of washed NCs with anhydrous toluene. The samples were stored under nitrogen in sealed quartz cuvettes. Absorption spectra were measured on a double beam Perkin-Elmer Lambda 16 UV/Vis spectrometer. Photoluminescence (PL) and PL excitation spectra were recorded on an Edinburgh Instruments FLS920 Spectrofluorimeter equipped with a 450 W Xenon lamp as excitation source and double grating monochromators. PL decay curves were obtained by time-correlated single-photon counting on a liquid nitrogen cooled Hamamatsu R5509-72 photomultiplier tube. A pulsed diode laser (EPL-445 Edinburgh Instruments, 441 nm, 55 ps pulse width, 0.2 MHz repetition rate) was used as the excitation source.

*X-ray Diffraction (XRD)* measurements were performed with a Bruker D2 Phaser, equipped with a Co K $\alpha$  X-ray source ( $\lambda = 1.79026$  Å). Thin NC solid films for XRD were prepared by drop-casting a concentrated NC solution in chloroform on a Si wafer and evaporating the solvent.

*Transmission Electron Microscopy (TEM)* images were acquired using a FEI Tecnai-10 microscope operating at 100 kV. Samples for TEM imaging were prepared by drop-casting a toluene solution of NCs onto a carbon-coated copper (400-mesh) TEM grid.

*High-Resolution Transmission Electron Microscopy (HRTEM)* images were acquired on a Titan electron microscope operating at 300 kV. The sample was drop-casted on an ultrathin grid to reduce the background signal from the carbon support and thereby improve the image quality.

*Electron tomography* experiments were performed on a Tecnai G2 operating at 200 kV. Tilt series of 15 projection images were acquired in HAADF-STEM mode with an angular range from  $-70^\circ$  to  $+70^\circ$  and a tilt increment of  $10^\circ$ . Because the acquisition of several images at the same region of interest was causing an accumulation of contamination, the ultrathin grids were baked at  $120^\circ\text{C}$  for several hours.

*Energy Dispersive X-ray Spectroscopy (EDS)* measurements were performed on a FEI Tecnai G2 electron microscope operated at 200 kV, using a dedicated low background holder and Cu-free Mo TEM grids. The EDS acquisition was carried out using a ChemiSTEM system and analyzed using the Bruker ESPRIT software. The following lines were used: S-K at 2.3 keV, In-L at 3.3 keV and Cu-K at 8.0 keV. The In-L and Cu-K are well-resolved but S-K partially overlaps with one of the Mo peaks at 2.4 keV. The software deconvoluted these two peaks in order to allow the quantification of the S content. To verify the elemental concentrations determined, EDS measurements were also performed on a FEI Tecnai-20F microscope operating at 200 kV, using a dedicated low background holder and Cu-free Al TEM grids. The EDS-signal is acquired with an EDAX Si(Li) detector and analyzed with the Tecnai Imaging and Analysis software, using the following lines: S-K at 2.3 keV, In-L at 3.3 keV and Cu-K at 8.0 keV.

## 7.3 Results and Discussion

### 7.3.1 Optical spectroscopy of CdSe/CdS and CuInSe<sub>2</sub>/CuInS<sub>2</sub> heteronanorods

Our approach is schematically depicted at the top of Figure 7.1, which also shows the optical spectra of a representative series of samples. The parent CdSe/CdS dot core/rod shell heteronanorods (NRs) show efficient PL at 2.07 eV and an absorption spectrum dominated by CdS transitions. After the Cu<sup>+</sup> for Cd<sup>2+</sup> CE reaction the NRs become non-luminescent and exhibit an absorption spectrum typical of Cu-chalcogenides. After removal from the reaction mixture and washing, the Cu-based NRs are subjected to a partial In<sup>3+</sup> for Cu<sup>+</sup> CE that yields NRs with PL in the NIR centered at 1.22 eV and an absorption spectrum that is consistent with CuIn-chalcogenide based NCs (Figure 7.1a). Sequential CE reactions (Cu<sup>+</sup> for Cd<sup>2+</sup> followed by partial In<sup>3+</sup> for Cu<sup>+</sup>) were also performed on other CdSe/CdS dot core/rod shell NR samples and yielded similar results (Figure 7.1b, core diameters range from 2.7 nm, 3.1 nm and 3.2 nm and nanorod length/diameter range from  $50.9\pm 14.5$  nm/ $5.2\pm 1.1$  nm,  $45.5\pm 4.2$  nm/ $4.6\pm 0.6$  nm and  $23.5\pm 2.7$  nm/ $4.3\pm 0.6$  nm, for NRs emitting at 1.22, 1.19, and 1.17 eV, respectively).

### 7.3.2 Conversion of CdSe/CdS heteronanorods into CuInSe<sub>2</sub>/CuInS<sub>2</sub> heteronanorods

Transmission Electron Microscopy (TEM) measurements show that the size and shape of the parent CdSe/CdS NRs is preserved in the product CuInSe<sub>2</sub>/CuInS<sub>2</sub> (CISe/CIS) NRs after the sequential CE reactions (Figure 7.2a–c). Energy Dispersive X-ray Spectroscopy (EDS) measurements show a Cd:S ratio of 1:1 for the parent CdSe/CdS NRs, a Cu:S ratio of 2.1:1 for the intermediate Cu-based NRs (Figure A7.1a) and a Cu:In:S ratio of 0.8:1.3:2 for the product CISe/CIS NRs (Figure A7.1c). Residual Cd<sup>2+</sup> is observed in the intermediate Cu-based NRs ( $\sim 2\%$ ), but is not detected in the product CISe/CIS NRs. These measurements indicate a successful sequential CE pathway toward CISe/CIS NRs. The product CISe/CIS NRs are accompanied by a by-product of the CE reaction that was not completely removed by the washing-up procedure

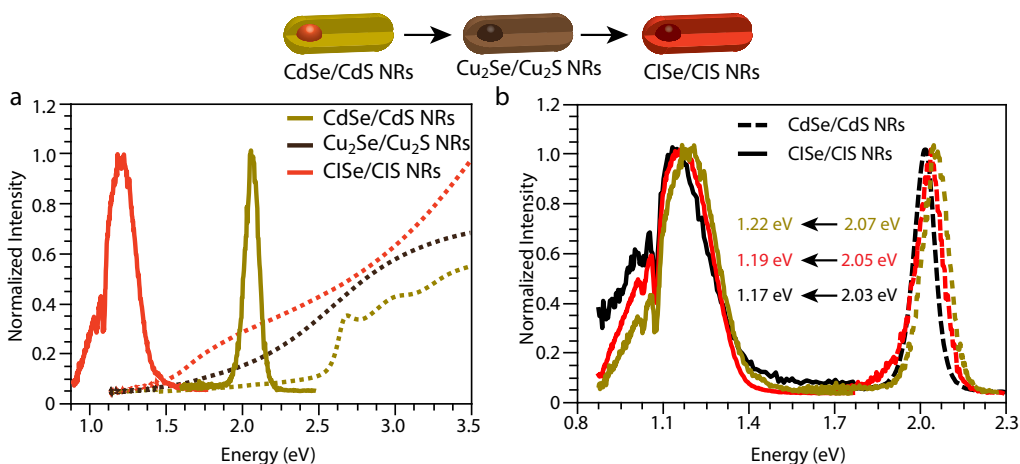


**Figure 7.1. Optical spectroscopy of CdSe/CdS and  $\text{CuInSe}_2/\text{CuInS}_2$  heteronanorods** Top: Schematic representation of the sequential cation exchange reaction, yielding ternary core/shell  $\text{CuInSe}_2/\text{CuInS}_2$  (CISE/CIS) heteronanorods. (a) Absorption (dashed lines) and photoluminescence (solid lines) spectra of the template CdSe/CdS NRs (orange lines), the intermediate  $\text{Cu}_2\text{Se}/\text{Cu}_2\text{S}$  NRs (brown lines) and the final product CISE/CIS NRs (red lines). (b) Photoluminescence (PL) spectra of product CISE/CIS dot core/rod shell nanorods (full lines) with different core and shell dimensions obtained from template CdSe/CdS dot core/rod shell nanorods by sequential cation exchange reactions ( $\text{Cu}^+$  for  $\text{Cd}^{2+}$  followed by partial  $\text{In}^{3+}$  for  $\text{Cu}^+$ ). The PL spectra of the parent CdSe/CdS core/shell nanorods are also shown (dashed lines). The PL peak energies prior to and after the cation exchange reactions are also given.

(see dark spots in Figure 7.2c). This by-product is probably residual TOP- $\text{InCl}_3$  (TOP: trioctylphosphine), since it consists only of In (*i.e.*, S and Cu peaks are not observed in the EDS measurements, Figure A7.1b). Therefore, EDS spectra which were collected over large areas containing both nanorods and by-product, provide a reliable Cu:S ratio (1:2), but overestimate the In content. We corrected for this contribution by measuring EDS spectra on single NRs, which revealed a Cu:In:S ratio that is consistent with the  $\text{CuInS}_2$  stoichiometry. EDS measurements were also carried out on small groups of isolated NRs, without the by-product, yielding a Cu:In:S ratio of 0.8:1.3:2 (Figure A7.1c). We note that the Se signal of the core is not detected since the majority of the volume of the NRs consists of the metal sulfide compositions (CdS,  $\text{Cu}_2\text{S}$  and CIS, respectively).

High-Resolution (HR) High-Angle Annular Dark Field Scanning TEM (HAADF-STEM) measurements also confirm the successful sequential cation exchange from parent CdSe/CdS dot core/rod shell NRs into product CISE/CIS dot core/rod shell NRs *via* intermediate  $\text{Cu}_2\text{Se}/\text{Cu}_2\text{S}$  dot core/rod shell NRs (Figure 7.2d–f). The HAADF-STEM investigation indicates that the parent CdSe/CdS core/shell NRs have the CdS wurtzite structure, since the Fast Fourier Transform (FFT) analysis of the HRTEM

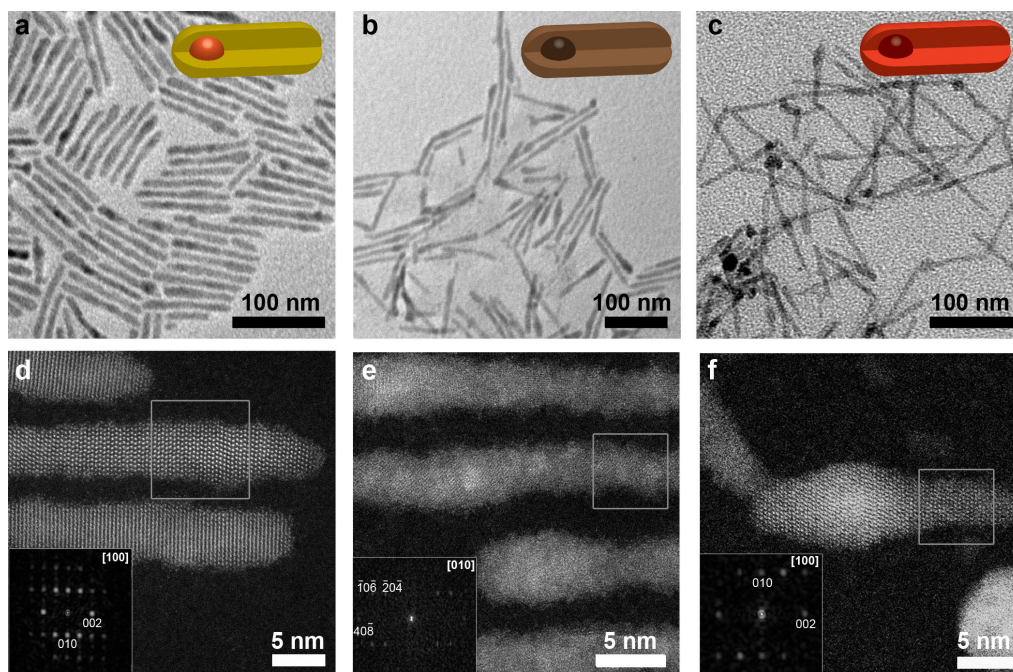


**Figure 7.2. Size and shape preservation after sequential cation exchange reactions.** Transmission Electron Microscopy (a–c) and High-Resolution HAADF-STEM (d–f) images of CdSe/CdS core/shell NRs (a,d), Cu<sub>2</sub>Se/Cu<sub>2</sub>S core/shell NRs (b,e) and CuInSe<sub>2</sub>/CuInS<sub>2</sub> (CISE/CIS) core/shell NRs (c,f). The CISE/CIS NRs shown in (c,f) were obtained by sequential CE (Cu<sup>+</sup> for Cd<sup>2+</sup> followed by partial In<sup>3+</sup> for Cu<sup>+</sup>) using the CdSe/CdS NRs shown in (a,d) as templates, and the Cu<sub>2</sub>Se/Cu<sub>2</sub>S NRs shown in (b,e) as intermediates. The squares in panels d–f indicate regions where FFT analysis was performed. The corresponding FFT patterns show characteristic {010} and {002} wurtzite CdS reflections for CdSe/CdS core/shell NRs (inset panel d), characteristic chalcocite Cu<sub>2</sub>S reflections for Cu<sub>2</sub>Se/Cu<sub>2</sub>S core/shell NRs (inset panel e), and characteristic wurtzite CIS reflections for CISE/CIS core/shell NRs (inset panel f). The zone axis is indicated in the insets as well.

image (Inset in Figure 7.2d) shows the characteristic {002} and {010} wurtzite CdS lattice planes. The thickness of the NRs varies from 9 to 15 atomic columns. Note that the majority of the volume of the NRs consists of CdS and therefore the contribution of the CdSe core is not detected. FFT analysis of the HRTEM measurements shows that the product CISE/CIS NRs have the wurtzite CuInS<sub>2</sub> crystal structure (Inset in Figure 7.2f and XRD pattern in Figure A7.2). From high-resolution HAADF-STEM imaging, we could determine that the resulting CISE/CIS NRs have a varying thickness of 8 to 14 atomic columns, consistent with the thickness of the template CdSe/CdS NRs. The position of the core was located by HAADF-STEM electron tomography (Figure 7.3). Since the intensity in HAADF-STEM images scales with the atomic number  $Z$ , this technique can distinguish between parts of the NRs containing Se ( $Z_{\text{Se}} = 34$ ) and S ( $Z_{\text{S}} = 16$ ). The electron tomography reconstruction shows that the cores are slightly

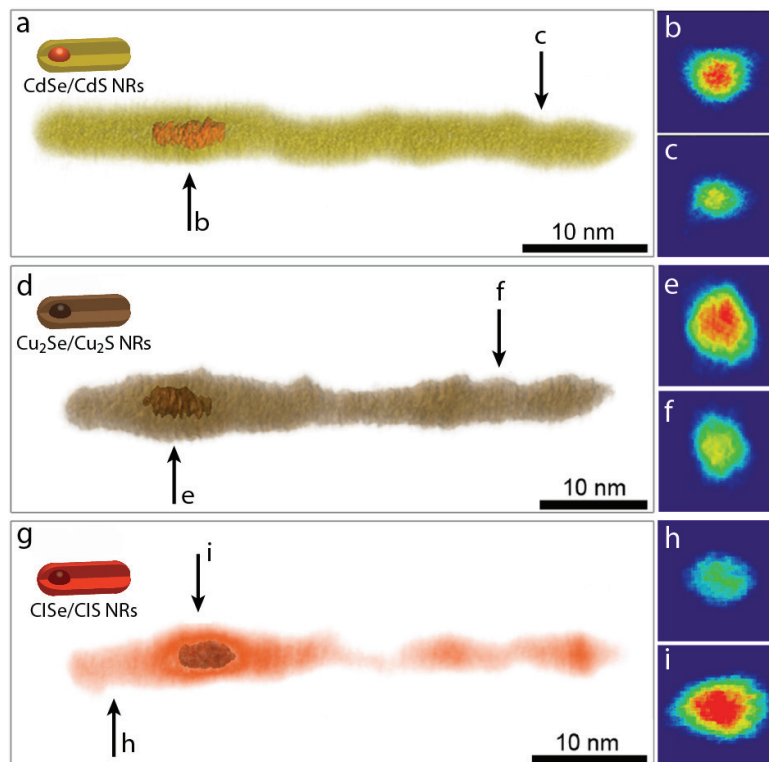


**Figure 7.3. Visualizations of tomographic 3D reconstructions** of (a) the template CdSe/CdS core/shell NRs (yellow: CdS, orange: CdSe), (d) the intermediate  $\text{Cu}_2\text{Se}/\text{Cu}_2\text{S}$  core/shell NRs (light brown:  $\text{Cu}_2\text{S}$ , dark brown:  $\text{Cu}_2\text{Se}$ ) and (g) the final product  $\text{CuInSe}_2/\text{CuInS}_2$  core/shell NRs (light red:  $\text{CuInS}_2$ , dark red:  $\text{CuInSe}_2$ ). Orthoslices at positions marked with **b** and **c** for CdSe/CdS NRs, **e** and **f** for  $\text{Cu}_2\text{Se}/\text{Cu}_2\text{S}$  NRs and **h** and **i** for  $\text{CuInSe}_2/\text{CuInS}_2$  NRs show the position of the Se-containing cores, due to the difference in Z-contrast ( $Z_{\text{Se}} = 34$  and  $Z_{\text{S}} = 16$ ).

elongated and that their shape is preserved in the product HNCs, showing that the anionic sublattice is not affected by the sequential CE reactions. We should note that the acquisition of several images at the same position of interest caused a lot of carbon contamination, due to the ligands covering the NRs. Therefore, the grids were baked at  $120\text{ }^\circ\text{C}$  for several hours in order to remove the organic ligands from the surface of the NRs. After this treatment, the organic contamination decreased, but also the shell of the CISE/CIS and  $\text{Cu}_2\text{Se}/\text{Cu}_2\text{S}$  NRs was slightly altered (Figure 7.3d,g).

### 7.3.3 Mechanism

Nanoscale cation exchange (CE) has emerged as a promising alternative for direct synthesis protocols, offering post-synthetic control over the composition and crystal structure, while preserving the size and shape of the parent NCs into the product

NCs.<sup>19</sup> This allows access to NCs and HNCs otherwise not attainable.<sup>19–32</sup> Copper-chalcogenide NCs are often used as parent (template) NCs or intermediates in sequential CE reactions, because  $\text{Cu}^+$  is easily exchanged by other cations.<sup>19,21–27</sup> For example, ZnSe/ZnS core/shell NRs<sup>21</sup> and ultrathin nanoplatelets (NPLs)<sup>27</sup> have been obtained by sequential CE ( $\text{Cu}^+$  for  $\text{Cd}^{2+}$  followed by  $\text{Zn}^{2+}$  for  $\text{Cu}^+$ ) in template CdSe/CdS core/shell NRs<sup>21</sup> and NPLs,<sup>27</sup> respectively, while wurtzite InP NPLs<sup>25</sup> were prepared by  $\text{Cu}^+$  for  $\text{In}^{3+}$  CE in template  $\text{Cu}_{3-x}\text{P}$  NPLs. The exchangeability of  $\text{Cu}^+$  stems from its small charge and size, resulting in fast diffusion rates at the nanoscale, in combination with the availability of Cu-extracting ligands in solution.<sup>19</sup> Tri-*n*-octylphosphine (TOP) is commonly used to extract  $\text{Cu}^+$  from NCs,<sup>21,22,24–26</sup> due to the strong affinity of the soft Lewis acid  $\text{Cu}^+$  (absolute hardness  $\eta = 6.28$  eV)<sup>33</sup> and the soft base TOP ( $\eta = 6$  eV).<sup>33</sup> In Chapter 6, we demonstrated that CE reactions can be used to produce NCs of ternary semiconductors, by performing partial  $\text{In}^{3+}$  for  $\text{Cu}^+$  CE in  $\text{Cu}_{2-x}\text{S}$  NCs, which resulted in luminescent wurtzite  $\text{CuInS}_2$  NCs.<sup>26</sup> Interestingly, the CE reaction is self-limited in this case, stopping when the ternary  $\text{CuInS}_2$  composition is reached. The self-limitation can be understood by considering the crystal structure of  $\text{In}_2\text{S}_3$ , which would require a reorganization of the anionic sublattice from hcp to fcc close-packing if the  $\text{In}^{3+}$  for  $\text{Cu}^+$  exchange were to reach completion forming  $\text{In}_2\text{S}_3$ .<sup>26</sup> This reorganization has a high activation barrier, since it requires the S-S distances of four out of every six anion layers to shift by over 58%.<sup>26</sup> We also found that the balance between the  $\text{In}^{3+}$  ingoing rate and the  $\text{Cu}^+$  outgoing rate is delicate and should be precisely balanced for a successful partial CE reaction to occur. When the out- and inward diffusion rates are not balanced, either the parent NCs dissolve or the CE reaction does not proceed at all. The imbalance between the in- and outgoing diffusion rates in  $\text{Cu}_{2-x}\text{S}$  nanoplatelets subjected to  $\text{In}^{3+}$  for  $\text{Cu}^+$  CE has also been recently reported to result in hollow  $\text{CuInS}_2$  nanoplatelets,<sup>35</sup> due to the nanoscale Kirkendall effect.<sup>34,35</sup>

In the present case, we apply an adaptation of our previous self-limited  $\text{In}^{3+}$  for  $\text{Cu}^+$  CE protocol<sup>26</sup> as the second step in a sequential topotactic CE reaction, through which template Cd-chalcogenide NCs and HNCs are first cation exchanged to Cu-chalcogenide NCs and HNCs, and subsequently subjected to a partial  $\text{In}^{3+}$  for  $\text{Cu}^+$  CE. To improve the balance between the  $\text{In}^{3+}$  incorporation and the  $\text{Cu}^+$  extraction rates, we used a nearly stoichiometric TOP-InCl<sub>3</sub> complex (TOP/In ratio = 1.1), which fulfilled the roles of both In-source and Cu-extracting agent (Figure 7.4). In this way, the extraction and incorporation rates are strongly coupled, since  $\text{Cu}^+$  ions can only be extracted by TOP ligands when the In-P bond is broken. This results in readily available  $\text{In}^{3+}$  ions at the same surface site from which the  $\text{Cu}^+$  is extracted, making the process a direct place exchange reaction (similar to the case of  $\text{Cd}^{2+}$  for  $\text{Zn}^{2+}$  in ZnSe NCs),<sup>20</sup> and shifting the overall energy balance in favor of the CE, since  $\text{In}^{3+}$  ions are more stable in the NCs and  $\text{Cu}^+$  ions are more stable as TOP-Cu complexes in solution (bond dissociation energies in the gaseous state:<sup>36</sup> In-P: 198 kJ/mol, In-S: 289 kJ/mol, Cu-S: 285 kJ/mol). Cu-P dissociation energy is not available, but a strong interaction between  $\text{Cu}^+$

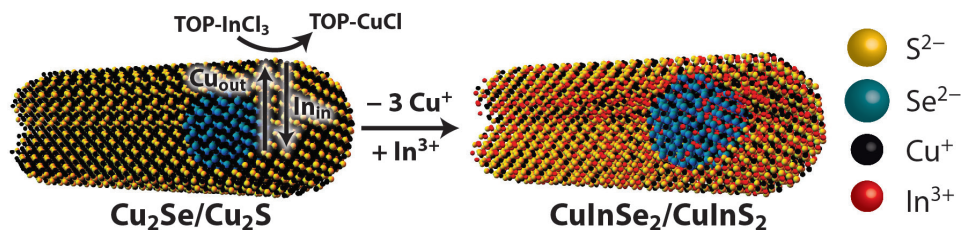


**Figure 7.4. Schematic representation of the In<sup>3+</sup> for Cu<sup>+</sup> single-step CE reaction in Cu<sub>2</sub>Se/Cu<sub>2</sub>S core/shell heteronanorods.** The Cu<sub>out</sub> and In<sub>in</sub> rates are now coupled, since Cu<sup>+</sup> can only be extracted by trioctylphosphine (TOP) when In<sup>3+</sup> is readily available for simultaneous incorporation.

and TOP can be expected based on their similar chemical hardness  $\eta$  (*viz.*, 6.28 and 6 eV,<sup>19,33</sup> respectively). This approach is in contrast with previous works (including ours),<sup>21,22,24–26</sup> in which a large excess of TOP was used, resulting in fast extraction of Cu<sup>+</sup> ions and decoupling of the in- and outward rates, since the Cu<sup>+</sup> extraction and the In<sup>3+</sup> incorporation then proceed by two separate chemical pathways.<sup>26</sup> As a result, the inward and outward rates can be influenced separately by choosing the right reaction parameters, but may also easily become imbalanced, especially in larger<sup>26</sup> and/or anisotropic NCs.<sup>35</sup> In our newly developed method, the imbalance is prevented, allowing controlled cation exchange to occur even in large and anisotropic heterostructured nanocrystals, such as the dot core/rod shell heteronanorods shown above (Figures 7.2 and 7.3). In agreement with our previous work<sup>26</sup> and the discussion above, the In<sup>3+</sup> for Cu<sup>+</sup> CE reaction is self-limited, stopping when the ternary core/shell composition is reached, despite the fact that In<sup>3+</sup> is in excess (both the Cu<sup>+</sup> for Cd<sup>2+</sup> and the In<sup>3+</sup> for Cu<sup>+</sup> CE reactions required a ~10:1 excess of the incoming cation with respect to the native cation).

It is interesting to note that our results imply that the inward and outward diffusion fluxes proceed at comparable rates through both the sulfide and selenide sublattices, since no evidence for a strong imbalance is observed. Based on the observations reported by Buhro and coworkers for In<sup>3+</sup> for Cu<sup>+</sup> CE in Cu<sub>2-x</sub>S nanoplatelets,<sup>35</sup> one could expect that either a hollow center would develop (if Cu<sub>out</sub> faster than In<sub>in</sub> in the selenide sublattice) or the shell would partially collapse (if Cu<sub>out</sub> faster than In<sub>in</sub> in the sulfide sublattice), in case the rates would be severely imbalanced. Our results provide no support for either of these limiting-case scenarios, indicating that the balance between the Cu<sub>out</sub> and In<sub>in</sub> rates is similar in both the selenide core and the sulfide shell (Figure 7.4). This is likely due to the similarity between the crystal structures and binding energies in the two materials (the lattice mismatch between wurtzite CISE and CIS is small, *viz.* ~4%,<sup>17,37</sup> and the bond dissociation energies are 247 and 289 kJ/mol,<sup>36</sup> for the In-Se and the In-S bonds, respectively, and 285 and 293 kJ/mol for the

Cu-S and Cu-Se bonds,<sup>36</sup> respectively).

It should also be noticed that TOP coordinates not only to the soft Lewis acid  $\text{Cu}^+$ , but also to chalcogenides. In fact, TOP-chalcogen complexes with S, Se and Te are widely used as chalcogen precursors in the synthesis of colloidal NCs of metal chalcogenides, and are also important ligands to passivate surface states in these NCs.<sup>1</sup> Recently, TOP has also been shown to bind to chalcogenide ions in Cu chalcogenide NCs.<sup>38</sup> When non-stoichiometric Cu selenide NCs are exposed to a large excess of TOP, both  $\text{Cu}^+$  and  $\text{Se}^{2-}$  ions are removed from the NCs,<sup>38</sup> increasing the concentration of vacancies and thereby accelerating the CE rates. However, in the present case, TOP is not in excess. In fact, all TOP available is complexed to  $\text{InCl}_3$  and therefore, TOP is able to select only the preferred ions according to HSAB theory, *i.e.* the softest acids, which, under the conditions prevalent in our experiments, will be the  $\text{Cu}^+$  ions. Furthermore, we see no evidence for restructuring of the NCs after the second CE reaction. The effect of solvation of chalcogens by TOP on the CE rates is therefore negligible in the present case, due to the use of a (nearly) stoichiometric TOP- $\text{InCl}_3$  complex.

#### 7.3.4 Exciton recombination in $\text{CuInSe}_2/\text{CuInS}_2$ heteronanorods

The PL excitation (PLE) spectrum of the CISE/CIS NRs closely matches the absorption spectrum (Figure 7.5a). This indicates that absorption anywhere in the CISE/CIS NR heterostructure, either in the CISE core or in the CIS rod shell, results in NIR emission. The situation is therefore analogous to the parent CdSe/CdS dot core/rod shell NRs, in the sense that the rod shell acts as an antenna that absorbs strongly, and funnels excited charge carriers to the emissive core. The PL decay curve was fitted with a biexponential decay curve, with a fast component of 103 ns and a slow component of 1078 ns (Figure 7.5b). Such slow decay dynamics (with  $\tau_1 \sim$  tens of ns and  $\tau_2 \sim$  hundreds of ns) are typically encountered in  $\text{CuInX}_2$  NCs.<sup>9,39,40</sup> Slow decay dynamics with a fast component of a hundred ns and a slow component of a  $\mu\text{s}$  could be beneficial for the implementation of these CISE/CIS core/shell NRs into devices, since typically long carrier lifetimes are crucial for the effective extraction of charge carriers in photovoltaics,<sup>41</sup> and are also beneficial for photocatalytic applications.<sup>42</sup> Furthermore, our ternary CISE/CIS core/shell NRs provide the first system to study charge carrier dynamics at nanoscale hetero-interfaces between two ternary I-III-VI semiconductors.

The carrier localization regime in semiconductor HNCs (*viz.*, Type-I, Type-I<sup>1/2</sup>, or Type-II) can be tuned by controlling the composition, size, and shape of each component of the HNC.<sup>1</sup> This allows a number of properties (*e.g.*, exciton radiative lifetimes, exciton-phonon coupling strength, PL peak position and bandwidth, Stokes shift, Auger recombination rates, lasing threshold) to be tailored,<sup>1,5-7,43-45</sup> and has therefore been extensively studied for HNCs based on Cd-chalcogenides and other II-VI semiconductors. In contrast, the impact of the energy offsets across nanoscale heterojunctions in HNCs based on ternary Cu-chalcogenides has not yet been

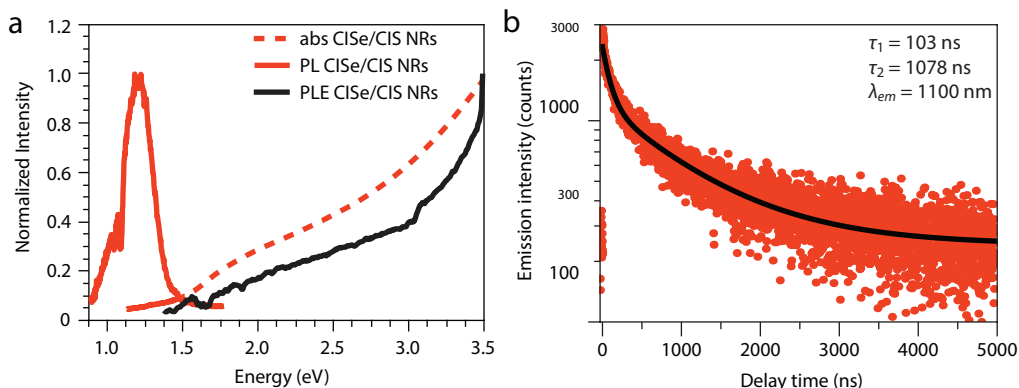


**Figure 7.5. Recombination in CuInSe<sub>2</sub>/CuInS<sub>2</sub> heteronanorods.** (a) Absorption (red dashed line), Photoluminescence (PL, red full line) and PL excitation (PLE, black line) spectra of CuInSe<sub>2</sub>/CuInS<sub>2</sub> core/shell NRs, obtained after sequential CE reactions. The PLE spectrum was acquired by setting the emission wavelength at the maximum of emission. (b) PL decay curve of CuInSe<sub>2</sub>/CuInS<sub>2</sub> core/shell NRs obtained by sequential CE. Fitting a biexponential to the data (black curve) yields a fast component with  $\tau_1 = 103$  ns and a slow component with  $\tau_2 = 1078$  ns. The emission wavelength was set at 1100 nm.

addressed in detail, and is likely to depend on the nature of the PL in these materials, which is nevertheless still under debate. Very often the PL of CIS NCs is assigned to a donor-acceptor pair recombination (DAP) involving native point defects.<sup>9,39,40</sup> However, some studies ascribe it to the radiative recombination of quantized valence band hole states with trapped electrons,<sup>46</sup> while others attribute it to recombination of quantized conduction band electron states with localized holes (as discussed in more detail in Chapter 2).<sup>13</sup> Recently, Efros and coworkers proposed that the PL of CIS QDs is analogous to that of the prototypical II-VI QDs, and also originates from the 1S(e) → 1S(h) exciton transition.<sup>47</sup> This model precludes the involvement of trapped carriers, and explains the intriguing characteristics of the PL of CIS NCs by the nature of the 1S(hole) fine-structure states.<sup>47</sup> The novel HNCs developed in the present work are likely to shed new light on the mechanisms behind the PL of CuIn chalcogenide NCs, thus contributing toward settling this long-standing debate.

### 7.3.5 Cation exchange toward other ternary CuInX<sub>2</sub> (hetero)architectures

To demonstrate the generality of our approach, we also carried out sequential CE reactions using spherical core/shell CdSe/CdS HNCs, prolate CdTe/CdSe HNCs, CdSe NRs and different sizes of CdSe and CdTe quantum dots (QDs) as templates. In all these cases, the intermediate Cu-chalcogenide NCs did not show PL, whereas after self-limited partial In<sup>3+</sup> for Cu<sup>+</sup> exchange, PL in the NIR was observed (Figure 7.6). It is interesting to notice that the NIR PL peak position is clearly correlated with the size, composition and shape/architecture of the product NC or HNC (*e.g.*, the PL peak is at 1.37 eV for 2.7 nm diameter product CITE QDs (Figure 7.6c) and at 1.18

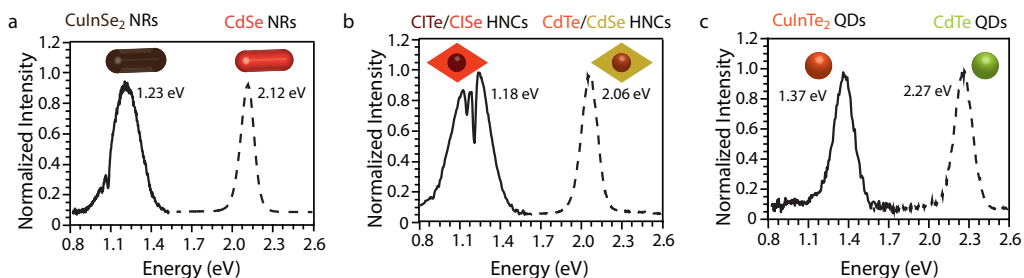


**Figure 7.6. Cation exchange toward other ternary  $\text{CuInX}_2$  (hetero)architectures.** (a) PL spectra of parent CdSe NRs (dashed line), and of product  $\text{CuInSe}_2$  NRs (solid line) obtained from the parent NCs by sequential CE (NR dimensions: 3 nm diameter, 4 nm long). (b) PL of parent core/shell CdTe/CdSe HNCs (dashed line) and of product  $\text{CuInTe}_2/\text{CuInSe}_2$  HNCs (solid line) obtained from the parent HNCs by sequential CE (core diameter: 2.6 nm, HNC length: 4 nm). The fine structure observed in the PL peak of  $\text{CuInTe}_2/\text{CuInSe}_2$  HNCs is due to absorption by the solvent used to disperse the HNCs (*viz.*, toluene). (c) PL of parent CdTe QDs (dashed line) and of product  $\text{CuInTe}_2$  QDs (solid line) obtained from the parent NCs by sequential CE (QD diameter: 2.7 nm). The PL peak energies prior to and after the CE reactions are also given.

eV for product CITE/CISE core/shell HNCs (Figure 7.6b), and shifts from 1.22 eV to 1.17 eV upon increase of the CISE core diameter in product CISE/CIS dot core/rod shell NRs from 2.7 nm to 3.2 nm). This illustrates that the NIR PL of the product NCs (HNCs) can be tuned by a proper choice of the size, shape, composition and hetero-architecture of the template NCs and/or HNCs. Moreover, as discussed above, it may be possible to tailor the carrier localization regime in  $\text{CuInX}_2$ -based HNCs by controlling their composition, size, and hetero-architecture. It should also be noted that topotactic  $\text{Cu}^+$  for  $\text{Cd}^{2+}$  exchange in template Cd-chalcogenide NCs has already been successfully used by several groups to obtain a variety of Cu-chalcogenide colloidal nanostructures, such as ultrathin  $\text{Cu}_2\text{Se}/\text{Cu}_2\text{S}$  nanoplatelets,<sup>27</sup>  $\text{Cu}_{2-x}\text{S}$  nanowires,<sup>28</sup> and  $\text{Cu}_{2-x}\text{Te}$  QDs, NRs and tetrapods.<sup>29</sup> This, in combination with the results reported here, indicate that our approach is general, and can be applied to any CdX (X = S, Se and Te) 0D,<sup>1</sup> 1D (nanorods and tetrapods)<sup>1</sup> or 2D<sup>48</sup> NC or HNC (*e.g.*, CdSe/CdS dot core/rod shell heteronanorods<sup>1,2</sup> and heterotetrapods,<sup>49</sup> CdSe/CdS concentric core/shell QDs,<sup>3</sup> CdTe/CdSe core/shell heteronanorods and hetero-multipods,<sup>43,44</sup> (Cd,Zn)Te/CdSe heteronanowires<sup>50</sup>), yielding size-, shape- and composition-controlled ternary  $\text{CuInX}_2$  NCs and HNCs that cannot be fabricated by direct synthesis methods.

## 7.4 Conclusions

In conclusion, we have shown successful sequential topotactic cation exchange ( $\text{Cu}^+$  for  $\text{Cd}^{2+}$  followed by partial  $\text{In}^{3+}$  for  $\text{Cu}^+$ ) from template Cd-chalcogenide core/shell HNCs into product CuIn-chalcogenide core/shell HNCs, *via* intermediate Cu-chalcogenide HNCs. The use of a stoichiometric TOP- $\text{InCl}_3$  complex efficiently couples the  $\text{Cu}^+$

extraction and In<sup>3+</sup> incorporation rates as well as the out- and inward diffusion fluxes, resulting in controlled cation exchange even in large and anisotropic hetero-structured nanocrystals. This allowed us to synthesize for the first time colloidal CuInSe<sub>2</sub>/CuInS<sub>2</sub> dot core/rod shell hetero-nanorods. The high-quality of these novel HNCs is attested by their near-infrared photoluminescence. The versatility of our method is demonstrated by successfully fabricating a variety of luminescent CuInX<sub>2</sub> (X = S, Se and Te) quantum dots, nanorods, and HNCs, by using Cd-chalcogenide NCs and HNCs as templates. The approach reported here is thus general and allows the high precision and versatility achieved for the synthesis of Cd-chalcogenide NCs and HNCs to be exploited to fabricate size-, shape- and composition-controlled ternary CuInX<sub>2</sub> (hetero) nanocrystals, opening up routes toward materials with unprecedented properties, which would otherwise remain inaccessible.

## Acknowledgments

The authors thank Gang Wang for XRD measurements, and Eline Hutter and Francesca Pietra for providing some of the CdSe/CdS NRs samples.

## References

- (1) Donega, C. d. M. *Chem. Soc. Rev.* **2011**, *40*, 1512–1546.
- (2) Carbone, L.; Nobile, C.; De Giorgi, M.; Della Sala, F.; Morello, G.; Pompa, P.; Hytch, M.; Snoeck, E.; Fiore, A.; Franchini, I. R. *et al. Nano Lett.* **2007**, *7*, 2942–2950.
- (3) Chen, O.; Zhao, J.; Chauhan, V. P.; Cui, J.; Wong, C.; Harris, D. K.; Wei, H.; Han, H.-S.; Fukumura, D.; Jain, R. K.; Bawendi, M. G. *Nat. Mater.* **2013**, *12*, 445–451.
- (4) Tessier, M. D.; Mahler, B.; Nadal, B.; Heuclin, H.; Pedetti, S.; Dubertret, B. *Nano Lett.* **2013**, *13*, 3321–3328.
- (5) Rabouw, F. T.; Lunnemann, P.; van Dijk-Moes, R. J. A.; Frimmer, M.; Pietra, F.; Koenderink, A. F.; Vanmaekelbergh, D. *Nano Lett.* **2013**, *13*, 4884–4892.
- (6) Chen, Y.; Vela, J.; Htoon, H.; Casson, J. L.; Werder, D. J.; Bussian, D. A.; Klimov, V. I.; Hollingsworth, J. A. *J. Am. Chem. Soc.* **2008**, *130*, 5026–5027.
- (7) Klimov, V. I.; Ivanov, S. A.; Nanda, J.; Achermann, M.; Bezel, I.; McGuire, J. A.; Piryatinski, A. *Nature* **2007**, *447*, 441–446.
- (8) Kruszynska, M.; Borchert, H.; Parisi, J.; Kolny-Olesiak, J. *J. Am. Chem. Soc.* **2010**, *132*, 15976–15986.
- (9) Kolny-Olesiak, J.; Weller, H. *ACS Appl. Mater. Interfaces* **2013**, *5*, 12221–12237.
- (10) Yarema, O.; Bozyigit, D.; Rousseau, I.; Nowack, L.; Yarema, M.; Heiss, W.; Wood, V. *Chem. Mater.* **2013**, *25*, 3753–3757.
- (11) Panthani, M.; Stolle, C. J.; Reid, D. K.; Rhee, D. J.; Harvey, T. B.; Akhavan, V. A.; Yu, Y.; Korgel, B. A. *J. Phys. Chem. Lett.* **2013**, *4*, 2030–2034.
- (12) Zhong, H.; Zhou, Y.; Ye, M.; He, Y.; Ye, J.; He, C.; Yang, C.; Li, Y. *Chem. Mater.* **2008**, *20*, 6434–6443.
- (13) Li, L.; Pandey, A.; Werder, D. J.; Khanal, B. P.; Pietryga, J. M.; Klimov, V. I. *J. Am. Chem. Soc.* **2011**, *133*, 1176–1179.
- (14) Wang, X.; Swihart, M. T. *Chem. Mater.* **2015**, *27*, 1786–1791.
- (15) De Trizio, L.; Prato, M.; Genovese, A.; Casu, A.; Povia, M.; Simonutti, R.; Alcocer, M. J. P.; D’Andrea, C.; Tassone, F.; Manna, L. *Chem. Mater.* **2012**, *24*, 2400–2406.
- (16) Stolle, C. J.; Schaller, R. D.; Korgel, B. A. *J. Phys. Chem. Lett.* **2014**, *5*, 3169–3174.
- (17) Lu, X.; Zhuang, Z.; Peng, Q.; Li, Y. *CrystEngComm* **2011**, *13*, 4039–4045.
- (18) Singh, A.; Coughlan, C.; Milliron, D. J.; Ryan, K. M. *Chem. Mater.* **2015**, *27*, 1517–1523.
- (19) Beberwyck, B. J.; Surendranath, Y.; Alivisatos, A. P. *J. Phys. Chem. C* **2013**, *117*, 19759–19770.

- (20) Groeneveld, E.; Witteman, L.; Lefferts, M.; Ke, X.; Bals, S.; van Tendeloo, G.; Donega, C. d. M. *ACS Nano* **2013**, *7*, 7913–7930.
- (21) Li, H.; Brescia, R.; Krahne, R.; Bertoni, G.; Alcocer, M. J. P.; D’Andrea, C.; Scotognella, F.; Tassone, F.; Zanella, M.; De Giorgi, M.; Manna, L. *ACS Nano* **2012**, *6*, 1637–1647.
- (22) van der Stam, W.; Gantapara, A. P.; Akkerman, Q. A.; Soligno, G.; Meeldijk, J. D.; van Roij, R.; Dijkstra, M.; Donega, C. d. M. *Nano Lett.* **2014**, *14*, 1032–1037.
- (23) Luther, J. M.; Zheng, H.; Sadtler, B.; Alivisatos, A. P. *J. Am. Chem. Soc.* **2009**, *131*, 16851–16857.
- (24) van der Stam, W.; Akkerman, Q. A.; Ke, X.; van Huis, M. A.; Bals, S.; Donega, C. d. M. *Chem. Mater.* **2015**, *27*, 283–291.
- (25) De Trizio, L.; Gaspari, R.; Bertoni, G.; Kriegel, I.; Moretti, L.; Scotognella, F.; Maserati, L.; Zhang, Y.; Messina, G. C.; Prato, M.; Marras, S.; Cavalli, A.; Manna, L. *Chem. Mater.* **2015**, *27*, 1120–1128.
- (26) van der Stam, W.; Berends, A. C.; Rabouw, F. T.; Willhammar, T.; Ke, X.; Meeldijk, J. D.; Bals, S.; Donega, C. d. M. *Chem. Mater.* **2015**, *27*, 621–628.
- (27) Bouet, C.; Laufer, D.; Mahler, B.; Nadal, B.; Heuclin, H.; Pedetti, S.; Patriarche, G.; Dubertret, B. *Chem. Mater.* **2014**, *26*, 3002–3008.
- (28) Zhang, D.; Wong, A. B.; Yu, Y.; Brittan, S.; Sun, J.; Fu, A.; Beberwyck, B.; Alivisatos, A. P.; Yang, P. *J. Am. Chem. Soc.* **2014**, *136*, 17430–17433.
- (29) Kriegel, I.; Rodriguez-Fernandez, J.; Wisnet, A.; Zhang, H.; Waurisch, C.; Eychmuller, A.; Dubavik, A.; Govorov, A. O.; Feldman, J. *ACS Nano* **2013**, *7*, 4367–4377.
- (30) Beberwyck, B. J.; Alivisatos, A. P. *J. Am. Chem. Soc.* **2012**, *134*, 19977–19980.
- (31) Rivest, J. B.; Jain, P. K. *Chem. Soc. Rev.* **2013**, *42*, 89–96.
- (32) Gupta, S.; Kershaw, S. V.; Rogach, A. L. *Adv. Mater.* **2013**, *25*, 6923–6944.
- (33) Pearson, R. G. *Inorg. Chem.* **1988**, *27*, 734–740.
- (34) Yin, Y.; Rioux, R. M.; Erdonmez, C. K.; Hughes, S.; Somorjai, G. A.; Alivisatos, A. P. *Science* **2004**, *304*, 711–715.
- (35) Mu, L.; Wang, F.; Sadtler, B.; Loomis, R. A.; Buhro, W. E. *ACS Nano* **2015**, *9*, 7419–7428.
- (36) Dean, J. A. *Lange’s Handbook of Chemistry*, McGraw-Hill, Inc., New York, **1972**, 15th ed. Section 4, Table 4.11, pages 4.44 and 4.47.
- (37) Norako, M. E.; Greaney, M. J.; Brutchey, R. L. *J. Am. Chem. Soc.* **2012**, *134*, 23–26.
- (38) Lesnyak, V.; Brescia, R.; Messina, G. C.; Manna, L. *J. Am. Chem. Soc.* **2015**, *137*, 9315–9323.
- (39) Zhong, H.; Bai, Z.; Zou, B. *J. Phys. Chem. Lett.* **2012**, *3*, 3167–3175.
- (40) Aldakov, D.; Lefrançois, A.; Reiss, P. *J. Mater. Chem. C* **2013**, *1*, 3756–3776.
- (41) McDonald, S. A.; Konstantatos, G.; Zhang, S.; Cyr, P. W.; Klem, E. J. D.; Levina, L.; Sargent, E. H. *Nat. Mater.* **2005**, *4*, 138–142.
- (42) Cowan, A. J.; Durrant, J. R. *Chem. Soc. Rev.* **2013**, *42*, 2281–2293.
- (43) Donega, C. d. M. *Phys. Rev. B* **2010**, *81*, 165303.
- (44) Krumer, Z.; Pera, S. J.; van Dijk-Moes, R. J. A.; Zhao, Y.; de Brouwer, A. F. P.; Groeneveld, E.; van Sark, W. G. J. H. M.; Schropp, R. E. I.; Donega, C. d. M. *Sol. Energy Mater. Sol. Cells* **2013**, *111*, 57–65.
- (45) Groeneveld, E.; Donega, C. d. M. *J. Phys. Chem. C* **2012**, *116*, 16240–16250.
- (46) Kraatz, I. T.; Booth, M.; Whitaker, B. J.; Nix, M. G. D.; Critchley, K. *J. Phys. Chem. C* **2014**, *118*, 24102–24109.
- (47) Shabaev, A.; Mehl, M. J.; Efros, A. L. *Phys. Rev. B* **2015**, *92*, 035431.
- (48) Lhuillier, E.; Pedetti, S.; Ithurria, S.; Nadal, B.; Heuclin, H.; Dubertret, B. *Acc. Chem. Res.* **2015**, *48*, 22–30.
- (49) Talapin, D. V.; Nelson, J. H.; Shevchenko, E. V.; Aloni, S.; Sadtler, B.; Alivisatos, A. P. *Nano Lett.* **2007**, *7*, 2951–2959.
- (50) Groeneveld, E.; van Berkum, S.; van Schooneveld, M. M.; Gloter, A.; Meeldijk, J. D.; van den Heuvel, D. J.; Gerritsen, H. C.; Donega, C. d. M. *Nano Lett.* **2012**, *12*, 749–757.
- (51) Li, H.; Zanella, M.; Genovese, A.; Povia, M.; Falqui, A.; Giannini, C.; Manna, L. *Nano Lett.* **2011**, *11*, 4964–4970.

## Appendices

### A7.1 Energy Dispersive X-ray Spectroscopy

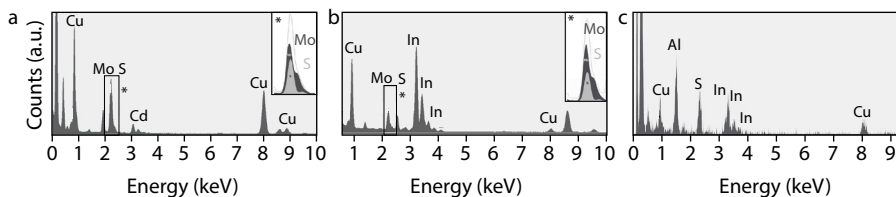


**Figure A7.1.** Energy Dispersive X-ray Spectroscopy (EDS) measurements on (a) intermediate Cu<sub>2</sub>Se/Cu<sub>2</sub>S dot core/rod shell nanorods, showing some residual Cd (~2%), and (b) final product CuInSe<sub>2</sub>/CuInS<sub>2</sub> dot core/rod shell nanorods. The EDS measurements were performed on regions containing a large number of nanorods in order to detect sufficient signal. In the insets (denoted by the asterisks), the identification of Mo, originating from the Mo TEM grid, and S are shown, as they have overlapping peaks around 2.30 keV. These peaks were deconvoluted prior to EDS quantification. The In signal in panel b is high, due to In-byproduct of the cation exchange protocol. This signal was corrected by performing EDS measurements on a small region containing several NRs and no In-byproduct and revealed a Cu:In:S ratio of 0.8 : 1.3 : 2. The Al-peak originates from the Al-grid used for the measurements.

### A7.2 X-ray Diffraction

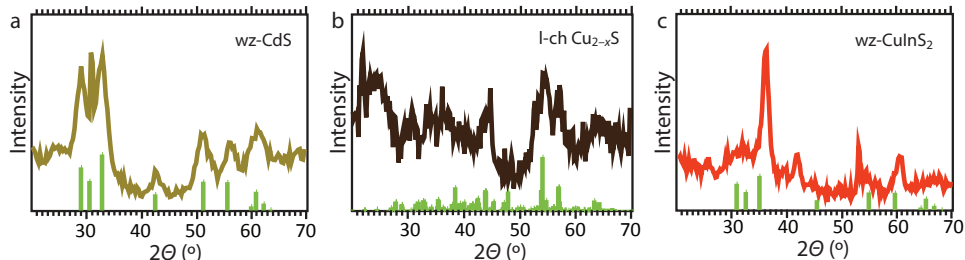


**Figure A7.2.** X-ray Diffraction (XRD) of (a) the parent CdSe/CdS dot core/rod shell nanorods, (b) the intermediate Cu<sub>2</sub>Se/Cu<sub>2</sub>S dot core/rod shell nanorods, and (c) the product CuInSe<sub>2</sub>/CuInS<sub>2</sub> (ClSe/ClS) dot core/rod shell nanorods (NRs). Reference bars (green lines) in (a)–(c) are from JCPDS cards 41-1049 (wurtzite CdS), R120113-9 (low-chalcocite Cu<sub>2</sub>S), and 01-077-9459 (wurtzite ClS). Note that the majority of the volume of the NRs consists of CdS, so the contribution of the small CdSe core is negligible. The same holds for the Cu<sub>2</sub>Se/Cu<sub>2</sub>S NRs and the ClSe/ClS NRs, where the majority of the volume of the NRs is comprised of Cu<sub>2</sub>S and ClS, respectively. The measurements are consistent with the HRTEM results, and show that the crystal structure changes from wurtzite CdS (a) to low-chalcocite Cu<sub>2</sub>S (b) after the Cu<sup>+</sup> for Cd<sup>2+</sup> cation exchange (CE), and from low-chalcocite into wurtzite CuInS<sub>2</sub> (c) after the partial In<sup>3+</sup> for Cu<sup>+</sup> CE. The sharp reflection at 36° in panel c is ascribed to the remaining TOP-InCl<sub>3</sub> by-product.



# PART C

## SUPERSTRUCTURE TAILORING



# Self-Assembly of Hexagonal Bipyramid- and Bifrustum-Shaped ZnS Nanocrystals into 2D Superlattices



## ABSTRACT

We present a combined experimental, theoretical, and simulation study on the self-assembly of colloidal hexagonal bipyramid- and hexagonal bifrustum-shaped ZnS nanocrystals (NCs) into two-dimensional superlattices. The simulated NC superstructures are in good agreement with the experimental ones. This shows that the self-assembly process is primarily driven by minimization of the interfacial free energies and maximization of the packing density. Our study shows that a small truncation of the hexagonal bipyramids is sufficient to change the symmetry of the resulting superlattice from hexagonal to tetragonal, highlighting the crucial importance of precise shape control in the fabrication of functional metamaterials by self-assembly of colloidal NCs.

Based on

**Self-Assembly of Hexagonal Bipyramid- and Bifrustum-Shaped ZnS Nanocrystals into 2D Superlattices**  
W. van der Stam, A. P. Gantapara, Q. A. Akkerman, G. Soligno, J. D. Meeldijk, R. van Roij, M. Dijkstra and C. de Mello Donega, *Nano Lett.*, **2014**, *14*, 1032–1037.

## 8.1 Introduction

Self-assembly of colloidal nanocrystals (NCs) into ordered superlattices (NC solids) is emerging as a versatile approach to design and fabricate novel metamaterials with tailored optoelectronic properties, which are promising for a variety of devices, such as solar cells, LEDs, photodetectors, and lasers.<sup>1–10</sup> The collective properties of NC solids arise from the intrinsic characteristics of the building blocks and the synergistic interactions between them, and can thus be engineered by a judicious choice of the colloidal NCs (composition, size, shape, surface), and the stoichiometry and spatial symmetry of the resulting self-assembled superstructure.<sup>1–4,11,12</sup> Nevertheless, a comprehensive set of design rules for NC superstructures has yet to emerge, although the concerted efforts of experimentalists and theoreticians worldwide have led to great advances over the past few years.<sup>1,2,13–20</sup>

Single- and multicomponent superlattices of isotropic, nearly spherical NCs have been extensively investigated over the last two decades, producing a remarkable variety of superstructures and greatly advancing the fundamental understanding of the self-assembly process.<sup>1,2,13–19</sup> Advances in the synthesis of colloidal NCs have dramatically extended the ability to control not only the shape, but also the composition of the NC, yielding a wealth of complex anisotropic NCs and hetero-NCs.<sup>21</sup> Moreover, theoretical and simulation techniques have been developed, allowing more complex problems to be solved.<sup>20,22–24</sup> This has led to a surge of experimental and simulation interest on superlattices of anisotropic NC building blocks.<sup>3,25–38</sup> In particular, two-dimensional (2D) superstructures of anisotropic NCs are attracting increasing attention, since their properties may be substantially different from those of three-dimensional (3D) NC superstructures, making them suitable for the fabrication of functional ultrathin films and membranes that take full advantage of the shape-dependent and directional properties of anisotropic NCs. For example, nanorods have been shown to form both 2D superlattices<sup>35–37</sup> and 3D mesoscopic supercrystals.<sup>38</sup> The formation of 2D and 3D self-assembled superstructures has also been studied for other anisotropic colloidal NCs, such as nanoplates, truncated cubes, octahedrons, or octapods, both experimentally and by theory and simulation.<sup>27–34</sup> Although these studies provided valuable insight in the self-assembly behavior of anisotropic colloidal NCs, the driving forces behind the self-organization process are still not fully understood. For instance, the relationship between the NC shape and the symmetry of the self-assembled superlattice has not yet been investigated in detail. This is particularly relevant not only from a fundamental viewpoint, but also as a step toward the development of a framework that allows the design and fabrication of tailored NC superstructures.

In this chapter, we report a combined experimental, theoretical, and simulation study on the self-assembly of hexagonal bipyramid- and hexagonal bipyramid-shaped ZnS NCs into 2D superlattices. The NC superstructures of these building blocks were

obtained by slow evaporation of the solvent on a dense liquid surface (ethylene glycol). The self-assembly process was theoretically studied by modelling the NCs as hard anisotropic polyhedral nanoparticles in a planar 2D solvent-air interface. The minimum free-energy configurations (position and orientation) of individual NCs at the interface were theoretically calculated<sup>20,39</sup> and used in isothermal-isobaric Monte Carlo simulations<sup>20,40,41</sup> to determine the phase behavior of the ensemble of NCs. The agreement between experimentally observed and simulated NC superstructures is very good, showing that under the conditions prevalent in our experiments the self-assembly process is primarily driven by minimization of the interfacial free energies and maximization of the packing density. Interestingly, the simulations show that the small truncation observed at the tips of the hexagonal bipyramid-shaped NCs has a dramatic impact on the symmetry of the resulting superlattice, changing it from hexagonal to tetragonal. This highlights the pivotal role of precise shape control in the design and fabrication of functional materials by self-assembly of colloidal NCs.

## 8.2 Methods

**Materials.** Copper(I) chloride (CuCl, 97%), copper(II) chloride dihydrate (CuCl<sub>2</sub>·2H<sub>2</sub>O, ≥99%), tin(IV) tetrabromide (SnBr<sub>4</sub>, 99%), zinc(II) chloride (ZnCl<sub>2</sub>, ≥98%), 1-dodecanethiol (DDT, ≥98%), di-tert-butyl disulfide (TBDS, 97%), oleylamine (OLAM, 70%), trioctylphosphine (TOP, 90%), 1-octadecene (ODE, tech., 90%), ethyleneglycol (EG, 99.8%), anhydrous methanol (MeOH), butanol (BuOH) and toluene were purchased from Sigma Aldrich and used as delivered, except for ODE and OLAM, which were degassed at 120 °C under vacuum for 2 hours.

*Colloidal hexagonal bipyramid-shaped Cu<sub>2-x</sub>S NCs* were synthesized based on a modification of the method described by Kuzuya *et al.*<sup>42</sup> Typically, 1.0 mmol CuCl and 0.5 mmol SnBr<sub>4</sub> were mixed in 8 mL 1-dodecanethiol (DDT) and 2 mL oleylamine (OLAM) and gradually heated to 225 °C. At first, a turbid white suspension was obtained at RT. The solution turned turbid yellow around 80 °C, and clear yellow at 130 °C. When the temperature reached 225 °C, the solution turned brown/black, indicating the formation and growth of Cu<sub>2-x</sub>S NCs. The solution was maintained at this temperature for one hour. Finally, the nanoparticles were washed by adding methanol/butanol solution (1:1 volume ratio) as anti-solvent, followed by centrifugation and redispersion in toluene. This cycle was repeated 3 times.

*Colloidal hexagonal bifrustum-shaped Cu<sub>2-x</sub>S NCs* were synthesized according to Li *et al.*<sup>43</sup> In a typical synthesis, 8 mmol of CuCl<sub>2</sub>·2H<sub>2</sub>O and 12 g OLAM were heated to 200 °C under nitrogen flow. After one hour, the clear dark brown solution was cooled to 180 °C and 2 mL TBDS (10 mmol) was swiftly injected. The solution was re-heated to 200 °C and after 40 minutes of growth the reaction mixture was cooled down to RT. Subsequently, the NCs were washed three times with a methanol/butanol solution (1:1 volume ratio) as anti-solvent, and redispersed in toluene.

*Cation exchange reactions of Zn<sup>2+</sup> for Cu<sup>+</sup>* were performed as described by Li *et al.*<sup>44</sup> First, 1 mmol ZnCl<sub>2</sub> was dissolved in 3 mL 1-octadecene and 2 mL OLAM (both previously degassed) at 250 °C. Subsequently, Cu<sub>2-x</sub>S NCs (~10<sup>-8</sup> M) dispersed in trioctylphosphine (TOP, 2 mL) were injected at that temperature. The mixture was allowed to react for 5 minutes under heating and stirring, after which the temperature was lowered to 70 °C, followed by the addition of several mL toluene. The final sample was precipitated by adding a methanol/butanol solution (1:1 volume ratio). The NCs were isolated by centrifugation and redispersed in toluene. This cycle was repeated twice.

*Self-assembled NC superlattices* were obtained by the liquid-air interface method, described by Dong *et al.*<sup>45</sup>

In this method, a concentrated NC solution is brought onto a very dense liquid surface (ethylene glycol). The toluene is allowed to slowly evaporate at room temperature, resulting in the formation of a continuous membrane at the liquid-air interface. These membranes were transferred to a TEM-grid by dipping it in the liquid substrate and subsequently the grid was dried overnight prior to further investigation.

*Ligand exchange reactions* were performed by dispersing the NCs with the native capping ligands in an excess of the new ligand at  $\sim 100$  °C for several hours. The NCs were subsequently precipitated by the addition of methanol/butanol solution, isolated by centrifugation, and redispersed in toluene.

*X-Ray Diffraction (XRD)* patterns were obtained by using a PW 1729 Philips diffractometer, equipped with a Cu K $\alpha$  X-ray source ( $\lambda = 1.5418$  Å). Samples for XRD analysis were prepared by depositing purified NCs on a Si wafer substrate under inert atmosphere. The purification procedure consisted of precipitating the NCs from a solution of NCs in toluene by adding anhydrous methanol (1:1 volume ratio). The sediment was isolated by centrifugation (3000 rpm, 15 min) and redispersed in chloroform. The concentrated solution of NCs was dropcasted on the Si wafer and the chloroform was allowed to evaporate at RT, resulting in a concentrated NC solid.

*Transmission Electron Microscopy (TEM)* and Energy Dispersive X-Ray Spectroscopy (EDS) measurements were performed on a Tecnai20F (FEI) microscope equipped with a Field Emission Gun, a Gatan 694 CCD camera and an EDAX spectrometer. The microscope was operated at 200 kV. Acquisition time for EDS measurements was 30 s. Samples for TEM imaging were prepared by dipping a carbon coated polymer film copper grid (300 mesh) into a self-assembled thin film on a dense ethylene glycol surface after evaporation of the solvent (toluene). The TEM-grids were dried overnight prior to imaging.

## 8.3 Results and Discussion

### 8.3.1 Self-assembly of ZnS polyhedral nanocrystals into 2D superstructures

The colloidal hexagonal bipyramid- and hexagonal bipyramid-shaped ZnS NCs used in the experiments were obtained by exchange of Zn<sup>2+</sup> for Cu<sup>+</sup> in Cu<sub>2-x</sub>S NCs.<sup>44,46</sup> The parent Cu<sub>2-x</sub>S NCs were synthesized by using methods adapted from the literature.<sup>42,43</sup> The NCs were characterized by Transmission and Scanning Electron Microscopy (TEM, SEM, Figure 8.1), X-ray Diffraction (XRD, Figure A8.1) and Energy Dispersive X-ray Spectroscopy (EDS). These techniques showed that djurleite Cu<sub>1.96</sub>S NCs were successfully exchanged into wurtzite ZnS NCs, with preservation of size and shape. As discussed in Chapter 2 and demonstrated in part B of this thesis, nanoscale cation exchange (CE) is a versatile strategy for obtaining colloidal NC compositions and morphologies that would not be attainable by conventional methods.<sup>47,48</sup> Very often the anionic framework remains unaffected during the CE reaction, and, as a result, the shape and size of the parent NC is preserved in the product NC, despite the change in composition.<sup>47,48</sup> CE reactions in which Cu<sup>+</sup> is exchanged by other metal cations with preservation of the anionic framework have been extensively investigated in copper chalcogenides, yielding NCs with metastable shapes and crystal structures.<sup>44,47,48</sup> This is also the case in the present study, since hexagonal bipyramid- and hexagonal bipyramid-shaped wurtzite ZnS NCs are obtained, rather than the thermodynamically stable zinc blende ZnS crystal structure.

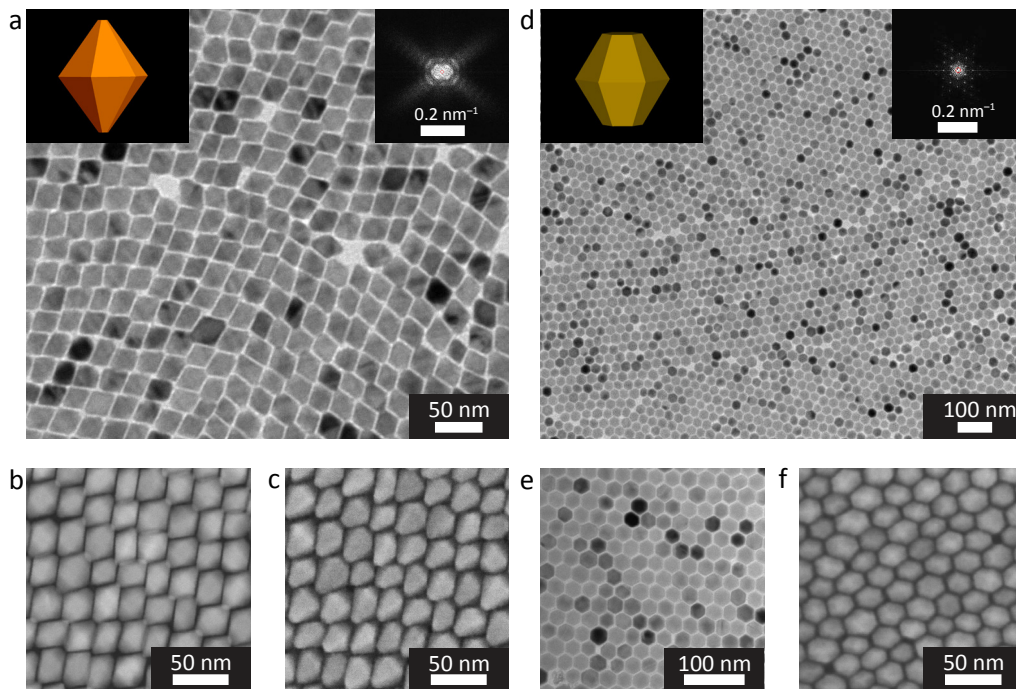


**Figure 8.1. Electron Microscopy images of self-assembled superlattices** of hexagonal bipyramid-shaped ZnS NCs (a–c, TEM, dark-field STEM, SEM, respectively), and hexagonal bifrustum-shaped ZnS NCs (d–f, TEM and SEM, respectively). Fast Fourier Transform (FFT) patterns of the superlattices are shown as insets in the top right corner of the corresponding TEM images (a and d). Insets in the top left corner show schematic representations of the shapes of the NCs (slightly truncated hexagonal bipyramid and hexagonal bifrustum, for a and d, respectively). The scale bars correspond to 50 nm in a–c and to 100 nm in d–f. FFT: 0.2 nm<sup>-1</sup>.

Colloidal hexagonal bipyramid and bifrustum ZnS NCs were self-assembled using the solvent evaporation technique on a liquid-air interface.<sup>45</sup> A solution of NCs in toluene ( $\sim 10^{-8}$  M) was drop casted on a dense ethylene glycol surface. Subsequently, the solvent was allowed to slowly evaporate at room temperature and the self-assembled superstructures were collected on a TEM-grid by gently dipping it in the liquid substrate. After collection, the superstructures were dried for several hours under vacuum prior to TEM imaging. Micrometer scale ordered superlattices were obtained in all cases (Figure 8.1). The bipyramid ZnS NCs (length: 38 nm; width: 28 nm) yielded self-assembled arrays with tetragonal symmetry (Figure 8.1a–c), whereas the bifrustum ZnS NCs (length: 33 nm; width: 33 nm) self-organized into hexagonal superlattices (Figure 8.1d–f). SEM analysis (Figure 8.1c) and Electron Tomography studies revealed that the bipyramid NCs are all oriented in the same direction, with one tip pointing upward, and the other adhered to the substrate (Figure 8.1c). It should

be noted that the tips of the hexagonal bipyramid ZnS NCs are slightly truncated. Tip truncation is very common in colloidal NCs, since it minimizes their overall free energy.<sup>21</sup> SEM showed that the bifrustum NCs can adopt multiple spatial orientations at the substrate (Figure 8.1f), while yielding similar hexagonal 2D TEM projections (Figure 8.1e). This is mainly due to the shape uniformity of the bifrustum NCs viewed from different directions. Interestingly, the parent Cu<sub>1.96</sub>S NCs did not form 2D superlattices under the conditions used in our experiments, but formed instead small domains of 3D superstructures (Figure A8.2). Considering that the size and shape of the parent Cu<sub>1.96</sub>S NCs are preserved in the product ZnS NCs, the disparity in their self-organization behavior can be ascribed to their dissimilar surfaces (both in terms of chemical composition and ligand capping), which could give rise to different inter-NC interactions, and hence alter the forces driving the self-assembly process.

### 8.3.2 Interfacial adsorption free energies

To understand the experimentally observed self-assembly behavior of both the product ZnS NCs and the parent Cu<sub>1.96</sub>S NCs, theoretical calculations and computer simulations were performed. First, the preferred orientation of the NC at a planar air-toluene interface (tension  $\gamma_{\text{air-toluene}}$  ( $\gamma_{\text{at}}$ ) = 28.52 mN/m) was theoretically obtained by calculating Pieranski-type interfacial adsorption free energies of individual NCs using a triangular tessellation technique,<sup>39</sup> and choosing the configuration that minimizes the adsorption free energy. The NCs were modeled as anisotropic polyhedral hard nanoparticles, with the same dimensions as those experimentally observed. Adsorption at the ethylene glycol (EG)-toluene interface is neglected, under the assumption that the self-assembly of the NCs occurs primarily at the air-toluene interface. This assumption is supported by an experimental study of the self-assembly of colloidal CdSe/CdS nanorods (NRs) by slow evaporation of toluene solutions on a EG surface, combining *in-situ* grazing-incidence small angle X-ray scattering (GISAXS) and *ex-situ* TEM, which clearly demonstrated that the superstructures are formed at the air-toluene interface.<sup>35</sup> Furthermore, NC adsorption at the toluene-diethylene glycol interface is likely to be negligible in comparison to that at the toluene-air interface, since the interfacial tension of air-toluene can be expected to be larger than that of toluene-diethylene glycol, as more Van der Waals interactions are broken at the air-toluene interface.

Following Pieranski,<sup>49</sup> we write the interfacial free energy of a nanoparticle with its center of mass at a height  $z$  (with respect to the planar air-toluene interface, indicated in Figure 8.2a), and with angles  $\varphi$  (the polar angle with respect to the interface normal) and  $\psi$  (the internal Euler angle about the long axis of the nanoparticle), as

$$F(z, \varphi, \psi) = \gamma_{\text{a}} S_{\text{a}}(z, \varphi, \psi) + \gamma_{\text{t}} S_{\text{t}}(z, \varphi, \psi) - \gamma_{\text{at}} S_{\text{at}}(z, \varphi, \psi) + \text{const.} \quad (8.1)$$

Here,  $S_{\text{a}}$  and  $S_{\text{t}}$  denote the area of the particle surface that is in contact with air and toluene, respectively, and  $S_{\text{at}}$  is the surface area taken out from the air-toluene interface

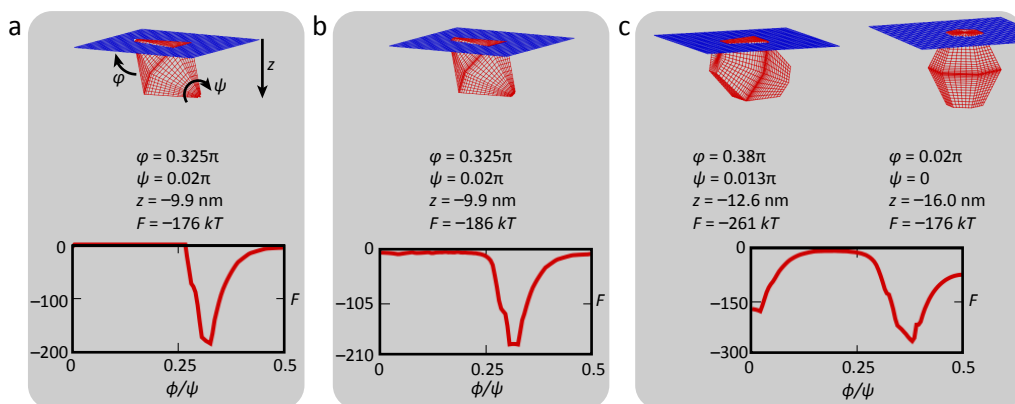


**Figure 8.2. Minimum free-energy configurations** (and their coordinates and minimal free energy) for three particle shapes in a planar air-toluene interface as obtained from eq. 8.1 and triangular tessellations of the surfaces: **(a)** perfect hexagonal bipyramid, **(b)** slightly truncated hexagonal bipyramid, and **(c)** hexagonal bifrustums. The bottom panels give the interfacial free-energy of the particle as a function of the polar angle  $\varphi$  minimized with respect to the particle height  $z$  and the internal Euler angle about the long axis of the nanoparticle,  $\psi$ . The parameters  $z$ ,  $\varphi$  and  $\psi$  are indicated in panel a

by the particle. All three areas  $S_a$ ,  $S_t$ , and  $S_{at}$  depend nontrivially on the position and orientation of the particle, and need to be calculated numerically. The particle-toluene tension is denoted by  $\gamma_t$ , the particle-air tension by  $\gamma_a$ , and the arbitrary constant in eq. 8.1 is chosen such that  $F = 0$  for a particle that is completely immersed in toluene. The adsorption free energy of eq. 8.1 ignores capillary deformations and line tension contribution for simplicity. In fact, given that the total particle surface area  $S_a + S_t$  is a constant, one easily checks that  $F(z, \varphi, \psi)$  does not depend on  $\gamma_t$  and  $\gamma_a$  separately, but only on their difference through the contact angle  $\theta$  defined by Young's equation,  $\cos\theta = (\gamma_a - \gamma_t)/\gamma_{at} = 0.8$ , where the numerical value is an estimate based on the observed favorable (low free-energy) configurations. It should be noted that although ignoring capillary deformations of the toluene-air interface gives rise to a violation of the force balance on the toluene-air-particle contact line, we expect this to have a negligible effect on the optimal configuration since the sharp edges of the flat facet adsorbed to the interface cause a rapid variation of the surface curvature, to which the air-toluene interface can adapt without any substantial deformation.

Using a triangular tessellation technique to calculate the surface areas  $S_a$ ,  $S_t$ , and  $S_{at}$ , we obtain the equilibrium configuration from minimizing  $F$  with respect to the particle configuration. For three nanoparticle shapes of interest, Figure 8.2 shows these equilibrium configurations, as well as their coordinates and free energies as a function of the polar angle  $\varphi$  (minimized with respect to  $z$  and the internal angle  $\psi$ ). The perfect hexagonal bipyramid has minimum free-energy when one of its triangular facets

is completely adhered to the interface (Figure 8.2a). For this configuration, a local minimum of *ca.*  $-200 k_B T$  is found. It is interesting to note that the particle remains completely immersed in the liquid phase, except for the facet that is adhered to the interface (whereas the particle pays a free energy penalty of  $F \approx 10^4 k_B T$  if it is completely in air). The colloidal NCs used in the self-assembly experiments are, however, not perfect hexagonal bipyramids, but instead have slightly truncated tips ( $\sim 5\%$  of their length). Nevertheless, according to our calculation this small truncation does not affect the single-particle equilibrium configuration at the interface, which remains essentially the same as that of a perfect hexagonal bipyramid (Figure 8.2b). By contrast, according to our calculations a hexagonal bistrustum nanoparticle has two possible equilibrium configurations, in which either one of the twelve trapezoidal facets or one of the two hexagonal facets is adhered to the interface (Figure 8.2c). Both free-energy minima are sufficiently deep to make the adhesion irreversible (Figure 8.2c), and consequently the hexagonal bistrustum nanoparticles have multiple options for interfacial adhesion.

### 8.3.3 Close-packing of hard particles

Once the equilibrium adsorption configurations of individual nanoparticles at the air-toluene interface are theoretically determined, we predict the self-assembled structures by using the floppy-box Monte Carlo (FBMC) method<sup>40,41</sup> in combination with the separating-axis-based overlap algorithm.<sup>50</sup> In the FBMC method, we perform Monte Carlo simulations in the isothermal-isobaric ensemble (*NPT*), and compress the system from the isotropic fluid phase to the solid phase using a variable shape of the simulation box. The immersion depth  $z$  and the polar angle  $\varphi$  of the nanoparticle with respect to the air-toluene interface are kept fixed according to the values determined for the equilibrium adsorption configurations, and the particles are only allowed to translate and rotate in the plane of the interface. Due to the symmetry of the hexagonal bistrustums (*ca.* 33 nm in all directions), the orientation of the NC is not important for the overall self-assembly behavior, since the NC can occupy a hexagonal site in the array regardless of whether a trapezoidal or hexagonal facet is adsorbed to the interface. Therefore, for simplicity, only the hexagonal adhered surface is considered in the FBMC simulations. The volume of the nanoparticles  $v$  is set to unity in all cases.

Subsequently, we use the predicted self-assembled structures in Monte Carlo simulations to determine the phase behavior of an ensemble of nanoparticles. To this end, we calculate the equations of state in Monte Carlo simulations. The change in the color of the particles depicts the orientation of the particles. The crystal structure can be determined from the reciprocal space pattern of the center of mass of the particles in the simulated NC superstructure. Figure 8.3 shows the reciprocal space patterns and the real space configurations of the NC superlattices formed during the FBMC simulations at two different reduced densities  $\rho^* = \rho v^{2/3} = 0.65$  and  $0.69$  with  $v$  the particle volume,  $\rho = N/A$  the areal number density,  $N$  the number of particles, and  $A$  the surface area of the interface. The experimentally observed NC superlattices are also included for

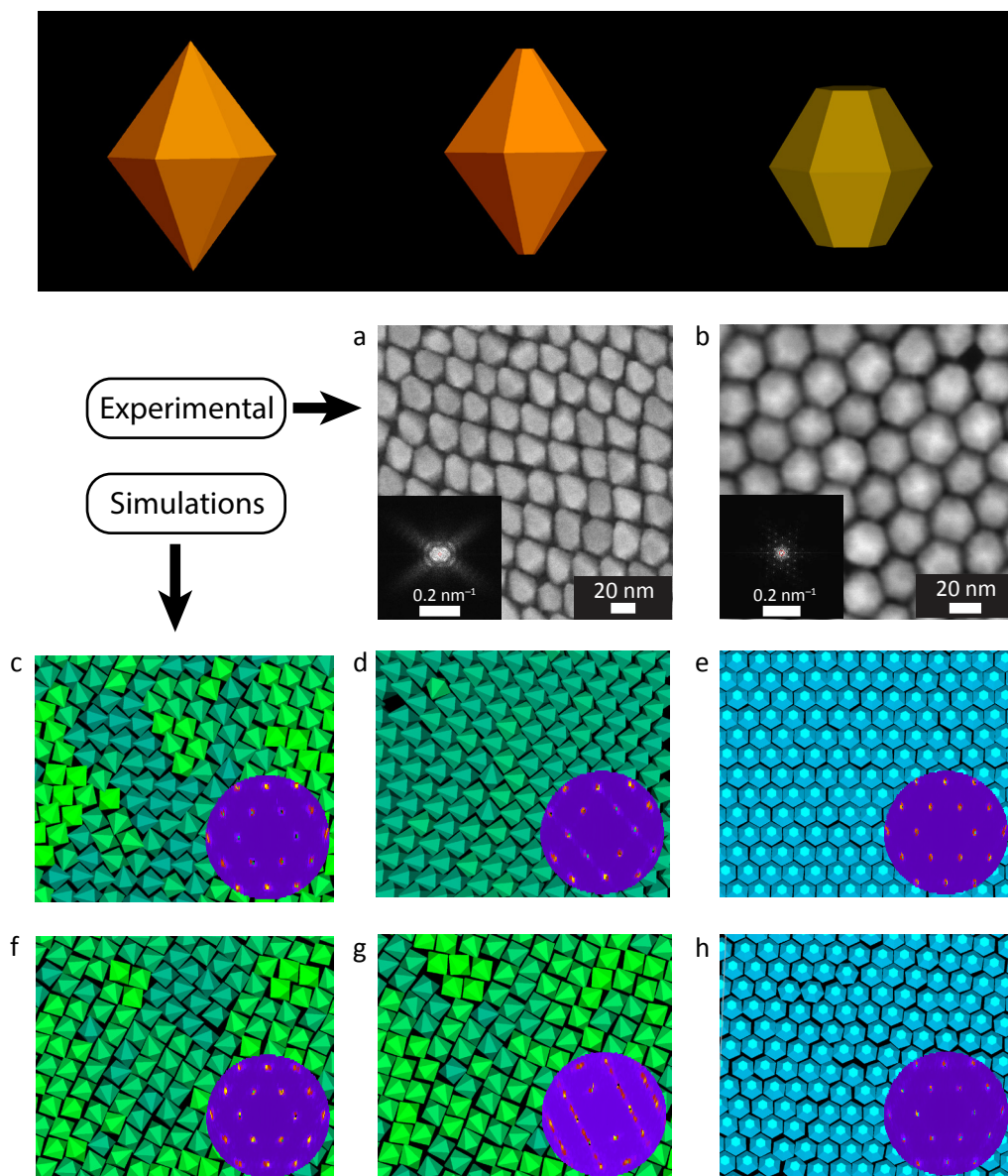


**Figure 8.3. Comparison between experimental observations and simulations of self-assembled superstructures.** Top panel: Schematics of the particle geometries used in the Monte Carlo simulations. SEM images of self-assembled superlattices of (a) hexagonal bipyramid-shaped ZnS NCs, and (b) hexagonal bifrustum-shaped ZnS NCs. The insets give the Fast Fourier Transform (FFT) patterns of the superlattices. Snapshots of the isothermal-isobaric Monte Carlo simulations showing the various structures that form during the 2D self-assembly of hexagonal bipyramids (c,d,f,g) and hexagonal bifrustums (e, h) adhered to an air-toluene interface. The corresponding reciprocal space patterns of the center of mass of the particles in the simulated NC superlattice are also displayed (bottom right insets). The relative orientation of the particles is color coded. (c–e) Simulation snapshots at a reduced density  $\rho^* = \rho v^{2/3} = 0.69$  with  $v$  the particle volume. (f–h) Simulation snapshots at  $\rho^* = 0.65$ .

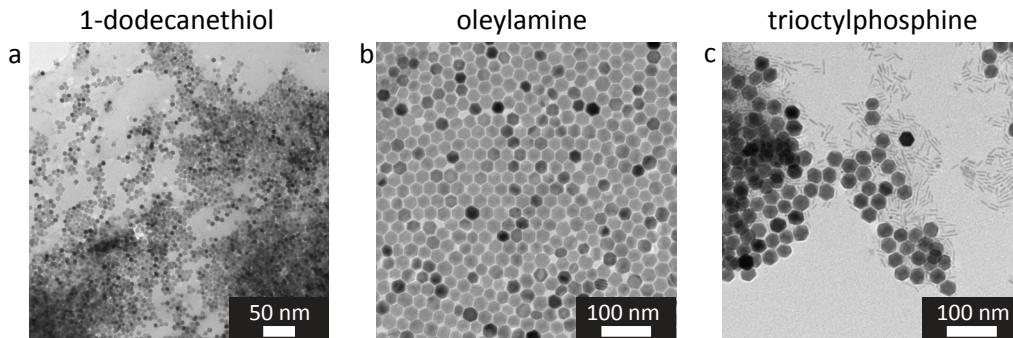


**Figure 8.4.** TEM images of the NC solids obtained from self-assembly experiments using hexagonal bifrustum ZnS NCs with different capping ligands: (a) 1-dodecanethiol (DDT), (b) additional oleylamine (OLAM), and (c) trioctyl phosphine (TOP). These experiments show that self-assembled superlattices of ZnS NCs were only obtained when OLAM is used as the capping ligand.

comparison (Figure 8.3a,b). The simulations show that perfect hexagonal bipyramids crystallize *via* a first-order phase transition with coexisting densities  $\rho^* \approx 0.56$  and  $0.57$  into a hexagonal superlattice (Figure 8.3c). Hexagonal bifrustums also crystallize *via* a first-order transition from the isotropic fluid into a hexagonal lattice with coexisting densities  $\rho^* \approx 0.50$  and  $0.52$  (Figure 8.3e). In contrast, slightly truncated bipyramids show a weak first-order transition from the isotropic phase to a tetragonal phase around  $\rho^* \approx 0.58$  (Figure 8.3d). This is remarkable, since the equilibrium configuration of the single NC adhered to the air-toluene interface was not significantly affected by the truncation (see above, Figure 8.2). This can be rationalized by considering that the truncation allows the NCs to come in closer proximity, thereby leading to a higher packing density, and hence a tetragonal rather than hexagonal lattice.

#### 8.3.4 Mechanism

The agreement between the simulated and experimentally observed self-assembled 2D NC superlattices (Figure 8.3) is very good, indicating that the self-assembly process of the ZnS NCs is driven primarily by minimization of the interfacial free energies and maximization of the packing densities. The inability of the parent  $\text{Cu}_{1.96}\text{S}$  NCs (Figure A8.2) to form 2D superlattices under the same conditions as used for the product ZnS NCs can be thus attributed to the presence of additional inter-NC interactions that disrupt the self-assembly process by modifying the interfacial tensions and/or introducing attractive/repulsive potentials. Considering that the size and shape of the ZnS and  $\text{Cu}_{1.96}\text{S}$  NCs are the same, the additional interactions must be due to the different surfaces of the two types of NCs, since the  $\text{Cu}_{1.96}\text{S}$  NCs are capped by alkylthiols, while the ZnS NCs are likely capped by oleylamine. Indeed, superlattices were no longer formed after the ligands coating the ZnS NCs were exchanged to 1-dodecanethiol (Figure 8.4a) or trioctylphosphine (Figure 8.4c), while an excess of

oleylamine did not affect the formation of the superlattices (Figure 8.4b).

## 8.4 Conclusions

In conclusion, our study shows that micrometer scale 2D superlattices of colloidal hexagonal bipyramid- and hexagonal bifrustum-shaped ZnS NCs can be obtained by self-assembly at the liquid-air interface. The self-assembly behavior is well described by a combination of theoretical adsorption free-energy calculations and Monte Carlo simulations, which shows that the superlattice formation is driven primarily by minimization of the interfacial free energies and maximization of the packing densities. Moreover, our results show that truncation of the tips of hexagonal bipyramids by as little as 5% is sufficient to change the symmetry of the resulting superlattice from hexagonal to tetragonal. This demonstrates that precise shape control is of crucial importance in the fabrication of functional materials by self-assembly of colloidal NCs. From this perspective, the strategy developed here is very promising, since colloidal  $\text{Cu}_{2-x}\text{A}$  ( $\text{A} = \text{S}, \text{Se}, \text{Te}$ ) NCs can be synthesized in a plethora of different shapes (see also Chapter 2),<sup>42,43</sup> and can easily be converted into NCs of other metal chalcogenides, with preservation of size and shape, by using cation exchange (see also Chapters 2, 4, 6 and 7).<sup>44,46–48</sup> Moreover, it has been demonstrated that  $\text{Zn}^{2+}$  in Zn chalcogenides can also be exchanged for other cations (*e.g.*,  $\text{Cd}^{2+}$ ,  $\text{Mn}^{2+}$ ).<sup>51–53</sup> The work described here may thus provide a versatile design and fabrication route for tailored 2D superlattices of anisotropic NCs of metal chalcogenides, in which cation exchange reactions are used to convert self-assembled superlattices of zinc chalcogenide NCs into different materials, while preserving the size and shape of the NC building blocks as well as the symmetry and long-range order of the superstructure. From a theoretical and modelling perspective it is very comfortable to note that the relatively simple Pieranski potential of eq. 8.1 combined with Monte Carlo simulations actually has quantitative predictive power, which may be further exploited in the study of other particle shapes and material parameters.

## References

- (1) Talapin, D. V.; Lee, J.; Kovalenko, M. V.; Shevchenko, E. V. *Chem. Rev.* **2010**, *110*, 389–458.
- (2) Vanmaekelbergh, D. *Nano Today* **2011**, *6*, 419–437.
- (3) Paik, T.; Murray, C. *Nano Lett.* **2013**, *13*, 2952–2956.
- (4) Nie, Z.; Petukhova, A.; Kumacheva, E. *Nat. Nanotechnol.* **2010**, *5*, 15–25.
- (5) Shirasaki, Y.; Supran, G. J.; Bawendi, M. G.; Bulović, V. *Nat. Photonics* **2013**, *7*, 13–23.
- (6) Sun, L.; Choi, J. J.; Stachnik, D.; Bartnik, A. C.; Hyun, B. R.; Malliaras, G. G.; Hanrath, T.; Wise, F. W. *Nat. Nanotechnol.* **2012**, *7*, 369–373.
- (7) Pisanello, F.; Martiradonna, L.; Spinicelli, P.; Fiore, A.; Hermier, J. P.; Manna, L.; Cingolani, R.; Giacobino, E.; De Vittorio, M.; Bramati, A. *Superlattices Microstruct.* **2010**, *47*, 165–169.
- (8) Talgorn, E.; Gao, Y.; Aerts, M.; Kunneman, L. T.; Schins, J. M.; Savenije, T. J.; van Huis, M. A.; van der Zant, H. S. J.; Houtepen, A. J.; Siebbeles, L. D. A. *Nat. Nanotechnol.* **2011**, *6*, 733–739.
- (9) Tang, J.; Kemp, K. W.; Hoogland, S.; Jeong, K. S.; Liu, H.; Levina, L.; Furukawa, M.; Wang, X.; Debnath, R.; Cha, D.; Chou, K. W.; Fischer, A.; Amassian, A.; Asbury, J. B.; Sargent, E. H. *Nat. Mater.* **2011**, *10*, 765–771.

- (10) Ip, A. H.; Thon, S. M.; Hoogland, S.; Voznyy, O.; Zhitomirsky, D.; Debnath, R.; Levina, L.; Rollny, L. R.; Carey, G. H.; Fischer, A.; *et al. Nat. Nanotechnol.* **2012**, *7*, 577–582.
- (11) Wang, R. Y.; Feser, J. P.; Lee, J.-S.; Talapin, D. V.; Segalman, R.; Majumdar, A. *Nano Lett.* **2008**, *8*, 2283–2288.
- (12) Kang, Y.; Ye, X.; Chen, J.; Qi, L.; Diaz, R. E.; Doan-Nguyen, V.; Xing, G.; Kagan, C. R.; Li, J.; Gorte, R. J.; Stach, E. A.; Murray, C. B. *J. Am. Chem. Soc.* **2013**, *135*, 1499–1505.
- (13) Urban, J. J.; Talapin, D. V.; Shevchenko, E. V.; Kagan, C. R.; Murray, C. B. *Nat. Mater.* **2007**, *6*, 115–121.
- (14) Shevchenko, E. V.; Talapin, D. V.; Kotov, N. A.; O'Brien, S.; Murray, C. B. *Nature* **2006**, *439*, 55–59.
- (15) Heath, J. R. *Nature* **2007**, *445*, 492–493.
- (16) Boneschanscher, M. P.; Evers, W. H.; Qi, W.; Meeldijk, J. D.; Dijkstra, M.; Vanmaekelbergh, D. *Nano Lett.* **2013**, *13*, 1312–1316.
- (17) Evers, W. H.; Goris, B.; Bals, S.; Casavola, M.; de Graaf, J.; Roij, R.; Van Dijkstra, M.; Vanmaekelbergh, D. *Nano Lett.* **2013**, *13*, 2317–2323.
- (18) Chen, Z.; O'Brien, S. *ACS Nano* **2008**, *2*, 1219–1229.
- (19) Grzelczak, M.; Vermant, J.; Furst, E.; Liz-Marzán, L. *ACS Nano* **2010**, *4*, 3591–3605.
- (20) Gantapara, A. P.; de Graaf, J.; van Roij, R.; Dijkstra, M. *Phys. Rev. Lett.* **2013**, *111*, 015501.
- (21) de Mello Donega, C. *Chem. Soc. Rev.* **2011**, *40*, 1512–1546.
- (22) Torquato, S.; Jiao, Y. *Nature* **2009**, *460*, 876.
- (23) Nguyen, T. D.; Jankowski, E.; Glotzer, S. C. *ACS Nano* **2011**, *5*, 8892–8903.
- (24) Sinkovits, D. W.; Luijten, E. *Nano Lett.* **2012**, *12*, 1743–1748.
- (25) Quan, Z.; Fang, J. *Nano Today* **2010**, *5*, 390–411.
- (26) Glotzer, S. C.; Solomon, M. J. *Nat. Mater.* **2007**, *6*, 557–562.
- (27) Reifsnnyder, D. C.; Ye, X.; Gordon, T. R.; Song, C.; Murray, C. B. *ACS Nano* **2013**, *7*, 4307–4315.
- (28) Gordon, T. R.; Paik, T.; Klein, D. R.; Naik, G. V.; Caglayan, H.; Boltasseva, A.; Murray, C. B. *Nano Lett.* **2013**, *13*, 2857–2863.
- (29) Qi, W.; de Graaf, J.; Qiao, F.; Marras, S.; Manna, L.; Dijkstra, M. *Nano Lett.* **2012**, *12*, 5299–5303.
- (30) Miszta, K.; de Graaf, J.; Bertoni, G.; Dorfs, D.; Brescia, R.; Marras, S.; Ceseracchi, L.; Cingolani, R.; van Roij, R.; Dijkstra, M.; Manna, L. *Nat. Mater.* **2011**, *10*, 872–876.
- (31) Du, W.; Qian, X.; Ma, X.; Gong, Q.; Cao, H.; Yin, J. *Chemistry* **2007**, *13*, 3241–3247.
- (32) Evers, W. H.; Goris, B.; Bals, S.; Casavola, M.; de Graaf, J.; van Roij, R.; Dijkstra, M.; Vanmaekelbergh, D. *Nano Lett.* **2013**, *13*, 2317–2323.
- (33) Baumgardner, W. J.; Whitham, K.; Hanrath, T. *Nano Lett.* **2013**, *13*, 3225–3231.
- (34) Ye, X.; Chen, J.; Engel, M.; Millan, J. A.; Li, W.; Qi, L.; Xing, G.; Collins, J. E.; Kagan, C. R.; Li, J.; Glotzer, S. C.; Murray, C. B. *Nat. Chem.* **2013**, *5*, 466–473.
- (35) Pietra, F.; Rabouw, F. T.; Evers, W. H.; Byelov, D. V.; Petukhov, A. V.; de Mello Donega, C.; Vanmaekelbergh, D. *Nano Lett.* **2012**, *12*, 5515–5523.
- (36) Carbone, L.; Nobile, C.; De Giorgi, M.; Della Sala, F.; Morello, G.; Pompa, P.; Htych, M.; Snoeck, E.; Fiore, A.; Franchini, I. R.; *et al. Nano Lett.* **2007**, *7*, 2942–2950.
- (37) Rivest, J. B.; Swisher, S. L.; Fong, L. K.; Zheng, H.; Alivisatos, A. P. *ACS Nano* **2011**, *5*, 3811–3816.
- (38) Wang, T.; Zhuang, J.; Lynch, J.; Chen, O.; Wang, Z.; Wang, X.; LaMontagne, D.; Wu, H.; Wang, Z.; Cao, Y. C. *Science* **2012**, *338*, 358–363.
- (39) De Graaf, J.; Dijkstra, M.; van Roij, R. *J. Chem. Phys.* **2010**, *132*, 164902.
- (40) De Graaf, J.; Fillion, L.; Marechal, M.; van Roij, R.; Dijkstra, M. *J. Chem. Phys.* **2012**, *137*, 214101.
- (41) Fillion, L.; Marechal, M.; van Oorschot, B.; Pelt, D.; Smalenburg, F.; Dijkstra, M. *Phys. Rev. Lett.* **2009**, *103*, 188302.
- (42) Kuzuya, T.; Tai, Y.; Yamamuro, S.; Sumiyama, K. *Sci. Technol. Adv. Mater.* **2005**, *6*, 84–90.
- (43) Li, W.; Shavel, A.; Guzman, R.; Rubio-Garcia, J.; Flox, C.; Fan, J.; Cadavid, D.; Ibáñez, M.; Arbiol, J.; Morante, J. R.; Cabot, A. *Chem. Commun.* **2011**, *47*, 10332–10334.
- (44) Li, H.; Zanella, M.; Genovese, A.; Povia, M.; Falqui, A.; Giannini, C.; Manna, L. *Nano Lett.* **2011**, *11*, 4964–4970.
- (45) Dong, A.; Chen, J.; Vora, P. M.; Kikkawa, J. M.; Murray, C. B. *Nature* **2010**, *466*, 474–477.
- (46) Zhao, Y.; Pan, H.; Lou, Y.; Qiu, X.; Zhu, J.; Burda, C. *J. Am. Chem. Soc.* **2009**, *131*, 4253–4261.
- (47) Rivest, J. B.; Jain, P. K. *Chem. Soc. Rev.* **2013**, *42*, 89–96.
- (48) Beberwyck, B. J.; Surendranath, Y.; Alivisatos, A. P. *J. Phys. Chem. C* **2013**, *117*, 19759–19770.
- (49) Pieranski, P. *Phys. Rev. Lett.* **1980**, *45*, 569–572.
- (50) Eberly, D. Intersection of Convex Objects: The Method of Separating Axes, <http://www.geometrictools.com/> (accessed April 2013).

- (51) Eilers, J.; Groeneveld, E.; de Mello Donega, C.; Meijerink, A. *J. Phys. Chem. Lett.* **2012**, *3*, 1663–1667.
- (52) Groeneveld, E.; van Berkum, S.; van Schooneveld, M. M.; Gloter, A.; Meeldijk, J. D.; van den Heuvel, D. J.; Gerritsen, H. C.; de Mello Donega, C. *Nano Lett.* **2012**, *12*, 749–757.
- (53) Groeneveld, E.; Witteman, L.; Lefferts, M.; Ke, X.; Bals, S.; van Tendeloo, G.; de Mello Donega, C. *ACS Nano* **2013**, *7*, 7913–7930.

## Appendices

### A8.1 X-ray Diffractometry

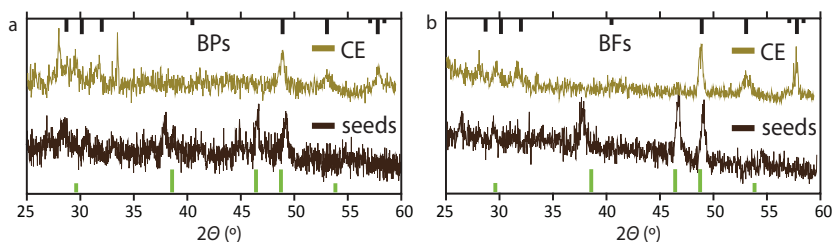


**Figure A8.1.** X-ray Diffraction patterns, indicating that (a) wurtzite ZnS hexagonal bipyramids (BPs, orange line) and (b) bifrustums (BFs, orange line) were successfully synthesized from djurleite  $\text{Cu}_{1.96}\text{S}$  hexagonal BPs (brown line in a) and BFs (brown line in b) by  $\text{Zn}^{2+}$  for  $\text{Cu}^+$  cation exchange. Reference bars are from JCPDS card no. [05-0492] and [20-0365] for wurtzite ZnS (black) and djurleite  $\text{Cu}_{1.96}\text{S}$  (green), respectively.

### A8.2 Self-assembly of $\text{Cu}_{1.96}\text{S}$ bifrustums at the liquid-air interface

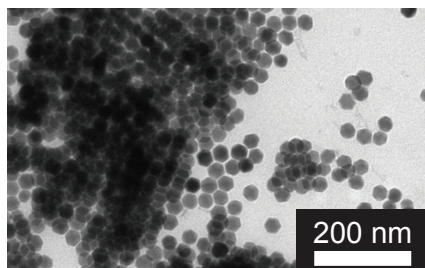


**Figure A8.2.** Self-assembled superstructures obtained from hexagonal bifrustum-shaped  $\text{Cu}_{1.96}\text{S}$  NCs, capped with alkylthiols.



# Oleic Acid-Induced Atomic Alignment of ZnS Polyhedral Nanocrystals



## ABSTRACT

Ordered 2-dimensional (2D) superstructures of colloidal nanocrystals (NCs) can be tailored by the size, shape, composition and surface chemistry of the NC building blocks, which can give directionality to the resulting superstructure geometry. The exact formation mechanism of 2D NC superstructures is however not yet fully understood. Here, we show that oleic acid (OA) ligands induce atomic alignment of wurtzite ZnS bipyramid-shaped NCs. We find that the {002} facets of the ZnS bipyramids preferentially adhere to the liquid-air interface in the presence of OA ligands. Furthermore, OA ligands induce inter-NC interactions that also orient the NCs in the plane of the liquid-air interface, resulting in atomically aligned 2D superstructures. With *in-situ* Grazing Incidence Small-Angle X-ray Scattering (GISAXS), we follow the self-assembly process in real-time, and we find that the NCs form a hexagonal superstructure at early stages, after which they come closer over time, resulting in a close-packed NC superstructure. Our results show the profound influence surface ligands have on the directionality of 2D NC superstructures and highlight the importance of detailed *in-situ* studies in order to understand the self-assembly of NCs into 2D superstructures.

Based on

**Oleic Acid-Induced Atomic Alignment of ZnS Polyhedral Nanocrystals**

W. van der Stam, F. T. Rabouw, S. J. W. Vonk, J. J. Geuchies, H. Ligthart, A. V. Petukhov, C. de Mello Donega, *Nano Lett.* **2016**, *16*, 2608–2614.

## 9.1 Introduction

Colloidal nanocrystals (NCs) are able to form 3-dimensional (3D) and 2-dimensional (2D) self-assembled superstructures of which the properties depend on the building block material as well as on the geometry into which they self-assemble.<sup>1–7</sup> Of key interest in this respect is the challenge of using the shape of the NC building blocks to program the final geometry of the superstructure.<sup>8–13</sup> The precise geometry can be important to the electrical transport properties of the structure,<sup>9,14</sup> or to the directionality and polarization of emitted light.<sup>4,6</sup> Besides, controlling the inter-NC interactions with surface ligands has been shown to have a dramatic impact on the directionality of the self-assembly process.<sup>9,15–19</sup> However, the exact mechanisms underlying the directional self-assembly process are not yet fully understood. In the previous chapter, we investigated the self-assembly of hexagonal bipyramid- and bifrustum-shaped ZnS NCs into 2D superlattices by using *ex-situ* transmission electron microscopy (TEM) in combination with interfacial free-energy calculations and Monte Carlo simulations.<sup>8</sup> On the basis of our results, we proposed a mechanism for the self-assembly process in which the NCs are confined to the liquid–air interface due to an irreversible adsorption, after which they close-pack into shape-directed geometries (tetragonal for hexagonal bipyramids and hexagonal for bifrustums).<sup>8</sup> This mechanism, however, was not experimentally verified, because we carried out only *ex-situ* TEM measurements. Moreover, we showed that the addition of surface ligands (*e.g.*, dodecanethiol, DDT) disrupts the self-organization process but the role of the ligands was not investigated in detail.<sup>8</sup>

In this chapter, we study *in-situ* the influence of oleic acid (OA) ligands on the self-assembly of hexagonal bifrustum ZnS NCs into 2D superstructures by adding OA ligands prior to the onset of the self-organization process. The self-assembled 2D NC superstructures are obtained by the liquid substrate procedure, in which a concentrated NC solution in toluene is drop-casted onto a dense liquid substrate (ethylene glycol, EG), and is subsequently allowed to dry out over the course of an hour (see Methods for details). A combination of *in-situ* time-resolved grazing incidence small-angle X-ray scattering (GISAXS) and grazing incidence wide-angle X-ray scattering (GIWAXS) is used to selectively probe the liquid-air interface at both nanometer and atomic length scales, simultaneously, allowing the NC and atomic order to be followed in real-time during the whole self-assembly process. Furthermore, the resulting 2D NC superstructures are collected on a TEM-grid, and analyzed *ex-situ* with TEM and Electron Diffraction (ED). We find that long-range hexagonal 2D ZnS NC superstructures are formed both in the absence and in the presence of OA ligands. However, in the presence of OA ligands the atomic planes of the wurtzite ZnS bifrustum-shaped NCs align themselves, forming an atomically ordered NC superlattice. These results highlight the huge impact of surface ligands on the directionality of the self-organization process, which may prove beneficial for the design of well-defined, high-quality 2D NC superstructures of

various compositions.

## 9.2 Grazing Incidence Small-Angle X-ray Scattering (GISAXS)

### 9.2.1 Total external reflection

X-ray radiation is particularly relevant for studying surface processes. When the angle of incidence ( $\alpha_i$ ) is very small, *i.e.* grazing, and smaller than the critical angle ( $\alpha_c$ ), the beam does not enter the liquid substrate (ethylene glycol, in this study).<sup>20</sup> In other words, under very small angle of incidence, the penetration depth of the X-ray beam into the substrate, or the ZnS NCs, is small (typically a few nm). When the beam is reflected at the interface, this is called total external reflection. When total external reflection occurs on an ordered superstructure, the beam is scattered at well-defined angles  $2\theta$  under an angle  $\alpha_f$  with respect to the interface.

Figure 9.1a displays the angles in a typical GISAXS experiment in more detail.<sup>20</sup> Scattering studied by GISAXS is described in reciprocal  $q$ -space, as introduced in section 5.2. Bragg's law states that  $\mathbf{q} = \mathbf{k}_f - \mathbf{k}_i$ . However, there is a constraint to this relation. Elastic scattering can only change the direction of the X-ray wavevector  $\mathbf{k}_i$  and not the magnitude. Therefore, the wavevector  $\mathbf{k}_f$  has to be somewhere on a sphere (Ewald's sphere, Figure 9.1b) with radius  $|\mathbf{k}_f| = |\mathbf{k}_i| = 2\pi/\lambda$ . From this it follows that the size of the Ewald's sphere is determined by the wavelength of the incoming X-ray beam.

### 9.2.2 Hexagonal order in GISAXS

If the ordered structure is a nanocrystal, scattering occurs on the atomic planes ( $\text{\AA}$  regime), so under wide angles (small objects scatter at large angles). If the ordered structure is an array of NCs, scattering occurs at small angles. This small-angle X-ray scattering under grazing incidence beam gives rise to structure factor rods in the GISAXS pattern.<sup>20</sup> For a hexagonal array of NCs, the structure factor rods arise from

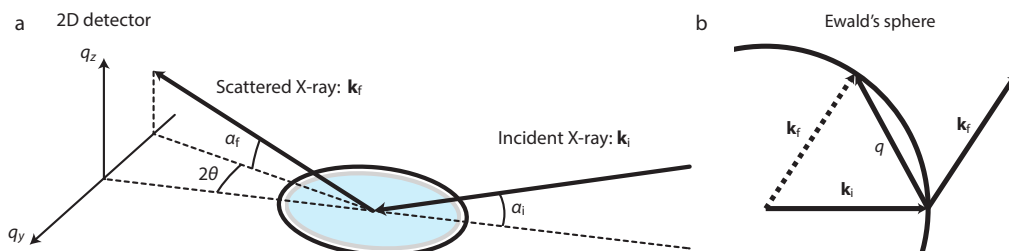


**Figure 9.1** Grazing Incidence Small-Angle X-ray Scattering (GISAXS). (a) If the angle of incidence ( $\alpha_i$ ) is small ( $<$ critical angle  $\alpha_c$ ), the beam is reflected at the same angle ( $\alpha_f$ ). Scattering on a periodic object (*i.e.* a nanocrystal or nanocrystal array) results in scattering at well defined angles  $2\theta$ . (b) The Ewald's sphere denotes the position of the reflected beam after scattering with respect to the scatterer and gives the size of the wavevector  $q$ . Adapted from ref. 20.

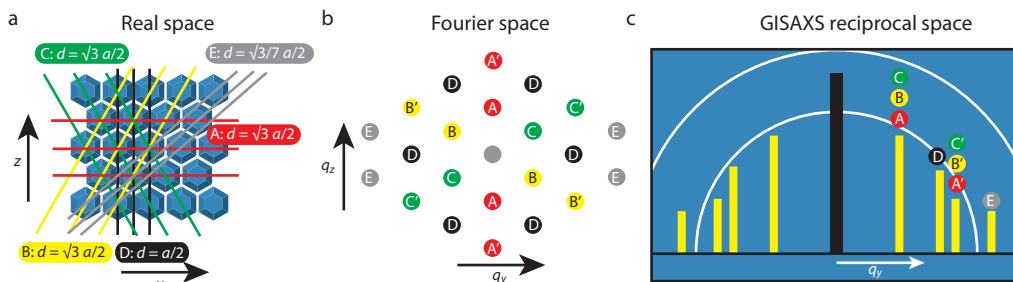


**Figure 9.2. Hexagonal order in real and reciprocal space.** (a) In a hexagonal array of nanocrystals (NCs), scattering occurs at well defined planes with characteristic interplane separations  $d$  ( $a$  denotes the interparticle separation). (b) Hexagonal order in Fourier space, which is rotated  $30^\circ$  with respect to the hexagonal array in real space. (c) In a GISAXS experiment, structure factor rods characteristic of an hexagonal array arise at relative  $q$ -values  $1:\sqrt{3}:2:\sqrt{7}$ . Note that when the separation between the lattice planes is small in real space, the structure factor rods appear at the largest  $q$ -values in reciprocal space. Adapted from ref. 21.

constructive interference on the planes indicated in Figure 9.2a in real space.<sup>21</sup> When converted to Fourier space, an hexagonal pattern is observed as well, but  $30^\circ$  tilted (Figure 9.2b). In the GISAXS pattern (Figure 9.2c) the structure factor rods have relative positions of  $1:\sqrt{3}:2:\sqrt{7}$ . In GISAXS experiments, only  $q_y$  holds information about the NC order in the plane of the superstructure, as indicated in more detail in Figure 9.2. As in SAXS experiments, GISAXS also holds information about the shape of the NCs. In SAXS experiments this is reflected in form factor modulations at large  $q$ , which is seen as multiple minima in the scattering pattern. In a GISAXS experiment, this is seen as half circles (Figure 9.2c), which correspond to local minima in the scattering intensity, correlated to the size and shape of the scatterers.

### 9.3 Methods

**Materials.** Copper (II) sulfate pentahydrate ( $\text{CuSO}_4 \cdot 5\text{H}_2\text{O}$ ,  $\geq 98\%$ ), Zinc chloride ( $\text{ZnCl}_2$ ,  $\geq 98\%$ ), 1-dodecanethiol (DDT, 98%), Oleylamine (OLAM, tech. 70%), 1-octadecene (ODE, 90%), Oleic acid (OA, 90%), Ethylene glycol (EG, anhydrous, 99.8%), Toluene (anhydrous, 99.8%), Methanol (MeOH, anhydrous, 99.8%), 1-Butanol (BuOH, anhydrous, 99.8%) were purchased from Sigma Aldrich. OLAM and ODE were degassed at  $120^\circ\text{C}$  for 2 hours before use, all other chemicals were used as received.

**Bifrustrum-shaped colloidal  $\text{Cu}_{2-x}\text{S}$  nanocrystals** were synthesized according to a method adapted from Lu *et al.*<sup>22</sup> First, 200 mg of  $\text{CuSO}_4 \cdot 5\text{H}_2\text{O}$  is mixed in 7.5 mL DDT and 6.0 mL OA. Next, the mixture is heated to  $200^\circ\text{C}$  for two hours, during which the  $\text{Cu}_{2-x}\text{S}$  nanocrystals form. The reaction was quenched by removal of the heating mantle and the addition of  $\sim 5$  mL toluene at  $70^\circ\text{C}$ . Afterward, the  $\text{Cu}_{2-x}\text{S}$  nanoparticles were washed by precipitation with 5 mL of an 1:1 MeOH:BuOH mixture and finally redispersed in  $\sim 5$  mL toluene. This washing cycle was repeated twice. For the final washing step, 1 mL of the NC solution in toluene were redispersed in  $\sim 2$  mL trioctylphosphine (TOP) by precipitation with the same MeOH:BuOH mixture and centrifugation.

**Cation exchange reactions of  $\text{Zn}^{2+}$  for  $\text{Cu}^+$**  were performed as described by Li *et al.*<sup>23</sup> First, 1 mmol

ZnCl<sub>2</sub> was dissolved in 3 mL ODE and 2 mL OLAM (both previously degassed) at 250 °C. Subsequently, the Cu<sub>2-x</sub>S NCs dispersed in trioctylphosphine (TOP) were injected at that temperature (concentration ~10<sup>-8</sup> M). The mixture was allowed to react for 5 min under heating and stirring, after which the temperature was lowered to 70 °C, followed by the addition of ~5 mL toluene. The NCs were precipitated by adding a 1:1 MeOH:BuOH solution. Afterward, the NCs were isolated by centrifugation and finally redispersed in ~3 mL toluene. This cycle was repeated twice.

*Self-assembled 2D NC superlattices* were obtained according to the method described by Chen *et al.*<sup>24</sup> First, the NC solution in toluene was diluted 4 times (final concentration ~3×10<sup>-9</sup> M, assuming stoichiometric reaction and no purification losses) and 0.5 mL of this diluted solution was brought onto a dense liquid surface (ethylene glycol, EG, 28 mL, in a Teflon petri dish with an inner diameter of 64 mm). Subsequently, the toluene was allowed to evaporate at room temperature over the course of an hour, resulting in the formation of a continuous membrane at the liquid-air interface. Finally, these 2D superstructures were scooped onto a TEM-grid and dried overnight prior to further *ex-situ* investigation with TEM and ED. In the experiments where additional ligands were added, 100 µL of a 0.03 M ligand in ethylene glycol stock-solution, prepared by dissolving 0.09 mmol ligand in 3 mL ethylene glycol, was added to the liquid ethylene glycol substrate. This gives a nominal ligand/NC ratio of 2×10<sup>6</sup>, which corresponds to roughly 3.5×10<sup>2</sup> added ligands per surface Zn site (assuming that 50% of the surface sites are Zn atoms and a spherical NC of 11 nm diameter).

*In-situ Grazing Incidence Small Angle X-ray Scattering (GISAXS) and Grazing Incidence Wide Angle X-ray Scattering (GIWAXS) measurements* were carried out at the European Synchrotron Radiation Facility (ESRF) in Grenoble, France, at the ID10 beamline. A photon energy of 8 keV was used and the angle of incidence was fixed at 0.3°. All GIWAXS signals were collected with a Pilatus-300K photon detector, with dimensions of 487×619 pixels and a pixelsize of 172×172 µm<sup>2</sup>. The distance from the liquid cell to the GIWAXS detector was approximately 20 cm. The 2D detector used for the GISAXS measurements was a Maxipix CCD sensor, with dimensions of 256×1296 pixels and a pixelsize of 52×52 µm<sup>2</sup>. The sample-to-detector distance was 50 cm.

*Calibration of the GISAXS and GIWAXS detectors.* The positions of the X-ray detectors relative to the middle of the sample cell were calibrated using reference samples of Ag-behenate (for GISAXS) and α-Al<sub>2</sub>O<sub>3</sub> (for GIWAXS). In the analysis, however, we have to take into account that the sample cell has a diameter of 6.4 cm, and the X-ray beam comes in at a very shallow angle. Therefore, a slight variation in the liquid level or in the curvature of the liquid surface may change the position on the sample cell where the X-ray beam hits. This position can shift from the middle of the sample cell to at most 3.2 cm back or forward along the direction of X-ray beam. We used the patterns recorded on the GIWAXS detector, where diffraction appears at known angles fixed by the wurtzite crystal structure of ZnS, to determine this shift. The shift determined in this way did not show abrupt changes as a function of time, and was at most 2.0 cm from the middle of the sample cell. All diffraction angles and scattering vectors given were corrected accordingly.

*Transmission Electron Microscopy (TEM) images* were acquired using a FEI Tecnai-10 microscope operating at 100 kV. Samples for TEM imaging were prepared by scooping the NC superstructures onto a carbon-coated copper (400-mesh) TEM grid. Electron Diffraction (ED) patterns were obtained without selected area diffraction aperture.

## 9.4 Results&Discussion

### 9.4.1 Self-assembled superstructures of bifrustum-shaped ZnS NCs

The techniques used in our study give information about the positional order of the NCs *in-situ* and *ex-situ* (GISAXS and TEM, respectively, Figure 9.3a), the orientational

order with respect to the liquid-air interface *in-situ* (GIWAXS, Figure 9.3a), and the orientational order in the plane of the interface (ED, Figure 9.3a). The wurtzite ZnS NCs studied here have two distinct types of crystal facets (*viz.*, two hexagonal {002} top and bottom facets and twelve trapezoidal {101} side facets, as displayed in the inset of Figure 9.3a). If we assume that the ZnS NCs are near-stoichiometric, then the {101} facets are alternatingly Zn- and S-terminated (Figure 9.3a). In this situation, both oleic acid (OA) and oleylamine (OLAM) ligands are expected to selectively bind to the Zn-terminated {101} facets,<sup>25,26</sup> since they are neutral Lewis bases (L-type ligands) and will therefore bind to Lewis acids (*e.g.*,  $\text{Zn}^{2+}$ ), but not to other Lewis bases (*e.g.*,  $\text{S}^{2-}$ ).<sup>27</sup> The native ligands on the ZnS NCs are OLAM molecules ( $\text{C}_{18}\text{H}_{35}\text{NH}_2$ ), which bind to the surface  $\text{Zn}^{2+}$  atoms through the donor N atom of the amine head group.<sup>26</sup> The added OA ligands ( $\text{C}_{17}\text{H}_{33}\text{COOH}$ ) are expected to replace the OLAM ligands *via* a ligand exchange reaction, since their carboxylic acid head group coordinates more strongly to

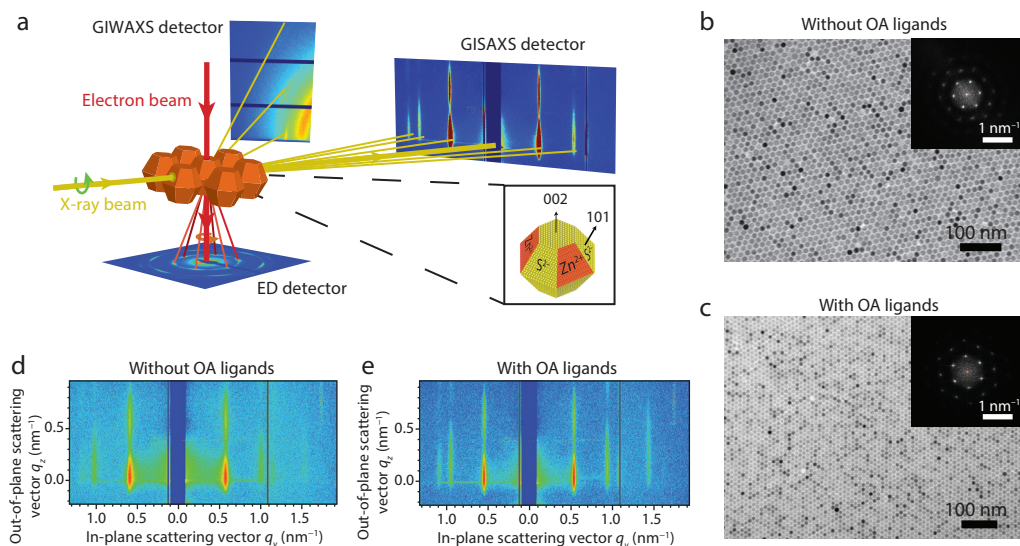


**Figure 9.3.** Schematic representation of the *in-situ* GISAXS and GIWAXS measurements, the *ex-situ* Electron Diffraction (ED) measurements and the geometry of the wurtzite bifrustum-shaped ZnS NCs. (a) The 2D ZnS NC superstructures were studied *in-situ* with GISAXS and GIWAXS, simultaneously, following the formation of the superlattice on nanocrystal and atomic length scales, respectively. *Ex-situ* ED analysis reveals the atomic order. The combination of *in-situ* GIWAXS and *ex-situ* ED provides information about the orientation of the NCs with respect to the liquid-air interface (GIWAXS), as well as in the plane of the interface (ED). The inset shows an enlargement of the wurtzite hexagonal bifrustum-shaped ZnS NCs, with two hexagonal {002} facets and twelve trapezoidal {101} facets. The {101} facets are alternating Zn- and S-terminated (orange area for Zn-terminated facets, inset). (b) *Ex-situ* Transmission Electron Microscopy (TEM) analysis on 2D ZnS NC superstructures shows long-range nanoparticle order with hexagonal symmetry, as evidenced by the FFT (insets), with an interparticle spacing of 12.2 nm without the addition of OA ligands and (c) 13.6 nm with the addition of OA ligands. (d,e) Snapshot of the *in-situ* GISAXS measurements during the formation of the 2D hexagonal 2D ZnS superstructure ( $t = 18$  min) reveals hexagonal symmetry with scattering rods in the in-plane scattering direction at relative  $q$ -values of 1: $\sqrt{3}$ :2: $\sqrt{7}$  both (d) without and (e) with OA ligands added.

Zn<sup>2+</sup> than amine groups, due to its bidentate character and the harder Lewis base nature of the O donor atoms.<sup>26,27</sup> Moreover, the added OA ligands are in excess with respect to the native OLAM ligands (lower limit estimate for the OA/surface Zn sites ratio is 350, see Methods). The self-assembly of the hexagonal bifrustum ZnS NCs (diameter: 11 nm) was investigated with and without adding OA to the EG substrate prior to the addition of the NC solution (see Methods). *Ex-situ* TEM analysis of the resulting NC superstructures shows long-range NC order over several  $\mu\text{m}^2$ , encompassing several thousands of NCs, both in the presence and in the absence of OA (Figure 9.3b,c). FFT analysis shows hexagonal NC order and an interparticle separation of 12.2 nm without added OA ligands (inset Figure 9.3b), and 13.6 nm with added OA ligands (inset Figure 9.3c). OLAM and OA have comparable chain lengths (*viz.*, 2 nm)<sup>28</sup> and a double bond between C9 and C10, differing only with respect to the head group (*i.e.*, NH<sub>2</sub> and COOH, respectively). Therefore, the observed increase in inter-particle separation in the presence of OA ligands cannot be explained by an increase in chain length due to OLAM for OA ligand exchange. However, as mentioned above, OA is a stronger and less dynamic ligand than OLAM,<sup>26,29,30</sup> and therefore the ligand coverage density of the Zn-terminated {101} facets of the NCs has likely increased due to the addition of OA ligands, which prevents the ligands to fully interdigitate,<sup>16</sup> resulting in larger inter-particle separations.

Hexagonal NC order is also evident from snapshots of the *in-situ* GISAXS measurements (Figure 9.3d,e;  $t = 18$  min in both cases). Scattering rods in the in-plane scattering direction are observed at relative  $q$ -values of  $1:\sqrt{3}:2:\sqrt{7}$ , which are characteristic for hexagonal 2D supercrystals (Figure 9.3d,e).<sup>9,12,31</sup> From the scattering rods, nearest-neighbor inter-particle separations of 11.2 nm (without OA ligands) and 11.5 nm (with OA ligands) were deduced at the end of the experiment ( $t = 60$  min). The discrepancy between the inter-NC separation deduced from *in-situ* (*viz.*, 11.2 and 11.5 nm, without and with OA, respectively) and *ex-situ* (*viz.*, 12.2 and 13.6 nm, without and with OA, respectively) measurements will be discussed in more detail below.

#### 9.4.2 *In-situ* atomic alignment

The difference between the superstructures formed in the presence or absence of OA ligands becomes apparent from the GIWAXS patterns. In the absence of OA, the GIWAXS signal shows rings (Figure 9.4a,b), indicating that the NCs have full rotational freedom at the liquid-air interface. In the presence of OA ligands, the atomic scattering is focused into spots (Figure 9.4c,d), which clearly demonstrates that the NCs adsorb with a preferred crystallographic orientation. The atomic {100}, {101} and {102} crystal planes scatter at well-defined azimuthal angles  $\phi$ , from which the NC orientation at the liquid-air interface can be deduced. For example, the orientation of the {101} reflection is  $28.6^\circ$  with respect to the plane of the superstructure, with  $12.5^\circ$  orientation distribution (Figure 9.4d). This indicates that the {002} facets are pointing upward. In fact, the experimental GIWAXS pattern, obtained in the presence of OA

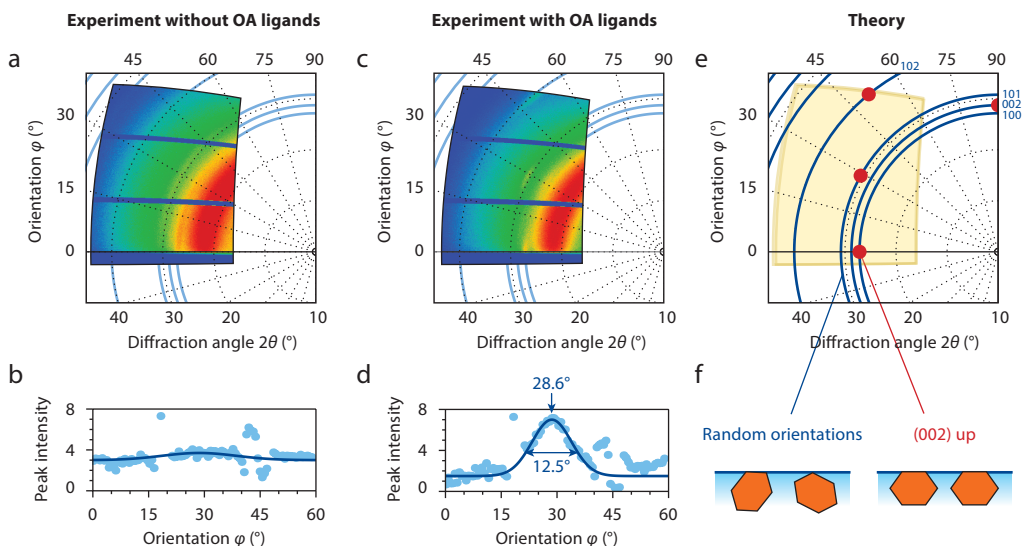


**Figure 9.4. Oleic acid induced atomic alignment.** (a) GIWAXS analysis of wurtzite ZnS 2D NC superstructures shows that in the absence of OA ligands, the NCs adsorbed at the liquid-air interface have full rotational freedom, evidenced by diffraction rings in the GIWAXS pattern. The broad intense scattering signal at small  $2\theta$  originates from the ethylene glycol (EG) liquid substrate. (b) The intensity profile of the  $\{101\}$  reflection as a function of azimuthal angle  $\varphi$  reveals no orientation in the absence of OA ligands. (c) In the presence of OA ligands, the  $\{100\}$ ,  $\{101\}$  and  $\{102\}$  reflections are concentrated into well-defined spots, indicating atomic alignment. (d) In the presence of additional OA ligands, the intensity profile of the  $\{101\}$  reflection as a function of azimuthal angle  $\varphi$  reveals that the  $\{101\}$  reflections are oriented at  $28.6^\circ$  with respect to the toluene-air interface, indicating that the  $\{002\}$  facets are pointing upward. The NCs have a  $12.5^\circ$  distribution in orientation (full-width-at-half-maximum). (e) Calculated GIWAXS pattern for wurtzite ZnS NCs with the  $\{002\}$  facet pointing upward (red dots). (f) Schematic representations of two hexagonal bifrustum ZnS nanocrystal adhered to the toluene-air interface with random orientations, resulting in diffraction rings (left), and with their  $\{002\}$  facets pointing upward, resulting in well-defined diffraction spots (right).

ligands, closely matches the simulated pattern for NCs adsorbed with a  $\{002\}$  facet at the liquid-air interface (Figure 9.4e,f). Wurtzite ZnS NCs adhered to the liquid-air interface with their  $\{101\}$  facets generate diffraction spots at different azimuthal angles  $\varphi$ , as experimentally verified by assembling hexagonal ZnS bipyramidal NCs (diameter: 28 nm, length: 38 nm) and larger hexagonal ZnS bifrustum NCs (diameter: 33 nm) (Figure 9.5). The assembly of larger ZnS bifrustums (diameter: 33 nm) into 2D superstructures shows both orientations, *i.e.*  $\{002\}$  and  $\{101\}$  facets pointing upward (Figure 9.5c,f,i). Presumably, this indicates that an increase in facet area, due to an increase in size of the entire NC, creates two deep local minima for the adsorption of the NCs to the air-toluene interface, in agreement with the theoretical calculations reported in the previous chapter.<sup>8</sup> Furthermore, we note that we also investigated the

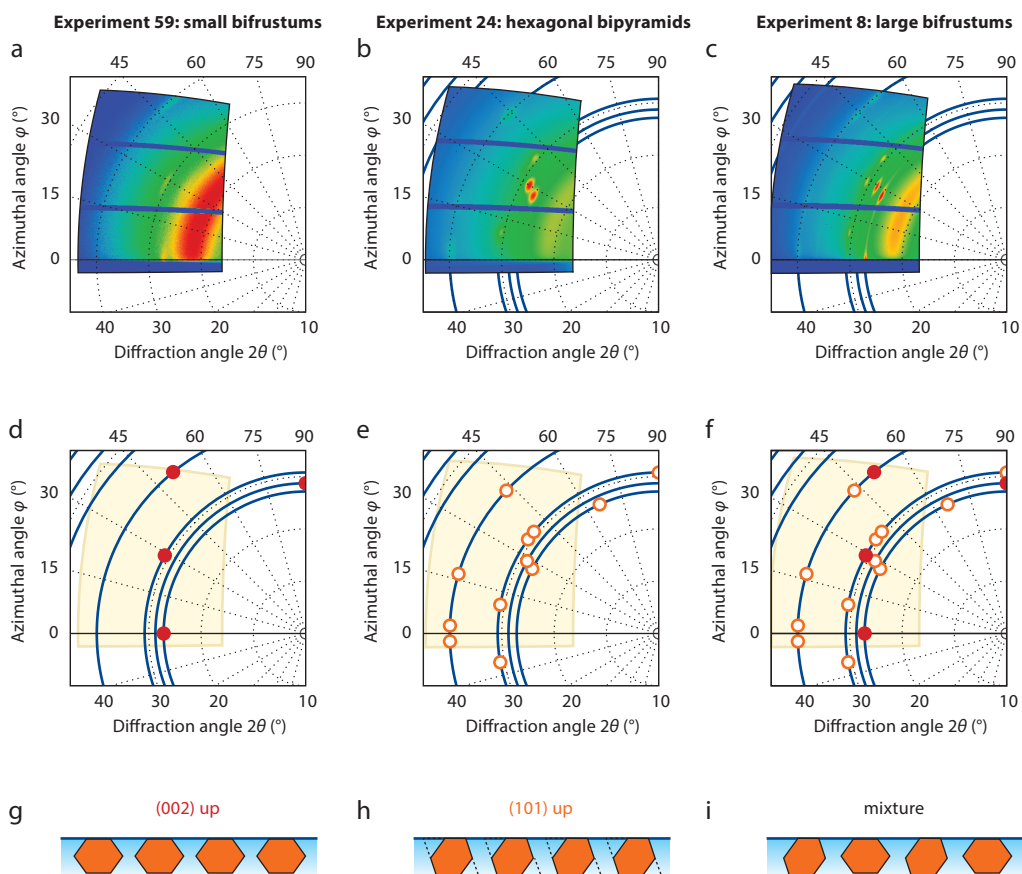


**Figure 9.5. Comparison of atomic alignment with {002} and {101} adhered to the interface.** Atomic alignment of (a,d,g) small hexagonal bifrustum ZnS nanocrystals (NCs), (b,e,h) hexagonal ZnS bipyramids and (c,f,i) large hexagonal ZnS NCs. For 2D NC superstructures of small bifrustum NCs, the {002} facets are all pointing upward (schematic representation in panel g), as evidenced by the comparison of (a) the experimental GIWAXS pattern and (d) calculated GIWAXS pattern. For 2D NC superstructures of hexagonal bipyramid NCs, the {101} facets are pointing upward (schematic representation in panel h). In this case, the {002} facets are too small to adsorb to the liquid-air interface, due to the relatively sharp tips of the bipyramids. (b) The experimental GIWAXS pattern closely matches (e) the calculated GIWAXS pattern. When large hexagonal bifrustum NCs self-assemble into 2D NC superstructures, a coexistence of {002} and {101} facets pointing up is observed (schematic representation in panel i). (c) Diffraction spots originating from both orientations are present in the GIWAXS pattern and the experimental pattern closely matches (f) the calculated pattern.

influence of additional DDT and OLAM ligands on the self-assembly of ZnS NCs and found that DDT disrupts the 2D self-assembly (*i.e.* results in 3D superstructures), whereas additional OLAM has no influence on the formation of 2D superstructures or on the atomic alignment of individual NCs.

### 9.4.3 *In-situ nanoparticle order*

Time-resolved GISAXS measurements of the NC ordering shows a shift of the scattering rods to larger  $q$ -values during the evaporation of the solvent toluene, as evidenced by the temporal evolution of the first scattering peak around  $0.6 \text{ nm}^{-1}$  (Figure 9.6a,c, see also Appendix A9.1 and Figure A9.1). This implies that the NCs come closer together in real space, *i.e.* the superstructure shrinks over time. The shifts of the scattering peaks in the GISAXS signal over the course of the entire experiment (duration: 60 min) are displayed in Figure 9.6b,d. This shows that the NCs order at the interface into a hexagonal structure already at early stages ( $t = 5 \text{ min}$ ) of the self-assembly process. Gradually, the inter-particle separation is reduced, presumably as more NCs adhere to the 2D interface. Eventually, this results into ordered close-packed 2D hexagonal superstructures with in-plane nearest-neighbor distances of  $11.2 \pm 0.2 \text{ nm}$  without OA ligands added and  $11.5 \pm 0.2 \text{ nm}$  with OA ligands added (the error is given as the standard deviation in nearest-neighbor distances calculated from the first- and higher-order scattering rods at both sides of the beam stop). These in-plane nearest-neighbor distances are 1–2 nm shorter than observed *ex-situ* by TEM (*viz.*, 12.2 and 13.6 nm without and with OA ligands added, respectively, see above), and very close to the diameter of the NCs (11 nm).

The surprisingly close in-plane NC separation observed *in-situ* and the discrepancy between the *in-situ* and *ex-situ* inter-NC separations can be explained in two ways. First, if we assume that the 2D plane of self-assembled NCs at the air-toluene interface is buckled (*i.e.*, some NCs are pushed out of the plane, either up or down), the inter-particle separation can be theoretically reduced from 13.6 nm (completely planar structure) to 10.4 nm (maximum buckling), even if the surface-to-surface distance is fixed at 2 nm by the ligand layers. Considering that no additional peaks are observed in the GISAXS patterns, the buckling would have to be aperiodic. Buckling has been previously observed for 2D superstructures, such as honeycomb superlattices with a silicene-like structure, formed by oriented attachment of PbSe NCs.<sup>9</sup> The PbSe NCs are atomically attached and therefore the buckled structure is mechanically stable and can be observed with TEM.<sup>9</sup> In the present case, however, the in-plane NC separation observed with *ex-situ* TEM is larger than that observed *in-situ*. This can be ascribed to the fact that the ZnS NCs are not attached, so that the buckled superstructure is allowed to relax back to the planar superstructure, under influence of the strong capillary forces acting during drying of the ZnS NC superstructures prior to TEM imaging. Alternatively, the *in-situ* surface coverage with OA ligands may be relatively low and therefore the ligands have rotational freedom on the NC surface, resulting in a ligand layer of  $\sim 0.5 \text{ nm}$ . Hanrath and coworkers have recently shown with Molecular Dynamics that at low surface coverage of PbSe NCs with OA ligands, inter-NC separations as small as 0.5 nm are indeed possible.<sup>25</sup> In this scenario, the larger inter-particle separation observed *ex-situ* could be explained by assuming that the surface coverage density by OA ligands increases during drying of the ZnS superstructures due to binding of OA

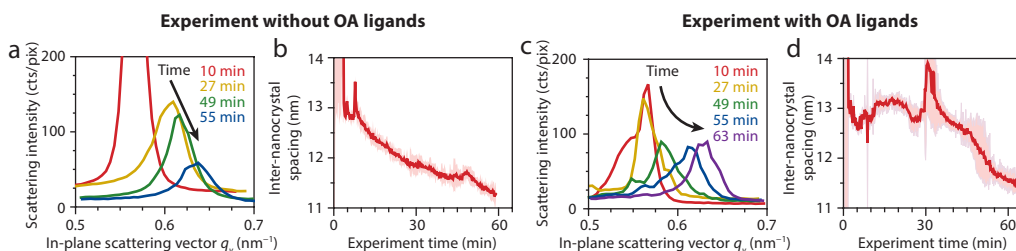


**Figure 9.6. GISAXS analysis of 2D ZnS NC hexagonal superstructures.** Time-resolved GISAXS measurements show a shift of the diffraction rods to larger in-plane scattering vectors, meaning a reduction in interparticle separation, *i.e.* shrinking of the superstructure, (a,b) without and (c,d) with the addition of OA ligands. (a,c) A zoom of the first scattering rod clearly shows the shift during the first hour, indicating that the NCs, while ordered, come closer together. The final in-plane nearest-neighbor distance in the 2D superstructure is (b)  $11.2 \pm 0.2$  nm without OA ligands added and (d)  $11.5 \pm 0.2$  nm with OA ligands.

ligands originally in solution.

#### 9.4.4 Ex-situ atomic order

As depicted in Figure 9.3a, preferred orientation of atomic planes can be observed *in-situ* with GIWAXS and *ex-situ* with ED. The two techniques reveal the degree of atomic orientation of the NCs in two different directions, namely the extent of rotational disorder in the plane perpendicular to the respective incoming beam (*i.e.* X-ray beam and electron beam). This is indicated in Figure 9.3a with the circled arrows. GIWAXS shows how strictly the NCs are adsorbed at the liquid-air interface with a particular facet adhered, as discussed above (Figure 9.4). ED shows not only how the NCs are adsorbed to the interface, but also how they are oriented in the 2D plane. Diffraction only occurs on planes oriented along the electron beam. In the case of NCs with a [002] axis pointing upward (*i.e.* with OA added), we therefore mainly see {100}, {110} and {200} reflections (Figure 9.7a). Furthermore, the ED pattern is six-fold rotationally symmetric, which proves that the NCs have a preferred atomic orientation in the 2D plane. Such preferred orientation is absent when no OA ligands were added. Instead, disordered spots on vague rings are observed, consistent with random orientation of ZnS NCs (Figure 9.7b). From the radially integrated 1D ED patterns with OA ligands (red data points in Figure 9.7c), it is directly evident that the {002} facets are pointing upward, since this reflection (which would be at  $2\theta = 0.78^\circ$ ) is almost absent in the integrated diffraction profile. The fraction of aligned and random NCs can be calculated by comparing the intensities of the different reflections. To this end, the integrated 1D ED patterns were fitted to the known XRD pattern of wurtzite ZnS (JCPDS-card no. [05-0492]) with the width of the peaks set by the Debye-Scherrer equation for NCs with a diameter of 11 nm. This analysis reveals that without OA ligands added, 48% of the NCs are oriented with their {002} facet pointing upward (yellow line in Figure

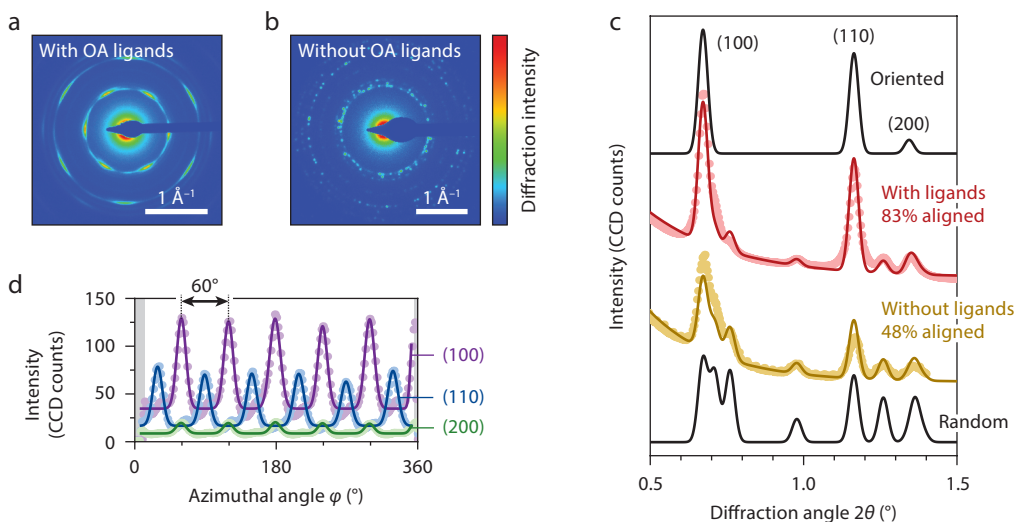


**Figure 9.7. Ex-situ electron diffraction (ED) measurements on 2D ZnS superstructures.** (a) ED pattern of 2D superstructure in the presence of oleic acid ligands, showing preferred orientation, evidenced by diffraction spots. (b) ED pattern of 2D superstructure in the absence of oleic acid ligands, showing random orientation, evidenced by diffraction rings. (c) By integration of the 2D ED pattern in (a) and (b), the 1D diffraction line profile is obtained. In the presence of OA, the  $\{100\}$  and  $\{110\}$  diffractions have increased intensity (compare red data points to yellow data points), consistent with  $\{002\}$  facets pointing upward. The black lines are the theoretical ED patterns (PDF-card no. [05-0492] and Debye-Scherrer equation for NCs with a diameter of 11 nm) for randomly oriented NCs (bottom) and NCs oriented with the  $[002]$  axis upward (top). The solid red and yellow line are fits to a combination of aligned and randomly oriented NCs. We find that 48% of the NCs is aligned without additional OA ligands (yellow line), but after the addition of OA ligands this value is 83%. (d) ED intensity profiles as a function of azimuthal angle, for the  $\{100\}$  (purple dots),  $\{110\}$  (blue dots), and  $\{200\}$  (green dots) reflections, showing sixfold symmetry, indicating preferred orientation in the  $xy$ -plane.

9.7c), whereas in the presence of OA ligands, 83% of the NCs are aligned (red line in Figure 9.7c). The ED intensity profiles as a function of azimuthal angle  $\varphi$  of the  $\{100\}$  (purple dots in Figure 9.7d),  $\{110\}$  (blue dots in Figure 9.7d), and  $\{200\}$  (green dots in Figure 9.7d) reflections show six-fold symmetry, because of preferred orientation in the  $xy$ -plane. As expected, the  $\{100\}$  and  $\{200\}$  diffraction spots occur at the same azimuthal angle (with a variation in orientation of  $\sigma = 6.2^\circ$ ) and the reflections are separated by  $60^\circ$ , whereas the  $\{110\}$  reflection is  $30^\circ$  out of phase with the  $\{100\}$  and  $\{200\}$  reflections (Figure 9.7d).

#### 9.4.5 Formation mechanism of 2D ZnS NC superstructures

The *in-situ* GISAXS and GIWAXS experiments, in combination with *ex-situ* TEM analysis, have provided us a full picture of the self-assembly process, including the effect of OA ligands. The first step of the self-assembly process is the adhesion of

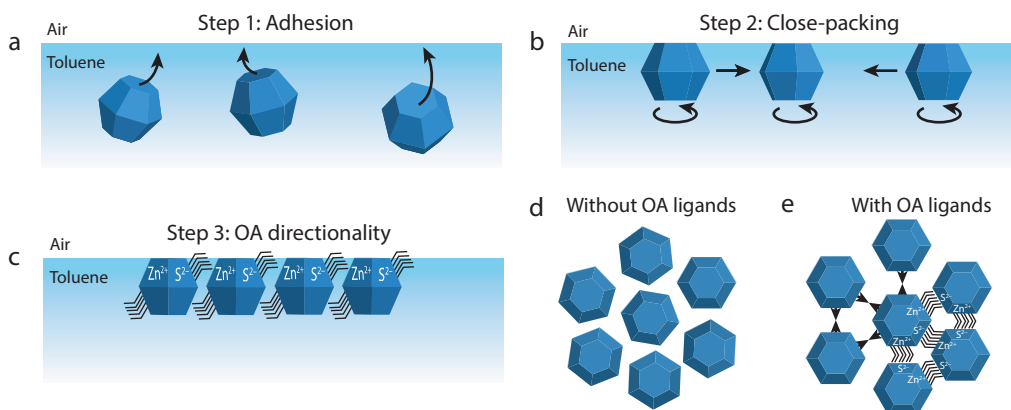


**Figure 9.8. Schematic representation of the formation mechanism of 2D ZnS nanocrystal superstructures.**

(a) Step 1: The hexagonal bifrustum-shaped ZnS nanocrystals adhere preferentially with their {002} facets to the air-toluene interface in the presence of OA ligands. (b) Step 2: After this adhesion, the NCs approach each other while confined to the interface and can only translate and rotate in the plane of the interface. (c) Step 3: OA ligands give directionality to the self-organization process by selectively adhering to the Zn-terminated {101} facets. (d) In the absence of OA ligands the NCs can rotate in the plane of the interface, without preferred orientation of the NCs. (e) The addition of OA ligands increases the surface coverage of the Zn-terminated {101} facets and therefore limits the rotational freedom of the NCs, resulting in preferred orientation of the atomic planes at the liquid-air interface.

the NCs to the air-toluene interface (step 1, Figure 9.8a). Theoretical calculations have shown that this step is irreversible.<sup>8</sup> The experimental results discussed above show that in the absence of OA ligands the adhesion of 11 nm diameter ZnS bifrustum NCs to the interface occurs randomly, without any preferential orientation. However, in the presence of OA ligands, the ZnS NCs preferentially adhere to the air-toluene interface with their {002} facets. This can be understood by assuming that the OA ligands selectively bind to the trapezoidal Zn-terminated {101} facets of the ZnS bifrustums. The polar {002} facets are either Zn- or S-terminated, and therefore at least one of them (*i.e.*, the S-terminated) would be free of capping ligands. Selective binding of OA to the {101} facets, would thus make their free-energy lower than that of the {002} facets. Consequently, the {002} facets adhere to the liquid-air interface to minimize the NC-toluene interfacial tension. As a result, the NCs are confined to the interface with a fixed orientation and are only allowed to rotate and translate in the plane of the interface.<sup>8</sup> During the evaporation of the toluene, the NCs are forced to close-pack into hexagonal 2D superstructures (step 2, Figure 9.8b). In the absence of OA ligands, the NCs also form hexagonal 2D superstructures, but the atomic planes of the building blocks are randomly oriented with respect to each other (Figure 9.8d), as the NCs are still allowed to rotate in the plane. In the presence of OA ligands, the NCs are atomically aligned. We propose that this alignment is due to directional interactions

between the OA ligands bound to the {101} facets (Figure 9.8c,e). The {101} facets are alternately Zn- and S-terminated and the added OA ligands are expected to selectively bind to the Zn-terminated {101} facets.<sup>26,27</sup> This results in three {101} facets above the hexagonal base capped with OA ligands, and three {101} facets below the hexagonal base. A second NC, with the same surface coverage, can then rotate such that its 'bare' S-terminated {101} facet orients to a fully covered Zn-terminated {101} facet (Figure 9.8c,e). This limits the rotational freedom of the NCs, resulting in preferred orientation of the atomic planes, since the {002} facet is already locked at the air-toluene interface.

## 9.5 Conclusions

In conclusion, we have shown that oleic acid (OA) ligands induce atomic alignment of hexagonal bifrustum-shaped wurtzite ZnS NCs in hexagonal 2D superstructures. GIWAXS and ED show that the {002} facets of the ZnS NCs preferentially adhere to the air-toluene interface in the presence of OA ligands, resulting in atomic alignment. This is ascribed to directional interactions between the NCs when confined to the *xy*-plane after adhesion, thereby limiting their in-plane rotational freedom. Our results highlight the importance of surface chemistry control on the design of ordered and atomically aligned NC superstructures, and show that the impact of ligands on the directionality of the self-organization process strongly depends not only on the morphology and faceting of the NC building blocks, but also on the chemical composition of the exposed facets and on the interaction between ligands. The approach described here can thus potentially be extended to other polyhedral shapes. Furthermore, our findings may prove beneficial for applications in the field of photovoltaic and plasmonic devices, in which ordered thin layers are crucial for optimal charge injection and carrier mobility.<sup>14,32–35</sup>

## Acknowledgments

The measurements were performed at the ID10 beamline at ESRF, Grenoble. The authors thank Oleg Kononov and Federico Zontone for valuable discussions.

## References

- (1) Vanmaekelbergh, D. *Nano Today* **2011**, 6, 419–437.
- (2) Cargnello, M.; Diroll, B. T.; Gaubing, E. A.; Murray, C. B. *Adv. Mater.* **2014**, 26, 2419–2423.
- (3) Reifsnnyder, D. C.; Ye, X.; Gordon, T. R.; Song, C.; Murray, C. B. *ACS Nano* **2013**, 7, 4307–4315.
- (4) Wang, T.; Zhuang, J.; Lynch, J.; Chen, O.; Wang, Z.; Wang, X.; LaMontagne, D.; Wu, H.; Wang, Z.; Cao, Y. *C. Science* **2012**, 338, 358–363.
- (5) Vanmaekelbergh, D.; van Vugt, L. K.; Bakker, H. E.; Rabouw, F. T.; de Nijs, B.; van Dijk-Moes, R. J. A.; van Huis, M. A.; Baesjou, P. J.; van Blaaderen, A. *ACS Nano* **2015**, 9, 3942–3950.
- (6) Abécassis, B.; Tessier, M. D.; Davidson, P.; Dubertret, B. *Nano Lett.* **2014**, 14, 710–715.
- (7) Cargnello, M.; Johnston-Peck, A. C.; Diroll, B. T.; Wong, E.; Datta, B.; Damodhar, D.; Doan-Nguyen, V. V. T.; Herzog, A. A.; Kagan, C. R.; Murray, C. B. *Nature* **2015**, 524, 450–453.
- (8) van der Stam, W.; Gantapara, A. P.; Akkerman, Q. A.; Soligno, G.; Meeldijk, J. D.; van Roij, R.; Dijkstra,

- M.; de Mello Donega, C. *Nano Lett.* **2014**, *14*, 1032–1037.
- (9) Boneschanscher, M. P.; Evers, W. H.; Geuchies, J. J.; Altantzis, T.; Goris, B.; Rabouw, F. T.; van Rossum, S. A. P.; van der Zant, H. S. J.; Siebbeles, L. D. A.; van Tendeloo, G.; Swart, I.; Hilhorst, J.; Petukhov, A. V.; Bals, S.; Vanmaekelbergh, D. **2014**, *344*, 1377–1381.
- (10) Ye, X.; Chen, J.; Engel, M.; Millan, J.; Li, W.; Qi, L. *Nat. Chem.* **2013**, *5*, 466–473.
- (11) Miszta, K.; de Graaf, J.; Bertoni, G.; Dorfs, D.; Brescia, R.; Marras, S.; Ceseracciu, L.; Cingolani, R.; van Roij, R.; Dijkstra, M.; Manna, L. *Nat. Mater.* **2011**, *10*, 872–876.
- (12) Pietra, F.; Rabouw, F. T.; Rhee, P. G. Van; Rijssel, J. Van; Petukhov, A. V.; Christianen, P. C. M.; Donega, C. D. M.; Erne, B. H.; Christianen, P. C. M.; Donega, C. d. M.; Vanmaekelbergh, D. *ACS Nano* **2014**, *8*, 10486–10495.
- (13) Bian, K.; Choi, J.; Kaushik, A.; Clancy, P.; Smilgies, D.-M.; Hanrath, T. *ACS Nano* **2011**, *5*, 2815–2823.
- (14) Evers, W. H.; Schins, J. M.; Aerts, M.; Kulkarni, A.; Capiod, P.; Berthe, M.; Grandidier, B.; Delerue, C.; van der Zant, H. S. J.; van Overbeek, C.; Peters, J. L.; Vanmaekelbergh, D.; Siebbeles, L. D. A. *Nat. Commun.* **2015**, *6*, 8195–8203.
- (15) Wang, Z.; Schliehe, C.; Bian, K.; Dale, D.; Bassett, W. A.; Hanrath, T.; Klinke, C.; Weller, H. *Nano Lett.* **2013**, *13*, 1303–1311.
- (16) Choi, J. J.; Bealing, C. R.; Bian, K.; Hughes, K. J.; Zhang, W.; Smilgies, D.-M.; Hennig, R. G.; Engstrom, J. R.; Hanrath, T. *J. Am. Chem. Soc.* **2011**, *133*, 3131–3138.
- (17) Nagaoka, Y.; Chen, O.; Wang, Z.; Cao, Y. C. *J. Am. Chem. Soc.* **2012**, *134*, 2868–2871.
- (18) Yu, Y.; Goodfellow, B. W.; Rasch, M. R.; Bosoy, C. A.; Smilgies, D.-M.; Korgel, B. A. *Langmuir* **2015**, *31*, 6924–6932.
- (19) Goodfellow, B. W.; Yu, Y.; Bosoy, C. A.; Smilgies, D.-M.; Korgel, B. A. *J. Phys. Chem. Lett.* **2015**, *6*, 2406–2412.
- (20) Renaud, G.; Lazzari, R.; Leroy, F. *Surf. Sci. Rep.* **2009**, *64*, 255–380.
- (21) Pietra, F.; Rabouw, F. T.; Evers, W. H.; Byelov, D. V.; Petukhov, A. V.; de Mello Donegá, C.; Vanmaekelbergh, D. *Nano Lett.* **2012**, *12*, 5515–5523.
- (22) Lu, X.; Zhuang, Z.; Peng, Q.; Li, Y. *CrystEngComm* **2011**, *13*, 4039–4045.
- (23) Li, H.; Zanella, M.; Genovese, A.; Povia, M.; Falqui, A.; Giannini, C.; Manna, L. *Nano Lett.* **2011**, *11*, 4964–4970.
- (24) Chen, J.; Dong, A.; Cai, J.; Ye, X.; Kang, Y.; Kikkawa, J. M.; Murray, C. B. *Nano Lett.* **2010**, 5103–5108.
- (25) Trembl, B. E.; Lukose, B.; Clancy, P.; Smilgies, D.-M.; Hanrath, T. *Sci. Rep.* **2014**, *4*, 6731–6737.
- (26) Donega, C. d. M. *Chem. Soc. Rev.* **2011**, *40*, 1512–1546.
- (27) Pearson, R. *Inorg. Chem.* **1988**, *27*, 734–740.
- (28) Wang, Z.; Wen, X.-D.; Hoffmann, R.; Son, J. S.; Li, R.; Fang, C.-C.; Smilgies, D.-M.; Hyeon, T. *Proc. Natl. Acad. Sci. U. S. A.* **2010**, *107*, 17119–17124.
- (29) Fritzing, B.; Capek, R. K.; Lambert, K.; Martins, J. C.; Hens, Z. *J. Am. Chem. Soc.* **2010**, *132*, 10195–10201.
- (30) Hassinen, A.; Moreels, I.; Donega, C. d. M.; Martins, J. C.; Hens, Z. *J. Phys. Chem. Lett.* **2010**, *1*, 2577–2581.
- (31) Heitsch, A. T.; Patel, R. N.; Goodfellow, B. W.; Smilgies, D.-M.; Korgel, B. A. *J. Phys. Chem. C* **2010**, *114*, 14427–14432.
- (32) Ip, A. H.; Thon, S. M.; Hoogland, S.; Voznyy, O.; Zhitomirsky, D.; Debnath, R.; Levina, L.; Rollny, L. R.; Carey, G. H.; Fischer, A.; Kemp, K. W.; Kramer, I. J.; Ning, Z.; Labelle, A. J.; Chou, K. W.; Amassian, A.; Sargent, E. H. *Nat. Nanotechnol.* **2012**, *7*, 577–582.
- (33) Ginger, D. S.; Greenham, N. C. *J. Appl. Phys.* **2000**, *87*, 1361.
- (34) McDonald, S. A.; Konstantatos, G.; Zhang, S.; Cyr, P. W.; Klem, E. J. D.; Levina, L.; Sargent, E. H. *Nat. Mater.* **2005**, *4*, 138–142.
- (35) Kim, G.-H.; Garcia de Arquer, F. P.; Yoon, Y. J.; Lan, X.; Liu, M.; Voznyy, O.; Yang, Z.; Fan, F.; Ip, A. H.; Kanjanaboos, P.; Hoogland, S.; Kim, J. Y.; Sargent, E. H. *Nano Lett.* **2015**, *15*, 7691–7696.

## Appendix

### A9.1 Calculating the theoretical GIWAXS patterns of aligned nanocrystals

The ZnS crystal structure is defined by a set of reciprocal lattice vectors  $\{\mathbf{g}_{hkl}\}$ , where  $hkl$  are the Miller indices that label the lattice vectors. In the experiment an X-ray beam with wave vector  $\mathbf{k}_{in}$  is incident on the sample. A nanocrystal can (elastically) diffract the beam if it is oriented such that one of the lattice vectors satisfies the conditions

$$\mathbf{k}_{out} = \mathbf{k}_{in} + \mathbf{g}_{hkl}, \quad (1)$$

$$|\mathbf{k}_{out}| = |\mathbf{k}_{in}|, \quad (2)$$

where  $\mathbf{k}_{out}$  is the wave vector of the diffracted beam.

We consider the situation of nanocrystals adsorbed to the liquid/air interface with a specific crystal facet, *i.e.* oriented with a specific lattice vector  $\mathbf{g}_{up}$  oriented upward, but with rotational freedom in the horizontal plane. Each reciprocal lattice vector  $hkl$  then has a fixed angle  $\alpha$  with respect to the interface normal, but can freely rotate in the horizontal plane:

$$\mathbf{g}_{hkl} = R(\beta)\mathbf{g}_{hkl}^0, \quad (3)$$

where  $R(\beta)$  is a rotation matrix for rotation in the horizontal plane over an angle  $\beta$ , and  $\mathbf{g}_{hkl}^0$  is the reciprocal lattice vector at angle  $\alpha$  with respect to  $\mathbf{g}_{up}$  but with some arbitrary orientation in the horizontal plane. We solve for the rotation angle  $\beta$  at which the diffraction condition (Eqs. 1 and 2) is matched. Knowing this angle, we can calculate  $\mathbf{k}_{out}$  (Eq. 1 with Eq. 3) and the azimuthal angle  $\varphi$  at which diffraction is expected:

$$\varphi = \arccos \frac{k_{out,y}}{\sqrt{k_{out,x}^2 + k_{out,y}^2}} \quad (4)$$

Here  $k_{out,x}$  is the component of  $\mathbf{k}_{out}$  parallel to the liquid/air interface but perpendicular to the incoming beam, and  $k_{out,y}$  is the component normal to the interface.

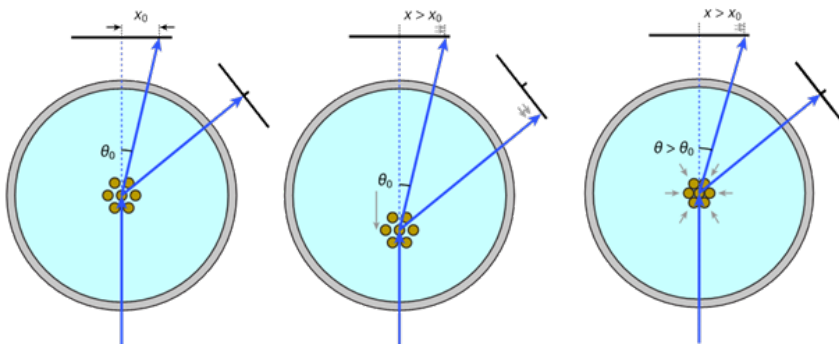


**Figure A9.1.** (Left Panel) Scattering from the center of the sample cell gives the in-plane NC separation on the GISAXS detector as well as the atomic alignment on the GIWAXS detector. (Center panel) Scattering from a point along the incident X-ray beam other than the center, results in scattering at a different position on both the GISAXS and GIWAXS detectors. (Right panel) Scattering from 2D superstructure in which the NCs come closer together, results in scattering peaks at different positions on the GISAXS detector only.





# Summary and Outlook



## ABSTRACT

In this thesis we have discussed several synthetic strategies toward tailored nanomaterials, which in some cases lead to interesting optoelectronic properties (*e.g.* near-infrared photoluminescence). The synthetic protocols that were developed provide a roadmap toward materials with tunable size, shape (Chapters 3–5), composition (Chapters 6 and 7) and superstructure geometry (Chapters 8 and 9), depending on the nanocrystal building blocks. In this chapter we summarize the main results and discuss future research that could be performed.

## 10.1 Shape Tailoring

Semiconductor nanocrystals (NCs) have drawn the attention of a lot of researchers worldwide, owing to their exciting optoelectronic properties that render them interesting materials for several applications. The optoelectronic properties of semiconductor NCs are size- and shape-dependent (Chapter 2), which has led to a surge of research efforts to prepare colloidal semiconductor NCs with narrow size and shape distributions. By carefully tuning the reaction parameters, different sizes of NCs can be obtained with tunable photoluminescence from red to blue (composition: CdSe). Anisotropic NCs are prepared by colloidal protocols as well, in which the facet selectivity of the present ligands determines the final NC geometry, changing it from 0D quantum dots to 1D nanorods and 2D nanoplatelets. Nowadays, the most investigated colloidal semiconductor nanocrystals contain heavy metals such as Cd and Pb, which hinders their successful implementation into applications due to toxicity issues.

In the first part of this thesis (Chapters 3–5), direct synthetic strategies toward  $\text{Cu}_{2-x}\text{S}$  NCs with polyhedral and anisotropic shapes are discussed.  $\text{Cu}_{2-x}\text{S}$  is a p-type semiconductor with a tunable bandgap, depending on the number of Cu vacancies, indicated by  $x$ . Furthermore,  $\text{Cu}_{2-x}\text{S}$  NCs consist of less-toxic and abundant elements, and  $\text{Cu}_{2-x}\text{S}$  NCs have shown unparalleled properties, such as localized surface plasmon resonances (LSPR). We have successfully developed a synthesis protocol that results in a variety of polyhedral NC shapes and relies on changing just one single reaction parameter, *i.e.* the concentration of  $\text{SnBr}_4$  added (Chapter 3, Figure 10.1a). Furthermore, we have shown that the addition of halides to a spherical  $\text{Cu}_{2-x}\text{S}$  NC synthesis protocol

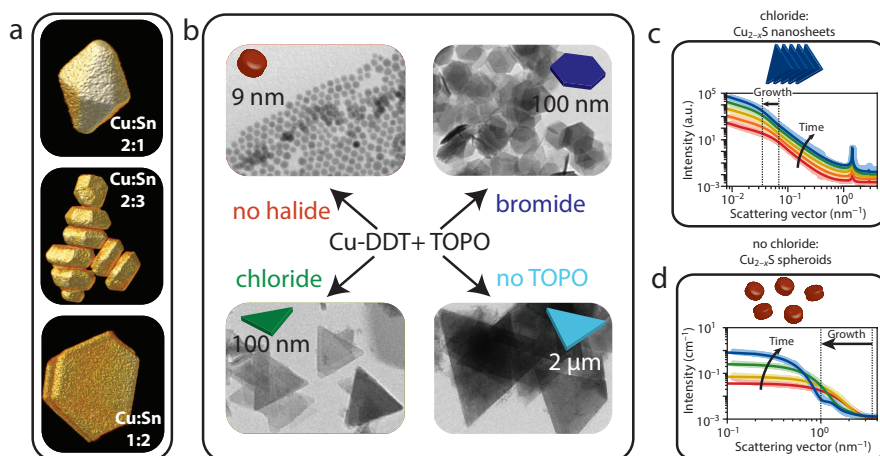


**Figure 10.1. Shape tailoring of  $\text{Cu}_{2-x}\text{S}$  nanocrystals (NCs).** (a) By solely changing the Sn-thiolate complex concentration in solution, polyhedral NCs are obtained (hexagonal bipyramids and nanoplatelets of various thicknesses). (b) The addition of halides to a spherical  $\text{Cu}_{2-x}\text{S}$  NC synthesis has a dramatic influence, resulting in ultrathin  $\text{Cu}_{2-x}\text{S}$  nanosheets. (c) *In-situ* SAXS experiments revealed that halides stabilize stacks of Cu-thiolate precursors, after which  $\text{Cu}_{2-x}\text{S}$  NSs nucleate and grow in stacks.

has a dramatic impact, resulting in ultrathin  $\text{Cu}_{2-x}\text{S}$  nanosheets (NSs, Chapter 4, Figure 10.1b), with variable lateral dimensions (ranging from 100 nm to 3  $\mu\text{m}$ ) and shape, but a constant thickness of 2 nm. The exact growth mechanism of these ultrathin  $\text{Cu}_{2-x}\text{S}$  NSs has been elucidated by *in-situ* Small-Angle X-ray Scattering (SAXS) experiments (Figure 10.1c,d). These experiments revealed that halides stabilize stacks of Cu-thiolate precursors, after which  $\text{Cu}_{2-x}\text{S}$  NSs nucleate and grow in stacks, thereby limiting the growth in thickness (Chapter 5, Figure 10.1c). Our results discussed in Chapters 3–5 highlight the size- and shape-tunability of colloidal  $\text{Cu}_{2-x}\text{S}$  NCs.

## 10.2 Composition Tailoring

The results discussed in Chapters 3–5 may have a more general impact, since  $\text{Cu}^+$  has been shown to be easily exchanged for other cations in  $\text{Cu}_{2-x}\text{S}$  NCs *via* topotactic cation exchange (CE) reactions. This is mainly due to the small size and low charge of  $\text{Cu}^+$  cations, which makes them extremely mobile within the anionic sublattice, almost behaving as a liquid. With CE reactions, metastable crystal structures can be obtained, which are not attainable in a direct fashion (*e.g.* wurtzite ZnS). Very often, the anionic framework remains unaffected by the CE reactions, thereby preserving the size and shape of the parent NCs in the product NCs. CE reactions might occur fully or partially, resulting in doped NCs, alloyed NCs, NCs with metastable structures or complex hetero-architectures.

In this thesis, we developed a strategy to prepare ternary Cu-chalcogenide nanomaterials from template  $\text{Cu}_{2-x}\text{S}$  NCs *via* cation exchange (CE) reactions. In this way,  $\text{CuInS}_2$  NCs

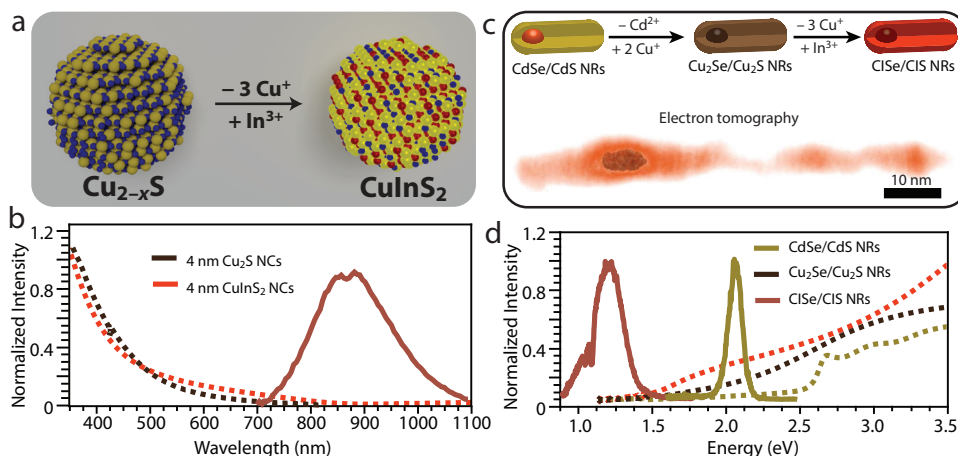


**Figure 10.2. Composition tailoring toward ternary Cu chalcogenides.** (a) Partial cation exchange reactions are used to convert binary  $\text{Cu}_{2-x}\text{S}$  NCs into ternary  $\text{CuInS}_2$  (CIS) nanocrystals (NCs). (b) The product CIS NCs have near-infrared (NIR) photoluminescence (PL), which cannot be attained in a direct fashion. (c) Sequential CE reactions result in  $\text{CuInSe}_2/\text{CuInS}_2$  dot-in-rods, by using a stoichiometric  $\text{InCl}_3$ -phosphine complex that couples the in- and outward diffusion rates. (d) The  $\text{CISE/CIS}$  NRs display tunable NIR PL.

were prepared with photoluminescence in the NIR, which cannot be synthesized in a direct fashion (Figure 10.2a,b, Chapter 6). The CE reaction is self-limiting, stopping when the ternary  $\text{CuInS}_2$  composition is reached. This can be understood from the anionic sublattice perspective, which has to transform from an hcp arrangement of anions to an fcc arrangement if the CE reaction was to reach completion, forming  $\text{In}_2\text{S}_3$ . The CE reaction is very delicate, and low temperatures were needed to slow down the Cu extraction rate, in order to balance with the In incorporation rate. Therefore, we extended our method to a single-step exchange, in which  $\text{Cu}^+$  can only be extracted when  $\text{In}^{3+}$  is deposited at the same surface site, by the use of a stoichiometric  $\text{InCl}_3$ -phosphine complex (Chapter 7). In this way, CE reactions even occur in large anisotropic (hetero) structures, such as dot-in-rod heteronanocrystals (Figure 10.2c,d). In our approach, the synthetic versatility of core/shell  $\text{CdSe/CdS}$  nanocrystals is exploited in a sequential cation exchange pathway (depicted in Figure 10.2c), in which  $\text{Cd}^{2+}$  is exchanged for  $\text{Cu}^+$  and subsequently  $\text{Cu}^+$  is partially exchanged for  $\text{In}^{3+}$ . The product  $\text{CuInSe}_2/\text{CuInS}_2$  dot core/rod shell nanorods display tunable NIR photoluminescence (Figure 10.2d), so by a judicious choice of the starting Cd based (hetero)architecture and corresponding visible PL, different emission wavelengths in the NIR can be obtained. Our results highlight the composition tunability of Cu chalcogenide nanomaterials *via* topotactic cation exchange reactions, which results in complex (hetero)architectures with unprecedented optoelectronic properties, such as NIR photoluminescence.

### 10.3 Superstructure Tailoring

Colloidal nanomaterials can self-assemble into 2D superstructures, of which the properties depend on the building block composition as well as on the geometry into which the building blocks self-assemble. The results discussed above are particularly relevant for the preparation of compositionally diverse 2D superstructures with different 2D superstructure geometries. By controlling the size and shape (*via* direct synthetic methods described in Chapters 3–5) and composition (*via* topotactic CE reactions, Chapters 6 and 7) different superstructures can be obtained. For example, when ZnS polyhedra (prepared from  $\text{Cu}_{2-x}\text{S}$  polyhedra *via*  $\text{Zn}^{2+}$  for  $\text{Cu}^+$  CE reactions) are self-assembled into 2D superstructures, the shape of the building blocks determines the final geometry (Figure 10.3a, Chapter 8). When perfect bipyramids are assembled (so with sharp tips), a hexagonal 2D superstructure is formed, whereas a mere 5% tip truncation changes the geometry to a tetragonal 2D superstructure. Further truncation (20%, bifrustums) changes the geometry back to a hexagonal arrangement. Furthermore, we have shown that surface functionalization can give directionality to the self-organization process (Chapter 9). We found with *in-situ* Grazing Incidence Small-Angle and Wide-Angle X-ray Scattering (GISAXS/GIWAXS) and *ex-situ* Electron Diffraction (ED, Figure 10.3b) that ZnS bifrustums atomically align in the presence of oleic acid ligands, whereas random orientation within the 2D plane is encountered for the native oleylamine ligands. These results further indicate that by a careful selection

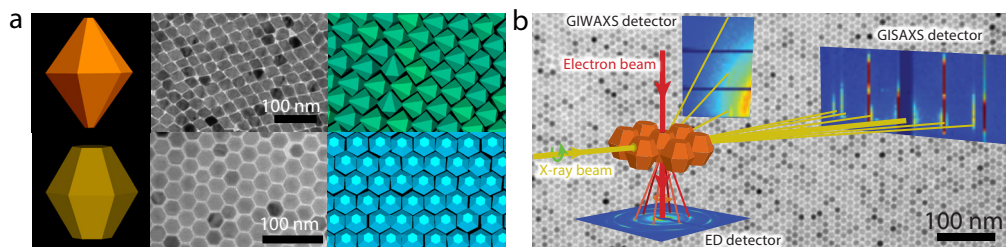


**Figure 10.3. Superstructure tailoring toward 2D ZnS NC superstructures.** (a) Wurtzite ZnS polyhedra can self-organize into 2D superstructures, of which the geometry depends on the shape of the individual building blocks, changing it from tetragonal (truncated bipyramids, top) to hexagonal symmetry (bipyramids, bottom). (b) The self-organization mechanism for the ZnS bipyramids was studied with *in-situ* GISAXS/GIWAXS and *ex-situ* ED, which revealed that the addition of oleic acid ligands gives directionality to the self-organization process.

of size, shape, composition and surface (*via* synthetic methods discussed and developed in this thesis) tailored 2D superstructures can be prepared with novel optoelectronic properties, which may prove beneficial for several applications (*e.g.* photovoltaics, plasmonics, light-emitting diodes, bioimaging).

## 10.4 Outlook

The results discussed in this thesis provide a pathway toward tailored superstructures with interesting properties. However, there are many other research lines that can still be followed.

For example, the exciton recombination in ternary Cu chalcogenides should be investigated in closer detail. Especially the band offset between different ternary Cu chalcogenides is an interesting topic of research, *i.e.* whether nanoscale Type-I, Type-I<sup>1/2</sup> or Type-II junctions are formed. For this purpose, different sizes of CuInSe<sub>2</sub> cores with either 2, 4 or 6 monolayers of CuInS<sub>2</sub> can be synthesized *via* a sequential topotactic CE reaction pathway from parent CdSe/CdS HNCs. Furthermore, the (collective) optoelectronic properties of 2D superstructures of various compositions could be investigated, *e.g.* lasing or plasmonics. Besides, the core/shell CISE/CIS NRs might be used in bioimaging applications, due to the lower toxicity of the components and the NIR PL tunability, which can be exactly in the NIR tissue absorption window.

Furthermore, the optoelectronic properties of the 2D Cu<sub>2-x</sub>S nanosheets synthesized in this work should be investigated. To this end, ultrafast spectroscopy techniques, such as terahertz (THz) and transient absorption (TA) spectroscopy, could be used to study the carrier dynamics within these materials.



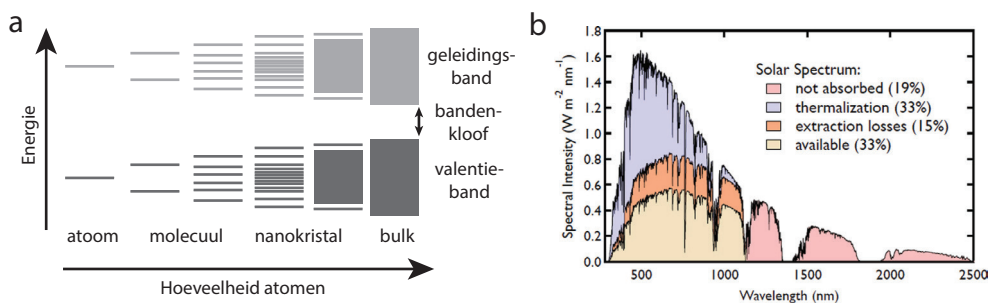
# Samenvatting in het Nederlands

## **SAMENVATTING**

In dit hoofdstuk wordt er wat achtergrond informatie gegeven over het onderzoek dat beschreven staat in dit proefschrift. Halfgeleiders en hun invloed in ons alledaagse leven worden kort besproken voor een breder publiek. Daarna worden de belangrijkste resultaten van het onderzoek kort samengevat en worden er suggesties gedaan voor toekomstig onderzoek.

## Halfgeleiders en halfgeleider nanokristallen

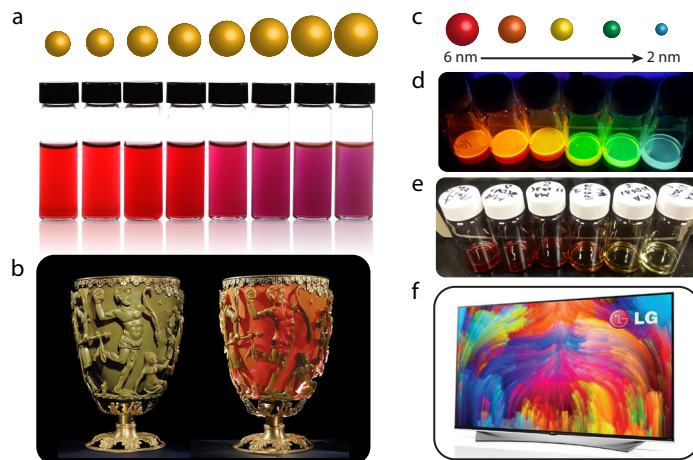
Halfgeleider materialen zijn cruciaal in ons alledaagse leven en veel mensen zouden niet eens meer zonder ze kunnen. Wat te denken van bijvoorbeeld je smartphone of televisie? Allebei bevatten ze een halfgeleider genaamd silicium. Ook de commerciële zonnecellen van vandaag de dag zijn gemaakt van silicium. Maar wat is een halfgeleider precies en wat maakt halfgeleiders zo speciaal? Een halfgeleider bevindt zich precies tussen een isolator (niet geleidend) en een metaal (zeer geleidend) en geleidt alleen onder speciale omstandigheden, bijvoorbeeld door de energie van het zonlicht op te nemen. Geleiding wordt veroorzaakt door de beweging van ladingen in een materiaal. In een halfgeleider zoals silicium zijn dit elektronen. Die vrij bewegende elektronen kunnen op verschillende manieren gecreëerd worden, zoals door het opnemen van zonlicht. Op deze manier wordt een elektron ‘aangeslagen’ naar een hogere toegestane energie toestand, wat weer een positieve lading, het gat, achterlaat. Een halfgeleider is opgebouwd uit toegestane elektron toestanden (banden genoemd) en verboden toestanden (de bandenkloof genoemd, Figuur 1a). Een van de banden is volledig gevuld met elektronen (de valentieband) en een band is compleet leeg (de geleidingsband). De bandenkloof van een bulk halfgeleider wordt bepaald door het materiaal, en in het geval van silicium (gebruikt in zonnecellen en chips in telefoons) heeft de bandenkloof een energie van 1.1 elektronvolt (eV). De zon zendt licht uit van verschillende energie, variërend van ultraviolet licht (hoge energie) tot zichtbaar licht (de kleuren van de regenboog bijvoorbeeld) en uiteindelijk infrarood licht (lage energie). Licht met een te lage energie kan er niet voor zorgen dat een elektron van de valentieband naar de geleidingsband gaat, terwijl licht met teveel energie zorgt voor verlies van energie in de vorm van warmte (Figuur 1b). Hierdoor kan maar een klein gedeelte (33%) van het zonlicht effectief gebruikt worden voor het creëren van vrij bewegende elektronen. Dit limiteert de efficiëntie van zonnecellen aanzienlijk en daarom zijn onderzoekers wereldwijd andere oplossingen aan het zoeken om het zonlicht efficiënter te kunnen



**Figuur 1. Halfgeleiders.** (a) Een halfgeleider bestaat uit twee banden waarvan een band compleet gevuld is met elektronen (valentieband) en een band compleet leeg is (geleidingsband), met daartussen verboden energie toestanden (de bandenkloof). (b) Als zonlicht met voldoende energie op een halfgeleiders valt, kan een elektron naar de lege geleidingsband gaan. Als de energie van het licht te laag is, gebeurt er niks. Is de energie te hoog, dan gaat veel energie verloren als warmte. Deze processen limiteren de efficiëntie van halfgeleiders in verschillende toepassingen, zoals zonnecellen.

gebruiken.

Een jaar of 30 geleden werden zogenaamde halfgeleider nanokristallen ‘ontdekt’. Als een halfgeleider (of een metaal) dimensies heeft op de nanoschaal (nanometer = een miljardste van een meter) veranderen de eigenschappen aanzienlijk. Er bestaat zelfs een voorbeeld uit de Romeinse tijd, de zogenaamde Lycurgus beker (Figuur 2b), waarin duidelijk te zien is dat de eigenschappen van gouddeeltjes van een paar nanometer substantieel anders zijn dan bulk goud zoals we het kennen in ringen bijvoorbeeld. De Romeinen maakten per ongeluk gebruik van dit fenomeen, omdat ze niet wisten dat ze hele kleine gouddeeltjes in hun glas hadden zitten. De Lycurgus beker is groen als het licht van de voorkant komt, maar als het licht van de achterkant komt gloeit hij rood op. Recenter hebben onderzoekers gouddeeltjes van verschillende grootte gemaakt, waarbij de kleur kan variëren van rood (kleine deeltjes) tot paars (grote deeltjes, Figuur 2a). Dit wordt veroorzaakt doordat de verschillende gouddeeltjes verschillende energieën opnemen, en dus voor het oog een andere kleur hebben. De eerdergenoemde ‘ontdekking’ 30 jaar geleden heeft te maken met een halfgeleider genaamd cadmium selenide. Als deze deeltjes klein genoeg gemaakt worden (ongeveer 2 tot 6 nm) dan zenden ze verschillende kleuren licht uit na excitatie van een elektron over de bandenkloof (Figuur 2c,d). Dit is dus het tegenovergestelde proces van het absorberen/opnemen van licht. Het uitzenden van licht wordt ook wel fotoluminescentie genoemd en heeft bijvoorbeeld een toepassing in het produceren van lampen. Het licht dat cadmium selenide nanokristallen uitzenden na excitatie heeft een hele felle kleur en tegenwoordig worden zulke deeltjes al gebruikt in verschillende televisies (Figuur 2f). Een groot nadeel van cadmium selenide nanokristallen is dat cadmium zeer giftig is.

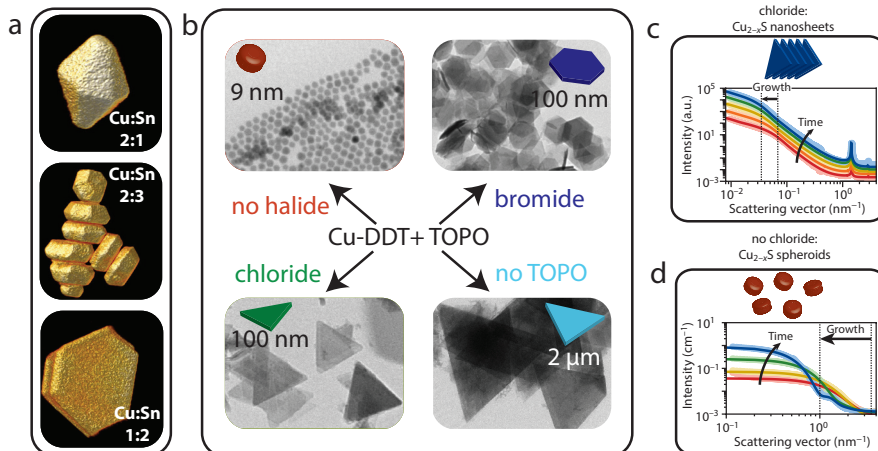


**Figuur 2. Eigenschappen op de nanoschaal.** (a) Gouddeeltjes van verschillende grootte absorberen andere kleuren licht. (b) Dit fenomeen werd (onbewust) al gebruikt in de Romeinse tijd. De Lycurgus beker is groen als het licht van de voorkant komt, maar wordt rood als het licht van achter komt. (c) Cadmium selenide is een halfgeleider, die, als de grootte wordt gevarieerd van 2 tot 6 nm, (d) andere kleuren licht uit gaat zenden. (e) De verschillen tussen deze deeltjes zijn een stuk minder duidelijk als we alleen naar de absorptie van licht kijken. (f) Vanwege de felle kleuren die deze deeltjes uitzenden, worden cadmium selenide nanokristallen tegenwoordig al gebruikt in televisie schermen.

Daarom wordt er momenteel veel onderzoek gedaan naar minder giftige nanokristallen, zoals koper-houdende nanokristallen, beschreven in dit proefschrift.

## De vorm op maat maken

Naast de grootte en samenstelling bepaalt de vorm van de nanokristallen ook de eigenschappen. Bijvoorbeeld, CdSe nanostaafjes (1-dimensionaal) en CdSe nanovelletjes (2-dimensionaal) kunnen gemaakt worden, met andere eigenschappen dan bolvormige CdSe nanokristallen. Onderzoekers proberen de laatste jaren om verschillende vormen te maken door met de synthese parameters te spelen, zoals temperatuur, concentratie en de anion en kation precursors. Daarnaast worden verschillende liganden gebruikt die voor anisotrope groei kunnen zorgen. Koper sulfide is een interessant materiaal voor het maken van complexe, anisotrope nanodeeltjes, omdat koper sulfide veel verschillende stabiele kristalstructuren heeft. Hierdoor kan de groei van de nanodeeltjes vrij gemakkelijk gemanipuleerd worden, waardoor de nanodeeltjes harder groeien in een bepaalde richting. In het eerste gedeelte van dit proefschrift worden verschillende synthese procedures besproken die resulteren in complexe, anisotrope koper sulfide nanodeeltjes. Bijvoorbeeld, hexagonale bipiramides en nanoplaatjes van verschillende dikte kunnen gemaakt worden door alleen de concentratie van de tin-thiolaat complexen te variëren (Hoofdstuk 3, Figuur 3a). Daarnaast kunnen ook 2D koper sulfide nanovelletjes gemaakt worden, die maar 2 nanometer dik zijn en een diameter van 100 nanometer tot 3 micrometer kunnen hebben (Hoofdstuk 4, Figuur 3b). Verder kan de vorm van deze nanovelletjes gemanipuleerd worden door verschillende halides te introduceren (bromide resulteert in hexagonale deeltjes en chloride in driehoekige

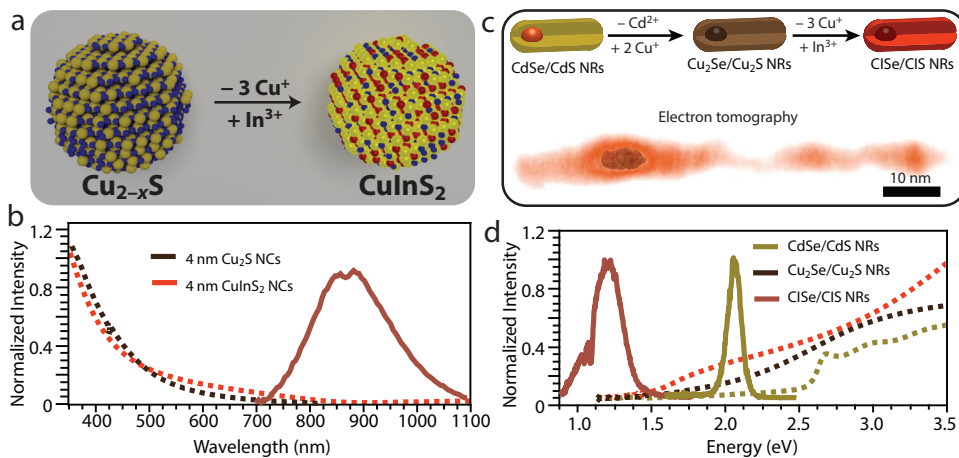


**Figuur 3. De vorm van koper sulfide nanodeeltjes op maat maken.** (a) Door alleen de concentratie tin-complexen te variëren, kunnen verschillende vormen koper sulfide nanodeeltjes gemaakt worden (bipiramides en dikke/dunne nanoplaatjes). (b) Als chloride toegevoegd wordt aan een koper sulfide nanodeeltjes synthese, worden hele dunne nanovelletjes gevormd. (c,d) *In-situ* X-ray verstrooiing experimenten laten zien dat chloride de precursors stabiliseert, waardoor dunne nanovelletjes vormen.

deeltjes). Het groei mechanisme is bestudeerd met *in-situ* kleine hoek X-ray verstrooiing experimenten (Hoofdstuk 5, Figuur 3c,d). Met deze experimenten hebben we gezien dat de halides de gestapelde koper-thiolaat precursor stabilizeren totdat de koper sulfide gevormd kan worden. Doordat de precursor gestapeld is, zijn de kleine koper sulfide nanovelletjes ook gestapeld, waardoor ze niet in de dikte kunnen groeien. De resultaten die in Hoofdstuk 3 tot 5 besproken worden, laten duidelijk zien dat koper sulfide nanodeeltjes heel veel vormen en maten kunnen hebben, wat, zoals later zal blijken, voordelig kan zijn voor verschillende toepassingen.

## De samenstelling op maat maken

De resultaten besproken in Hoofdstuk 3 tot 5 kunnen ook in een breder perspectief gezien worden. Dit komt doordat koper ionen in koper sulfide nanokristallen gemakkelijk uitgewisseld kunnen worden voor andere kationen (kation uitwisseling genoemd). Dit komt voornamelijk door het feit dat koper ionen heel klein zijn en daardoor ook gemakkelijk door de nanodeeltjes kunnen bewegen. Op deze manier kunnen nanodeeltjes gemaakt worden die anders niet mogelijk zouden zijn. Meestal blijven de anionen op hun plek tijdens de kation uitwisseling, waardoor de vorm van de nanodeeltjes behouden blijft. Hierdoor kunnen veel complexe materialen gemaakt worden die anders niet mogelijk waren geweest, zoals gedoteerde nanodeeltjes of kern/schil nanodeeltjes.



**Figuur 4. De samenstelling op maat maken.** (a) Gedeeltelijke kation uitwisseling kan gebruikt worden om koper sulfide te veranderen in koper indium sulfide nanodeeltjes. (b) De koper indium sulfide nanodeeltjes hebben fotoluminescentie in het infrarood, wat met directe synthese niet mogelijk is. (c) Complexe kern/schil nanostaafjes kunnen gemaakt worden als cadmium selenide/cadmium sulfide nanostaafjes als begin deeltjes gebruikt worden. Eerst wordt de cadmium voor koper uitgewisseld en daarna een deel van de koper voor indium. Dit is mogelijk met een stoichiometrisch indium-phosphine complex, wat ervoor zorgt dat koper de nanostaafjes kan verlaten als er tegelijkertijd indium aanwezig is. (d) Op deze manier kunnen nanostaafjes met variërende infrarood fotoluminescentie gemaakt worden.

---

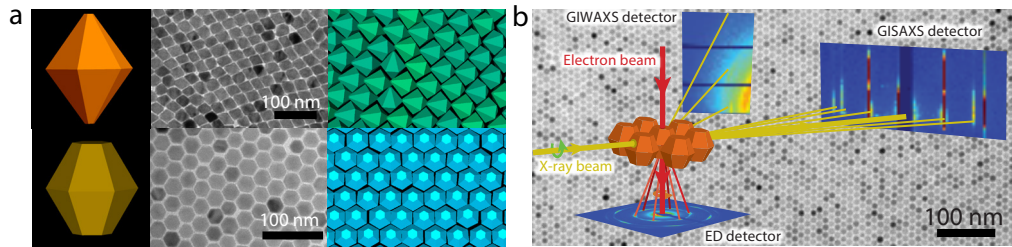
---

In dit proefschrift worden ook kation uitwisseling reacties besproken. Koper ionen in koper sulfide nanodeeltjes kunnen uitgewisseld worden voor indium ionen, waardoor koper indium sulfide nanodeeltjes gevormd worden (Hoofdstuk 6, Figuur 4a). Koper indium sulfide nanodeeltjes zijn heel interessant omdat ze fotoluminescentie vertonen die kan variëren van rood licht (kleine deeltjes) tot infrarood licht (grote deeltjes, Figuur 4b). Het bleek zo te zijn dat de uitwisseling van indium voor koper heel subtiel moet gebeuren, omdat anders de deeltjes volledig oplossen. Daarvoor moest de reactie op hele lage temperatuur uitgevoerd worden. Verder bleek de reactie zelf te stoppen als ongeveer de helft van de koper ionen was uitgewisseld voor indium ionen. Dit kunnen we begrijpen als we naar het anion rooster kijken. Zoals eerder vermeld, is het anion rooster heel erg sterk en kunnen de kationen er gemakkelijk uit bewegen. Maar om alle koper te vervangen voor indium, moeten de anionen ook van positie veranderen. Dit is zeer ongunstig, waardoor maar de helft van de koper ionen uitgewisseld wordt.

We hebben onze strategie voor kation uitwisseling daarom aangepast naar een enkele stap reactie. Hierbij kan koper alleen uit de nanodeeltjes gehaald worden, als indium ook gelijk aanwezig is om erin te gaan (Hoofdstuk 7, Figuur 4c). Hiervoor hebben we een stoichiometrisch indium chloride phosphine complex gebruikt, dat de in- en uitgaande snelheid aan elkaar koppelt. Doordat de snelheden aan elkaar gekoppeld zijn, kan de uitwisseling zelfs plaatsvinden in grote, anisotrope, complexe heterostructuren, wat resulteert in koper indium selenide / koper indium sulfide kern/schil nanostaafjes. Deze nanostaafjes vertonen ook infrarood fotoluminescentie (Figuur 4d). Om deze complexe structuren te maken, hebben we gebruik gemaakt van cadmium selenide / cadmium sulfide heteronanostaafjes, waarin de cadmium eerst voor koper uitgewisseld wordt, waarna de koper gedeeltelijk vervangen wordt door indium. Door de keuze van de grootte van de cadmium selenide/cadmium sulfide nanostaafjes, kunnen we uiteindelijk verschillende golflengtes infrarood licht maken. Deze resultaten laten zien dat de samenstelling van koper houdende nanodeeltjes makkelijk gemanipuleerd kan worden, waardoor structuren gemaakt kunnen worden die anders onmogelijk waren gebleven.

## **De superstructuur op maat maken**

Colloïdale nanokristallen kunnen ook zichzelf organiseren in 2-dimensionale superstructuren, waarvan de eigenschappen bepaald worden door de samenstelling van de bouwstenen (die dus gecontroleerd kan worden door kation uitwisseling bijvoorbeeld) alsmede door de ordering van de bouwstenen ten opzichte van elkaar. De ordering kan beïnvloed worden door de vorm van de bouwstenen (die bepaald kan worden door de keuze voor de synthese procedure). Bijvoorbeeld, de bipyramides en bifrustums, besproken in Hoofdstuk 3, kunnen getransformeerd worden in zink sulfide nanodeeltjes, na zink voor koper uitwisseling. Deze zink sulfide nanodeeltjes vormen vervolgens een 2-dimensionale superstructuur, waarbij de bipyramides een tetragonale



**Figuur 5. Superstructuren op maat maken.** (a) Wurtziet ZnS nanodeeltjes kunnen zelf-organiseren in 2D superstructuren, waarvan de ordening afhangt van de vorm van de nanodeeltjes. Als de bipiramides afgeknot zijn, hebben de deeltjes een tetragonale ordening, terwijl verder afgeknotte deeltjes (bifrustums) een hexagonale ordening hebben in een 2D superstructuur. (b) Het mechanisme van de zelf-organisatie kan bestudeerd worden met X-ray verstrooiing experimenten en electronen diffractie. Deze experimenten laten zien dat de ZnS nanodeeltjes zich atomair uitlijnen ten opzichte van elkaar als oliezuur wordt toegevoegd.

ordering hebben, en de bifrustums een hexagonale ordening (Hoofdstuk 8, Figuur 5a). Als deze resultaten vergeleken worden met berekeningen aan de zelf organisatie van perfecte bipiramides (dus met scherpe punten), zien we dat perfecte bipiramides ook een hexagonale structuur vormen. De berekeningen voor een klein beetje afgeknotte bipiramides (ongeveer 5%) laten daarentegen een tetragonale ordening zien, zoals in het experiment. Als de nanodeeltjes verder afgeknot worden (ongeveer 20%, bifrustum), verandert de superstructuur weer naar een hexagonale ordening. Daarnaast hebben we zelf-organisatie experimenten gedaan waarbij oliezuur liganden toegevoegd werden aan zink sulfide bifrustums (Hoofdstuk 9). We hebben gezien dat de oliezuur liganden ervoor zorgen dat de deeltjes zich atomair uitlijnen ten opzichte van elkaar. We hebben dit proces *in-situ* bestudeerd met kleine en grote hoek verstrooiing van Röntgen straling onder een scherpende hoek van inval, alsmede *ex-situ* elektronen diffractie. Met deze combinatie van technieken konden we heel effectief de nanodeeltjes op het vloeistof-lucht oppervlak bekijken en zowel de ordening op nanometer als atomaire schaal bekijken.

Onze resultaten (Hoofdstuk 3 tot 9) laten zien dat door een bewuste keuze van de vorm, grootte, samenstelling en oppervlak van de nanodeeltjes, op maat gemaakte 2D superstructuren gemaakt kunnen worden. Met deze aanpak kunnen materialen gemaakt worden die voordelig zijn voor verschillende toepassingen, zoals zonnecellen en LED-lampen.

## Toekomstig onderzoek

Alhoewel de resultaten besproken in dit proefschrift al een zeer interessante route zijn naar op maat gemaakte materialen voor verschillende toepassingen, is er nog steeds veel toekomstig onderzoek mogelijk. De recombinitie van ladingen in koper-houdende

---

---

nanomaterialen, wat resulteert in fotoluminescentie, kan in meer detail bestudeerd worden. Daarnaast kunnen de eigenschappen en toepassingen van verschillende 2D superstructuren bestudeerd worden, zoals plasmonische eigenschappen of lasers. Verder kunnen de kern/schil koper-houdende nanostaafjes getest worden in biologische toepassingen, vanwege de fotoluminescentie in het infrarood, wat niet door weefsel opgenomen wordt.

Daarnaast kunnen de eigenschappen van de 2D koper sulfide nanovelletjes in meer detail bestudeerd worden. Hiervoor kunnen hele snelle spectroscopie technieken gebruikt worden, zoals terahertz (THz) en transiënte absorptie spectroscopie. Hiermee kan de dynamica van de ladingen in deze nanovelletjes gemeten worden in deze nieuwe materialen.





## Acknowledgments

“This is the end” zingt Jim Morrison. En dit is het einde van mijn tijd bij CMI. Het is een cliché, maar 4 jaar PhD vliegt echt voorbij. Maar als je dan rustig terugdenkt aan alle mooie momenten en alle mensen die je hebt ontmoet door de jaren heen, lijkt het ook weer een hele lange tijd. Ik wil dan ook al deze mensen persoonlijk bedanken voor hun bijdrage aan dit proefschrift, want zonder dat je het naar je zin hebt, is onderzoek doen niet mogelijk.

Ik wil graag met **Celso** beginnen, want zonder jou was dit proefschrift er natuurlijk nooit gekomen. Je enthousiasme voor het onderzoek heeft mij altijd weten te motiveren. Ik kan me nog goed het eerste college Nanomaterialen herinneren, waarin je vol enthousiasme het quantum confinement effect uitlegde, en daarmee mijn liefde voor nanomaterialen hebt aangewakkerd. Ik heb ontzettend genoten van onze (vaak lange) brainstorm-sessies, waar we gedurende een aantal uur wilde ideeën naar elkaars hoofd wierpen (soms tot verwarring van aanwezige studenten aan toe) en het dan toch vaak wisten te presteren om met een interessant onderzoek op de proppen te komen. Daarnaast heb ik ook van je geleerd dat er Brazilianen bestaan die niet van voetbal en carnaval houden, een belangrijke les.

Naast Celso wil ik ook **Andries** als begeleider bedanken. Ook al was je niet direct betrokken bij mijn onderzoek, je toonde er wel altijd veel interesse voor tijdens het jaarlijkse gesprek. En wat ik nooit zal vergeten is dat je al je werk neerlegde om mijn oma van 94 een rondleiding inclusief minicollege te geven. Maar naast het onderzoek, heb ik genoten van je extreme spelvreugde (gemixt met fanatisme) tijdens het jaarlijkse CMI bowlen, het kerst-klaverjastoernooi, de Debye sportdag en de potjes klaverjassen tijdens de lunch (met leverpastei uiteraard!). En niet te vergeten de flinke pan boerenkool met worst die elk jaar door jou gemaakt wordt voor het CMI kerstdiner.

Ik had het geluk (of was het wijsheid) om in de leukste kamer van CMI te zitten: OL158. Samen met **Freddy**, **Joost** (of **Jozef**, zoals Freddy en ik hem noemen) en **Herman** heb ik 3 jaar in deze kamer gezeten. Het ging regelmatig over wetenschap, waarin we elkaar goed konden goereren (Jozef: AFM/STM-goeroe, Freddy: luminescentie-goeroe), maar het ging ook vaak genoeg niet over wetenschap, zoals het organiseren van ‘sociale activiteiten’ (OL158 casino- en spareribs-avonden bijvoorbeeld), welk nummer Jozef nou weer voor de hele week op repeat ging zetten (keuzes: Cut your teeth van Kygo, Sultans of Swing van Dire Straits of Catch & Release van Matt Simons) of wie er nou het ‘braafst’ was (waar Freddy op de een of andere manier altijd voor mij koos). Freddy wil ik daarnaast nog bedanken voor de talloze sociale activiteiten, het delen van je kennis (over bijna alles) en het verrijken van de Nederlandse/Engelse taal met woorden als ‘supperpromising’, ‘sociale activiteit’, ‘duckling’ en ‘braveling’. Daarnaast vind ik het geweldig dat je mijn paranimf wilt zijn. Although Jozef did not tolerate anyone

---

---

else to be in our office, he made an exception when **Daniel Gamelin** arrived as a guest professor. Although you did break my phone (and paid for it), it was a pleasure to have you in our office. When we heard you would be in our lab for a second time, we offered you your desk again and we were actually surprised you accepted it. Maybe you liked ‘Cut your teeth’ from Kygo a lot? And thanks again for the All Stars you gave me after the mudwalking to Schiermonnikoog, it is an honor to wear the shoes worn by such a promising professor. Het laatste jaar nam **Jaco** de plek van Freddy over. Ik heb ervan genoten dat je mij soms probeerde weg te pesten door Kensington op te zetten, maar dat je het vervolgens dan weer goed maakte door wel een goed nummer op te zetten. Daarnaast hebben we fantastisch samen gewerkt aan de SAXS (Hoofdstuk 5) en GISAXS (Hoofdstuk 9) experimenten en hebben we buiten CMI ook nog veel leuke dingen samen ondernomen, zoals BBQs, een Golden Earring concert en natuurlijk onze USA California trip, maar daar kom ik later nog op terug. The last few months I had the pleasure of having **Maryam** in my office as well. And although we don’t know each other that long, we already call each other brother and sister. It was an absolute pleasure to get to know you and enjoy your Persian cooking, your kindness and your humor. In some way you are always able to make me smile, my sister!

Tijdens mijn PhD heb ik ook een aantal master studenten begeleid. Vrijwel gelijk toen ik begon met mijn PhD onderzoek, begonnen Quinten en Josine aan hun masteronderzoek bij mij. **Quinten**, jouw vindingrijkheid qua syntheses is bewonderenswaardig en we zaten vaak op een lijn qua ideeën. Het is heel knap om 2 papers uit je masteronderzoek te halen (Hoofdstuk 5 en 8) en jij hebt het voor elkaar gekregen! Het is dan ook niet vreemd dat het in Italië ook erg goed met je gaat en ik wens je nog veel succes in de toekomst. **Josine**, jij had wat minder geluk met het onderzoek, maar desondanks heb je nooit opgegeven en dat is in je te prijzen. Ik wil je ook nog bedanken voor het verzinnen van de naam ‘team Kesterite’ en de gezellige tijd die we gehad hebben en ik wens je heel veel succes bij Shell.

Na een jaartje sloot een nieuw lid zich aan bij team Kesterite: **Anne**. Ook jij wist vrij snel je weg op het lab te vinden, wat mooie resultaten heeft opgeleverd. In eerste instantie hebben we wat geploeterd met het werkend krijgen van de cation exchange, maar uiteindelijk is het gelukt, wat een prachtige publicatie heeft opgeleverd. Daarna heb je je verder ontwikkeld tot gewaardeerd collega, CIS-koningin en koffiejuffrouw.

Als laatste master student kwam **Stijn**, de grootste braveling van Midden-Nederland volgens Freddy, zijn onderzoek bij mij doen. Stijn, je hebt je weten te ontwikkelen in een cation exchange expert, en daarom schrijf je (terecht) het paper ook zelf. Ik bewonder je doorzettingsvermogen, je gedetailleerde analyses, je computer-skills en je vriendelijke persoonlijkheid. Het was kortom een groot plezier om met je samen te werken en ik ben ervan overtuigd dat je het geweldig gaat doen in je PhD.

Naast master studenten heb ik ook 4 bachelor studenten (of ducklings, zoals ze vaak ook genoemd werden) mogen begeleiden: Mark, Nienke, Sander en Angela. **Mark**, je hebt mooi werk gedaan aan het controleren van de zink voor koper uitwisseling, wat zeker nog toekomstig onderzoek verdient. **Nienke**, jij hebt prachtig werk geleverd aan  $\text{CuInS}_2\text{-Cu}_2\text{S}$  heteronanodeeltjes en daar zelfs zonnecellen van gemaakt. Je was een heel zelfstandige student, want ondanks dat ik veel weg was vanwege Grenoble-experimenten, heb je een super mooie thesis geschreven en fantastische experimenten gedaan. **Sander**, jij was een van de drijvende krachten achter Hoofdstuk 9 van dit proefschrift. Jij mocht mee met onze Grenoble-experimenten op ID10, waar je eerst tijdens een maand stage in Grenoble heel veel geleerd hebt over de theorie, en die vervolgens fantastisch hebt toegepast op de data-analyse van onze experimenten. Ik zal onze beamtrip met polonaise op 'Eet veel bananen' van Ronnie Ruysdael en Zanger Rinus echt nooit vergeten. De laatste bachelor student was **Angela**. Jou wil ik graag bedanken voor de enorme berg experimenten die je gedaan hebt, ondanks dat het voor jou en voor mij een hele drukke periode was. Het feit dat je nog langer door bent gegaan omdat het nog niet naar je zin was, geeft je doorzettingsvermogen aan en dat heb ik zeer gewaardeerd. **Laura** en **Thomas** wil ik nog bedanken voor hun harde werk tijdens hun eerstejaarsproject. Het waren mooie resultaten, helaas ben ik er nooit echt aan toe gekomen om de vervolgent experimenten te doen zodat we het misschien konden publiceren.

De goede werkomgeving bij CMI is natuurlijk te danken aan al mijn collega's. **Hans**, bedankt voor je technische assistentie met veel dingen voor mijn onderzoek en op het lab. Wat je ogen zien, maken je handen, dat is echt een kwaliteit die bij CMI gemist gaat worden nu je met pensioen bent. Daarnaast was het altijd fijn om de week te beginnen met een kop koffie in jouw kantoor samen met Jozef. **Daniel**, bedankt voor het altijd fout voorspellen van voetbalwedstrijden, dan wist ik altijd waar ik op moest gaan inzetten. **Ingmar**, jij bent een van de weinige collega's die mij live bij DESTO heeft zien voetballen. Daarnaast wil ik je bedanken voor onze voetbalanalyses op maandag van het afgelopen Eredivisieweekend. **John Kelly**, thanks for the fun talks about our mutual passion for FC Utrecht! **Tim** en **Robin**, met jullie heb ik (na Freddy) de meeste klaverjasuurtjes doorgebracht. Ook al ging het vaak op het scherpst van de snede, het was vooral vaak ook erg grappig. Daarnaast hebben we ook vaak als 'De Beunhazen' niet onverdienstelijk aan de pubquiz meegedaan. **Joep(ske)**, ook wel 'social boy' genoemd om een reden, een van de grappigste dagen van mijn PhD heb ik met jou en Hans gehad in Grenoble. Als je bier niet lekker vindt, hoef je echt geen halve liter over je broek te gooien hoor! En als ik je dan ga uitlachen, hoef je voortaan ook niet meer met me te gaan vechten, je bent geen partij! **Elleke**, het was leuk om met iemand van het X-c practicumgroepje op dezelfde groep te werken, wij gaan echt 'way back'. **Mathijs**, je bent een fantastische kerel en een uitstekende wetenschapper (ook al gaat Bismut het niet redden ben ik bang). Dankzij jou weet ik dat artikelen met een vraagteken in de titel gewoon geaccepteerd worden. Bedankt voor de avonden

---

---

bankhangen, sterke verhalen vertellen, pizza eten en pils drinken. **Federico**, my tiny Italian friend, I had such a great time with you and I hope (and think actually) that we stay in touch. There are numerous social activities that I can mention, but our candy trip to Paris with Freddy, our 3 weeks in South-Korea/Japan and our Euro2016 trip to Lille to watch Italy-Ireland really stand out. It is a pleasure that you want to be my paranimf and that you will inherit my desk in OL158. Treat it well! **Annalisa**, you arrived at CMI almost at the same time as Maryam and Federico and we got along quite fast. Thanks for your kindness and good luck with your research. Verder wil ik de huidige groepsleden van CMI die ik nog niet genoemd heb bedanken: **Allan, Annelies, Carlo, Chenghui, Christa, Christiaan, Chun Che, Harold, Jacobine, Marlou, Nadine, Onno, Stephan, Tim Prins** en **Winston**.

There are also some former group members that I would like to thank. **Francesca**, my VGFF, your enthusiasm and happiness always made me happy as well. **Rosa**, the same holds for you as for Francesca actually, the two of you always made other people happy. I really enjoyed our visit to Bilbao in 2015, that was very bonding! **Joren**, je BBQ feestjes op de Cambridgelaan waren legendarisch, maar niet zo legendarisch als onze California trip met Jaco in een rode Mustang convertible! Santa Maria en het Sequoia National park in de nacht zonder zaklamp horen nog steeds bij mijn meest angstige momenten ooit, bedankt daarvoor. **Esther, Wiel, Mark B** en **Relinde** wil ik graag bedanken voor hun hulp toen ik nog masterstudent bij CMI was. Ook al had ik officieel geen begeleider, ik kon altijd bij jullie langs komen met vragen. And **Shun**, although you only spend a few months in our lab, I got the know you as a very friendly, fun guy. I had a lot of fun with you during the FOM party and when we met in Tokyo and climbed the Tokyo tower.

Next to collaborations with group members, I also had some external collaborations. Allereerst wil ik **Hans Meeldijk** noemen, want we hebben aardig wat uren achter de microscoop samen doorgebracht. Ik vond het altijd wel mooi dat je eerste vraag aan mij was: Wat heb je nou weer voor zoi gemaakt? En dat we dan wat metingen gingen doen en je dan vaak toch wel enthousiast was en graag mooie plaatje wilde schieten. **Anjan Gantapara, Giuseppe Soligno, René van Roij** and **Marjolein Dijkstra** I would like to thank for our very fruitful collaboration on the experimental and computational self-assembly of truncated polyhedra. I would like to mention **Andrei Petoukhov** for his help with the synchrotron experiments in Grenoble and for the candy during the meetings we had to discuss the proposals and the results. I would like to thank **Sabine Gradmann** and **Marc Baldus** for our collaboration on the Sn(IV)-complexes, which they studied with <sup>119</sup>Sn-NMR. It took us quite some time, but in the end we managed to get a great publication out. Whenever I wanted cool images, I turned to **Marijn van Huis** (UU) or **Sara Bals** (EMAT, Antwerp). I had a huge amount of collaborations with the EMAT group in Antwerp, and they always managed to get great results. Special thanks to **Thomas Altantzis, Tom Willhammar, Xiaoxing Ke** and **Eva Bladt** for their

great work. There were also some collaborations that did not result in publications (yet), but I would like to thank these people as well: **Da Wang/Alfons van Blaaderen** (UU), **Ivan Ivanov/Mischa Bonn** (Max Planck Mainz) and **Diana Car/Erik Bakkers** (TU Eindhoven).

En als laatste, mijn vrienden en familie. Als ik niet bezig was met mijn PhD, was ik of aan het voetballen of andere leuke dingen aan het doen met mijn vrienden. **Nick, Bliem, Evert, Floris, Remco, Jan-Maarten** en **Steek**, de meesten van jullie ken ik al vanaf een jaar of 7-8 toen we allemaal bij Geinoord in Nieuwegein voetbalden en we zijn nog steeds vrienden en dat zullen we blijven ook. Toen ik in Utrecht ging wonen en dus ook voetballen, ging ik eerst samen met Bliem, maar al snel had ik veel nieuwe vrienden bij DESTO. **Jurre, Koef, Kemp, Teun, Tijs** en **Jan-Jaap**, ook dankzij jullie heb ik een geweldige tijd in Utrecht gehad en ik ben ervan overtuigd dat ook hier vriendschappen voor het leven ontstaan zijn. **Mamma, Pappa** en **Rosanne**, jullie hebben altijd voor me klaar gestaan, niet alleen tijdens mijn PhD, maar uiteraard ook daarvoor en straks erna. Jullie hebben altijd veel interesse in mijn onderzoek getoond, ook al begrepen jullie er vaak volgens eigen zeggen niks van. Alhoewel Roos nog wel eens een fout uit een poster van mij heeft gehaald. Ik hou heel erg veel van jullie! En natuurlijk niet te vergeten mijn oma, **oma Koekoek**, die op 94 jarige leeftijd voor het eerst op een onderzoeksgroep kwam kijken en haar ogen uitkeek. Ik ben ontzettend blij en trots dat je mijn oma bent en dat je deze dag meemaakt. En oom **Bert** en **Theo**, nu mag ik eindelijk op de bovenste trede op de foto met jullie!

En als allerlaatste, **Elientje**. Een van de mooiste dingen, zo niet de mooiste, die ik uit Utrecht meeneem ben jij. Ik vind je geweldig en ons leven samen is zo mogelijk nog leuker. Je maakt me aan het lachen en je bent er altijd voor me, en ik hoop dat er nog vele prachtige jaren gaan volgen, te beginnen in Delft. Ik hou van je.

Zoals ik al zei, zong Jim Morrison “This is the end”. De volgende zin in dat nummer is “My only friend, the end”. Zoals je hier hebt kunnen lezen, klopt dat niet als je een PhD doet, want naast het diploma, hou je er ook veel vrienden aan over.



## About the author

Ward van der Stam was born in Nieuwegein, The Netherlands, on April 14, 1989. He graduated from Oosterlicht College Nieuwegein in 2007. He started his Chemistry education at Utrecht University and obtained his BSc degree in 2010, after which he entered the master programme Nanomaterials: Chemistry & Physics. He received his MSc degree *cum laude* in 2012 with a thesis entitled “Colloidal Nanostructures for Application in Quantum Dot Sensitized Solar Cells”, under the supervision of dr. Esther Groeneveld and prof. dr. Celso de Mello Donegá. He performed a 6 months MSc internship at Istituto Italiano di Tecnologia, Genova, Italy, under the supervision of dr. Hongbo Li and prof. dr. Liberato Manna, working on colloidal heteronanostructures.

In October 2012 he started working as a PhD student at Condensed Matter and Interfaces, Utrecht University, under the supervision of prof. dr. Andries Meijerink and dr. Celso de Mello Donegá. During his PhD, he worked on several topics, including synthesis of anisotropic (hetero)nanostructures, which consist of earth-abundant components, *via* direct synthesis protocols and cation exchange reactions. Furthermore, he studied the self-assembly of polyhedral nanocrystals into 2-dimensional superstructures. Most of the results described in this thesis have been published in international scientific journals and have been presented at several international conferences. During his PhD research, he supervised 4 master students and 4 bachelor students and was a teaching assistant for several courses of the Chemistry education at Utrecht University.

